Distribution Agreement

In presenting this thesis or dissertation as a partial fulfillment of the requirements for an advanced degree from Emory University, I hereby grant to Emory University and its agents the non-exclusive license to archive, make accessible, and display my thesis or dissertation in whole or in part in all forms of media, now or hereafter known, including display on the world wide web. I understand that I may select some access restrictions as part of the online submission of this thesis or dissertation. I retain all ownership rights to the copyright of the thesis or dissertation. I also retain the right to use in future works (such as articles or books) all or part of this thesis or dissertation.

Signature:

_____ _____

Hongjin Lv Date

Polyoxometalate-based Multi-Electron-Transfer Catalysts for Solar Energy Conversion

By

Hongjin Lv
Doctor of Philosophy

Chemistry

_____
Craig L. Hill
Advisor

_____
Cora E. MacBeth
Committee Member

_____
Khalid Salaita
Committee Member

Accepted:

_____
Lisa A. Tedesco, Ph.D.
Dean of the James T. Laney School of Graduate Studies

_____
Date

Polyoxometalate-based Multi-Electron-Transfer Catalysts for Solar Energy Conversion

By

Hongjin Lv
B.S. Wuhan University, China, 2010

Advisor: Craig L. Hill

An Abstract of
A dissertation submitted to the Faculty of the James T. Laney School of Graduate Studies of Emory University in partial fulfillment of the requirements for the degree of
Doctor of Philosophy in Chemistry

2015

ABSTRACT

Polyoxometalate-based Multi-Electron-Transfer Catalysts for Solar Energy Conversion

The chemistry of polyoxometalates (POMs) has been extensively and increasingly studied in recent years. The high tunability of POM redox, acid-base and other properties makes them attractive candidates for transition-metal-based multi-electron-transfer catalysis. The focus of this thesis is to design/synthesize functional transition-metal-substituted POMs, explore their structural and electronic features and investigate their applications in solar energy conversion field: mainly focusing on POM-based water oxidation catalysts (WOCs) and water reduction catalysts (WRCs).

This dissertation contains four major parts: The first part reports the synthesis, characterization, and catalysis of a novel banana-shaped hexanuclear cobalt-containing tungstovanadate complex, $[(Co(OH_2)Co_2VW_9O_{34})_2(VW_6O_{26})]^{17-}$. Considering the instability of such a complex in basic borate buffer solution that is used for water oxidation catalysis, its catalytic activity for the H_2O_2-based epoxidation of 1-hexene and cyclohexene has been studied instead in 1,2-dichloroethane solvent. The second major part focuses on the preparation, characterization and water oxidation activity of a carbon-free, tetra-Co-containing polyoxometalate, $[Co_4(H_2O)_2(VW_9O_{34})_2]^{10-}$. This complex shows remarkable stability and efficiency for homogeneously catalyzing water oxidation with turnover frequency (TOF) approaching 1000 s^{-1}. Also, a family of *N*-alkylated derivatives of the complex $[Ru(\mathbf{1})_2]^{2+}$ (**1** = 4'-(4-pyridyl)-2,2':6',2''-terpyridine) has been investigated in conjunction with $[Co_4(H_2O)_2(PW_9O_{34})_2]^{10-}$ catalyst for catalytic water oxidation. The structure-activity correlation is established. The third important part presents a systematic, multifaceted approach to address one of the important problems in POM-based water oxidation catalysis, that is, distinguishing between homogeneous and heterogeneous catalysis. One specific new protocol (tetra-*n*-heptylammonium nitrate (THpA)-toluene extraction) involves quantitatively separating and quantifying different soluble species with water oxidation activity that are present simultaneously under turnover conditions. This conceptually-simple but powerful experiment has been widely used by other groups to evaluate the homogeneity of POM-based WOC systems. The forth significant part includes the use of transition-metal-substituted POM-catalysts for the multi-electron reduction of water to hydrogen under homogeneous, visible-light, and noble-metal-free conditions. In this part, several known and novel transition-metal-substituted POM-catalysts (e.g. $[M_4(H_2O)_2(XW_9O_{34})_2]^{10-}$ (M = Mn, Ni, Cu; X = P, V), $[\{Ni_4(OH)_3AsO_4\}_4(B\text{-}\alpha\text{-}PW_9O_{34})_4]^{28-}$, and $[\{Ni_4(OH)_3PO_4\}_4(A\text{-}\alpha\text{-}PW_9O_{34})_4]^{28-}$) has been rationally prepared and systematically characterized using multiple spectroscopic and computational methods. Their activity towards catalyzing hydrogen evolution has also been thoroughly studied.

Polyoxometalate-based Multi-Electron-Transfer Catalysts for Solar Energy Conversion

By

Hongjin Lv
B.S. Wuhan University, China, 2010

Advisor: Craig L. Hill

A dissertation submitted to the Faculty of the James T. Laney School of Graduate Studies of Emory University in partial fulfillment of the requirements for the degree of Doctor of Philosophy in Chemistry

2015

Acknowledgement

At the moment of an important milestone in my life, I would to acknowledge many wonderful people for their kind help and sincere support during my Ph.D. study.

First and most importantly, I would like to thank my advisor, Professor Craig L. Hill. Prof. Hill is not only a creative scientist in chemistry, a great advisor in research, but also a nice mentor in everyday life and a remarkable teacher in English and Geography! As a creative scientist, I can always learn novel ideas in my discussion with him. Whenever Prof. Hill came back from an important meeting, he will talk to us either in person or in the group meeting about central remarks. What an enjoyable and brainstorming moment! As a great advisor, Prof. Hill has always given me enough trust, freedom and guidance to pursue my research projects. He puts necessary but limited control on my experiments, while at the same time letting me work independently to a very large extent. He will always be available offering valuable advice and informative suggestions *via* emails, short meetings or phone calls with great patience. Also, I appreciate his valuable suggestion and strong support to me finding a postdoctoral position. As a nice mentor in everyday life, Prof. Hill teaches me to be confident and optimistic when facing frustration and obstacles. "That is life and it is not the end of world." says by Prof. Hill. Last but not least, Prof. Hill is also a remarkable teacher in English and Geography. For each manuscript I drafted, Prof. Hill has let me work together with him revising the manuscript and teaching me how to precisely choose words, prepositions or phrases. When we take a rest after working for a while, he will open Google Earth and show me the places where he has been and he wants to go. It's really a wonderful experience to be exposed to such geographical knowledge (e.g. the highest mountain, deepest point and hottest place in the world, etc.) from him. Of course, there is also unhappy moment when I keep bugging him to revise and submit my manuscript. I understand you are very busy but I just want to publish my work timely and efficiently. I sincerely appreciate your tolerance towards my impatient attitude at times.

I also would like to particularly thank my committee members, Prof. Cora MacBeth and Prof. Khalid Salaita. They have been supervising my yearly research presentations as well as my proposal talk the past four years; indeed each time I give a talk, they offer insightful comments and suggestions on my research. I especially appreciate their support and encouragement for writing letters of recommendation on my behalf to find a postdoctoral position and others. I still remember the short meeting with Prof. MacBeth: she discussed the potential postdoctoral positions with me, analyzed the *pros and cons* with respect to choosing the postdoctoral advisors *versus* the ranking of universities and gave me suggestions on my career development. That was really helpful! At this special moment, I really want to say "Sorry" to Prof. Salaita for being unable to work with you on cutting-edge research. Five years ago, you interviewed me *via* phone call and offered me the opportunity to study at Emory. I was initially admitted to Bio-division due to my major of Chemical Biology in college. However, all of my research background focused on Inorganic and Physical Chemistry. I really appreciate your understanding for saying that "It is good for you to work on the research in which you are interested".

I want to thank Professor Tianquan Lian. Prof. Lian who is a great physical chemist and expert in ultrafast laser spectroscopy. I have had very close collaborations with the Lian

lab members for doing ultrafast laser spectroscopy experiments. I sincerely enjoyed the collaborative experience with these people, including Dr. Haiming Zhu, Dr. Ye Yang, Dr. Kaifeng Wu and Dr. Zheyuan Chen. Also I would thank those former or current group members in Prof. Lian's lab: we have been hanging out together and having parties frequently. Such unforgettable experience have been very enjoyable to me.

I also sincerely thank Dr. Djamaladdin G. Musaev in *Cherry L. Emerson Center for Scientific Computation* at Emory for his valuable time and thoughtful suggestions on my collaborative research projects. Dr. Musaev is remarkable computational scientist, he has conducted many computational studies for my projects which highly improved the level and impact of my work. He is always nice, considerate and helpful in providing research and job-seeking advice.

I also need to give my special thanks to Dr. Yurii V. Geletii. He is a very generous and helpful person in everyday life and also a very knowledgeable and extremely careful scientist in research. Since I joined the group, he has provided many good suggestions to my research and guided me step by step to be an independent researcher. He can always flush out the tiniest flaws of any research work and think deeply on the details of a problem. By working with him, I have garnered much knowledge regarding kinetics fitting and modeling and also how to be a mighly meticulous researcher who consequently minimizes mistakes.

I really appreciate Dr. Ken Hardcastle and Dr. John Bacsa for their kind help doing X-ray crystallography. Both of them are top and remarkable crystallographers. They have solved many single crystal structures for me. Without their effort and time, I could not have made many significant research achievements.

I would like to also thank Dr. Shaoxiong Wu and Dr. Bing Wang for their instructions in conducting NMR experiments. Our group has done many NMR studies on uncommon heavy metals (e.g. V, Si, W), and their help has been greatly appreciated! Dr. Fred Strobel in Mass Spectrometry Center at Emory is also highly acknowledged for collecting ESI-MS data for one of my important studies.

I am thankful for the administrative coordinator of our lab, Leslie R. Chauvin and the graduate student coordinator of the chemistry department, Ann Dasher. They have been very helpful in completing my important paperwork as well as providing valuable advice in life. With their help, I can spend more time doing cutting-edge research and attending important meetings.

I also need to express my thanks to many collaborators who have helped me on my academic research. Prof. Paul Kögerler and his student Jan van Leusen in RWTH Aachen University provided considerable assistance in temperature-dependent magnetic studies on the POM complexes I made. Prof. Tianbo Liu, his student Dr. Panchao Yin in Lehigh University and Prof. En-bo Wang in Northeast Normal University are also acknowledged for our enjoyable collaborative experience on an important project. Prof. Petro Zhuk in National Aviation University has worked together with Dr. Geletii on kinetic modeling of the reaction mechanism in my project. Special thanks also to Prof. Catherine E. Housecroft, Prof. Edwin C. Constable and Dr. Jennifer A. Rudd for

supplying the Ru-based photosensitizers that have been used in one of my key research research efforts.

I am also grateful to all the previous and current Hill group members. I am so lucky to have known and worked with these wonderful people during my doctoral study. They are nice, hard-working and energetic, I have had a lot of fun and also learned many things by working with them. As Prof. Hill said many times, our group is current very strong, effective and visible. Without these wonderful guys in the lab, it would be impossible to make these achievements. Herein, I would like to express my special gratitude to the former group members: Dr. Jie Song, Dr. Yingnan Chi, Dr. John Fielden, Dr. Zhen Luo, Dr. Guibo Zhu, Dr. Chongchao Zhao, Dr. Yu Hou, Jordan Sumliner, Naifei Zhang, Juncheng Yang, Yimu Hu, Masoumeh Chamack, Ji Young Lee, and others; and also to the current group members: Dr. James Vickers, Weiwei Guo, Yuanzhe Gao, Elliot Glass, Sarah M. Lauinger, Kevin Sullivan, Qiushi Yin, Marika Wieliczko, Mooeung Kim, Daniel Collins-Wildman, Azam Aliakbari, and others in Hill lab. I will always remember you guys.

I would like to also thank a bunch of friends at Emory, including: Sha Li (the only person who has been my schoolmate for 9 years), Dongmei Xiang, Tao Jiang (my former roommate), Hanchao Liu, Yang Liu, Dr. Zheng Liu, Yazhu Li, Lewen Yang, Chi Zhou, Li Zhang, Xiaohong Wang, Chen Qu, Yun Zhang, Hanquan Su, many previous and current members in Prof. Lian's Lab, and anyone who ever helped me either in daily life or in academic research.

I also want to give my special acknowledgment to my research advisor in Wuhan University, Prof. Tianyou Peng. He is the person who first introduced me to laboratory research. I sincerely appreciate the education, valuable advice, instructive suggestions and lab skills that you taught me, and thank you very much for your support and encouragement to study in United States.

I will give my best gratitude to my father (Guozeng Lv), mother (Yurong Liu) and older sister (Wenwen Lv). Since I was a little kid, my parents and sister have always given me their unconditional love! They are proud of me, and this always encourages me to do better and to be more successful. It has been five years since I celebrated the Chinese Spring Festival with them. I really miss them! "I LOVE YOU!" I sincerely wish them happiness and good healthy forever!

Last but not least, I am always grateful for my beloved wife, Man Wang. She has been my girlfriend since Jul. 4th, 2008 and we got married on May 28th, 2013. Over these years, we have shared happiness and sorrow together. There are many valuable memories which will never be forgotten throughout my entire life. She is pretty, smart, and diligent; I am a lucky dog to have her in my life. Man always gives maximum support, encouragement and understanding towards my research work and helps me overcome unhappiness in life. I am unconditionally appreciative of her dedication, encouragement and endless love!!

Table of Contents

List of Figures

List of Tables

List of Schemes

List of Abbreviations

Å	Angstrom
a, *b*, *c*	unit cell axial lengths
An	actinide
anal.	analysis
bpy	2,2′-bipyridine
bpy'	partially oxidized 2,2′-bipyridine
ºC	degrees Celsius
calcd.	calculated
CAdSV	cathodic adsorptive stripping voltammetry
CAPS	*N*-cyclohexyl-3-aminopropanesulfonic acid
cif	crystallographic information file
cm^{-1}	reciprocal centimeter (wavenumber)
Co_{app}	cobalt containing species including: aqueous Co^{2+}, a Co(II)-POM fragment, or any other Co(II)-containing species
CoO_x	cobalt oxide
DLS	dynamic light scattering
DMG	dimethylglyoxime
DPV	differential pulse voltammetry
E^0	standard cell potential
$E_{1/2}$	formal potential
F(000)	structure factor for the unit cell
FT-IR	Fourier transform infrared spectroscopy
FTO	fluorine doped tin oxide
GC	gas chromatography
g	gram(s)
h	hour(s)
HEPES	2-[4-(2-hydroxyethyl)piperazin-1-yl]ethanesulfonic acid
Hz	Hertz
I	emission intensities of $[Ru(bpy)_3]^{2+*}$ or $[Ir(ppy)_2(dtbbpy)]^{+*}$ with quencher
I_0	emission intensities of $[Ru(bpy)_3]^{2+*}$ or $[Ir(ppy)_2(dtbbpy)]^{+*}$ without quencher
ICP-MS	inductively coupled plasma mass spectrometry
ITO	indium tin oxide
$[Ir(ppy)_2(dtbbpy)][PF_6]$	(4,4'-di-*tert*-butyl-2,2'-dipyridyl)-bis-(2-phenylpyridine(-1H))-iridium(III) hexafluorophosphate
J	coupling constant in Hertz
K	Kevin
L	ligand
Ln	lanthanide
LoD	limit of detection
m	medium (IR)
M	molarity
mg	milligram(s)
MHz	megahertz
min	minute(s)
mL	milliliter(s)
mmol	millimole
NaBi	sodium borate buffer
NaPi	sodium phosphate buffer
NHE	normal hydrogen electrode
nm	nanometer
NMR	nuclear magnetic resonance spectroscopy
OEC	oxygen-evolving center

pH	potential of hydrogen, a measure of the acidity or alkalinity
PCET	proton-coupled electron transfer
PIPES	piperazine-N,N′-bis(2-ethanesulfonic acid)
POM	polyoxometalate
ppm	part per million
PSII	photosystem II
R	discrepancy index for crystal structure refinement
RPM	revolutions per minute
$[Ru(bpy)_3]Cl_2$	Tris(2,2'-bipyridyl)dichlororuthenium(II) hexahydrate
$[Ru(bpy)_3]^{3+}$	Tris(2,2'-bipyridyl)triperchlororuthenium(III)
s	strong (IR)
sh	shoulder (IR)
SYS-114	magnetically-coupled stirring system SPECTROCELL
TBA	tetrabutylammonium
THpABr	tetra-*n*-heptylammonium bromide
TOF	turnover frequency
TON	turnover number
TGA	thermogravimetric analysis
TMA	trimethyl acetamide
UV	ultraviolet
UV-Vis	ultraviolet-visible
w	weak (IR)
WOC	water oxidation catalyst
WRC	water reduction catalyst
Z	number of molecules per unit cell
Φ_{CY}	chemical yield
Φ_{QY}	quantum yield
α, β, γ	interaxial angles between unit cell vectors
δ	chemical shift (expressed in ppm for NMR)
ε	molar extinction (or absorption) coefficient
θ	the glancing angle of the X-ray beam to the "reflecting plane"
λ	wavelength
μ	the total linear absorption coefficient (with unit of cm^{-1})

Chapter 1

Introduction:
Structures, Features, and Applications of Polyoxometalates in Renewable Energy Utilization

(Published in *Chem. Soc. Rev.* **2012**, *41,* 7572-7589.) -- Reproduced partially by permission of The Royal Society of Chemistry.

With Yurii V. Geletii, Chongchao Zhao, James W. Vickers, Guibo Zhu, Zhen Luo, Jie Song, Tianquan Lian, Djamaladdin G. Musaev, Craig L. Hill*

1.1 General Energy Concerns and Possible Solutions

The world's present energy requirements are a subject of rapidly increasingly concern due to explosive growth in the global population. Although this increasing demand could, in principle, be met by utilizing traditional fossil fuels, which constitute more than 70% of our current energy, the increased CO_2 output would undoubtedly have deleterious consequences (rising global temperatures, acidification of the oceans, rising sea level, and etc.).[1-3] An approach to address this urgent situation is to harness the abundant energy from the sun: the amount of solar energy that shines on the earth's surface per hour is more than mankind currently consumes in a year. As a consequence, most aspects of solar energy utilization have been an increasing concern recently because technical institutions as well as government divisions realize both the significant need and the extraordinary opportunity that exists in the development of green, sustainable sources of energy. For example, photovoltaic (PV) devices are increasingly competitive with respect to efficiency, production costs and operating lifetime. Specifically, the best single crystal Si-based PV devices have already obtained an efficiency of 22%; but they remain prohibitively expensive for large-scale use. In contrast, dye-sensitized solar cells (DSSCs) are only about half this efficient but have the potential to be produced in quantity at far lower cost.[4,5] However, due to the lower energy density (weight and molar energy density) of our current batteries, the PV technology is largely limited to generation and storage of electrical energy.[6-9] Unfortunately, nuclear energy, like fossil fuel energy, and to lesser extent all the other sources of energy, are subject to a host of national and local issues, and these change with time. Although nuclear fission does not produce greenhouse gases it does create waste whose safe and effective long-term disposal still represents a

significant ongoing challenge.[10] Nuclear fusion is promising for an inexhaustible source of energy to power the planet,[11,12] however, it is not likely to be viable for some time. Thus, ever more research attention has been focused on the direct production of fuel by utilizing sunlight.

In nature, the process that achieves production of "solar fuel" by utilizing sunlight is photosynthesis. Sadly, however, even this process, optimized over billions of years,[13] is less than 1% efficient for most terrestrial plants.[14,15] These facts define not only a pressing need for "solar fuels" but also a major opportunity for scientific researchers in this burgeoning area. Photosynthesis uses solar energy to generate carbohydrate biofuels, coupled with the oxidation of water catalyzed by the oxygen-evolving complex (OEC, Mn_4CaO_5)[16] in photosystem II (PSII). Photosynthetic carbohydrates are the primary source of energy required and used by nearly all life forms on earth.[14] Inspired by the ramarkable natural photosystem (NP), tremendous efforts have been made to develop artificial photosynthetic (AP) systems. The main two AP reactions are sunlight-driven water splitting (eq. 1) and the reduction of carbon dioxide to CH_3OH (eq. 2) and other carbon-based fuels.[1,6,7,9,13,17-21]

$$2H_2O \xrightarrow[catalyst]{hv(sun)} O_2 + 2H_2 \qquad \textbf{(1-1)}$$

$$CO_2 + 2H_2O \xrightarrow[catalyst]{hv(sun)} CH_3OH + O_2 \qquad \textbf{(1-2)}$$

In typical NP and most AP systems, there are four indispensable processes (**Scheme 1-1**), in the photosynthesis cycle. As shown in **Scheme 1-1**, the first process is light harvesting or light absorption. The most effective photosensitizers will absorb with a large molar

extinction coefficient and absorb broadly so as to maximize overlap with the terrestrial solar spectrum (utilization of sunlight energy).[7,22] In the second process, the absorption of light converts the reaction centers from the ground electronic state to an electronic excited state that is long-lived and displays effective charge separation (electrons and holes in these molecules, arrays or other devices have significant plus-minus character). The third process involves harvesting the electron in this excited state and using it to reduce low-energy molecules, particularly CO_2 and H_2O, thus converting them into high energy molecules (stored chemical energy in molecules or "fuels"); and the forth process requires the capture of the hole (positive charge) in the excited state four times sequentially to oxidize water to oxygen.[23]

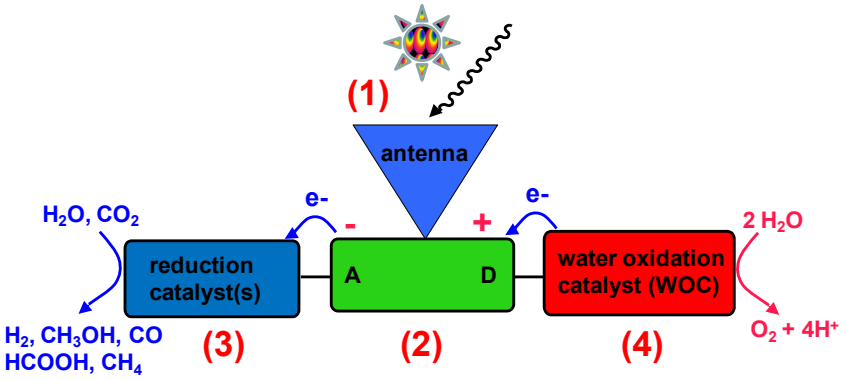

Scheme 1-1 A schematic illustration for artificial photosynthesis: an antenna light-absorption and charge separating structure interfaced with multielectron catalysts.

Recently, much work has addressed energy and electron transfer between antenna and photosensitizers or between photosensitizers and catalysts.[6,7,17,22-26] For the light-absorption part, the main focus is to design a highly efficient photosensitizer with a long-lived charge-separated excited state because the longer lived the charge-separated state is, the more likely it can be captured chemically before rapid electron-hole pair recombination happens. For the catalysts part, a central thrust of many researchers has

been the design, preparation, and optimization of water reduction catalysts (WRCs)[13,27-31] and water oxidation catalysts (WOCs).[9,32-38]

In the development of successful AP or solar fuel generating systems, three factors are centrally important: (1) the ability to control the relative rates of several key processes. This is important not only for the functioning of each catalyst (WRC or WOC) in such systems but also for the overall 3- or 4-unit assembly (**Scheme 1-1**) processes; (2) the ability to efficiently convert one-electron processes (absorption of photons and some simple charge transfer processes) into the multielectron processes represented in eqs **1-1** and **1-2** above; (3) Water must be the ultimate source of electrons and protons in a successful solar fuel generating system. For laboratory experiments, sacrificial electron donors (triethanolamine, triethylamine, sodium sulfide, etc.) for catalytic water reduction or sacrificial electron acceptors ($AgNO_3$, $Na_2S_2O_8$, etc.) for catalytic water oxidation could be used for detailed elucidation of the catalytic processes and for system optimization. However, no reducing agent but water has the capacity, ultimately, to meet the projected demand for fuel energy on a global scale while producing no waste. In summary, sunlight and water must be employed sooner or later as the energy and electron + proton sources to produce a good percentage of fuel in the future for practical AP or solar fuel generating systems.

1.2 Requirements and Rational Analysis of Viable WRCs and WOCs

As mentioned above, the development of successful AP or solar fuel generating systems requires development of effective catalysts (WRCs or WOCs) for the key reactions (water or CO_2 reduction and water oxidation) in part because these processes are

frequently thermodynamically unfavorable.[1,6,7,13,18-21] Considering the intrinsic complexity of catalytic water splitting (four-electron redox processes, etc.), current research endeavors are focusing on the development of efficient, robust, inexpensive, selective, and environmentally-benign catalysts for each half reaction (water oxidation or water reduction) or water splitting. The reduction of protons to H_2 is a two-electron process, however the oxidation of H_2O to O_2 is a four-electron process. Therefore, the development of viable WOCs has proven particularly more challenging than the investigation of WRCs. Both WRCs and WOCs must be capable of reducing/oxidizing water at a potential minimally above the thermodynamic value; reductively/oxidatively, while being hydrolytically and thermally stable under operating conditions; and, critically, fast enough. (A commercially viable solar fuel generating device will likely have to last for at least 10^8 turnovers).

In the process of developing targeted catalysts, both heterogeneous and homogeneous systems are used. In heterogeneous systems, light-driven water oxidation/reduction has been demonstrated in several ways, including electrolysis using photovoltaic cells,[26,39] semiconductor-based photoelectrodes,[40] dispersed catalysts in the reaction solution,[41,42] and catalytic systems composed of transition-metal photosensitizers and transition-metal-based (Ir and Ru) catalysts.[43-46] Generally, heterogeneous catalysts have the advantages of low cost, high stability and availability; however, these systems tend to deactivate by surface poisoning or aggregation process and are harder to study and thus optimize at the molecular level. Moreover, almost all heterogeneous catalyst have the disadvantages of very low turnover number (TON) or turnover frequency (TOF) per catalytic metal site. In contrast, homogeneous catalysts not only exhibit higher rates and selectivities, but also

are far easier to study. Almost every individual active site in a homogeneous catalyst is, in principle, available to bind and transform the substrate; this frequently results in high TON and TOF values. The ease of quantitative investigation for soluble catalysts entails elucidation of the catalyst's geometric and electronic structures as well as their mechanism(s) of action through use of spectroscopic, crystallographic, and computational techniques. Such detailed molecular-level information leads to a more rational optimization of turnover rates, interface chemistry with light absorbers (photosensitizers, etc.) and stability. Although homogeneous catalysts have advantages over heterogeneous catalysts in term of rates and ease of investigation on molecular level, they nonetheless have some appreciable disadvantages. For homogeneous WRCs, many synthetic iron,[47-53] cobalt,[54-69] nickel,[67,70-78] and molybdenum[79-81]-based organometallic molecular catalysts for photochemically- and/or electrochemically-driven hydrogen production have the problems of (a) low efficiency, (b) limited solubility in aqueous media, (c) instability towards strong acidic environments, or (d) they deactivate by ligand dissociation, decomposition and/or hydrogenation under reducing conditions.[82,83] Similarly, since water oxidation happens in highly oxidizing environments, almost all the molecular, homogeneous organometallic WOCs have the critical drawback that their organic ligands are thermodynamically unstable with respect to oxidative degradation and formation of CO_2 and H_2O. All coordination complex WOCs deactivate by oxidative decomposition of their organic ligands after a modest number of turnovers, and this level of stability is orders of magnitude lower than what will be needed for viable solar fuel production structures and devices.[84-87]

Based on above analyses, one approach to optimally viable catalysts (WRCs and WOCs) is to combine the advantages of heterogeneous metal oxide catalysts (typically stability and durability) and those of homogeneous catalysts (usually high activity, selectivity, and tunability). In this context, homogeneous transition-metal-containing polyoxometalate (POM)-based WOCs or WRCs seem to be an effective, rational choice because they not only have similar or higher catalytic activity than organic-ligand-based homogeneous catalysts in most cases, but also are based on earth-abundant elements. The latter point is critical for practical use at the needed large-scale commercial levels. Also, since polyoxometalates (POMs) are carbon-free, early-transition-metal oxygen anion clusters, they are not susceptible to deactivation by oxidative degradation under oxidizing conditions nor to reductive hydrogenation under reducing conditions unlike many organic ligands. Importantly, the catalysis-relevant properties of POMs (redox potentials, charges, acid-base chemistry, solubilities, etc.) are highly tunable through systematic syntheses.[88-90] This also makes them attractive candidates for multi-electron-transfer catalysts.[88,89,91-94]

1.3 Overview of Polyoxometalates

Polyoxometalates (POMs) are early transition metal oxygen anion clusters that spontaneously form in water through the aggregation and condensation of either soluble, molecular monomeric transition metal precursors such as $[WO_4]^{2-}$ or insoluble metal hydroxides or oxides such as WO_3 hydrate or V_2O_5 at appropriate pH.[88,90,91,93,95-101] POMs are typically formed by corner-, edge- and face-sharing of the MO_6 octahedral building blocks which are the most common linkages found in POMs. The history of POM exploration has been almost 200 years, the first example of polyoxometalate was

reported as an ammonium phosphomolybdate with the formula of $(NH_4)_3[PMo_{12}O_{40}]$ by Berzelius in 1826.[102] After that, great efforts have been made to solve and determine its geometrical structure, Linus Pauling was one of the first trying to describe its structure, in terms of ionic radii.[103] However, such structure was not unambiguously solved until the tungstate analogue $[PW_{12}O_{40}]^{3-}$ was reported in 1934 by Keggin.[104] Largely thanks to the advances in modern high-resolution, sophisticated instrumentation (e.g. X-ray crystallography) as well as the diversity of synthetic and anlytical methods, this area has been extensively investigated resulting in the isolation and identification of numerous POM structures since the mid twentieth century.[91,97,98,105] The most abundant POMs are based on W(VI), Mo(VI), V(V), V(VI), Nb(V) or Ta(V) in that order.[92,95,99] There are thousands of polyoxotungstates (polytungstates)[106-111] and only very small amount of polyniobates and polytantalates.[112,113] More recently, the first-row transition metals (e.g. Fe, Ni) have also been reported to form Keggin-type frameworks.[114,115] The fundamental properties of these POM-forming elements (W, Mo, V, Nb, and Ta) dictate that polytungstates, polymolybdates and polyvanadates are more compatible at lower pH ranges (pH below 9), while the polyniobates and polytantalates are more stable at higher pH ranges (pH above 11.5).[116,117] Thus, the use of mixed starting elements under appropriate conditions will lead to the formation of polyniobotungstates or polytantalotungstates[118-120] which might be hydrolytically stable in intermediate pH values (pH from 8 to 12).

Given the compositional elements of POMs, the structures formed exclusively from the building blocks containing only metal ions and oxygen atoms are defined as "isopolyanions", such as $[W_{10}O_{32}]^{4-}$, $[Mo_7O_{24}]^{6-}$, $[Nb_6O_{19}]^{8-}$, and $[V_{10}O_{28}]^{6-}$;[88] while the

POMs constructed by including one or more heteroatoms (typically p or d block elements found in one or more positions internal to the polyanion unit) in the internal positions of regular isopolyanions are designated as "heteropolyanions". These "heteropolyanions" or "heteropoly compounds" tend to be stable hydrolytically over wider pH ranges than the isopolyanions, thus leading to more versatile structures in a range of different conditions. Based on the geometrical structures of POMs, two major structural families of plenary polytungstates, namely the Keggin ($[XW_{12}O_{40}]^{n-}$, X = P or Si is the most popular; **Figure 1-1**)[104,121,122] and the Wells-Dawson ($[X_2W_{18}O_{62}]^{6-}$, X = P in most common case, **Figure 1-2**)[123] structures, have been well documented. Other more types of POMs, particularly the giant ring-shaped polymolybdates pioneered by Achim Müller,[124-140], the Anderson type,[141,142] Weakley-Yamase type,[143] and Dexter-Silverton type[144] structures, are also prepared in one-pot condensation reactions at the right pH, ionic strength, and temperature. Generally, the central heteroatom in the common Keggin structure can be virtually most of the element in the periodic table including V^V, Sb^{III}, etc.[145,146] in contrast, the choice of heteroatom in the Wells-Dawson structure (P has been used in a majority of cases) seems to be much narrower although some Si-, As-, V-, and even S-centered Dawson POMs are reported by limited number of groups in recent decade.[147-153] The traditional plenary Keggin or Wells-Dawson POMs are sensitive to pH so that one or several terminal $[W=O]^{4+}$ building blocks can be removed *via* base hydrolysis under appropriate conditions (pH, temperature, ionic strength, etc), resulting in the formation of defect or "lacunary" POMs. These lacunary POMs are diamagnetic, multidentate O-donor ligands that can incorporate various mono- or multinuclear d- and f-block

transition metals including those with appended organic groups,[154-156] thus leading to the generation of thousands of transition-metal-substituted POMs (TMSPOMs).

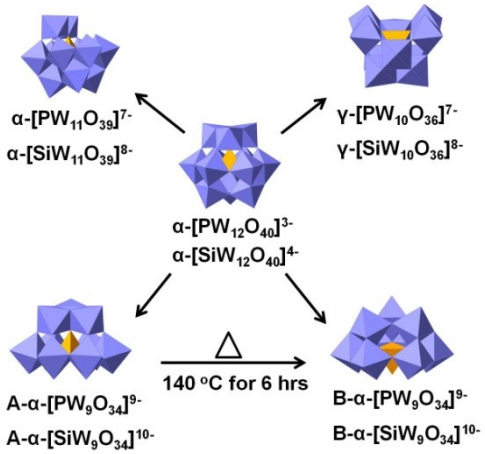

Figure 1-1 X-ray structures of representative plenary and lacunary Keggin type POMs

Figure 1-1 summarizes the general transformation between plenary Keggin type polytungstates and their lacunary derivatives. As can be seen, the Keggin structure is formed by a central XO_4 (X = P or Si) tetrahedron capped by four W_3O_{13} triads at each of its vertices. These triads are connected through corner-sharing or edge-sharing linkage with each other and the central tetrahedron. Geometrically, five isomers (α, β, γ, δ and ε isomers) will be generated by successive 60º rotation of the four W_3O_{13} triads as proposed by Baker and Figgis.[121] The α-Keggin structure with the idealized T_d symmetry is the most thermodynamically stable one. By successive rotating one, two, three or four W_3O_{13}, the overall symmetry will change from T_d to C_{3v} or C_{2v}, which will correspondingly increase the overall energy caused by the coulombically-unfavorable edge-shared contacts of two highly charged building blocks, thus resulting in less thermodynamically stable isomers (e.g. γ, δ and ε isomers). Under appropriate conditions (pH, ionic strength, temperature, etc.), the plenary Keggin POM can be transformed to various lacunary ligands (**Figure 1-1**). For example, the monovacant $[\alpha\text{-}PW_{11}O_{39}]^{7-}$ or [α-

$SiW_{11}O_{39}]^{8-}$ can be obtained from their corresponding parent Keggin structures by losing one $[W=O]^{4+}$ unit; the resulting monovacant ligands are readily to coordinate most transition divalent or trivalent metal ions[157] or even lanthanide (Ln) and actinide (An) ions[143,158-160] exhibiting interesting catalytic activity or spectroscopic properties. Other well-known, widely-used lacunary Keggin type ligands are the trivacant derivatives, [A-α-$PW_9O_{34}]^{9-}$ and [B-α-$PW_9O_{34}]^{9-}$,[161-163] where the A-type derivative is generated by removing three corner-sharing WO_6 octahedron units and the B-type derivative is formed from the removal of one of the four edge-sharing W_3O_{13} triads. The A-type derivative can be transformed to the B-type one through solid-state isomerization by heating at 140 ^oC for 6 hours. Unlike the monovacant ligand ([α-$PW_{11}O_{39}]^{7-}$), the trivacant ligands (both A-type and B-type) can usually incorporate multiple transition metal ions forming interesting structures with attractive properties.[38,106,164-168] It's noted that some small anions (e.g. HPO_4^{2-}, $HAsO_4^{2-}$ HCO_3^- or CO_3^{2-}, etc.) can be incorporated as linkers to connect the multi-transition metal centers to the POM ligands; it's believed that these anions can work as template to considerably increase the stability of the whole structure in both solution and solid state.[165,167,169,170] In addition, the plenary Keggin POM can also produce the Keggin-type divacant ligands, [γ-$SiW_{10}O_{36}]^{8-}$ and [γ-$PW_{10}O_{36}]^{7-}$.[171-173] Many novel transition-metal-containing POMs using those divacant ligands have been prepared for various catalytic applications.[33,34,174-177]

Similar to Keggin type POMs, the Wells-Dawson type plenary POMs also exhibit very rich solution chemistry. Taking [α-$P_2W_{18}O_{62}]^{6-}$ as an example, such plenary POM is formed by two central PO_4 tetrahedra, two W_3O_{13} triad caps and two W_6O_{14} belts linked together by corner-sharing oxygen atoms (**Figure 1-2**). The plenary Wells-Dawson type

POM is proposed to have six isomers by Baker and Figgis,[121] but only four of them have been experimentally discovered to date[148] and the α and β isomers are the most common ones. Like the Keggin type POM, several lacunary Wells-Dawson type POMs can also be prepared and isolated by precisely controlling the hydrolysis conditions, the chemistry of lacunary Wells-Dawson type ligands is more diverse comparing to that of Keggin type ones mainly due to the complexity of their composition as well as their less symmetrical structure. Two types of monovacant isomers can be derived from the controlled degradation of the plenary Wells-Dawson structure. The α_1-$[P_2W_{17}O_{61}]^{10-}$ isomer can be obtained by the removal of a $[W{=}O]^{4+}$ unit at the belt position, while the α_2-$[P_2W_{17}O_{61}]^{10-}$ isomer will be formed through the removal of an apical $[W{=}O]^{4+}$ unit from the plenary structure. The α_1-$[P_2W_{17}O_{61}]^{10-}$ lacunary ligand can slowly transform to α_1-$[P_2W_{17}O_{61}]^{10-}$ isomer through hydrolysis. Both types of monovacant ligands can react with various transition metal ions to form the 1:1 monomeric complex (α_1- or α_2-$[M(H_2O)P_2W_{17}O_{61}]^{n-}$)[178,179] or with f-block lanthanide (Ln) and actinide (An) ions to yield the 1:2 bridging complex ($\{M[\alpha_1/\alpha_2\text{-}P_2W_{17}O_{61}]_2\}^{n-}$)[158,180] and the 1:1 dimeric complex ($\{M[\alpha_1/\alpha_2\text{-}P_2W_{17}O_{61}]\}_2^{n-}$).[181] Similar to the trivacant $[B\text{-}\alpha\text{-}PW_9O_{34}]^{9-}$ ligand, the trivacant Wells-Dawson polyanion $[P_2W_{15}O_{56}]^{12-}$ can also be generated by the removal of one edge-sharing W_3O_{13} unit from the plenary structure. Such trivacant Wells-Dawson ligand has been widely used for the preparation of a variety of POM architectures by reacting either with several low valent transition metal cations to produce regular sandwich structure[164,182-184] or high valent metal ions (W^{VI}, V^{V} and Nb^{V}) to regenerate the plenary Wells-Dawson structure, $[M_3P_2W_{15}O_{62}]^{n-}$.[185-189] In addition, the metastable hexavacant α-$[H_2P_2W_{12}O_{48}]^{12-}$ can also be synthesized by removing six tungsten units from the one side

of the plenary Wells-Dawson structure. Such hexavacant polyanion is stable at its natural pH and ionic strength in aqueous solution, thus it has been used to prepare novel multi-metal-containing polyperoxo complex.[190,191] While acidifying the solution of $[H_2P_2W_{12}O_{48}]^{12-}$ polyanion in the absence of tungstate source (WO_4^{2-}), the crown-shaped superlacunary tetramer $[H_7P_8W_{48}O_{184}]^{33-}$ can be formed by connecting four $[H_2P_2W_{12}O_{48}]^{12-}$ units *via* the caps (**Figure 1-2**). The resulting $[H_7P_8W_{48}O_{184}]^{33-}$ polyanion is very stable in aqueous solution over a wide pH range (1-8).[192] The coordination chemistry of such superlacunary $[H_7P_8W_{48}O_{184}]^{33-}$ polyanion has been largely studied by Kortz's group in recent years.[192-200] Recent study by Wang's group also reported the trimeric aggregates of $[H_2P_2W_{12}O_{48}]^{12-}$ units in solution.[201]

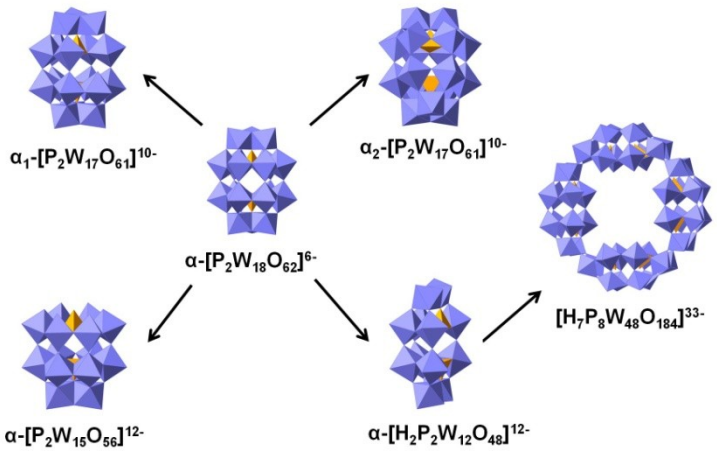

Figure 1-2 X-ray structures of representative plenary and lacunary Wells-Dawson type POMs

To date, POM study has been becoming quite multidisciplinary which attracts extensive attention and collaboration from many experts all around the world in the areas of chemistry, physics, medicine, material science, and theoretical computation. The versatile synthetic methodology and the highly tunable physicochemical properties (acidity, thermal stability, redox potentials, solubility, size, shape, charges, acid-base chemistry, etc.) of POMs make them show wide potential applications in various areas

including medicine,[119,202-214] magnetism,[139,215-218] high performance materials,[219] chirality,[220-229] light absorbers,[230-233] and others.[234] However, the dominant application of POMs is in catalysis.[108,235-250] Several processes have been commercialized where the POM serves either as an acid catalyst (usually a superacid) or an oxidation catalyst.[244,246] In recent years, a host of organic POM derivatives have been made,[156,251-257] and some of these may also be of value in the construction of solar fuel production assemblies or devices. More importantly, many Co, Ni, Mn, Ru and Ir-containing POMs have been studied in context with artificial photosynthesis as catalysts for both water oxidation under thermal,[34,36,38,258-261] photochemical[35,166,167,262-269] and electrochemical[270-274] conditions and water reduction[168,275-279] under visible light irradiation, that will be comprehensively discussed in the following **Section 1.4**.

1.4 Applications of POMs as WRCs and WOCs

As mentioned in previous **Sections** (**1.1 to 1.3**), POMs (or transition-metal-substituted POMs) are very promising candidate for both water oxidation and water reduction reactions considering their highly tunable, rich catalysis-relevant properties. The idea of using POMs as water/proton reduction catalysts can date back to 1960s, when Pope and Papaconstantinou reported a series of systematical research on electronic, spectroscopic and magnetic properties of reduced heteropolytungstates and heteropolymolybdates.[280-283] The preparation reduced POMs (also called "heteropoly blues") can be achieved either electrochemically using bulk electrolysis technique[284,285] or photochemically by irradiating the POM solution with ultraviolet (UV) light in the presence of sacrificial electron donors (e.g. alcohol, TEOA, TEA, etc.).[286-288] Upon UV light irradiation, the intramolecular oxygen-to-tungsten (or molybdate) charge-transfer ($O_{2p} \rightarrow W_{5d}$, or Mo_{4d})

happens in the POM frameworks.[289] The electrons from a spin-paired, doubly occupied bonding orbital (HOMO) (mainly O_{2p} orbitals) will be promoted to and delocalized over the empty anti-bonding orbital (LUMO) (mainly W_{5d} orbitals);[290] the generated holes in the O_{2p} orbitals are highly oxidizing for organic substrate oxidation. Such process will finally lead to reduced POMs which exhibit a deep blue color comparing to the ground state POMs (usually colorless or pale-yellow in nature). Since the POMs or reduced POMs are highly negatively charged, they can store many protons at the same time. With the help of appropriate catalysts (e.g. Pt(0)), the reduced POMs with coupling protons can release hydrogen gas quite efficiently.[291-295] However, in all of these studies, either Pt or other noble water reduction catalysts were used. Also, most of these works were done under UV light irradiation. Therefore, the development of more viable (fast, selective and stable), more efficient, and noble-metal-free molecular WRCs which works under visible light region remains a substantial challenge. To date, there are only few reports on visible-light-driven H_2 evolution by POM WRCs.[275-279] The representative work is done by Artero and coworkers where no Pt(0) co-catalyst has been used in their system.[296] In their work, a covalently-linked Ir(III)-photosensitized polyoxometalate complex is reported, which catalyzes H_2 production with a TON of 41 after 7 days of visible light irradiation.[277] However, both the TON and TOF values of this system are quite low and far beyond the possible practical application. One important goal of this thesis is to develop more viable transition-metal-substituted POMs-based WRCs, to optimize the visible-light-driven reaction systems for higher rates and final yields of H_2 production, and to understand the reaction mechanisms.

Comparing to the use of POM for catalyzing water reduction reaction, the application of transition-metal-substituted POMs as water oxidation catalysts is quite new. As mentioned above, the lacunary POM ligands can incorporate and stabilize many transition metal ions to form thousands of novel transition-metal-substituted POM structures, thus which will offer a variety of option for obtaining desired/targeted POM-based WOCs. More importantly, POM-based WOCs will be free of oxidative degradation because (1) they are carbon-free and (2) all the stabilizing ligands are in their highest oxidation states. Dating back to 2004, Shannon and co-workers reported the electrochemical production of oxygen catalyzed by a $Na_{14}[Ru^{III}_2Zn_2(H_2O)_2(ZnW_9O_{34})_2]$ (**Ru_2Zn_2POM**, **Figure 1-3a**) complex using pulsed voltammetry in 0.1 M sodium phosphate buffer (pH 8.0) solution.[297] A catalytic current of oxygen production has been observed when applying positive potential to the working electrode. The electrocatalytic oxygen evolution happens at a potential of $E_{1/2}$ (~0.750 V) approaching to the thermodynamic value (~0.760 V *vs.* NHE). Subsequently, both our group (Hill lab) and the Bonchio group in Italy published separately two papers reporting the synthesis with different methods, solid state and solution characterization of a tetra-ruthenium polytungstate, $[Ru_4(\mu\text{-}O)_4(\mu\text{-}OH)_2(H_2O)_4(\gamma\text{-}SiW_{10}O_{36})_2]^{10-}$ (**Ru_4SiPOM**, **Figure 1-3b**).[221,222] Such novel tetra-Ru POM show interesting catalytic water oxidation activity in homogeneous aqueous solution when combining with the chemical oxidant $[Ru(bpy)_3]^{3+}$ or Ce(IV) nitrate. The reported turnover frequency (TOF) values in Hill and Bonchio systems reach 0.45 – 0.6 s^{-1} and 0.125 s^{-1}, respectively. Later on, Hill group extended the dark water oxidation system to the photo-driven water oxidation system using $[Ru(bpy)_3]^{2+}$ as a photosensitizer, $S_2O_8^{2-}$ as a sacrificial electron acceptor and **Ru_4SiPOM**

as water oxidation catalyst (**Figure 1-3d**).[35,298-300] This work is pioneered to utilize visible light as kind of energy source to drive the reaction, which further moves the step toward solar energy conversion. Under turnover conditions, up to 350 TONs were achieved with an initial TOF and quantum yield ($\Phi(O_2)$) of 0.08 s^{-1} and 9%, respectively. In addition, the mechanism of water oxidation by using $[Ru(bpy)_3]^{3+}$ or Ce(IV) oxidants has also been studied in depth by both groups and others.[37,301-303] Multiple stability studies show no appreciable hydrolytic decomposition of the **Ru_4SiPOM** WOC into the metal oxides (RuO_2, WO_3) under either thermal or photo-driven water oxidation conditions.

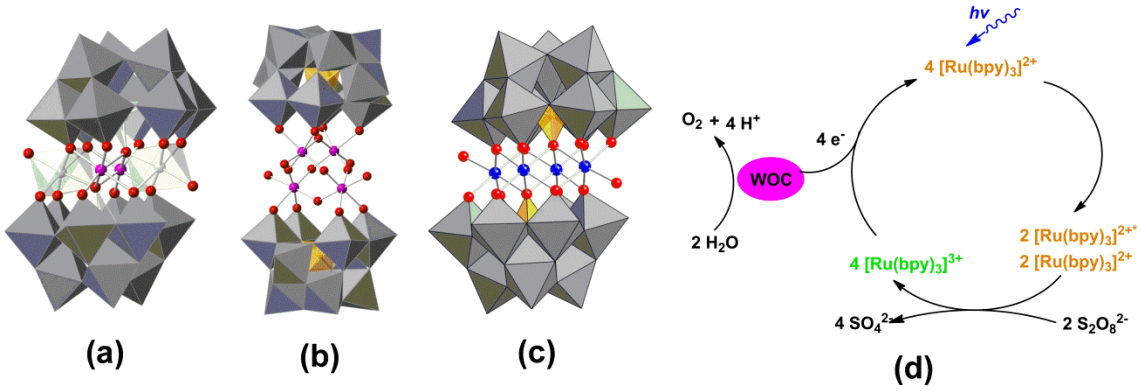

Figure 1-3 X-ray structures of (a) $[Ru^{III}_2Zn_2(H_2O)_2(ZnW_9O_{34})_2]^{14-}$ **(Ru_2Zn_2POM)** (b) $[Ru^{IV}_4O_4(OH)_2(OH_2)_4(\gamma\text{-}SiW_{10}O_{36})_2]^{12-}$ (**Ru_4SiPOM**), and (c) $[Co_4(H_2O)_2(PW_9O_{34})_2]^{10-}$ (**Co_4PPOM**) as well as (d) the homogeneous light-driven water oxidation system.

The major breakthrough in POM-based WOCs field has been successfully achieved by Hill group in 2010. A tetracobalt-substituted polytungstate, $[Co_4(H_2O)_2(PW_9O_{34})_2]^{10-}$ (**Co_4PPOM**; **Figure 1-3c**),[38] was demonstrated to catalyze water oxidation in the dark using $[Ru(bpy)_3]^{3+}$ as a chemical oxidant in aqueous phosphate buffer solution at pH 8.0. The TON per active site metal reaches over 1000 in 3 min affording a TOF of 5 s^{-1}, which is highest value in WOC field at that time.[38] The stability of **Co_4PPOM** has been evaluated before and after catalytic reaction using multiple spectroscopic techniques

including UV-vis, FT-IR and ^{31}P NMR spectra, etc, which confirmed that **Co_4PPOM** remains molecular and does not decompose under these turnover conditions. Subsequently, **Co_4PPOM** was also demonstrated to catalyze efficient water oxidation under photo-driven conditions as shown in **Figure 1-3d**.[166] Under optimal conditions, a TON of over 220 and high quantum yield of 30% were obtained in pH 8.0 borate buffer.

Following these pioneering works, many other Co, Ni, Mn, Ru and Ir-containing POMs have been synthesized and studied as catalysts for water oxidation under thermal,[258-261] photochemical[167,262-269] and electrochemical[270-274,304] conditions, most of these works have been comprehensively discussed in our recent review article.[108] Some of these reported POM WOCs (e.g. **Ru_4SiPOM** and **Co_4PPOM**) have also been used to construct nanostructured oxygen evolution devices by anchoring them onto the surface of robust, conductive supports (such as multi-wall carbon nanotubes, graphene, or mesoporous carbon nitride) with the goal of improving the surface areas, thermal stabilities as well as the mechanical properties of these nanostructured composites.[270,272-274,304] Other very recent works also show that multiple nuclear ($n \geq 9$) Co or Ni-containing POMs efficiently catalyze water oxidation under visible-light-driven conditions.[167,259,269] The other major goal of this thesis is to design and develop more efficient and stable (both hydrolytically and oxidatively) POM WOCs, to understand detailed reaction mechanism through kinetics modeling as well as DFT calculations, and to address the homogeneity versus heterogeneity nature of the reaction system as raised by recent works[306,307] although they were conducted under quite different conditions and cannot be simply extrapolated to the chemical oxidant-containing systems.

1.5 Goals of This Work and Outline

The first objective of this dissertation is to develop more efficient and stable (both hydrolytically and oxidatively) POM WOCs, to understand detailed reaction mechanism through kinetics modeling as well as theoretical DFT calculations, and to address the homogeneity versus heterogeneity nature of the water oxidation reaction system. **Chapter 2** reports the synthesis [307]and characterization of a novel banana-shaped hexanuclear cobalt-containing POM complex, $[(Co(OH_2)Co_2VW_9O_{34})_2(VW_6O_{26})]^{17-}$. Such complex was initially designed for catalytic water oxidation; however, it's unstable in basic borate buffer solution and slowly transforms to a more stable species, $[Co_4(H_2O)_2(VW_9O_{34})_2]^{10-}$. Thus the catalytic activity for the H_2O_2-based epoxidation of 1-hexene and cyclohexene by $[(Co(OH_2)Co_2VW_9O_{34})_2(VW_6O_{26})]^{17-}$ has been studied instead in 1,2-dichloroethane solvent. **Chapter 3** is related to the **Chapter 1**, this chapter focuses on the preparation and characterization of the above-mentioned tetra-Co-containing complex, $[Co_4(H_2O)_2(VW_9O_{34})_2]^{10-}$. It shows remarkable stability and efficiency for homogeneously catalyzing water oxidation with turnover frequency (TOF) approaching 1000 s^{-1}, kinetics modeling, DFT calculations and the temperature-dependent magnetic studies have been used to illustrate the difference between this complex and its phosphorous-centered analogue, $[Co_4(H_2O)_2(PW_9O_{34})_2]^{10-}$. In **Chapter 4**, a family of *N*-alkylated derivatives of the complex $[Ru(\mathbf{1})_2]^{2+}$ (**1** = 4'-(4-pyridyl)-2,2':6',2''-terpyridine) has been investigated as photosensitizers in conjunction with $[Co_4(H_2O)_2(PW_9O_{34})_2]^{10-}$ catalyst for catalytic water oxidation. The structure-activity relationship is established in this part by analyzing the reaction kinetics. Then, in order to address the homogeneity versus heterogeneity nature of the reaction system as raised by

recent works,[305,306] a series of carefully-designed, systematic, and multifaceted experiments have been conducted in **Chapter 5**. These experiments are powerful to distinguish the homogeneous or heterogeneous catalysis in our POM-based water oxidation systems. One specific conceptually-simple but powerful new protocol (tetra-n-heptylammonium nitrate (THpA)-toluene extraction) has been designed and widely used by other groups to evaluate the homogeneity of POM-based WOC systems.

The second subjective of this dissertation is to develop more viable transition-metal-substituted POMs-based WRCs, to optimize the visible-light-driven reaction systems for higher rates and final yields of H_2 production, and to understand the reaction mechanisms. The second subjective contains four separate **Chapters**. In **Chapter 6**, a tetra-Mn-substituted polyoxometalate, $[Mn_4(H_2O)_2(VW_9O_{34})_2]^{10-}$, that is isostructural to the efficient water oxidation catalyst, $[Co_4(H_2O)_2(VW_9O_{34})_2]^{10-}$, has been synthesized and characterized. This complex catalyzes the reduction of water to evolve hydrogen under visible light irradiation using $[Ru(bpy)_3]^{2+}$ as photosensitizer and TEOA as a sacrificial electron donor although the TON values obtained in these experiments are not quite high. To develop more viable (fast, selective and stable), more efficient, and noble-metal-free molecular WRCs, a tetra-nickel-substituted polyoxometalate, $[Ni_4(H_2O)_2(PW_9O_{34})_2]^{10-}$, is reported in **Chapter 7**. Experimental results show that polyanion $[Ni_4(H_2O)_2(PW_9O_{34})_2]^{10-}$ works an efficient and robust molecular catalyst for H_2 production in a three-component system upon visible light irradiation, the highest TON value (~6,500) is achieved in one week with no significant loss in activity. In **Chapter 8**, we tend to understand whether the number of transition metals incorporated in the POM structure can affect the reactivity and stability of target POM catalysts for catalytic

hydrogen production. Thus two hexadecanuclear Ni-containing POMs, $[\{Ni_4(OH)_3AsO_4\}_4(\textit{B}\text{-}\alpha\text{-}PW_9O_{34})_4]^{28-}$ and $[\{Ni_4(OH)_3PO_4\}_4(\textit{A}\text{-}\alpha\text{-}PW_9O_{34})_4]^{28-}$, have been rationally prepared and systematically characterized using multiple spectroscopic and computational methods. Their activity towards catalyzing hydrogen evolution has also been thoroughly studied. Finally, in **Chapter 9**, we target to explore new highly earth-abundant and inexpensive Cu-containing POM structure for catalytic water reduction reaction. Despite the conventional wisdom that Cu-based complexes are inefficient WRCs due to the high free energy of hydrogen adsorption (ΔG_H) on Cu, we found that the tetra-Cu-substituted POM, $[Cu_4(H_2O)_2(PW_9O_{34})_2]^{10-}$, is actually quite active catalyst for hydrogen evolution. The stability evaluation as well as the quenching mechanistic studies have also been reported along with its catalytic hydrogen evolution activity.

References

(1) Bard, A. J.; Fox, M. A. *Acc. Chem. Res.* **1995**, *28*, 141.

(2) Chow, J.; Kopp, R. J.; Portney, P. R. *Science* **2003**, *302*, 1528.

(3) Lewis, N. S.; Nocera, D. G. *Proc. Natl. Acad. Sci.* **2006**, *103(43)*, 15729.

(4) Grätzel, M. *Nature* **2001**, *414*, 338.

(5) Grätzel, M. *Inorg. Chem.* **2005**, *44*, 6841.

(6) Hammarstrom, L.; Hammes-Schiffer, S. *Acc. Chem. Res.* **2009**, *42*, 1859.

(7) Gust, D.; Moore, T. A.; Moore, A. L. *Acc. Chem. Res.* **2009**, *42*, 1890.

(8) Cook, T. R.; Dogutan, D. K.; Reece, S. Y.; Surendranath, Y.; Teets, T. S.; Nocera, D. G. *Chem. Rev.* **2010**, *110*, 6474.

(9) Hambourger, M.; Moore, G. F.; Kramer, D. M.; Gust, D.; Moore, A. L.; Moore, T. A. *Chem. Soc. Rev.* **2009**, *38*, 25.

(10) Slovic, P.; Flynn, J. H.; Layman, M. *Science* **1991**, *254*, 1603.

(11) Kodama, R.; Shiraga, H.; Shigemori, K.; Toyama, Y.; Fujioka, S.; Azechi, H.; Fujita, H.; Habara, H.; Hall, T.; Izawa, Y.; Jitsuno, T.; Kitagawa, Y.; Krushelnick, K. M.;

Lancaster, K. L.; Mima, K.; Nagai, K.; Nakai, M.; Nishimura, H.; Norimatsu, T.; Norreys, P. A.; Sakabe, S.; Tanaka, K. A.; Youssef, A.; Zepf, M.; Yamanaka, T. *Nature* **2002**, *418*, 933.

(12) Nuttall, W. J. *Fusion as an energy source: Challenges and Opportunities, Institute of Physics report*, Institute of Physics report, 2008.

(13) Dubois, M. R.; Dubois, D. L. *Acc. Chem. Res.* **2009**, *42*, 1974.

(14) Kê, B. *Photosynthesis: Photobiochemistry and Photobiophysics*; Springer-Kluwer Academic Dordrecht; Boston, 2001.

(15) McEvoy, J. P.; Brudvig, G. W. *Chem. Rev.* **2006**, *106*, 4455.

(16) Umena, Y.; Kawakami, K.; Shen, J.-R.; Kamiya, N. *Nature* **2011**, *473*, 55.

(17) Gust, D.; Moore, T. A.; Moore, A. L. *Acc. Chem. Res.* **1993**, *26*, 198.

(18) Meyer, T. *Acc. Chem. Res.* **1989**, *22*, 163.

(19) Rüttinger, W.; Dismukes, G. C. *Chem. Rev.* **1996**, *97*, 1.

(20) Dau, H.; Zaharieva, I. *Acc. Chem. Res.* **2009**, *42*, 1861.

(21) Gray, H. B. *Nature Chem.* **2009**, *1*, 7.

(22) Hammarström, L.; Sun, L.; Åkermark, B.; Styring, S. *Catal. Today* **2000**, *58*, 57.

(23) Balzani, V.; Credi, A.; Venturi, M. *ChemSusChem* **2008**, *1*, 26.

(24) Flamigni, L.; Collin, J.-P.; Sauvage, J.-P. *Acc. Chem. Res.* **2008**, *41*, 857.

(25) Li, J.; Shiota, Y.; Yoshizawa, K. *J. Am. Chem. Soc.* **2009**, *131*, 13584.

(26) Youngblood, W. J.; Lee, S.-H. A.; Kobayashi, Y.; Hernandez-Pagan, E. A.; Hoertz, P. G.; Moore, T. A.; Moore, A. L.; Gust, D.; Mallouk, T. E. *J. Am. Chem. Soc.* **2009**, *131*, 926.

(27) Du, P.; Schneider, J.; Jarosz, P.; Eisenberg, R. *J. Am. Chem. Soc.* **2006**, *128*, 7726.

(28) Esswein, A. J.; Nocera, D. G. *Chem. Rev.* **2007**, *107*, 4022.

(29) Dempsey, J. L.; Brunschwig, B. S.; Winkler, J. R.; Gray, H. B. *Acc. Chem. Res.* **2009**, *42*, 1995.

(30) LeGoff, A.; Artero, V.; Jousselme, B.; Tran, P. D.; Guillet, N.; Métayé, R.; Fihri, A.; Palacin, S.; Fontecave, M. *Science* **2009**, *326*, 1384.

(31) Karunadasa, H. I.; Chang, C. J.; Long, J. R. *Nature Lett.* **2010**, *464*, 1329.

(32) Gersten, S. W.; Samuels, G. J.; Meyer, T. J. *J. Am. Chem. Soc.* **1982**, *104*, 4029.

(33) Besson, C.; Huang, Z.; Geletii, Y. V.; Lense, S.; Hardcastle, K. I.; Musaev, D. G.; Lian, T.; Proust, A.; Hill, C. L. *Chem. Commun.* **2010**, 2784.

(34) Geletii, Y. V.; Botar, B.; Kögerler, P.; Hillesheim, D. A.; Musaev, D. G.; Hill, C. L. *Angew. Chem. Int. Ed.* **2008**, *47*, 3896.

(35) Geletii, Y. V.; Huang, Z.; Hou, Y.; Musaev, D. G.; Lian, T.; Hill, C. L. *J. Am. Chem. Soc.* **2009**, *131*, 7522.

(36) Sartorel, A.; Carraro, M.; Scorrano, G.; Zorzi, R. D.; Geremia, S.; McDaniel, N. D.; Bernhard, S.; Bonchio, M. *J. Am. Chem. Soc.* **2008**, *130*, 5006.

(37) Sartorel, A.; Miro, P.; Salvadori, E.; Romain, S.; Carraro, M.; Scorrano, G.; Valentin, M. D.; Llobet, A.; Bo, C.; Bonchio, M. *J. Am. Chem. Soc.* **2009**, *131*, 16051.

(38) Yin, Q.; Tan, J. M.; Besson, C.; Geletii, Y. V.; Musaev, D. G.; Kuznetsov, A. E.; Luo, Z.; Hardcastle, K. I.; Hill, C. L. *Science* **2010**, *328*, 342.

(39) Walter, M. G.; Warren, E. L.; McKone, J. R.; Boettcher, S. W.; Mi, Q.; Santori, E. A.; Lewis, N. S. *Chem. Rev.* **2010**, *110*, 6446.

(40) Subraman.S; Fisher, H. F. *Roczniki Chemii* **1971**, *45*, 933.

(41) Maeda, K.; Teramura, K.; DalingLu; Takata, T.; Saito, N.; Inoue, Y.; Domen, K. *Nature* **2006**, *440*, 295.

(42) Higashi, M.; Domen, K.; Abe, R. *J. Am. Chem. Soc.* **2012**, *134*, 6968.

(43) Hong, D.; Yamada, Y.; Nomura, A.; Fukuzumi, S. *Phys. Chem. Chem. Phys.* **2013**, *15*, 19125.

(44) Yamada, Y.; Yano, K.; Hong, D.; Fukuzumi, S. *Phys. Chem. Chem. Phys.* **2012**, *14*, 5753.

(45) McDaniel, N. D.; Coughlin, F. J.; Tinker, L. L.; Bernhard, S. *J. Am. Chem. Soc.* **2007**, *130*, 210.

(46) Wasylenko, D. J.; Ganesamoorthy, C.; Koivisto, B. D.; Henderson, M. A.; Berlinguette, C. P. *Inorg. Chem.* **2010**, *49*, 2202.

(47) Gloaguen, F.; Lawrence, J. D.; Rauchfuss, T. B. *J. Am. Chem. Soc.* **2001**, *123*, 9476.

(48) Tard, C.; Liu, X.; Ibrahim, S. K.; Bruschi, M.; De, G. L.; Davies, S. C.; Yang, X.; Wang, L.-S.; Sawers, G.; Pickett, C. J. *Nature (London, U. K.)* **2005**, *433*, 610.

(49) Streich, D.; Astuti, Y.; Orlandi, M.; Schwartz, L.; Lomoth, R.; Hammarstroem, L.; Ott, S. *Chem.--Eur. J.* **2010**, *16*, 60.

(50) Li, X.; Wang, M.; Chen, L.; Wang, X.; Dong, J.; Sun, L. *ChemSusChem* **2012**, *5*, 913.

(51) Singh, W. M.; Pegram, D.; Duan, H.; Kalita, D.; Simone, P.; Emmert, G. L.; Zhao, X. *Angew. Chem. Int. Ed.* **2012**, *51*, 1653.

(52) Berggren, G.; Adamska, A.; Lambertz, C.; Simmons, T. R.; Esselborn, J.; Atta, M.; Gambarelli, S.; Mouesca, J. M.; Reijerse, E.; Lubitz, W.; Happe, T.; Artero, V.; Fontecave, M. *Nature* **2013**, *499*, 66.

(53) Orain, C.; Quentel, F.; Gloaguen, F. *ChemSusChem* **2014**, *7*, 638.

(54) Hu, X.; Brunschwig, B. S.; Peters, J. C. *J. Am. Chem. Soc.* **2007**, *129*, 8988.

(55) Fihri, A.; Artero, V.; Razavet, M.; Baffert, C.; Leibl, W.; Fontecave, M. *Angew. Chem. Int. Ed.* **2008**, *47*, 564.

(56) Du, P.; Knowles, K.; Eisenberg, R. *J. Am. Chem. Soc.* **2008**, *130*, 12576.

(57) Lazarides, T.; McCormick, T.; Du, P.; Luo, G.; Lindley, B.; Eisenberg, R. *J. Am. Chem. Soc.* **2009**, *131*, 9192.

(58) Dempsey, J. L.; Winkler, J. R.; Gray, H. B. *J. Am. Chem. Soc.* **2009**, *132*, 1060.

(59) Probst, B.; Rodenberg, A.; Guttentag, M.; Hamm, P.; Alberto, R. *Inorg. Chem.* **2010**, *49*, 6453.

(60) McCormick, T. M.; Calitree, B. D.; Orchard, A.; Kraut, N. D.; Bright, F. V.; Detty, M. R.; Eisenberg, R. *J. Am. Chem. Soc.* **2010**, *132*, 15480.

(61) McNamara, W. R.; Han, Z.; Alperin, P. J.; Brennessel, W. W.; Holland, P. L.; Eisenberg, R. *J. Am. Chem. Soc.* **2011**, *133*, 15368.

(62) Stubbert, B. D.; Peters, J. C.; Gray, H. B. *J. Am. Chem. Soc.* **2011**, *133*, 18070.

(63) Zhang, P.; Jacques, P.-A.; Chavarot-Kerlidou, M.; Wang, M.; Sun, L.; Fontecave, M.; Artero, V. *Inorg. Chem.* **2012**, *51*, 2115.

(64) Marinescu, S. C.; Winkler, J. R.; Gray, H. B. *Proc. Natl. Acad. Sci. USA* **2012**, *109*, 15127.

(65) Singh, W. M.; Baine, T.; Kudo, S.; Tian, S.; Ma, X. A. N.; Zhou, H.; DeYonker, N. J.; Pham, T. C.; Bollinger, J. C.; Baker, D. L.; Yan, B.; Webster, C. E.; Zhao, X. *Angew. Chem. Int. Ed.* **2012**, *51*, 5941.

(66) McNamara, W. R.; Han, Z.; Yin, C.-J.; Brennessel, W. W.; Holland, P. L.; Eisenberg, R. *Proc. Natl. Acad. Sci. USA* **2012**, *109*, 15594.

(67) Nippe, M.; Khnayzer, R. S.; Panetier, J. A.; Zee, D. Z.; Olaiya, B. S.; Head-Gordon, M.; Chang, C. J.; Castellano, F. N.; Long, J. R. *Chemical Science* **2013**, *4*, 3934.

(68) Khnayzer, R. S.; Thoi, V. S.; Nippe, M.; King, A. E.; Jurss, J. W.; El Roz, K. A.; Long, J. R.; Chang, C. J.; Castellano, F. N. *Energy Environ. Sci.* **2014**, *7*, 1477.

(69) Chen, L.; Wang, M.; Han, K.; Zhang, P.; Gloaguen, F.; Sun, L. *Energy Environ. Sci.* **2014**, *7*, 329.

(70) Kilgore, U. J.; Roberts, J. A. S.; Pool, D. H.; Appel, A. M.; Stewart, M. P.; DuBois, M. R.; Dougherty, W. G.; Kassel, W. S.; Bullock, R. M.; DuBois, D. L. *J. Am. Chem. Soc.* **2011**, *133*, 5861.

(71) Helm, M. L.; Stewart, M. P.; Bullock, R. M.; DuBois, M. R.; DuBois, D. L. *Science* **2011**, *333*, 863.

(72) O'Hagan, M.; Ho, M.-H.; Yang, J. Y.; Appel, A. M.; DuBois, M. R.; Raugei, S.; Shaw, W. J.; DuBois, D. L.; Bullock, R. M. *J. Am. Chem. Soc.* **2012**, *134*, 19409.

(73) McLaughlin, M. P.; McCormick, T. M.; Eisenberg, R.; Holland, P. L. *Chem. Commun.* **2011**, *47*, 7989.

(74) Han, Z.; Qiu, F.; Eisenberg, R.; Holland, P. L.; Krauss, T. D. *Science* **2012**, *338*, 1321.

(75) Han, Z.; McNamara, W. R.; Eum, M.-S.; Holland, P. L.; Eisenberg, R. *Angew. Chem. Int. Ed.* **2012**, *51*, 1667.

(76) Cui, H.-h.; Wang, J.-y.; Hu, M.-q.; Ma, C.-b.; Wen, H.-m.; Song, X.-w.; Chen, C.-n. *Dalton Trans.* **2013**, *42*, 8684.

(77) Small, Y. A.; DuBois, D. L.; Fujita, E.; Muckerman, J. T. *Energy Environ. Sci.* **2011**, *4*, 3008.

(78) Han, Z.; Shen, L.; Brennessel, W. W.; Holland, P. L.; Eisenberg, R. *J. Am. Chem. Soc.* **2013**, *135*, 14659.

(79) Karunadasa, H. I.; Chang, C. J.; Long, J. R. *Nature* **2010**, *464*, 1329.

(80) Karunadasa, H. I.; Montalvo, E.; Sun, Y.; Majda, M.; Long, J. R.; Chang, C. J. *Science* **2012**, *335*, 698.

(81) Thoi, V. S.; Karunadasa, H. I.; Surendranath, Y.; Long, J. R.; Chang, C. J. *Energy Environ. Sci.* **2012**, *5*, 7762.

(82) Hawecker, J.; Lehn, J. M.; Ziessel, R. *Nouv. J. Chim.* **1983**, *7*, 271.

(83) Collin, J. P.; Sauvage, J. P. *Coord. Chem. Rev.* **1989**, *93*, 245.

(84) Schley, N. D.; Blakemore, J. D.; Subbaiyan, N. K.; Incarvito, C. D.; D'Souza, F.; Crabtree, R. H.; Brudvig, G. W. *J. Am. Chem. Soc.* **2011**, *133*, 10473.

(85) Hong, D.; Murakami, M.; Yamada, Y.; Fukuzumi, S. *Energy Environ. Sci.* **2012**, *5*, 5708.

(86) Wang, L.; Duan, L.; Tong, L.; Sun, L. *J. Catal.* **2013**, *306*, 129.

(87) Hong, D.; Jung, J.; Park, J.; Yamada, Y.; Suenobu, T.; Lee, Y.-M.; Nam, W.; Fukuzumi, S. *Energy Environ. Sci.* **2012**, *5*, 7606.

(88) Pope, M. T. In *Comprehensive Coordination Chemistry II: From Biology to Nanotechnology*; Wedd, A. G., Ed.; Elsevier Ltd.: Oxford, UK, 2004; Vol. 4, p 635.

(89) Hill, C. L. In *Comprehensive Coordination Chemistry-II: From Biology to Nanotechnology*; Wedd, A. G., Ed.; Elsevier Ltd.: Oxford, UK, 2004; Vol. 4, p 679.

(90) Long, D.-L.; Tsunashima, R.; Cronin, L. *Angew. Chem. Int. Ed.* **2010**, *49*, 1736.

(91) *Special Thematic Issue on Polyoxometalates*; Hill, C. L., Ed., 1998; Vol. 98, No. 1.

(92) *Polyoxometalate Chemistry From Topology via Self-Assembly to Applications*; Pope, M. T.; Müller, A., Eds.; Kluwer Academic Publishers: Dordrecht, 2001.

(93) Borrás-Almenar, J. J.; Coronado, E.; Müller, A.; Pope, M. T. *Polyoxometalate Molecular Science. Proceedings of the NATO Advanced Study Institute, Tenerife, Spain from 25 August to 4 September 2001*; Kluwer Academic Publishers: Dordrecht, 2003; Vol. 98.

(94) Long, D.-L.; Burkholder, E.; Cronin, L. *Chem. Soc. Rev.* **2007**, *36*, 105.

(95) Pope, M. T. *Heteropoly and Isopoly Oxometalates*; Springer-Verlag: Berlin, 1983.

(96) Day, V. W.; Klemperer, W. G. *Science* **1985**, *228*, 533.

(97) Pope, M. T. In *Comprehensive Coordination Chemistry*; Wilkinson, G., Gillard, R. D., McCleverty, J. A., Eds.; Pergamon Press: New York, 1987; Vol. 3, p Chapter 38.

(98) Pope, M. T.; Müller, A. *Angew. Chem. Int. Ed.* **1991**, *30*, 34.

(99) *Polyoxometalates: From Platonic Solids to Anti-retroviral Activity*; Pope, M. T.; Müller, A., Eds.; Kluwer Academic Publishers: Dordrecht, Netherlands, 1993.

(100) Hill, C. L. *Chem. Rev.* **1998**, *98*, 1.

(101) Kortz, U.; Müller, A. *J. Cluster Sci.* **2006**, *17*, 139.

(102) Berzelius, J. J. *Poggendorfs Ann. Phys. Chem.* **1826**, *6*, 369.

(103) Pauling, L. *J. Am. Chem. Soc.* **1929**, *51*, 2868.

(104) Keggin, J. F. *Nature* **1933**, *131*, 908.

(105) Pope, M. T. In *Prog. Inorg. Chem.*; Lippard, S. J., Ed.; John Wiley & Sons, Inc.: New York, 1991; Vol. 39, p 181.

(106) Zheng, S.-T.; Yang, G.-Y. *Chem. Soc. Rev.* **2012**, *41*, 7623.

(107) Song, Y.-F.; Tsunashima, R. *Chem. Soc. Rev.* **2012**, *41*, 7384.

(108) Lv, H.; Geletii, Y. V.; Zhao, C.; Vickers, J. W.; Zhu, G.; Luo, Z.; Song, J.; Lian, T.; Musaev, D. G.; Hill, C. L. *Chem. Soc. Rev.* **2012**, *41*, 7572.

(109) Lopez, X.; Carbo, J. J.; Bo, C.; Poblet, J. M. *Chem. Soc. Rev.* **2012**, *41*, 7537.

(110) Clemente-Juan, J. M.; Coronado, E.; Gaita-Arino, A. *Chem. Soc. Rev.* **2012**, *41*, 7464.

(111) Nyman, M.; Burns, P. C. *Chem. Soc. Rev.* **2012**, *41*, 7354.

(112) Fullmer, L. B.; Molina, P. I.; Antonio, M. R.; Nyman, M. *Dalton Trans.* **2014**, First published online 05 Sep 2014.

(113) Nyman, M. *Dalton Trans.* **2011**, *40*, 8049.

(114) Dong, L.; Huang, R.; Wei, Y.; Chu, W. *Inorg. Chem.* **2009**, *48*, 7528.

(115) Sadeghi, O.; Zakharov, L. N.; Nyman, M. *Science* **2015**, *347*, 1359.

(116) Besecker, C. J.; Klemperer, W. G. *J. Am. Chem. Soc.* **1980**, *25*, 7598.

(117) Day, V. W.; Klemperer, W. G.; Schwartz, C. *J. Am. Chem. Soc.* **1987**, *109*, 6030.

(118) Kim, G.; Zeng, H.; Rhule, J. T.; Weinstock, I. A.; Hill, C. L. *J. Chem. Soc., Chem. Commun.* **1999**, 1651.

(119) Judd, D. A.; Nettles, J. H.; Nevins, N.; Snyder, J. P.; Liotta, D. C.; Tang, J.; Ermolieff, J.; Schinazi, R. F.; Hill, C. L. *J. Am. Chem. Soc.* **2001**, *123*, 886.

(120) Li, S.; Liu, S.; Liu, S.; Liu, Y.; Tang, Q.; Shi, Z.; Ouyang, S.; Ye, J. *J. Am. Chem. Soc.* **2012**, *134*, 19716.

(121) Baker, L. C. W.; Figgis, J. S. *J. Am. Chem. Soc.* **1970**, *92*, 3794.

(122) Brown, G. M.; Noe-Spirlet, M. R.; Busing, W. R.; Levy, H. A. *Acta Crystallogr., Sect. B: Struct. Sci.* **1977**, *B33*, 1038.

(123) Wells, A. F. *Structural Inorganic Chemistry*; Clarendon Press: Oxford, 1945.

(124) Müller, A.; Meyer, J.; Krickemeyer, E.; Diemann, E. *Angew. Chem. Int. Ed.* **1996**, *35*, 1206.

(125) Müller, A.; Meyer, J.; Krickemeyer, E.; Beugholt, C.; Bogge, H.; Peters, F.; Schmidtmann, M.; Kogerler, P.; Koop, M. J. *Chem. Eur. J.* **1998**, *4*, 1000.

(126) Müller, A.; Peters, F.; Pope, M. T.; Gatteschi, D. *Chem. Rev.* **1998**, *98*, 239.

(127) Müller, A.; Kögerler, P. *Coord. Chem. Rev.* **1999**, 3.

(128) Müller, A.; Sarkar, S.; Shah, S. Q. N.; Bögge, H.; Schmidtmann, M.; Sarkar, S.; Koegerler, P.; Hauptfleisch, B.; Trautwein, A. X.; Schuenemann, V. *Angew. Chem. Int. Ed.* **1999**, *38*, 3238.

(129) Müller, A.; Shah, S. Q. N.; Bogge, H.; Schmidtmann, M. *Nature* **1999**, *397*, 48.

(130) Müller, A.; Serain, C. *Acc. Chem. Res.* **2000**, *33*, 2.

(131) Cronin, L.; Beugholt, C.; Müller, A. *J. Mol. Struct.* **2000**, *500*, 181.

(132) Cronin, L.; Kögerler, P.; Müller, A. *J. Solid State Chem.* **2000**, *152*, 57.

(133) Yamase, T.; Prokop, P. V. *Angew. Chem. Int. Ed.* **2002**, *41*, 466.

(134) Müller, A.; Roy, S. *Coord. Chem. Rev.* **2003**, *245*, 153.

(135) Botar, B.; Kögerler, P.; Müller, A.; Garcia-Serres, R.; Hill, C. L. *Chem. Commun.* **2005**, 5621.

(136) Botar, B.; Kögerler, P.; Hill, C. L. *Chem. Commun.* **2005**, *25*, 3138.

(137) Botar, B.; Kögerler, P.; Hill, C. L. *J. Am. Chem. Soc.* **2006**, *128*, 5336.

(138) Merca, A.; Bögge, a.; Schmidtmann, M.; Zhou, Y.; Haupt, E. T. K.; Sarker, M. K.; Hill, C. L.; Müller, A. *Chem. Commun.* **2008**, 948.

(139) Kögerler, P.; Tsukerblat, B.; Müller, A. *Dalton Trans.* **2010**, *39*, 21.

(140) Miras, H. N.; Cooper, G. J. T.; Long, D.-L.; Bögge, H.; Müller, A.; Streb, C.; Cronin, L. *Science* **2010**, *327*, 72.

(141) Capon, B. S., M. Cecil; Anderson, E.; Dahm, R. H.; Sankey, G. H. *J. Chem. Soc. B* **1969**, *8*, 1038.

(142) Nomiya, K.; Takahashi, T.; Shirai, T.; Miwa, M. *Polyhedron* **1987**, *6*, 213.

(143) Peacock, R. D.; Weakley, T. J. R. *J. Chem. Soc. A* **1971**, 1937.

(144) Dexter, D. D.; Silverton, J. V. *J. Am. Chem. Soc.* **1968**, *90*, 3589.

(145) Naruke, H.; Yamase, T. *Acta Crystallogr., Sect. C: Cryst. Struct. Commun.* **1992**, *48*, 597.

(146) Khan, M. I.; Cevik, S.; Hayashi, R. *J. Chem. Soc., Dalton Trans.* **1999**, 1651.

(147) Contant, R.; Thouvenot, R. *Can. J. Chem. - Revue Canadienne de Chimie* **1991**, *69*, 1498.

(148) Contant, R.; Thouvenot, R. *Inorg. Chim. Acta* **1993**, *212*, 41.

(149) Laronze, N.; Marrot, J.; Hervé, G. *Chem. Commun.* **2003**, 2360.

(150) Long, D.-L.; Kögerler, P.; Cronin, L. *Angew. Chem. Int. Ed.* **2004**, *43*, 1817.

(151) Long, D.-L.; Abbas, H.; Kögerler, P.; Cronin, L. *Angew. Chem. Int. Ed.* **2005**, *44*, 3415.

(152) Miras, H. N.; Long, D.-L.; Kogerler, P.; Cronin, L. *Dalton Trans.* **2008**, *0*, 214.

(153) Wang, J.; Li, S.; Shen, Y.; Niu, J. *Cryst. Growth Des.* **2008**, *8*, 372.

(154) Chorghade, G. S.; Pope, M. T. *J. Am. Chem. Soc.* **1987**, *109*, 5134.

(155) Weeks, M. S.; Hill, C. L.; Schinazi, R. F. *J. Med. Chem.* **1992**, *35*, 1216.

(156) Gouzerh, P.; Proust, A. *Chem. Rev.* **1998**, *98*, 77.

(157) Hill, C. L.; Brown, R. B., Jr. *J. Am. Chem. Soc.* **1986**, *108*, 536.

(158) Kato, C. N.; Shinohara, A.; Hayashi, K.; Nomiya, K. *Inorg. Chem.* **2006**, *45*, 8108.

(159) Soderholm, L.; Liu, G. K.; Muntean, J.; Malinsky, J.; Antonio, M. R. *J. Phys. Chem.* **1995**, *99*, 9611.

(160) Mialane, P.; Lisnard, L.; Mallard, A.; Marrot, J.; Antic-Fidancev, E.; Aschehoug, P.; Vivien, D.; Sécheresse, F. *Inorg. Chem.* **2003**, *42*, 2102.

(161) Robert, F.; Tézé, A. *Acta Crystallogr.* **1981**, *B37*, 318.

(162) Randall, W. J.; Droege, M. W.; Mizuno, N.; Nomiya, K.; Weakley, T. J. R.; Finke, R. G. In *Inorg. Synth.*; Cowley, A. H., Ed.; John Wiley & Sons, Inc.: New York, 1997; Vol. 31, p 167.

(163) Bosing, M.; Loose, I.; Pohlmann, H.; Krebs, B. *Chem. Eur. J.* **1997**, *3*, 1232.

(164) Finke, R. G.; Droege, M. W.; Domaille, P. J. *Inorg. Chem.* **1987**, *26*, 3886.

(165) Zhang, H.-M.; Li, Y.-G.; Lu, Y.; Clérac, R.; Zhang, Z.-M.; Wu, Q.; Feng, X.-J.; Wang, E.-B. *Inorg. Chem.* **2009**, *48*, 10889.

(166) Huang, Z.; Luo, Z.; Geletii, Y. V.; Vickers, J.; Yin, Q.; Wu, D.; Hou, Y.; Ding, Y.; Song, J.; Musaev, D. G.; Hill, C. L.; Lian, T. *J. Am. Chem. Soc.* **2011**, *133*, 2068.

(167) Han, X.-B.; Zhang, Z.-M.; Zhang, T.; Li, Y.-G.; Lin, W.; You, W.; Su, Z.-M.; Wang, E.-B. *J. Am. Chem. Soc.* **2014**, *136*, 5359.

(168) Lv, H.; Guo, W.; Wu, K.; Chen, Z.; Bacsa, J.; Musaev, D. G.; Geletii, Y. V.; Lauinger, S. M.; Lian, T.; Hill, C. L. *J. Am. Chem. Soc.* **2014**, ASAP September 22.

(169) Clemente-Juan, J. M.; Coronado, E.; Galán-Mascarós, J., J. R. ; Gómez-García, C. J. *Inorg. Chem.* **1999**, *38*, 55.

(170) Ibrahim, M.; Lan, Y. H.; Bassil, B. S.; Xiang, Y. X.; Suchopar, A.; Powell, A. K.; Kortz, U. *Angew. Chem. Int. Ed.* **2011**, *50*, 4708.

(171) Canny, J.; Tézé, A.; Thouvenot, R.; Hervé, G. *Inorg. Chem.* **1986**, *25*, 2114.

(172) Domaille, P. J. In *Inorg. Synth.*; Ginsberg, A. P., Ed.; John Wiley and Sons: New York, 1990; Vol. 27, p 96.

(173) Nsouli, N. H.; Bassil, B. S.; Dickman, M. H.; Kortz, U.; Keita, B.; Nadjo, L. *Inorg. Chem.* **2006**, *45*, 3858.

(174) Mizuno, N.; Nozaki, C.; Kiyoto, I.; Misono, M. *J. Am. Chem. Soc.* **1998**, *120*, 9267.

(175) Kamata, K.; Yonehara, K.; Sumida, Y.; Yamaguchi, K.; Hikichi, S.; Mizuno, N. *Science* **2003**, *300*, 964.

(176) Mizuno, N.; Yamaguchi, K.; Kamata, K. *Coord. Chem. Rev.* **2005**, *249*, 1944.

(177) Botar, B.; Geletii, Y. V.; Kögerler, P.; Musaev, D. G.; Morokuma, K.; Weinstock, I. A.; Hill, C. L. *J. Am. Chem. Soc.* **2006**, *128*, 11268.

(178) Bartis, J.; Kunina, Y.; Blumenstein, M.; Francesconi, L. C. *Inorg. Chem.* **1996**, *35*, 1497.

(179) Luo, Q.; Howell, R. C.; Bartis, J.; Dankova, M.; DeW. Horrocks, J., William; Rheingold, A. L.; Francesconi, L. C. *Inorg. Chem.* **2002**, *41*, 6112.

(180) Zhang, C.; Bensaid, L.; McGregor, D.; Fang, X.; Howell, R. C.; Burton-Pye, B.; Luo, Q.; Todaro, L.; Francesconi, L. C. *J. Cluster Sci.* **2006**, *17*, 389.

(181) Sadakane, M.; Dickman, M. H.; Pope, M. T. *Inorg. Chem.* **2001**, *40*, 2715.

(182) Finke, R. G.; Droege, M. W. *Inorg. Chem.* **1983**, *22*, 1006.

(183) Weakley, T. J. R.; Finke, R. G. *Inorg. Chem.* **1990**, *29*, 1235.

(184) Gómez-García, C. J.; Borrás-Almenar, J. J.; Coronado, E.; Ouahab, L. *Inorg. Chem.* **1994**, *33*, 4016.

(185) Harmalker, S. P.; Leparulo, M. A.; Pope, M. T. *J. Am. Chem. Soc.* **1983**, *105*, 4286.

(186) Finke, R. G.; Rapko, B.; Saxton, R. J.; Domaille, P. J. *J. Am. Chem. Soc.* **1986**, *108*, 2947.

(187) Edlund, D. J.; Saxton, R. J.; Lyon, D. K.; Finke, R. G. *Organometallics* **1988**, *7*, 1692.

(188) Pohl, M.; Lin, Y.; Weakley, T. J. R.; Nomiya, K.; Kaneko, M.; Weiner, H.; Finke, R. G. *Inorg. Chem.* **1995**, *34*, 767.

(189) Nomiya, K.; Pohl, M.; Mizuno, N.; Lyon, D. K.; Finke, R. G. *Inorg. Synth.* **1997**, *31*, 186.

(190) Judd, D. A.; Chen, Q.; Campana, C. F.; Hill, C. L. *J. Am. Chem. Soc.* **1997**, *119*, 5461.

(191) Godin, B.; Chen, Y.-G.; Vaissermann, J.; Ruhlmann, L.; Verdaguer, M.; Gouzerh, P. *Angew. Chem. Int. Ed.* **2005**, *44*, 3072.

(192) Bassil, B. S.; Ibrahim, M.; Mal, S. S.; Suchopar, A.; Biboum, R. N.; Keita, B.; Nadjo, L.; Nellutla, S.; Tol, J. v.; Dalal, N. S.; Kortz, U. *Inorg. Chem.* **2010**, *49*, 4949.

(193) Jabbour, D.; Keita, B.; Nadjo, L.; Kortz, U.; Mal, S. S. *Electrochem. Commun.* **2005**, *7*, 841.

(194) Mal, S. S.; Kortz, U. *Angew. Chem. Int. Ed.* **2005**, *44*, 3777.

(195) Mal, S. S.; Nsouli, N. H.; Dickman, M. H.; Kortz, U. *Dalton Trans.* **2007**, 2627.

(196) Pichon, C.; Mialane, P.; Dolbecq, A.; Marrot, J.; Rivière, E.; Keita, B.; Nadjo, L.; Sécheresse, F. *Inorg. Chem.* **2007**, *46*, 5292.

(197) Mal, S. S.; Dickman, M. H.; Kortz, U.; Todea, A. M.; Merca, A.; Bögge, H.; Glaser, T.; Müller, A.; Nellutla, S.; Kaur, N.; Tol, J. v.; Dalal, N. S.; Keita, B.; Nadjo, L. *Chem. Eur. J.* **2008**, *14*, 1186.

(198) Mitchell, S. G.; Gabb, D.; Ritchie, C.; Hazel, N.; Long, D.-L.; Cronin, L. *CrystEngComm* **2009**, *11*, 36.

(199) Mitchell, S. G.; Streb, C.; Miras, H. N.; Boyd, T.; Long, D.-L.; Cronin, L. *Nature Chem.* **2010**, *2*, 308.

(200) Mitchell, S. G.; Boyd, T.; Miras, H. N.; Long, D.-L.; Cronin, L. *Inorg. Chem.* **2011**, *50*, 136.

(201) Zhang, Z.-M.; Yao, S.; Li, Y.-G.; Wang, Y.-H.; Qi, Y.-F.; Wang, E.-B. *Chem. Commun.* **2008**, 1650.

(202) Barnard, D. L.; Hill, C. L.; Gage, T.; Matheson, J. E.; Huffman, J. H.; Sidwell, R. W.; Otto, M. I.; Schinazi, R. F. *Antiviral Res.* **1997**, *34*, 27.

(203) Hill, C.; Weeks, M.; Schinazi, R. F. *J. Med. Chem.* **1990**, *33*, 2767.

(204) Schinazi, R. F.; Sijbesma, R.; Srdanov, G.; Hill, C. L.; Wudl, F. *Antimicrob. Agents Chemother.* **1993**, *37*, 1707.

(205) Shigeta, S.; Mori, S.; Watanabe, J.; Baba, M.; Khenkin, A. M.; Hill, C. L.; Schinazi, R. F. *Antiviral Chem. Chemother.* **1995**, *6*, 114.

(206) Yamase, T.; Fukuda, N.; Tajima, Y. *Biol. Pharm. Bull.* **1996**, *19*, 459.

(207) Fukuda, N.; Yamase, T. *Biol. Pharm. Bull.* **1997**, *20*, 927.

(208) Shigeta, S.; Mori, S.; Watanabe, J.; Soeda, S.; Takahashi, K.; Yamase, T. *Antimicrob. Agents Chemother.* **1997**, *41*, 1423.

(209) Shigeta, S.; Mori, S.; Kodama, E.; Kodama, J.; Takahashi, K.; Yamase, T. *Antiviral Res.* **2003**, *58*, 265.

(210) Hasenknopf, B. *Front. Biosci.* **2005**, *10*, 275.

(211) Rhule, J. T.; Hill, C. L.; Judd, D. A.; Schinazi, R. F. *Chem. Rev.* **1998**, *98*, 327.

(212) Clayette, P.; Dormont, D. *Topics in Molecular Organization and Engineering* **1994**, *10*, 387.

(213) Lee, I. S.; Long, J. R.; Prusiner, S. B.; Safar, J. G. *J. Am. Chem. Soc.* **2005**, *127*, 13802.

(214) Wille, H.; Shanmugam, M.; Murugesu, M.; Ollesch, J.; Stubbs, G.; Long, J. R.; Safar, J. G.; Prusiner, S. B. *Proc. Natl. Acad. Sci.* **2009**, *106*, 3740.

(215) Coronado, E.; Gómez-García, C. J. *Chem. Rev.* **1998**, *98*, 273.

(216) Coronado, E.; Day, P. *Chem. Rev.* **2004**, *104*, 5419.

(217) Clemente-Juan, J. M.; Coronado, E. *Chem. Rev.* **1999**, *193-195*, 361.

(218) Speldrich, M.; Schilder, H.; Lueken, H.; Kögerler, P. *Isr. J. Chem.* **2011**, *51*, 215.

(219) Busche, C.; Vila-Nadal, L.; Yan, J.; Miras, H. N.; Long, D.-L.; Georgiev, V. P.; Asenov, A.; Pedersen, R. H.; Gadegaard, N.; Mirza, M. M.; Paul, D. J.; Poblet, J. M.; Cronin, L. *Nature* **2014**, *515*, 545.

(220) Hasenknopf, B.; Micoine, K.; Lacôte, E.; Thorimbert, S.; Malacria, M.; Thouvenot, R. *Eur. J. Inorg. Chem.* **2008**, 5001.

(221) Hou, Y.; Fang, X.; Hill, C. L. *Chem. Eur. J.* **2007**, *13*, 9442.

(222) Fang, X.; Anderson, T. M.; Hill, C. L. *Angew. Chem. Int. Ed.* **2005**, *44*, 3540.

(223) Fang, X.; Anderson, T. M.; Hou, Y.; Hill, C. L. *Chem. Commun.* **2005**, 5044.

(224) Yan, L.; López, X.; Carbó, J. J.; Sniatynsky, R.; Duncan, D. C.; Poblet, J. M. *J. Am. Chem. Soc.* **2008**, *130*, 8223.

(225) Carraro, M.; Modugno, G.; Sartorel, A.; Scorrano, G.; Bonchio, M. *Eur. J. Inorg. Chem.* **2009**, 5164.

(226) Jahier, C.; Cantuel, M.; McClenaghan, N. D.; Buffeteau, T.; Cavagnat, D.; Agbossou, F.; Carraro, M.; Bonchio, M.; Nlate, S. *Chem. Eur. J.* **2009**, *15*, 8703.

(227) Lu, M.; Kang, J.; Wang, D.; Peng, Z. *Inorg. Chem.* **2005**, *44*, 7711.

(228) An, H.-Y.; Wang, E.-B.; Xiao, D.-R.; Li, Y.-G.; Su, Z.-M.; Xu, L. *Angew. Chem. Int. Ed.* **2006**, *45*, 904.

(229) Long, D.-L.; Kögerler, P.; Farrugia, L. J.; Cronin, L. *Chem. Asian J.* **2006**, *1*, 352.

(230) Zhao, C.; Huang, Z.; Rodríguez-Córdoba, W.; Kambara, C. S.; O'Halloran, K. P.; Hardcastle, K. I.; Musaev, D. G.; Lian, T.; Hill, C. L. *J. Am. Chem. Soc.* **2011**, *133*, 20134.

(231) Zhao, C.; Kambara, C. S.; Yang, Y.; Kaledin, A. L.; Musaev, D. G.; Lian, T.; Hill, C. L. *Inorg. Chem.* **2013**, *52*, 671.

(232) Zhao, C.; Rodríguez-Córdoba, W.; Kaledin, A. L.; Yang, Y.; Geletii, Y. V.; Lian, T.; Musaev, D. G.; Hill, C. L. *Inorg. Chem.* **2013**, *52*, 13490.

(233) Glass, E. N.; Fielden, J.; Kaledin, A. L.; Musaev, D. G.; Lian, T.; Hill, C. L. *Chem. Eur. J.* **2014**, *20*, 4297.

(234) Katsoulis, D. E. *Chem. Rev.* **1998**, *98*, 359.

(235) Harrup, M. K.; Hill, C. L. *Inorg. Chem.* **1994**, *33*, 5448.

(236) Weinstock, I. A.; Atalla, R. H.; Reiner, R. S.; Moen, M. A.; Hammel, K. E.; Houtman, C. J.; Hill, C. L.; Harrup, M. K. *J. Mol. Catal. A: Chem.* **1997**, *116*, 59.

(237) Weinstock, I. A.; Barbuzzi, E. M. G.; Wemple, M. W.; Cowan, J. J.; Reiner, R. S.; Sonnen, D. M.; Heintz, R. A.; Bond, J. S.; Hill, C. L. *Nature* **2001**, *414*, 191.

(238) Hill, C. L.; Prosser-McCartha, C. M. *Coord. Chem. Rev.* **1995**, *143*, 407.

(239) Neumann, R. *Prog. Inorg. Chem.* **1998**, *47*, 317.

(240) Neumann, R. *Mod. Oxidation Methods* **2004**, 223.

(241) Neumann, R. In *Transition Metals for Organic Synthesis (2nd Edition)*; Beller, M., Bolm, C., Eds.; Wiley-VCH: Weinheim, 2004; Vol. 2, p 415.

(242) Vazylyev, M.; Dorit, S.-R.; Haimov, A.; Maayan, G.; Neumann, R. *Top. Catal.* **2005**, *34(1-4)*, 93.

(243) Mizuno, N.; Misono, M. *Chem. Rev.* **1998**, *98*, 199.

(244) Misono, M.; Ono, I.; Koyano, G.; Aoshima, A. *Pure Appl. Chem.* **2000**, *72*, 1305.

(245) Okuhara, T.; Mizuno, N.; Misono, M. *Appl. Catal., A* **2001**, *222*, 63.

(246) Okuhara, T.; Mizuno, N.; Misono, M. *Adv. Catal.* **1996**, *41*, 113.

(247) Kozhevnikov, I. V. *Catalysis by Polyoxometalates*; Wiley: Chichester, England, 2002; Vol. 2.

(248) Kozhevnikov, I. V. *Chem. Rev.* **1998**, *98*, 171.

(249) Moffat, J. B. *Metal-Oxygen Clusters: The Surface and Catalytic Properties of Heteropoly Oxometalates.*; Kluwer Academic/Plenum Publishers: New York, 2001; Vol. 9.

(250) Hill, C. L. *Synlett* **1995**, 127.

(251) Villanneau, R.; Delmont, R.; Proust, A.; Gouzerh, P. *Chem. Eur. J.* **2000**, *6*, 1184.

(252) Santoni, M.-P.; Pal, A. K.; Hanan, G. S.; Proust, A.; Hasenknopf, B. *Inorg. Chem.* **2011**, *50*, 6737.

(253) Proust, A.; Thouvenot, R.; Gouzerh, P. *Chem. Commun.* **2008**, 1837.

(254) Dolbecq, A.; Dumas, E.; Mayer, C. R.; Mialane, P. *Chem. Rev.* **2010**, *110*, 6009.

(255) Kim, G. S.; Hagen, K. S.; Hill, C. L. *Inorg. Chem.* **1992**, *31*, 5316.

(256) Zeng, H.; Newkome, G. R.; Hill, C. L. *Angew. Chem. Int. Ed.* **2000**, *39*, 1771.

(257) Hou, Y.; Hill, C. L. *J. Am. Chem. Soc.* **1993**, *115*, 11823.

(258) Murakami, M.; Hong, D.; Suenobu, T.; Yamaguchi, S.; Ogura, T.; Fukuzumi, S. *J. Am. Chem. Soc.* **2011**, *133*, 11605.

(259) Goberna-Ferrón, S.; Vigara, L.; Soriano-López, J.; Galán-Mascarós, J. R. *Inorg. Chem.* **2012**, *51*, 11707.

(260) Stracke, J. J.; Finke, R. G. *ACS Catal.* **2013**, *3*, 1209.

(261) Schiwon, R.; Klingan, K.; Dau, H.; Limberg, C. *Chem. Commun.* **2014**, *50*, 100.

(262) Car, P.-E.; Guttentag, M.; Baldridge, K. K.; Albertoa, R.; Patzke, G. R. *Green Chem.* **2012**, *14*, 1680.

(263) Tanaka, S.; Annaka, M.; Sakai, K. *Chem. Commun.* **2012**, *48*, 1653.

(264) Zhu, G.; Glass, E. N.; Zhao, C.; Lv, H.; Vickers, J. W.; Geletii, Y. V.; Musaev, D. G.; Song, J.; Hill, C. L. *Dalton Trans.* **2012**, *41*, 13043.

(265) Vickers, J. W.; Lv, H.; Sumliner, J. M.; Zhu, G.; Luo, Z.; Musaev, D. G.; Geletii, Y. V.; Hill, C. L. *J. Am. Chem. Soc.* **2013**, *135*, 14110.

(266) Song, F.; Ding, Y.; Ma, B.; Wang, C.; Wang, Q.; Du, X.; Fu, S.; Song, J. *Energy Environ. Sci.* **2013**, *6*, 1170.

(267) Vickers, J. W.; Sumliner, J. M.; Lv, H.; Morris, M.; Geletii, Y. V.; Hill, C. L. *Phys. Chem. Chem. Phys.* **2014**, *16*, 11942.

(268) Lv, H.; Song, J.; Geletii, Y. V.; Vickers, J. W.; Sumliner, J. M.; Musaev, D. G.; Kögerler, P.; Zhuk, P. F.; Bacsa, J.; Zhu, G.; Hill, C. L. *J. Am. Chem. Soc.* **2014**, *136*, 9268.

(269) Han, X.-B.; Li, Y.-G.; Zhang, Z.-M.; Tan, H.-Q.; Lu, Y.; Wang, E.-B. *J. Am. Chem. Soc.* **2015**, *137*, 5486.

(270) Toma, F. M.; Sartorel, A.; Iurlo, M.; Carraro, M.; Parisse, P.; Maccato, C.; Rapino, S.; Gonzalez, B. R.; Amenitsch, H.; Ros, T. D.; Casalis, L.; Goldoni, A.; Marcaccio, M.; Scorrano, G.; Scoles, G.; Paolucci, F.; Prato, M.; Bonchio, M. *Nature Chem.* **2010**, *2*, 826.

(271) Soriano-López, J.; Goberna-Ferrón, S.; Vigara, L.; Carbó, J. J.; Poblet, J. M.; Galán-Mascarós, J. R. *Inorg. Chem.* **2013**, *52*, 4753.

(272) Guo, S.-X.; Liu, Y.; Lee, C.-Y.; Bond, A. M.; Zhang, J.; Geletii, Y. V.; Hill, C. L. *Energy Environ. Sci.* **2013**, *6*, 2654.

(273) Liu, Y.; Guo, S.-X.; Bond, A. M.; Zhang, J.; Geletii, Y. V.; Hill, C. L. *Inorg. Chem.* **2013**, *52*, 11986.

(274) Wu, J.; Liao, L.; Yan, W.; Xue, Y.; Sun, Y.; Yan, X.; Chen, Y.; Xie, Y. *ChemSusChem* **2012**, *5*, 1207.

(275) Liu, X.; Li, Y.; Peng, S.; Lu, G.; Li, S. *Int. J. Hydrogen Energy* **2012**, *37*, 12150.

(276) Zhang, Z.; Lin, Q.; Zheng, S.-T.; Bu, X.; Feng, P. *Chem. Commun.* **2011**, *47*, 3918.

(277) Matt, B.; Fize, J.; Moussa, J.; Amouri, H.; Pereira, A.; Artero, V.; Izzet, G.; Proust, A. *Energy Environ. Sci* **2013**, *6*, 1504.

(278) Suzuki, K.; Tang, F.; Kikukawa, Y.; Yamaguchi, K.; Mizuno, N. *Chem. Lett.* **2014**, *43*, 1429.

(279) Zhao, J.; Ding, Y.; Wei, J.; Du, X.; Yu, Y.; Han, R. *Int. J. Hydrogen Energy* **2014**, *39*, 18908.

(280) Pope, M. T.; Papaconstantinou, E. *Inorg. Chem.* **1967**, *6*, 1147.

(281) Papaconstantinou, E.; Pope, M. T. *Inorg. Chem.* **1967**, *6*, 1152.

(282) Varga, G. M.; Papaconstantinou, E.; Pope, M. T. *Inorg. Chem.* **1970**, *9*, 662.

(283) Papaconstantinou, E.; Pope, M. T. *Inorg. Chem.* **1970**, *9*, 667.

(284) Keita, B.; Nadjo, L. *J. Electroanal. Chem.* **1987**, *217*, 287.

(285) Keita, B.; Kortz, U.; Holzle, L. R. B.; Brown, S.; Nadjo, L. *Langmuir* **2007**, *23*, 9531.

(286) Pope, M. T. *NATO Adv. Study Inst. Ser., Ser. C* **1980**, *58*, 365.

(287) Wang, E.; Han, F.; Wang, Z.; Shen, E. *Huaxue Xuebao* **1991**, *49*, 1114.

(288) Wang, E. B.; Zhang, L. C.; Wang, Z. P.; Huang, R. D.; Zhang, B. J.; Zhan, R. Y.; Liu, Y. Y. *Acta Chim. Sinica* **1993**, *51*, 352.

(289) Hill, C. L.; Prosser-McCartha, C. M. In *Photosensitization and Photocatalysis Using Inorganic and Organometallic Compounds*; Kalyanasundaram, K., Grätzel, M., Eds.; Kluwer Academic Publishers: Dordrecht, 1993; Vol. 14, p 307.

(290) Duncan, D. C.; Netzel; L., T.; Hill, C. L. *Inorg. Chem.* **1995**, *34*, 4640.

(291) Savinov, E. N.; Saidkhanov, S. S.; Parmon, V. N.; Zamaraev, K. I. *React. Kinet. Catal. Lett.* **1981**, *17*, 407.

(292) Ioannidis, A.; Papaconstantinou, E. *Inorg. Chem.* **1985**, *24*, 439.

(293) Hill, C. L.; Bouchard, D. A. *J. Am. Chem. Soc.* **1985**, *107*, 5148.

(294) Yamase, T.; Cao, X.; Yazaki, S. *J. Mol. Catal. A: Chem.* **2007**, *262*, 119.

(295) Rausch, B.; Symes, M. D.; Chisholm, G.; Cronin, L. *Science* **2014**, *345*, 1326.

(296) Matt, B.; Fize, J.; Moussa, J.; Amouri, H.; Pereira, A.; Artero, V.; Izzet, G.; Proust, A. *Energy Environ. Sci.* **2013**, *6*, 1504.

(297) Howells, A. R.; Sankarraj, A.; Shannon, C. *J. Am. Chem. Soc.* **2004**, *126*, 12258.

(298) Shafirovich, V. Y.; Khannanov, N. K.; Strelets, V. V. *Nouveau J. Chim.* **1980**, *4*, 81.

(299) Harriman, A.; Porter, G.; Walters, P. *J. Chem. Soc., Faraday Trans. 2* **1981**, *77*, 2373.

(300) White, H. S.; Becker, W. G.; Bard, A. J. *J. Phys. Chem.* **1984**, *88*, 1840.

(301) Geletii, Y. V.; Besson, C.; Hou, Y.; Yin, Q.; Musaev, D. G.; Quinonero, D.; Cao, R.; Hardcastle, K. I.; Proust, A.; Kögerler, P.; Hill, C. L. *J. Am. Chem. Soc.* **2009**, *131*, 17360.

(302) Kuznetsov, A. E.; Geletii, Y. V.; Hill, C. L.; Morokuma, K.; Musaev, D. G. *J. Am. Chem. Soc.* **2009**, *131*, 6844.

(303) Quiñonero, D.; Kaledin, A. L.; Kuznetsov, A. E.; Geletii, Y. V.; Besson, C.; Hill, C. L.; Musaev, D. G. *J. Phys. Chem. A* **2010**, *114*, 535.

(304) Quintana, M.; López, A. M.; Rapino, S.; Toma, F. M.; Iurlo, M.; Carraro, M.; Sartorel, A.; Maccato, C.; Ke, X.; Bittencourt, C.; Da Ros, T.; Van Tendeloo, G.; Marcaccio, M.; Paolucci, F.; Prato, M.; Bonchio, M. *ACS Nano* **2013**, *7*, 811.

(305) Stracke, J. J.; Finke, R. G. *J. Am. Chem. Soc.* **2011**, *133*, 14872.

(306) Natali, M.; Berardi, S.; Sartorel, A.; Bonchio, M.; Campagna, S.; Scandola, F. *Chem. Commun.* **2012**, *48*, 8808.

Chapter 2

Novel Banana-shaped Multi-Cobalt-Containing Tungstovanadate: $[(Co(OH_2)\ Co_2VW_9O_{34})_2(VW_6O_{26})]^{17-}$

(Published in *Eur. J. Inorg. Chem.* **2013**, 1720-1725.) -- Reproduced by permission of John Wiley and Sons, License number: 3692520110111.

With Jie Song, Yurii V. Geletii, Weiwei Guo, John Bacsa and Craig L. Hill*

2.1 Introduction

In the past few decades, the versatility and accessibility of polyoxometalates (POMs) have attracted much attention due to their functional properties and many practical applications in catalysis, electrocatalysis, medicine, materials science, photochemistry, analytical chemistry, and molecular magnetism.[1-8] Typically, the framework of many POMs are composed of clusters of groups V and VI d^0 metals (Mo, W, V, Nb, Ta) bound to oxo (O^{2-}) ligands which render them oxidatively resistant and hence particularly attractive as homogeneous and heterogeneous catalysts.[9-20] Generally, POMs are sensitive to the pH of the solution, and one or more skeletal MO_6 building blocks can be removed/added in different pH environments forming lacunary POM ligands.[21,22] These lacunary POM ligands can be used to further prepare numerous structures because the oxygen atoms at the defect site(s) are quite negative and consequently much more reactive than the other POM oxygens. The most common use of lacunary POMs as ligands is in the production of transition-metal-substituted (TMS) heteropolyoxoanions with interesting catalytic and magnetic properties.[2,7,23-29]

Among those TMS heteropolyoxoanions based on lacunary Keggin or Wells-Dawson fragments, the sandwich-type structures have attracted much attention because two or more of these lacunary species [frequently $[XW_9O_{34}]^{n-}$ ($X = P^V$, As^V, Si^{IV}, Ge^{IV}), $[XW_9O_{33}]^{n-}$ ($X = Sb^{III}$, Bi^{III}) or $[X_2W_{15}O_{56}]^{n-}$ ($X = P^V$, As^V)][24-26,30-55] can bind multiple metal ions each in a strong multi-dentate fashion. In addition, a second class of sandwich-type POMs, [typically $[WM_3(H_2O)_2(XW_9O_{34})_2]^{12-}$ ($X = M = Zn^{II}$ or Co^{II}),[56] $[M_4(H_2O)_2(XW_9O_{34})_2]^{n-}$ ($M = X = Cu^{II}$ or Fe^{III}),[57] $[Ni_4(H_2O)_2(NiW_9O_{34})_2]^{16-}$,[58] and

$[M_4(H_2O)_2(XW_9O_{34})_2]^{10-}$ ($M = Co^{II}$ or Mn^{II}, $X = V^V$)],[59] involving early transition metals as heteroatoms, are also well documented.

In contrast to the above classes of sandwich-type POMs, there are far fewer examples of other sandwich-type POMs including the V-shaped or banana-shaped POMs, in which two tri-lacunary (tri-defect) POM ligands and one bridging multi-defect POM incorporate two sets of transition metal ions.[60-66] Because these banana-shaped POMs contain up to seven redox active and strongly bound 3d metals and three potentially modifiable heteroatoms, they are of great potential interest in context with multi-electron-transfer catalysts (particularly water oxidation), and catalysts for conventional organic oxidation processes. Thus this study targets and achieves both the replacement of $[PO_4]$ heteroatom units with redox-active $[VO_4]$ heteroatom units,[67-69] while incorporating six cobalt centers. We herein report the synthesis, crystal structure, electrochemistry and catalytic epoxidation activity of the new banana-shaped hexa-cobalt-containing tungstovanadate, $Na_{17}[(Co(OH_2)Co_2VW_9O_{34})_2(VW_6O_{26})]\bullet 31H_2O$ (**1**).

2.2 Experimental

2.2.1. General Methods and Materials

All chemical reagents used were from commercially available sources and were of the highest purity. Infrared spectra (2% sample in KBr pellet) were taken on a Nicolet TM 6700 FT-IR spectrometer. Elemental analyses (Na, Co, V and W) were done by Galbraith Laboratories (Knoxville, Tennessee). Electronic spectra were taken on a Hewlett-Packard 8453 diode array spectrophotometer using a 1.0-cm-optical-path quartz cuvette with water as the solvent. Cyclic voltammograms were obtained at room temperature using a

BAS CV-50W voltammetric analyzer, a Pt-wire auxiliary electrode, a glassy-carbon working electrode, and a Ag/AgCl (3 M NaCl) BAS reference electrode. Thermogravimetric analyses were performed on a STA 6000 thermal analyzer. ^{51}V NMR (151.6 MHz) spectra were obtained at 298 K in 5 mm O.D. NMR tubes on a Unity Plus 600 spectrometer equipped with a Varian 600 SW/PF6 probe head. All the chemical shifts were referenced to neat $VOCl_3$ (taken as 0 ppm at 25 ^{o}C). Organic oxidation products were quantified using a Hewlett-Packard 6890 gas chromatograph fitted with a 5% phenyl methyl silicone capillary column, a flame ionization detector, and a Hewlett-Packard 6890 series integrator (with N_2 as the carrier gas).

2.2.2. Synthesis

Synthesis of $Na_{17}[(Co(OH_2)Co_2VW_9O_{34})_2(VW_6O_{26})]\cdot 31H_2O$ (Na_{17}1). The banana-shaped polyanion **1** was synthesized by the following procedure. A 4:30:3 mole ratio of $Co(NO_3)_2\cdot 6H_2O$, $Na_2WO_4\cdot 2H_2O$ and V_2O_5 was mixed in 0.5 M acetate buffer (120 mL, pH 4.8) and the mixture vigorously stirred. The resulting turbid solution was heated to 80 °C for 2 hours forming a hot dark brown solution which was then filtered to remove any precipitate and left to crystallize for approximately one week. Dark block crystals of Na_{17}**1** formed; yield = 0.92 g (ca. 23.6 % yield based on tungsten). The systhesis also works using Na_3VO_4 in place of V_2O_5 but the yield of **1** is lower. Elemental Analysis for Na_{17}**1**: Calcd for Co, 4.75; V, 2.05; W, 59.27; found for Co, 4.80; V, 2.16; W, 60.08 FT-IR (cm^{-1}): 3436(br), 1620(s), 957(m), 876(s), 825(s), 748(sh), 702(s), 510(sh), 490(m). UV-Vis ($M^{-1}cm^{-1}$): ε_{305} = 1061; ε_{400} = 957; ε_{580} = 176. ^{51}V NMR: -509.6 ($\Delta\nu_{1/2}$ = 33.7 Hz), -524.6 ppm ($\Delta\nu_{1/2}$ = 21.6 Hz).

The tetrabutylammonium (TBA) salt was prepared using a modification of the generic method of Katsoulis and Pope.[70] Typically, an aqueous solution (10 ml H_2O) of Na_{17}**1** (0.01 mmol, 0.076 g) was added to a solution of TBA bromide (0.17 mmol, 0.055 g) in CH_2Cl_2. The resulting mixture was shaken vigorously to transfer **1** to the organic layer. The same procedure was repeated for 5 times. The brown organic layer was separated and washed with deionized water (15 mL × 6) to remove excess TBA bromide. The product was then dried *in vacuo*. The purity was confirmed by FT-IR. Crystalline material was obtained by dissolving the TBA salt in 10 mL of acetonitrile and allowing diethyl ether vapor to diffuse into the solution.

Transformation of the banana-shaped polyanion, 1, to the conventional sandwich-type polyanion, $[Co_4(H_2O)_2(VW_9O_{34})_2]^{10-}$ (2). Polyanion **2** was prepared by dissolving 50 mg of **1** in 2 mL of sodium borate buffer (40 mM, pH 8.0). The resulting dark-orange solution was left to crystallize for *ca.* 5 days to give dark needle-like crystals with a yield of ~19%. FT-IR (cm^{-1}): 3400(br), 1610(s), 960(m), 890(s), 820(s), 755(sh), 700(s), 520(sh), 485(m). UV-Vis (M^{-1} cm^{-1} in water): $\varepsilon_{400} = 1323$; $\varepsilon_{580} = 158$. ^{51}V NMR: -506.8 ppm, $\Delta\nu_{1/2} = 38.9$ Hz.

2.2.3. X-ray Crystallography

A suitable crystal of **1** or **2** was coated with Paratone N oil, suspended on a small fiber loop, and placed in a stream of cooled nitrogen (173 K) on a Bruker D8 SMART APEX CCD sealed tube diffractometer with graphite monochromated Mo Kα (0.71073 Å) radiation. A sphere of data were collected using a combination of phi and omega scans with 10 s frame exposures and 0.5º frame widths. Data collection, indexing and initial cell refinements were all carried out using SMART software.[71] Frame integration and

final cell refinements were done using SAINT software based on optimal reflections.[72] Scattering factors and anomalous dispersion corrections are taken from the *International Tables for X-ray crystallography*.[73] Structure solution, refinement, graphics and generation of publication materials were performed by using SHELXTL, V6.12 software.[74] The crystallographic data are summarized in **Table 2-1**.

Table 2-1 Crystallographic data and structure refinement for Na_{17}**1** and Na_{10}**2**

	Na_{17}**1**	Na_{10}**2**
Empirical Formula	$Na_{17}H_{90}Co_6V_3W_{24}O_{137}$	$Na_{10}H_{64}Co_4V_2W_{18}O_{100}$
Formula Weight	7592.11	5541.31
Temperature	110 K	110 K
Wavelength	0.71073 Å	0.71073 Å
Crystal system	Monoclinic	Triclinic
Space group	$P2_1/c$	$P\bar{1}$
Unit cell dimensions	a = 15.706(3) Å	a = 11.4999(13)Å
	α = 90°	α = 97.716(2)°
	b = 21.973(5) Å	b = 12.8318(14)Å
	β = 97.420(3)°	β = 106.586(2)°
	c = 35.080(8) Å	c = 17.2679(19)Å
	γ = 90°	γ = 111.564(2)°
Volume	12005(5) $Å^3$	2187.9(4) $Å^3$
Z	4	1
Density calculated	4.201 Mg/m^3	4.206 Mg/m^3
Absorption coefficient	24.108 mm^{-1}	24.667 mm^{-1}
F(000)	13514	2460
Crystal size	0.48 x 0.14 x 0.10 mm^3	0.356 x 0.285 x 0.135 mm^3
Reflections collected	192337	30743
Independent reflections	32279 [R(int) = 0.0945]	11727 [R(int) = 0.0552]
Refinement method	Full-matrix least-squares on F^2	Full-matrix least-squares on F^2
Goodness-of-fit on F^2	1.110	1.029
Final R indices [I>2σ(I)]	$^{[a]}$R1 = 0.0709, $^{[b]}$wR2 = 0.1557	$^{[a]}$R1 = 0.0480, $^{[b]}$wR2 = 0.1276

R indices (all data)	R1 = 0.1033, wR2 = 0.1747	R1 = 0.0532, wR2 = 0.1320	

[a] $R_1 = \Sigma||F_0| - |F_c|| / \Sigma|F_0|$; [b] $wR_2 = \Sigma[w(F_0^2 - F_c^2)^2]/ \Sigma[w(F_0^2)^2]^{1/2}$

2.2.4. Catalysis

The TBA salt of **1** was used as a catalyst for the epoxidation of two representative alkenes. In a typical experiment, the alkene substrate (1.0 mmol), 2 mL of the POM stock solution in 1,2-dichloroethane (containing 1 μmol of **1**), and 3 μL of decane (internal standard) were stirred at 25 °C under Ar in a sealed vial. The reaction was initiated by the addition of 68 μL of 30% aqueous H_2O_2 (0.002 mol). The organic products were identified and quantified by GC using decane as the internal standard.

2.3 Results and Discussion

2.3.1. Synthesis and Structure

The synthesis of the novel polyoxoanion **1**, $[(Co(OH_2)Co_2VW_9O_{34})_2(VW_6O_{26})]^{17-}$, is based on reaction of the three components V_2O_5, Na_2WO_4 and $Co(NO_3)_2$ in acetate buffer. The key parameter in this synthesis is the molar ratio of the starting materials, especially the ratio of Co^{2+} to WO_4^{2-}. When the Co^{2+} to WO_4^{2-} molar ratio is increased from 1:7.5 to 1:5 at parity of other conditions, single crystals of the product can be obtained, however, the heptanuclear cobalt-containing polyoxoanion, $[(Co(OH_2)Co_2VW_9O_{34})_2(VCoW_6O_{26})]^{15-}$ (the polyanion isostructural to **1** but with an additional Co(II) in the central capping position) is isolated when the ratio reaches 1:5. The structure and physical properties of this heptanuclear cobalt-containing polyoxoanion will be published elsewhere.

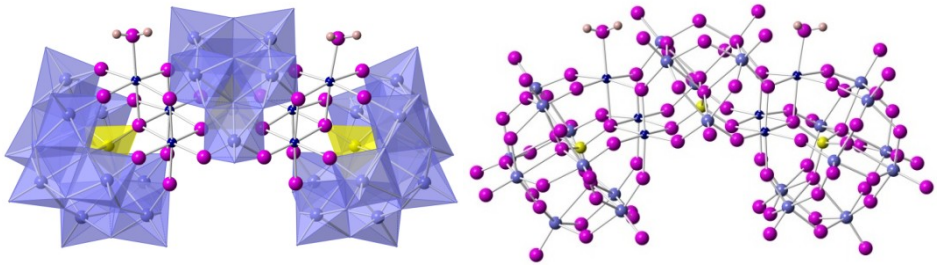

Figure 2-1 Polyhedral and ball-and-stick representations of X-ray crystal structure of 1. Magenta: oxygen; blue: cobalt; yellow balls/tetrahedra: VO_4; light blue balls/octahedra: WO_6.

Single-crystal X-ray analysis indicates that the polyoxoanion, $[((Co(OH_2)Co_2VW_9O_{34})_2(VW_6O_{26})]^{17-}$, **1**, crystallizes in the monoclinic space group $P2_1/c$ (**Figure 2-1**). This polyoxoanion structure consists of two tri-Co^{II} substituted B-α-$[(Co(OH_2)Co_2VW_9O_{39})]$ Keggin units connected by one unique $[VW_6O_{16}]$ fragment (**Figure 2-2**). The Keggin subunit was formed by the trivacant $[VW_9O_{34}]$ tungstovanadate ligand incorporating three edge-sharing CoO_6 octahedra, with one of these Co centers bearing a terminal aqua ligand. The Co2-O1W and Co4-O2W bond distances are 2.176 Å and 2.080 Å, respectively. The bridging $[VW_6O_{16}]$ subunit is related to the parent plenary α-Keggin $[VW_9O_{40}]$ unit by removal of two edge-sharing W_3O_{12} moieties from the latter. These three fragments are connected through the bridging oxygens (O25, O33, O34, O53, O54, O57, O60, O63, O65, O66) (**Figure 2-3**), leading to a banana-shaped structure with idealized C_{2v} symmetry (**Figures 2-1 and 2-2**). The polyoxoanion **1** can also be considered as a double-sandwich structure containing two $[VW_9O_{34}]$ units and one $[VW_6O_{16}]$ unit separated by two distinct Co_3O_6 fragments. This kind of banana-shaped polyoxoanion architecture was initially reported by Coronado *et al.* for the cobalt(II)-containing tungstophosphate $[Co_7(H_2O)_2(OH)_2P_2W_{25}O_{94}]^{16-}$,[61] but in this case, two tri-cobalt substituted Keggin units are bridged by a CoW_7O_{18} unit with a tetrahedral cobalt as the central heteroatom.

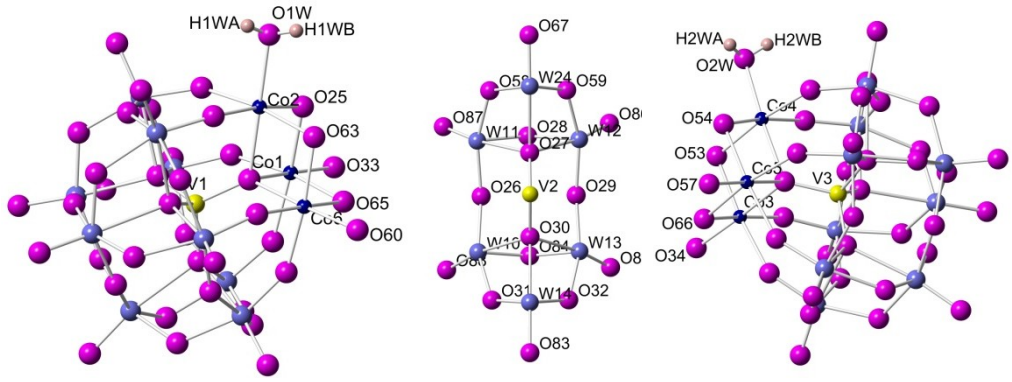

Figure 2-2 Fragments of ball-and-stick representations of X-ray single crystal structure of 1. Magenta: oxygen; blue: cobalt; yellow: V; light blue: W.

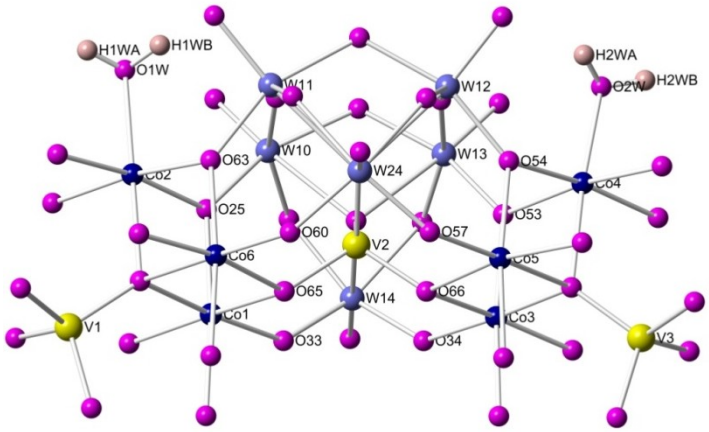

Figure 2-3 Ball-and-stick representation of the central fragment of 1. Magenta: oxygen; blue: cobalt; yellow balls: V; light blue balls: W.

Subsequently, similar banana-shaped tungstoarsenates $[M_6(H_2O)_2(AsW_9O_{34})_2(AsW_6O_{26})]^{17-}$ (M^{2+} = Ni^{2+}, Mn^{2+}, Co^{2+}, Zn^{2+} or mixed Mn^{2+}/Ni^{2+}) were reported by the groups of Kortz, Yamase and Niu.[62,63,66] Hill et al. reported the hexa-cobalt and hexa-manganese-containing tungstophosphates from the decomposition of the corresponding sandwich-type polyoxometalates, $[(M(H_2O)_2)_3(A\text{-}\alpha\text{-}PW_9O_{34})_2]^{12-}$ (M^{2+} = Mn^{2+}, Co^{2+}).[64] More recently, Yang et al. reported a banana-shaped hexa-iron-substituted tungstogermanate by the reaction of A-α-$[GeW_9O_{34}]^{10-}$ with $FeSO_4$ under hydrothermal

conditions.[65] To our knowledge, polyoxoanion **1** is the first example of hexa-cobalt-containing banana-shaped tungstovanadate.

2.3.2. Physicochemical properties

The FT-IR spectrum of **1** is shown in **Figure 2-4**. The spectrum shows very broad terminal W-O_t stretching band at 957 cm^{-1} that is superposed on the ν_{as} (V=O) stretch.[75-77] The bands between 876 cm^{-1} and 490 cm^{-1} are attributed to the asymmetric W-O_b-W, W-O_c-W bending vibrations which overlap with the V-O stretching bands.[75,78-80]

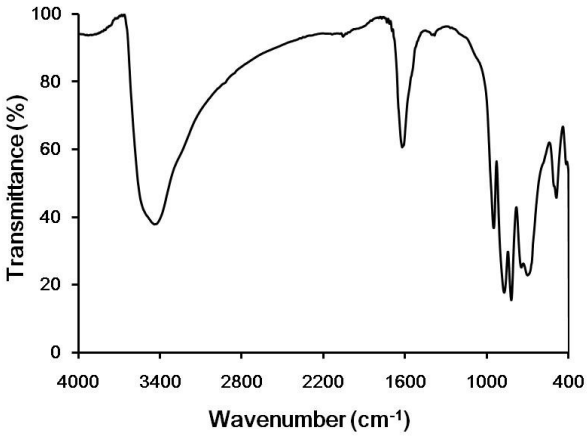

Figure 2-4 FT-IR spectrum of Na_{17}**1**.

The thermogravimetric analysis (TGA) curve (**Figure 2-5**) shows a total weight loss of ~8.07 % between 30 and 500 °C, corresponding to the loss of 31 water molecules of crystallization and two terminally bound aqua ligands on the Co2 and Co4 centers.

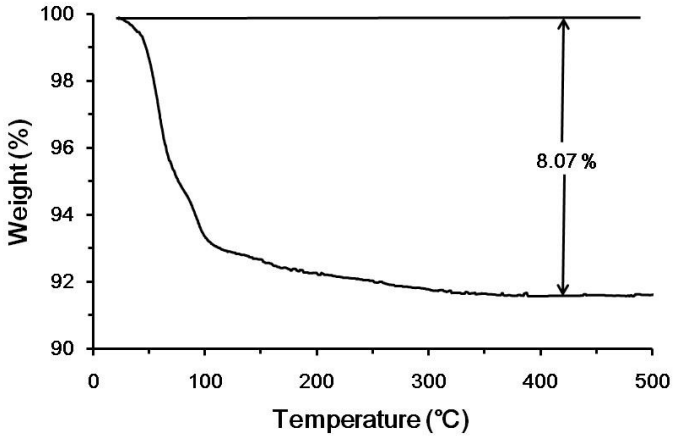

Figure 2-5 Thermogravimetric analysis of Na_{17}**1**. The calculated weight percent of water loss corresponds to 33 water molecules.

The UV-vis spectrum of **1** in aqueous solution shows characteristic absorption bands at 400 nm (ε_{400} = 957 M^{-1} cm^{-1}) and 580 nm (ε_{580} = 176 M^{-1} cm^{-1}) due to the ligand-to-metal charge transfer (LMCT) and d-d transitions, respectively (**Figure 2-6**).[64]

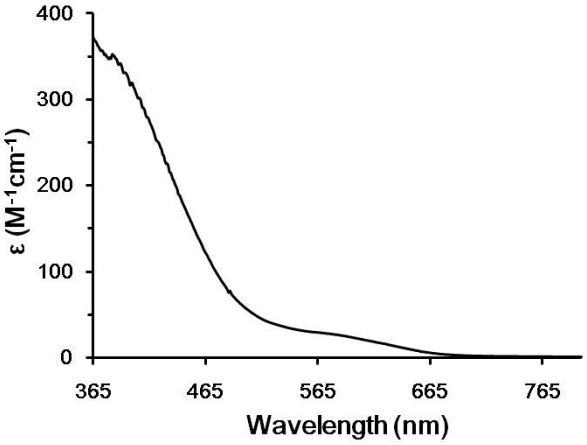

Figure 2-6 UV-vis spectrum of Na_{17}**1** in aqueous solution.

The solution structure of **1** is confirmed by ^{51}V NMR: **Figure 2-7** shows two peaks at -509.6 ppm ($\Delta\nu_{1/2}$ = 33.7 Hz) and -524.6 ppm ($\Delta\nu_{1/2}$ = 21.6 Hz) in D_2O in a 1:2 ratio corresponding to the three central pseudotetrahedral vanadium centers in the bridging $[VW_6O_{16}]$ subunit and two symmetry-equivalent $[VW_9O_{34}]^{9-}$ ligands, respectively.

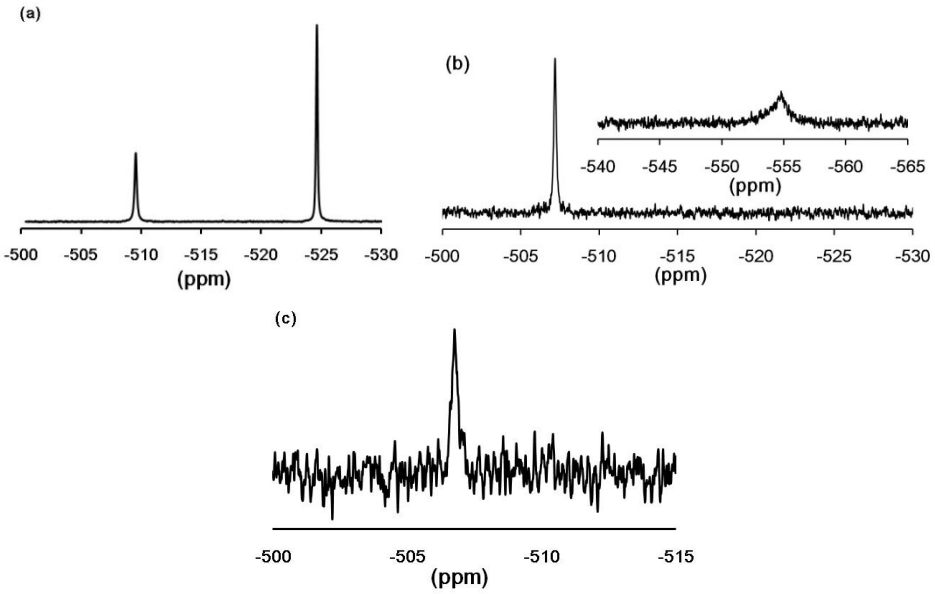

Figure 2-7 ^{51}V NMR spectrum of polyoxoanion **1** in (a) D_2O; (b) 40 mM borate buffer prepared in D_2O (pH 8.0); and polyoxoanion **2** in (c) 40 mM borate buffer prepared in D_2O (pH 8.0). Chemical shifts relative to pure $VOCl_3$ at 25 ^oC (0 ppm).

The cyclic voltammogram (CV) of **1** in sodium acetate buffer solution (pH 4.8) at a scan rate of 25 mV s^{-1} is shown in **Figure 2-8**. In the potential range from 0.6 V to -0.6 V, three quasi-reversible redox couples are detected with the mean potentials $E_f = (E_{pa} + E_{pc})/2$ of -0.173 V (I/I′), 0.017 V (II/II′) and 0.203 V (III/III′) (vs. Ag/AgCl), respectively. The first couple (I/I′) corresponds to the tungsten-centered redox processes. These are shifted to more positive potentials relative to the isostructural Co_6P_3 analogue.[59,81,82] The couples (II/II′ and III/III′) can be assigned as the redox processes associated with the V centers (V^{IV}/V^{III} and V^{V}/V^{IV}, respectively), which are consistent with the reported vanadium redox values.[83,84] These do not appear in similar banana-shaped POMs without V heteroatoms.[62,63] In measured potential range, no obvious redox processes for the Co centers are observed. This is almost always the case in Co-containing POMs.[59,85]

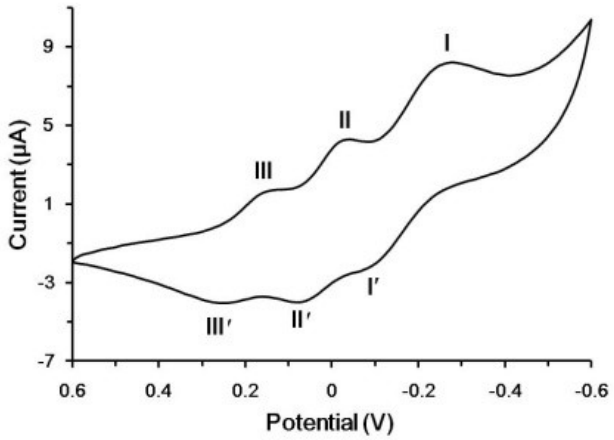

Figure 2-8 Cyclic voltammogram of a 1 mM sodium acetate buffer solution of complex 1 at pH 4.8 (scan rate = 25 mV/s). The working electrode is glassy carbon and the reference electrode is Ag/AgCl (in 3 M NaCl).

2.3.3. Stability study and the conversion of 1 to 2

In order to assess **1** as a possible water oxidation catalyst, we first checked the stability of this polyanion in sodium borate buffer (pH 8.0). Complex **1** is quite unstable in this medium; the UV-vis spectra show fast decomposition of **1** into other species during the first two hours, a reaction that slowly reaches a plateau (**Figure 2-9**).

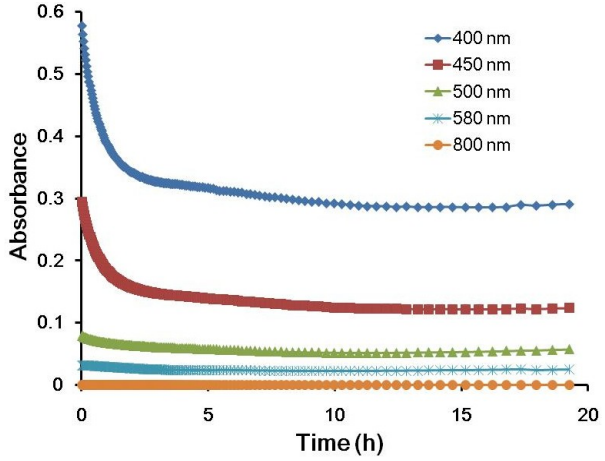

Figure 2-9 Changes in UV-vis spectra of **1** in 80 mM sodium borate buffer at pH 8.0 over a 24-hour period.

To better understand this decomposition process, the ^{51}V NMR spectra of **1** in borate buffer was measured (**Figure 2-7b**). The ^{51}V peak at -524.6 ppm ($\Delta\nu_{1/2}$ = 21.6 Hz) in this medium disappears, and a new peak at -554.7 ppm ($\Delta\nu_{1/2}$ = 51.6 Hz) appears, which corresponds to the vanadium-containing decomposition product. Interestingly, the peak at -507.2 ppm ($\Delta\nu_{1/2}$ = 35.7 Hz) remains, which has the similar chemical shift as the vanadium center in pure $[Co_4(H_2O)_2(VW_9O_{34})_2]^{10-}$ (**2**) (**Figure 2-7c**). The crystal structure of **2** is shown in Figure S5. To further confirm the conversion of **1** to **2**, we tried to recrystallize **1** in borate buffer and obtained crystals of **2** in *ca.* 19% yield (see **Table 2-1** and **Figure 2-10**).

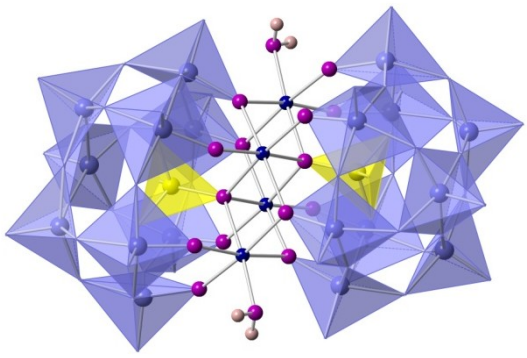

Figure 2-10 Polyhedral and ball-and-stick representation of the X-ray crystal structure of 2. Magenta: oxygen; blue: cobalt; yellow balls/tetrahedra: VO_4; light blue balls/octahedra: WO_6.

2.3.4. Catalysis

Although **1** is hydrolytically unstable in borate buffer solution, we found that it is very stable in 1,2-dichloroethane solution. We obtained the 1,2-dichloroethane-soluble TBA salt of **1** (TBA**1**) by ion exchange (TBA^+ for Na^+). The catalytic activity of TBA**1** for H_2O_2-based oxidation of two representative alkenes (1-hexene and cyclohexene) was assessed. After three days of reaction, conversions of only ~3% and ~5% for cyclohexene and 1-hexene, were achieved. These correspond to turnover numbers (TON = moles of

reacted alkene substrate after 3 days / moles of catalyst) of ~30 and ~50, respectively. The FT-IR spectra of **1** before and after reaction were identical, indicating no decomposition of the catalyst, within the limits of detection, during turnover.

2.4 Conclusions

We have synthesized and characterized a new hexanuclear cobalt-containing tungstovanadate complex, $Na_{17}[(Co(OH_2)\ Co_2VW_9O_{34})_2(VW_6O_{26})]\bullet 31H_2O$, **1**. In pH 8.0 borate buffer solution, **1** ultimately transforms to the tetracobalt-containing sandwich-type polyoxoanion, **2**, as confirmed by ^{51}V NMR and X-ray crystallography. Complex **1** shows catalytic activity for the H_2O_2-based epoxidation of 1-hexene and cyclohexene in 1,2-dichloroethane solvent.

References

(1) Pope, M. T. *Heteropoly and Isopoly Oxometalates*; Springer-Verlag: Berlin, 1983.

(2) *Special Thematic Issue on Polyoxometalates*; Hill, C. L., Ed., 1998; Vol. 98, No. 1.

(3) *Polyoxometalate Chemistry From Topology via Self-Assembly to Applications*; Pope, M. T.; Müller, A., Eds.; Kluwer Academic Publishers: Dordrecht, 2001.

(4) *Polyoxometalate Chemistry for Nano-Composite Design*; Yamase, T.; Pope, M. T., Eds.; Kluwer Academic/Plenum Publishers: New York, 2002; Vol. 2.

(5) Pope, M. T.; Müller, A. *Angew. Chem. Int. Ed.* **1991**, *30*, 34.

(6) Pope, M. T. In *Comprehensive Coordination Chemistry II: From Biology to Nanotechnology*; Wedd, A. G., Ed.; Elsevier Ltd.: Oxford, UK, 2004; Vol. 4, p 635.

(7) Hill, C. L. In *Comprehensive Coordination Chemistry-II: From Biology to Nanotechnology*; Wedd, A. G., Ed.; Elsevier Ltd.: Oxford, UK, 2004; Vol. 4, p 679.

(8) Hill, C. L.; Brown, R. B., Jr. *J. Am. Chem. Soc.* **1986**, *108*, 536.

(9) Hill, C. L.; Prosser-McCartha, C. M. *Coord. Chem. Rev.* **1995**, *143*, 407.

(10) Okuhara, T.; Mizuno, N.; Misono, M. *Adv. Catal.* **1996**, *41*, 113.

(11) Mizuno, N.; Misono, M. *Chem. Rev.* **1998**, *98*, 199.

(12) Kozhevnikov, I. V. *Chem. Rev.* **1998**, *98*, 171.

(13) Neumann, R. *Prog. Inorg. Chem.* **1998**, *47*, 317.

(14) Kozhevnikov, I. V. *Catalysis by Polyoxometalates*; Wiley: Chichester, England, 2002; Vol. 2.

(15) Geletii, Y. V.; Botar, B.; Kögerler, P.; Hillesheim, D. A.; Musaev, D. G.; Hill, C. L. *Angew. Chem. Int. Ed.* **2008**, *47*, 3896.

(16) Sartorel, A.; Carraro, M.; Scorrano, G.; Zorzi, R. D.; Geremia, S.; McDaniel, N. D.; Bernhard, S.; Bonchio, M. *J. Am. Chem. Soc.* **2008**, *130*, 5006.

(17) Geletii, Y. V.; Huang, Z.; Hou, Y.; Musaev, D. G.; Lian, T.; Hill, C. L. *J. Am. Chem. Soc.* **2009**, *131*, 7522.

(18) Yin, Q.; Tan, J. M.; Besson, C.; Geletii, Y. V.; Musaev, D. G.; Kuznetsov, A. E.; Luo, Z.; Hardcastle, K. I.; Hill, C. L. *Science* **2010**, *328*, 342.

(19) Lv, H.; Geletii, Y. V.; Zhao, C.; Vickers, J. W.; Zhu, G.; Luo, Z.; Song, J.; Lian, T.; Musaev, D. G.; Hill, C. L. *Chem. Soc. Rev.* **2012**, *41*, 7572.

(20) Song, J.; Luo, Z.; Britt, D.; Furukawa, H.; Yaghi, O. M.; Hardcastle, K. I.; Hill, C. L. *J. Am. Chem. Soc.* **2011**, *133*, 16839.

(21) Contant, R. In *Inorg. Synth.*; Ginsberg, A. P., Ed.; John Wiley and Sons: New York, 1990; Vol. 27, p 104.

(22) Domaille, P. J. In *Inorg. Synth.*; Ginsberg, A. P., Ed.; John Wiley and Sons: New York, 1990; Vol. 27, p 96.

(23) Peacock, R. D.; Weakley, T. J. R. *J. Chem. Soc. A* **1971**, 1937.

(24) Weakley, T. J. R.; Evans, H. T., Jr.; Showell, J. S.; Tourné, G. F.; Tourné, C. M. *J. Chem. Soc., Chem. Commun.* **1973**, *4*, 139.

(25) Finke, R. G.; Droege, M.; Hutchinson, J. R.; Gansow, O. *J. Am. Chem. Soc.* **1981**, *103*, 1587.

(26) Evans, H. T.; Tourné, C. M.; Tourné, G. F.; Weakley, T. J. R. *J. Chem. Soc., Dalton Trans.* **1986**, 2699.

(27) Katsoulis, D. E.; Tausch, V. S.; Pope, M. T. *Inorg. Chem.* **1987**, *26*, 215.

(28) Miras, H. N.; Yan, J.; Long, D.-L.; Cronin, L. *Chem. Soc. Rev.* **2012**, *41*, 7403.

(29) Kögerler, P.; Cronin, L. *Angew. Chem. Int. Ed.* **2005**, *44*, 844.

(30) Finke, R. G.; Droege, M. W. *Inorg. Chem.* **1983**, *22*, 1006.

(31) Finke, R. G.; Droege, M. W.; Domaille, P. J. *Inorg. Chem.* **1987**, *26*, 3886.

(32) Wasfi, S. H.; Rheingold, A. L.; Kokoszka, G. F.; Goldstein, A. S. *Inorg. Chem.* **1987**, *26*, 2934.

(33) Weakley, T. J. R.; Finke, R. G. *Inorg. Chem.* **1990**, *29*, 1235.

(34) Gómez-García, C. J.; Coronado, E.; Borrasalmenar, J. J. *Inorg. Chem.* **1992**, *31*, 1667.

(35) Casañ-Pastor, N.; Bas-Serra, J.; Coronado, E.; Pourroy, G.; Baker, L. C. W. *J. Am. Chem. Soc.* **1992**, *114*, 10380.

(36) Gómez-García, C. J.; Coronado, E.; Gómez-Romero, P.; Casañ-Pastor, N. *Inorg. Chem.* **1993**, *32*, 3378.

(37) Gómez-García, C. J.; Borrás-Almenar, J. J.; Coronado, E.; Ouahab, L. *Inorg. Chem.* **1994**, *33*, 4016.

(38) Zhang, X. Y.; Pope, M. T.; Chance, M. R.; Jameson, G. B. *Polyhedron* **1995**, *14*, 1381.

(39) Zhang, X.; Chen, Q.; Duncan, D. C.; Campana, C.; Hill, C. L. *Inorg. Chem.* **1997**, *36*, 4208.

(40) Zhang, X.; Chen, Q.; Duncan, D. C.; Lachicotte, R. J.; Hill, C. L. *Inorg. Chem.* **1997**, *36*, 4381.

(41) Qu, L.; Sun, Y.; Chen, Y.; Yu, M.; Peng, J. *Synth. React. Inorg. Met.-Org. Chem.* **1994**, *24*, 1339.

(42) Meng, L.; Liu, J. F.; Wu, Y. J.; Zhao, D. Q.; Xiao, Y. W. *Polyhedron* **1995**, *14*, 2127.

(43) Kortz, U.; Nellutla, S.; Stowe, A. C.; Dalal, N. S.; Rauwald, U.; Danquah, W.; Ravot, D. *Inorg. Chem.* **2004**, *43*, 2308.

(44) Botar, B.; Yamase, T.; Ishikawa, E. *Inorg. Chem. Commun.* **2000**, *3*, 579.

(45) Boesing, M.; Noeh, A.; Loose, I.; Krebs, B. *J. Am. Chem. Soc.* **1998**, *120*, 7252.

(46) Bosing, M.; Loose, I.; Pohlmann, H.; Krebs, B. *Chem. Eur. J.* **1997**, *3*, 1232.

(47) Kortz, U.; Savelieff, M. G.; Bassil, B. S.; Keita, B.; Nadjo, L. *Inorg. Chem.* **2002**, *41*, 783.

(48) Bi, L.-H.; Reicke, M.; Kortz, U.; Keita, B.; Nadjo, L.; Clark, R. J. *Inorg. Chem.* **2004**, *43*, 3915.

(49) Keita, B.; Mialane, P.; Sécheresse, F.; Oliveira, P. d.; Nadjo, L. *Electrochem. Commun.* **2007**, *9*, 164.

(50) Tan, H. Q.; Zhang, Z. M.; Liu, D.; Qi, Y. F.; Wang, E. B.; Li, Y. G. *J. Cluster Sci.* **2008**, *19*, 543.

(51) Clemente-Juan, J. M.; Coronado, E.; Galán-Mascarós, J., J. R. ; Gómez-García, C. J. *Inorg. Chem.* **1999**, *38*, 55.

(52) Bi, L. H.; Wang, E. B.; Peng, J.; Huang, R. D.; Xu, L.; Hu, C. W. *Inorg. Chem.* **2000**, *39*, 671.

(53) Bi, L. H.; Huang, R. D.; Peng, J.; Wang, E. B.; Wang, Y. H.; Hu, C. W. *J. Chem. Soc., Dalton Trans.* **2001**, 121.

(54) Kortz, U.; Isber, S.; Dickman, M. H.; Ravot, D. *Inorg. Chem.* **2000**, *39*, 2915.

(55) Rosu, C.; Crans, D. C.; Weakley, T. J. R. *Polyhedron* **2002**, *21*, 959.

(56) Tourné, C. M.; Tourné, G. F.; Zonnevijlle, F. *J. Chem. Soc., Dalton Trans.* **1991**, *1*, 143.

(57) Limanski, E. M.; Piepenbrink, M.; Droste, E.; Burgemeister, K.; Krebs, B. *J. Cluster Sci.* **2002**, *13*, 369.

(58) Wang, J.; Ma, P.; Shen, Y.; Niu, J. *Cryst. Growth Des.* **2007**, *7*, 603.

(59) Li, B.; Yan, Y.; Li, F.; Xu, L.; Bi, L.; Wu, L. *Inorg. Chim. Acta* **2009**, 2796.

(60) Borrás-Almenar, J. J.; Clemente-Juan, J. M.; Clemente-Leon, M.; Coronado, E.; Galán-Mascarós, J. R.; Gómez-Garcia, C. J.; Pope, M. T., Müller, A., Eds.; Kluwer: Dordrecht: The Netherlands, 2001, p 231.

(61) Clemente-Juan, J. M.; Coronado, E.; Forment-Aliaga, A.; Galán-Mascarós, J. R.; Giménez-Saiz, C.; Gómez-García, C. J. *Inorg. Chem.* **2004**, *43*, 2689.

(62) Mbomekalle, I. M.; Keita, B.; Nierlich, M.; Kortz, U.; Berthet, P.; Nadjo, L. *Inorg. Chem.* **2003**, *42*, 5143.

(63) Fukaya, K.; Yamase, T. *Bull. Chem. Soc. Jpn.* **2007**, *80*, 178.

(64) Ritorto, M. D.; Anderson, T. M.; Neiwert, W. A.; Hill, C. L. *Inorg. Chem.* **2004**, *43*, 44.

(65) Li, B.; Zhao, J.-W.; Zheng, S.-T.; Yang, G.-Y. *Inorg. Chem. Commun.* **2009**, *12*, 69.

(66) Ma, P.; Chen, L.; Zhao, J.; Wang, W.; Wang, J.; Niu, J. *Inorg. Chem. Commun.* **2011**, *14*, 415.

(67) Flynn, C. M., Jr.; Pope, M. T. *Inorg. Chem.* **1971**, *10*, 2745.

(68) Zhang, S. W.; Huang, G. Q.; Shao, M. C.; Tang, Y. Q. *J. Chem. Soc., Chem. Commun.* **1993**, 37.

(69) Khan, M. I.; Cevik, S.; Hayashi, R. *J. Chem. Soc., Dalton Trans.* **1999**, 1651.

(70) Katsoulis, D. E.; Pope, M. T. *J. Am. Chem. Soc.* **1984**, *106*, 2737.

(71) Bruker AXS, I.; Analytical X-ray Sysems: Madison, WI, 2003.

(72) Bruker AXS, I.; Analytical X-ray Systems: Madison, WI, 2003.

(73) *International Tables for X-ray Crystallography, Volume C.*; Kluwer Academic Publishers: Dordrecht, 1992; Vol. C.

(74) Bruker AXS, I. Madison, WI, 2003.

(75) Canny, J.; Thouvenot, R.; Tézé, A.; Hervé, G.; Leparulo-Loftus, M.; Pope, M. T. *Inorg. Chem.* **1991**, *30*, 976.

(76) Joo, N.; Hossu, M.; Rusu, D.; Marcu, A.; Rusu, M.; Pasca, C.; David, L. *Acta Chim. Slov.* **2007**, *54*, 749.

(77) Corella-Ochoa, M. N.; Miras, H. N.; Kidd, A.; Long, D.-L.; Cronin, L. *Chem. Commun.* **2011**, *47*, 8799.

(78) Blyholder, G.; Allen, M. C. *Inorg. Chem.* **1970**, *9*, 302.

(79) Voronkov, M. G.; Shergina, N. I.; Lapsin', A. F. *Irkutsk Institute of Organic Chemistry, Siberian Branch, Academy of Sciences of the USSR* **1972**, 2745.

(80) Hermosilla-Ibáñez, P.; Car, P. E.; Vega, A.; Costamagna, J.; Caruso, F.; Pivan, J.-Y.; Fur, E. L.; Spodine, E.; Venegas-Yazigi, D. *CrystEngComm* **2012**, 5604.

(81) Kortz, U.; Mbomekalle, I. M.; Keita, B.; Nadjo, L.; Berthet, P. *Inorg. Chem.* **2002**, *41*, 6412.

(82) Nsouli, N. H.; Bassil, B. S.; Dickman, M. H.; Kortz, U.; Keita, B.; Nadjo, L. *Inorg. Chem.* **2006**, *45*, 3858.

(83) Grigoriev, V. A.; Hill, C. L.; Weinstock, I. A. *J. Am. Chem. Soc.* **2000**, *122*, 3544.

(84) Grigoriev, V. A.; Cheng, D.; Hill, C. L.; Weinstock, I. A. *J. Am. Chem. Soc.* **2001**, *123*, 5292.

(85) Ruhlmann, L.; Nadjo, L.; Canny, J.; Contant, R.; Thouvenot, R. *Eur. J. Inorg. Chem.* **2002**, 975.

Chapter 3

An Exceptionally Fast Homogeneous Carbon-free Cobalt-based Water Oxidation Catalyst

(Published in *J. Am. Chem. Soc.* **2014***, 136,* 9268-9271.)

With Jie Song, Yurii V. Geletii, James W. Vickers, Jordan M. Sumliner, Djamaladdin G. Musaev, Paul Kögerler, Petro F. Zhuk, John Bacsa, Guibo Zhu, and Craig L. Hill*

3.1 Introduction

The development of fast, selective and stable water oxidation catalysts (WOCs) continues to be centrally important to the conversion of light energy into chemical energy.[1-5] As a consequence, there has been substantial work on both homogeneous[6-17] and heterogeneous[18-29] WOCs. Insightful recent studies of Ru-[28] and Co-based[29] WOCs with organic ligands show very high base-dependent catalytic water oxidation rates (~10^3). In recent years, many carbon-free, robust, molecular WOCs comprising polydentate polyoxometalate (POM) ligands stabilizing a mononuclear or polynuclear transition metal cores have been reported.[7,30-47] This family of catalysts eliminates the problem of ligand oxidative instability, while being very stable thermally and readily immobilized on a variety of electroactive surfaces;[33,48,49] however, they are still slow for use in efficient artificial photosynthetic systems. Here, we report the synthesis, characterization and water oxidation activity of the carbon-free homogenous WOC, $[Co_4(H_2O)_2(VW_9O_{34})_2]^{10-}$ (**1-V2**).

3.2 Experimental

3.2.1. Synthesis

$Na_{10}[Co_4(H_2O)_2(VW_9O_{34})_2]\cdot 35H_2O$ (Na_{10}**1-V2)** was synthesized according to modified literature method[50] as follows: $Co(NO_3)_2\cdot 6H_2O$ (1.2 g) and $Na_2WO_4\cdot 2H_2O$ (6.0 g) were dissolved in 0.5 M sodium acetate buffer (120 mL, pH 4.8) and vigorously stirred for about 5 minutes before $NaVO_3$ (0.27 g) was added. The resulting turbid mixture was then heated to 80 °C for 2 hours. The hot brown mixture was filtered to remove any precipitate and left to crystallize for about one week to give dark block crystals of **1-V2**, a single crystal of which was submitted to structural analysis by X-ray crystallography (**Figure 3-**

1 and **Table 3-1**) and the bulk sample analyzed by elemental analysis (yield 0.72 g; ca. 12.5 %, first batch only, based on tungstate). Elemental analysis for Na_{10}**1-V2**: calcd. for Co, 4.21; V, 1.82; W, 59.14%; found for Co, 4.09; V, 1.80; W, 60.7%. FT-IR (cm^{-1}, **Figure 3-2**): V-O stretching: 960(m), terminal W=O stretching: 882(s), corner-/edge-sharing W-O-W bending: 818(s), 760(sh), 694(s), 513(sh), and 485(m). UV-Vis (M^{-1} cm^{-1} in water, **Figure 3-3**): $\varepsilon_{400} = 1320$; $\varepsilon_{580} = 158$. ^{51}V NMR (**Figure 3-4**): –506.8 ppm, $\Delta\nu_{1/2} = 30.5$ Hz.

$K_{10}[Co_4(H_2O)_2(VW_9O_{34})_2]\cdot 24H_2O$ (K_{10}**1-V2)** was obtained by using all potassium-containing precursors and following the same procedure as above. The data on single crystal X-ray structure are summarized in **Table 3-1**.

$TBA_{10}[Co_4(H_2O)_2(VW_9O_{34})_2]$ (TBA-**1-V2),** tetrabutylammonium salt of **1-V2**, was prepared according to general literature procedure of Katsoulis and Pope with some modifications.[51] The product was then dried *in vacuo*. The purity was confirmed by FT-IR and ^{51}V NMR (**Figure 3-4**).

$Na_{10}[Co_4(OH)_2(PW_9O_{34})_2]\cdot 27H_2O$ (Na_{10}**1-P2)** was prepared as described in the literature.[6] The purity was confirmed by FT-IR (**Figure 3-2**) and UV-vis spectroscopies (**Figure 3-3**).

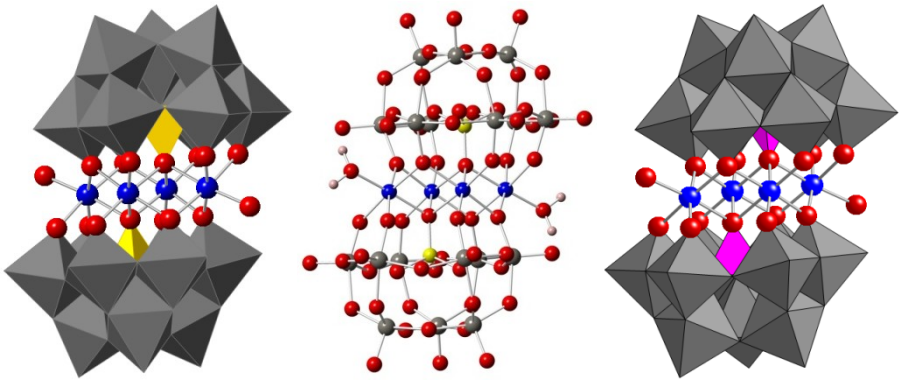

Figure 3-1 Polyhedral and ball-and-stick representation of the cobalt-containing polytungstate complexes, 1-V2 (left and middle) and 1-P2 (right). Blue: Co; Red: Oxygen; Grey: WO_6 or W; Yellow: VO_4 or V; Pink: PO_4.

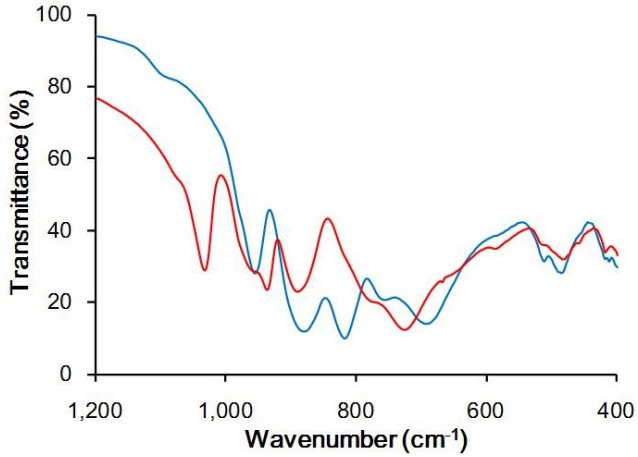

Figure 3-2 FT-IR spectrum of Na_{10}**1-V2** (blue) and Na_{10}**1-P2** (red), 2 wt % in KBr.

$Ru(bpy)_3(ClO_4)_3$ was prepared by literature procedure with minor modifications.[52] To a solution of $[Ru(bpy)_3]Cl_2 \cdot$**$6H_2O$** (300 mg, 0.4 mmol) dissolved in 0.6 M sulfuric acid (10 mL), solid PbO_2 (1.5 g) was added and the resulting orange-red solution was vigorously stirred until it turned green. After removing the solid PbO_2 powder *via* a filter with fine porosity frit, the solution was cooled down in ice-bath and then 2.2 mL of 70% (11.6 M) $HClO_4$ was slowly added. The resulting dark green precipitate was filtered through a medium-sized frit and then dried under water pump vacuum to remove most of

the water. The samples were further dried under high-vacuum for 3-6 hrs and stored in a sealed glass container at 15 °C until use. Yield: ~ 200 mg.

3.2.2. X-ray Crystallography

The complete datasets for Na_{10}**1-V2**, and K_{10}**1-V2** were collected at Emory University. A suitable crystal of each compound was coated with Paratone N oil, suspended in a small fiber loop and placed in a cooled nitrogen gas stream at 173 K on a Bruker D8 APEX II CCD sealed tube diffractometer with graphite monochromated MoKα (0.71073 Å) radiation. Data were collected using a combination of phi and omega scans with 10 s frame exposures and 0.5° frame widths. Data collection, indexing and initial cell refinements were all carried out using APEX II software.[53] Frame integration and final cell refinements were done using SAINT software[54] based on optimal reflections. Scattering factors and anomalous dispersion corrections are taken from the International Tables for X-ray crystallography. Structure solution, refinement, graphics and generation of publication materials were performed by using SHELXTL, V6.12 software.[55,56] The results are summarized in **Table 3-1**.

Table 3-1 Crystallographic data and structure refinement for Na_{10}**1-V2** and K_{10}**1-V2**.

	Na_{10}**1-V2**	K_{10}**1-V2**
empirical formula	$H_{70}Co_4Na_{10}O_{103}V_2W_{18}$	$H_{52}Co_4K_{10}O_{94}V_2W_{18}$
formula weight	5595.36 g mol^{-1}	5594.32 g mol^{-1}
crystal system	Triclinic	Monoclinic
space group	$P\bar{1}$	$P2_1/n$
unit cell	a = 11.5631(19) Å	a = 12.3089(3) Å
	b = 12.879(2) Å	b = 12.8318(14) Å
	c = 17.329(3) Å	c = 17.2679(19) Å
	α = 97.440(2)°	α = 90°

	β = 106.720(2)°	β = 92.3150(10)°
	γ = 112.080(2)°	γ = 90°
volume	2196.6(6) Å^3	4113.46(17) Å^3
Z	1	2
density (calcd.)	4.153 g cm^{-3}	4.517 g cm^{-3}
temperature	173(2) K	110 K
wavelength	0.71073 Å	0.71073 Å
abs. coeff.	24.449 mm^{-1}	26.684 mm^{-1}
Reflections collected	41939	89273
Independent reflections	15186 [R(int) = 0.0384]	9460 [R(int) = 0.0535]
GOF	1.051	1.054
final R_1[a] [$I > 2\sigma(I)$]	0.0399	0.0243
final wR_2[b] [$I > 2\sigma(I)$]	0.1093	0.0590

[a] $R_1 = \Sigma||F_0| - |F_c|| / \Sigma|F_0|$; [b] $wR_2 = \Sigma[w(F_0^2 - F_c^2)^2]/ \Sigma[w(F_0^2)^2]^{1/2}$

3.2.3. UV-Vis spectroscopy

All UV-Vis spectra were acquired using a diode array Agilent 8453 spectrophotometer equipped with an Agilent 89090A cell temperature controller unit. The spectra of Na_{10}**1-V2** and Na_{10}**1-P2** are given in **Figure 3-3**.

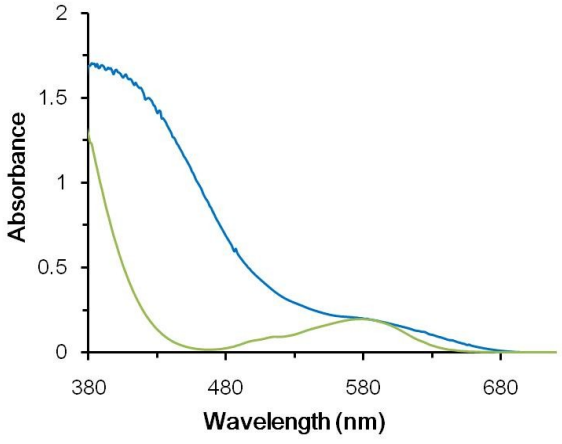

Figure 3-3 UV-vis spectra of 1.28 mM Na_{10}**1-V2** (blue line) and Na_{10}**1-P2** (green line) in H_2O.

3.2.4. ^{51}V NMR spectra and characterization of the post-catalysis solution

^{51}V NMR (151.6 MHz) spectra were obtained at 298 K in 5 mm O.D. NMR tubes on a Unity Plus 600 spectrometer equipped with a Varian 600 SW/PF6 probehead. All the chemical shifts were given relative to neat $VOCl_3$ (reference as 0 ppm at 25 °C). Acquisition parameters were as follows: pulse width 15 μs (~90° flip angle), time domain window 100 kHz (600 ppm), and acquisition time of 0.640 s. The exemplary spectra are given in **Figures 3-4**.

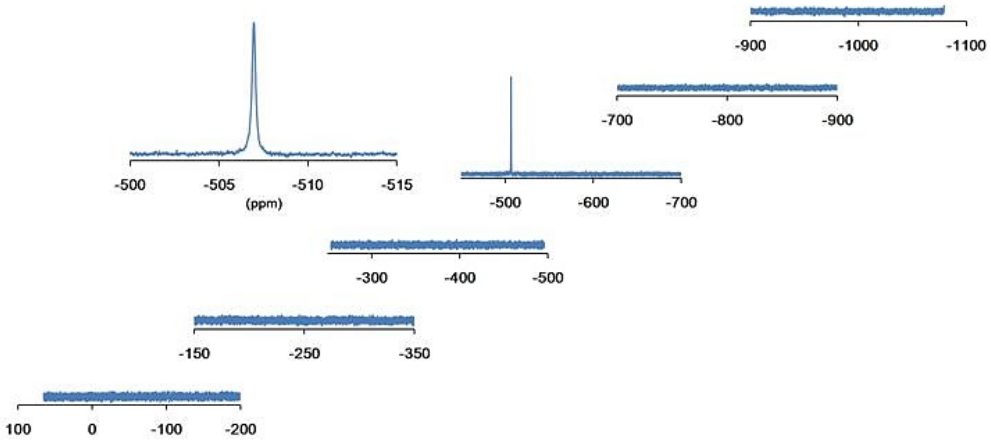

Figure 3-4 ^{51}V NMR spectra of 1-V2 in D_2O and 40 mM sodium borate buffer at pD 9.0 prepared with D_2O. The peak at –506.8 ppm ($\Delta\nu_{1/2}$ = 30.5 Hz) corresponds to the V atoms in the $[VW_9O_{34}]$ units. The solutions were aged for 4 weeks and no change was observed.

Preparation of the solution for ^{51}V NMR. The ^{51}V NMR test solution was prepared by dissolving the **1-V2** in pure D_2O or in 40 mM borate buffer (pD 9.0, in D_2O). The solution for ^{51}V NMR test before and after the light-driven reaction was prepared by the following procedures. A 0.5 mL aliquot of the reaction solution ($Ru(bpy)_3Cl_2 \cdot 6H_2O$ (3.3 mM), $Na_2S_2O_8$ (12.6 mM), **1-V2** (67 μM)) was mixed with 0.2 mL D_2O for ^{51}V NMR test before illumination. The other separate reaction solution were illuminated under 17 mW

LED light for 50 min, the final oxygen yield was checked by GC. A 0.5 mL aliquot of post-reaction solution was then filtered using a Millipore micro-filter (0.2 μm) and mixed with 0.2 mL D_2O for ^{51}V NMR test.

Re-isolation of catalyst from the reaction solution. A 20 mL reaction solution was prepared with the concentrations of $Ru(bpy)_3Cl_2 \cdot 6H_2O$ (1 mM), $Na_2S_2O_8$ (10 mM), **1-V2** (0.16 mM) in 80 mM sodium borate buffer (pH 9.0). After thorough deaeration by purging with Ar, the reaction solution was exposed to 17 mW LED light for 1 hour. The (**1-V2**$\cdots[Ru(bpy)_3]^{2+}$) complex was precipitated from the post-reaction solution by adding 5 mL of concentrated $[Ru(bpy)_3]^{2+}$ solution. The same procedure was used with solution before the reaction. The FT-IR spectra of precipitates were recorded as 2.0 wt % samples in KBr.

3.2.5. ESI Mass Spectrometry and Peak Assignments

Mass spectrometry determinations were carried out on a Thermo Finnigan LTQ-FTMS spectrometer with electrospray (ESI) ionization. For ESI-MS experiments, the solution of TBA-**1-V2** in acetonitrile has been used because TBA^+ cations have a higher mass than Na^+ or K^+ and thus give a large separation between signals with different charges or protonated states. The spectra are given in **Figure 3-5**. **Table 3-2** listed the main peak assignments of the ESI-MS spectra of TBA-**1-V2**, which proves the integrity of **1-V2** polyanions in solution.

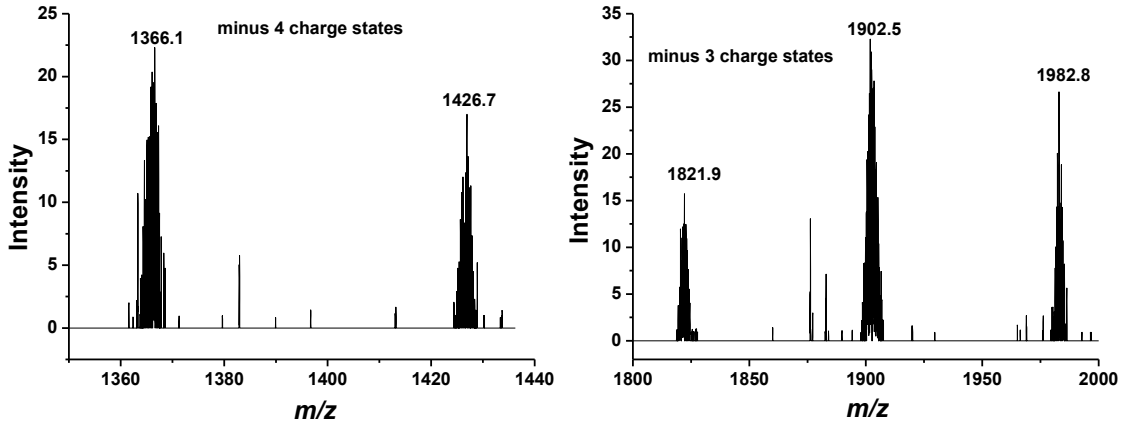

Figure 3-5 ESI-MS spectra obtained for TBA-**1-V2** in acetonitrile, the main peak envelopes with –4 and –3 charges are marked with numbers.

Table 3-2 List of *m/z* peak assignments in the ESI-MS spectra of the TBA salt of **1-V2**.

Peak assignments	Observed m/z	Calculated m/z
$(C_{16}H_{36}N)_2(CH_3CN)_5H_4[Co_4(H_2O)_2(VW_9O_{34})_2]^{4-}$	1366.1	1366.2
$(C_{16}H_{36}N)_3(CH_3CN)_5H_3[Co_4(H_2O)_2(VW_9O_{34})_2]^{4-}$	1426.7	1426.6
$(C_{16}H_{36}N)_2(CH_3CN)_5H_5[Co_4(H_2O)_2(VW_9O_{34})_2]^{3-}$	1821.9	1821.9
$(C_{16}H_{36}N)_3(CH_3CN)_5H_4[Co_4(H_2O)_2(VW_9O_{34})_2]^{3-}$	1902.5	1902.4
$(C_{16}H_{36}N)_4(CH_3CN)_5H_3[Co_4(H_2O)_2(VW_9O_{34})_2]^{3-}$	1982.8	1982.9

3.2.6. Computational Procedures

All calculations were performed using the Gaussian 09 program.[57] The geometries of all species were optimized without any symmetry constraint at the B3LYP[58-60] level of theory by including solvent effects at the self-consistent reaction field IEF-PCM level[61] with water as a solvent (dielectric constant ε = 78.39). In these calculations we used Hay-Wadt effective core potentials (ECPs) with the associated Lanl2dz basis set for transition metals[62-64] and the standard 6-31G* split-valence-polarization basis set for all other atoms.

3.2.7. Magnetochemical Characterization

Magnetic susceptibility data of Na_{10}**1-V2** and Na_{10}**1-P2** were recorded between 2.0 and 290 K at 0.1 Tesla using a Quantum Design MPMS-5XL SQUID magnetometer, with the polycrystalline samples compacted and immobilized in a cylindrical PTFE sample holder. Data were corrected for the contribution of the sample holder and the diamagnetic and temperature-independent paramagnetic contribution of **1-V2** and **1-P2**. The latter was established using increments determined from diamagnetic derivatives of these species.

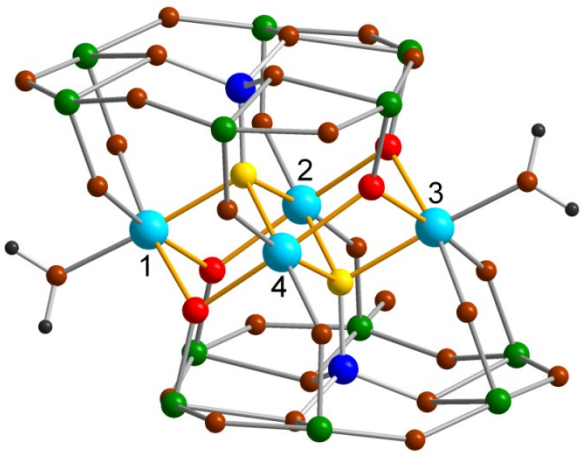

Figure 3-6 Core segment of **1-P2** and **1-V2** emphasizing the μ-O-mediated exchange pathways between the Co^{2+} centers (large light blue spheres), highlighted by orange bonds. Color code: O sites involved in exchange pathways: μ_3-O, red, μ_4-O, yellow; V/P, dark blue; Mo, dark green; O, brown; H, black.

The susceptibility characteristics of both compounds are primarily determined by the single-ion effects of the four octahedrally coordinated, thus orbitally degenerate, Co(II) sites ($^4T_1$, S = 3/2) as well as weak exchange interactions between these four centers, mediated by two μ-O bridges per Co···Co contact (**Figure 3-6**). Using the computational framework CONDON 2.0,[65] modeling of the susceptibility data employed a complete Hamiltonian taking into account all relevant single-ion effects, i.e. interelectronic repulsion (quantified by fixed Racah parameters B = 1115 cm^{-1} and C = 4366 cm^{-1}),

spin-orbit coupling (using spin-orbit coupling constant ζ = 533 cm^{-1}), the ligand-field effect (parameterized using ligand field parameters in Wyborne notation, B^k_q), and the Zeeman effect of an applied field, see reference for the full definition of these terms.[65]

The ligand field operator with reference to the C_4 axis for the angular part of the wave function then reads

$$\hat{H}_{\text{ligand field}} = B^2_0 \sum_{i=1}^{N} C^2_0(i) + B^4_0 \sum_{i=1}^{N} C^4_0(i) + B^4_4 \sum_{i=1}^{N} \left(C^4_{-4}(i) + C^4_{4}(i) \right)$$

Note that this Hamiltonian is applied to the total of 120 microstates of the 3d^7 ions. The total Hamiltonian is then augmented by a Heisenberg-Direck-van Vleck-type exchange coupling term (H_{ex}):

$$\hat{H}_{\text{ex}} = -2\left[J_1(\hat{\boldsymbol{S}}_1 \cdot \hat{\boldsymbol{S}}_2 + \hat{\boldsymbol{S}}_3 \cdot \hat{\boldsymbol{S}}_4 + \hat{\boldsymbol{S}}_2 \cdot \hat{\boldsymbol{S}}_3 + \hat{\boldsymbol{S}}_1 \cdot \hat{\boldsymbol{S}}_4) + J_2(\hat{\boldsymbol{S}}_2 \cdot \hat{\boldsymbol{S}}_4) \right]$$

Here, the nearest-neighbor couplings are grouped into two types of contacts for both **1-V2** and **1-P2** (**Figure 3-6**):

J_1: the four virtually identical pairs (1-2, 2-3, 3-4, and 1-4), characterized by Co···Co distances of 3.210 Å (1-2, 3-4) and 3.204Å (2-3, 1-4), as well as Co-O-Co angles comparably close to 90° (Co–(μ_3-O)–Co: 98.25°/98.69°; Co–(μ_4-O)–Co: 96.16°/96.37°) for **1-V2**; for **1-P2** these values are 3.212 Å (1-2, 3-4) and 3.209 Å (2-3, 1-4); Co–(μ_3-O)–Co: 99.42°/100.70°; Co–(μ_4-O)–Co: 92.19°/93.29°.

J_2: the diagonal pair (2-4), characterized by a slightly higher Co···Co separation of 3.365 Å, where both oxo bridges belong to the vanadate templates, resulting in a larger Co–(μ_4-O)–Co angle of 101.28° for **1-V2**; for **1-P2**: 3.293Å, Co–(μ_4-O)–Co: 94.84°. The

four CoO_6 environments in both **1-V2** and **1-P2** slightly deviate from an regular O_h-symmetric octahedron and are approximated as tetragonally distorted, which in the fitting procedure translates to a set of three independent ligand field parameters (Wyborne pseudotensors B^2_0, B^4_0, and B^4_4) that are treated as uniform for all four Co centers. Least-squares fitting to the model Hamiltonian for **1-V2** yields the ligand field parameters B^2_0 = –2170 cm^{-1}, B^4_0 = +17300 cm^{-1} and B^4_4 = +13700 cm^{-1}, as well as the (all-ferromagnetic exchange energies) J_1 = +2.10 cm^{-1} and J_2 = +0.71 cm^{-1} (SQ = 0.8%). For **1-P2**, B^2_0 = +4032 cm^{-1}, B^4_0 = +18020 cm^{-1}, B^4_4 = +8460 cm^{-1}, J_1 = –0.04 cm^{-1}, and J_2 = +2.41 cm^{-1} (SQ = 0.8%).

Note that J_1 and J_2 are fully in line with the geometry differences of the relevant exchange pathways: For **1-V2**, the Co–O–Co angles for the shorter contacts (J_1) of ca. 96–98° are closer to 90°, for which a maximum in ferromagnetic exchange energy is expected, while the Co–O–Co angle of ca. 101° for the longer, diagonal Co···Co contact is significantly higher. For **1-P2** on the other hand, the wider Co–(μ_3-O)–O angles of ca. 100° and smaller Co–(μ_4-O)–O angles of 92–93° result in a crossover into a negative (antiferromagnetic) coupling constant J_1 (as also postulated in an early magnetochemical study of **1-P2**), whereas a much larger diagonal Co–O–Co angle (ca. 95°) significantly increases the ferromagnetic coupling constant J_2 vs. **1-V2**.

The electronic effects of the substitution of P^V centers in **1-P2** with V^V centers in **1-V2** are evident from magnetic susceptibility comparisons, as these centers directly coordinate to the two μ_4-O bridges that are part of all exchange coupling pathways between the Co(II) spin sites. The temperature-dependent susceptibility of both compounds is primarily determined by the single-ion effects of the octahedrally coordinated, thus

orbitally degenerate, Co(II) sites ($^4T_1$, S = 3/2) as well as weak ferromagnetic exchange interactions between these four centers, mediated by two μ-O bridges per Co···Co contact.

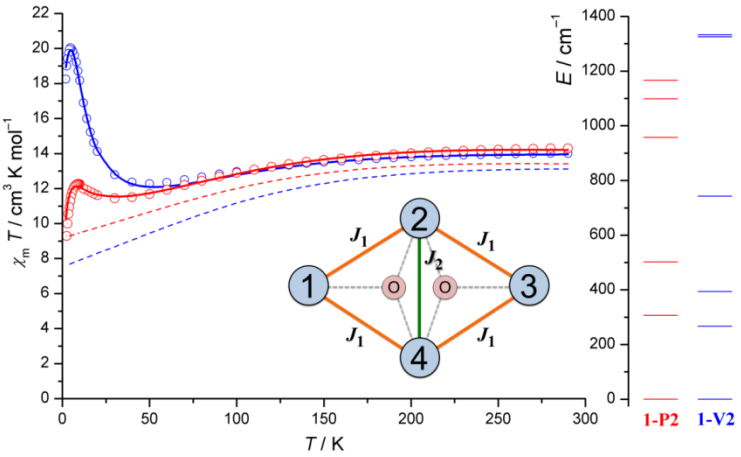

Figure 3-7 Left: Temperature dependence of $\chi_m T$ for **1-V2** (blue) and **1-P2** (red) at 0.1 Tesla. Open circles: experimental data, solid graphs: least-squares fit to complete model, dashed graphs: single-ion contribution of the four (uncoupled) Co(II) sites. Inset: Exchange coupling scheme defining the exchange constants J_1 and J_2 for the planar Co_4 spin cluster in both **1-V2** and **1-P2**. The two oxygen sites symbolize the positions of the μ_4-O sites (one above, one below the Co_4 plane) belonging to phosphate (**1-P2**) or vanadate (**1-V2**) groups. Right: Ligand field splitting of the $^4T_1$ ground state into the $(2S + 1)(2L + 1) = 12$ microstates for each Co^{2+}.

The susceptibility for **1-V2** and **1-P2** (**Figure 3-7**) are accurately reproduced by modeling both the single-ion effects and the exchange coupling between two types of $Co(\mu_{3/4}\text{-}O)_2Co$ (i.e. J_1) and $Co(\mu_{4/4}\text{-}O)_2Co$ (J_2) pairs.[65] The pronounced maxima in $\chi_m T$ at 4.8 K (**1-V2**) and 8.0 K (**1-P2**) reflect minor differences in the superexchange pathways, specifically the frontier orbitals of the μ-O bridges, which translate into different exchange coupling energies. Whereas all nearest-neighbor interactions in **1-V2** are ferromagnetic (J_1 = +2.10 cm^{-1}; J_2 = +0.71 cm^{-1}; cf. inset in **Figure 3-7**), both ferromagnetic (J_2 = +2.41 cm^{-1}) and weak antiferromagnetic (J_1 = –0.04 cm^{-1}) coupling is found for **1-P2**. This is in line with the geometrical differences of the $\mu_{3/4}$-O bridges

centers also involving the phosphate or vanadate templates, respectively. The different ligand fields of the CoO_6 environments in **1-V2** and **1-P2**, which in particular determine the higher temperature regime, account for differences in the single-ion contributions of 5.15 μ_B vs. 5.19 μ_B (per Co^{2+}) at room temperature (i.e. the temperature of our catalysis experiments), with an ligand field overall splitting (LFOS) of the $^4T_1$ ground state of 1332 cm^{-1} (**1-V2**) vs. 1166 cm^{-1} (**1-P2**).

3.2.8. Kinetics of Water Oxidation by $[Ru(bpy)_3]^{3+}$, O_2 Yield Measurements and Turnover Frequency

The rapid kinetics of catalytic $[Ru(bpy)_3]^{3+}$ decay was monitored using a Hi-Tech Stopped Flow SF-61SX2 instrument equipped with a diode array spectrophotometer (400-700 nm). One of the feeding syringes was filled with a solution of $[Ru(bpy)_3](ClO_4)_3$ and the second with a freshly prepared buffered solution of the catalyst. The consumption of $[Ru(bpy)_3]^{3+}$ was followed by a decrease in absorbance at 670 nm (ε_{670} = 4.2 × 10^2 M^{-1} cm^{-1}) with optical path length l = 10 mm. The data were acquired and treated using KinetAsyst™ 3.0 software. The exemplary data are shown on **Figures 3-8**.

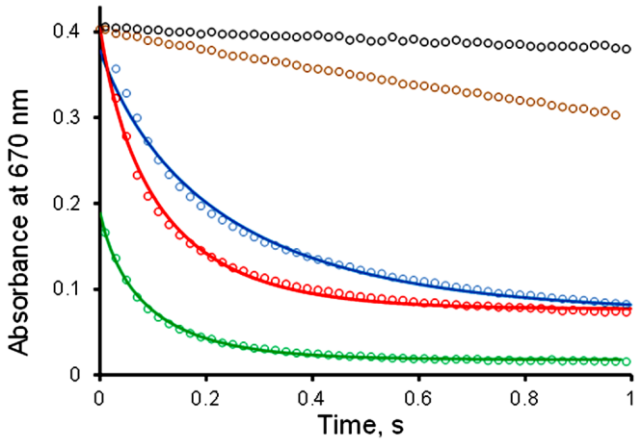

Figure 3-8 Kinetics of $[Ru(bpy)_3]^{3+}$ catalytic reduction measured at 670 nm: no catalyst (black circles); 1 μM **1-P2** with 1 mM $[Ru(bpy)_3]^{3+}$ (brown circles); 0.5 μM **1-V2** with 1 mM $[Ru(bpy)_3]^{3+}$ (blue circles); 1 μM **1-V2** with 1 mM $[Ru(bpy)_3]^{3+}$ (red circles); 1 μM **1-V2** with 0.5 mM $[Ru(bpy)_3]^{3+}$ (green circles). Conditions: 80 mM sodium borate buffer at pH 9.0, 298 K. Solid lines are fittings to eqs **3-2** to **3-7**.

The catalytic water oxidation by $[Ru(bpy)_3]^{3+}$ proceeds very quickly with reaction time shorter than 0.1 s (**Figure 3-8**). The manual mixing time of two solutions is significantly slower. Therefore, a Hi-Tech Scientific SF-61SX2 mixing apparatus was utilized for consistent fast-mixing of two deaerated reaction solutions. After mixing, the solution was delivered via short PEEK tubing to a PEEK T-joint custom drilled to accommodate the oxygen probe. All joints were sealed with Teflon tape and DAP Blue Stik adhesive putty. The oxygen concentration was measured by an Ocean Optics Neofox Phase Measurement System with a calibrated FOXY-R probe and FOXY-AF-MG coating. Repeated shots were performed until the oxygen reading was constant for three consecutive experiments. The oxygen yield under different catalyst concentration was shown in **Figure 3-9**. The O_2 yield per initial $[Ru(bpy)_3^{3+}]_o$, $Y = 4[O_2]/[Ru(bpy)_3^{3+}]_o$, is lower than 100%, indicating that the $[Ru(bpy)_3]^{3+}$ is consumed in two processes, eqs **3-1a** and **3-1b**:

$$4\,[Ru(bpy)_3]^{3+} + 2\,H_2O \rightarrow 4\,[Ru(bpy)_3]^{2+} + O_2 + 4\,H^+ \qquad (\mathbf{3\text{-}1a})$$

$$[Ru(bpy)_3]^{3+} \rightarrow [RuL(bpy)_2], \qquad (\mathbf{3\text{-}1b})$$

where L is the product of bpy ligand oxidation.

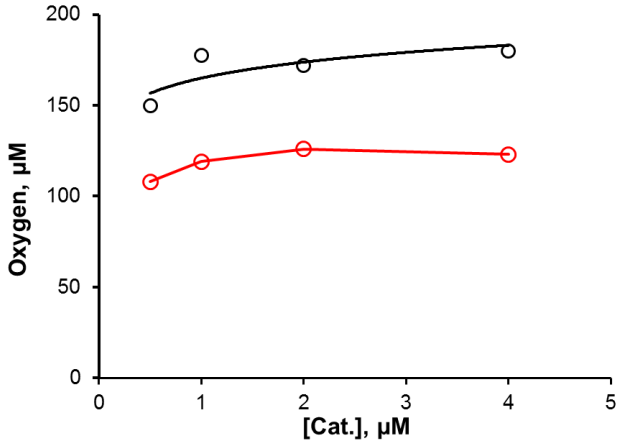

Figure 3-9 Oxygen yield in the reaction given in eq 1a catalyzed by different concentrations of **1-V2** (black circles) and **1-P2** (red circles). Conditions: 1.0 mM $[Ru(bpy)_3]^{3+}$, 80 mM sodium borate buffer at pH 9.0, 298 K.

The proposed reaction mechanism for this water oxidation process is eqs **3-2** to **3-6**.

$$[Ru(bpy)_3]^{3+} + Cat0 \rightarrow [Ru(bpy)_3]^{2+} + Cat1 \quad (\mathbf{3\text{-}2})$$

$$[Ru(bpy)_3]^{3+} + Cat1 \rightarrow [Ru(bpy)_3]^{2+} + Cat2 \quad (\mathbf{3\text{-}3})$$

$$[Ru(bpy)_3]^{3+} + Cat2 \rightarrow [Ru(bpy)_3]^{2+} + Cat3 \quad (\mathbf{3\text{-}4})$$

$$[Ru(bpy)_3]^{3+} + Cat3 = [Ru(bpy)_3]^{2+} + Cat4 \quad (\mathbf{3\text{-}5})$$

$$Cat4 + 2\,H_2O \rightarrow Cat0 + 4\,H^+ + O_2 \quad (\mathbf{3\text{-}6})$$

The reactions in eqs **3-2** to **3-4** are fast, and in eqs 5-6 control the reaction rate:

$$d[[Ru(bpy)_3]^{3+}]/dt = -4k_6k_5[[Ru(bpy)_3]^{3+}][Cat3]/\{[Cat4](k_{-5}[[Ru(bpy)_3]^{2+}] + k_6)\} \quad (\mathbf{3\text{-}7})$$

We plotted initial rates as functions of $[Cat]_o$ and $[Ru(bpy)_3]^{3+}$concentrations, **Figure 3-10**. The reaction rate is close to the first order with respect to $[Cat]_o$ and approaching to

zero order with respect to $[[Ru(bpy)_3]^{3+}]_o$ (at > 1.0 mM). Under these conditions the eq 7 simplifies to eq 8:

$$(d[[Ru(bpy)_3]^{3+}]/dt)_o = -4k_6[Cat]_o \quad \textbf{(3-8)}$$

The data on **Figure 3-10** gives the slope ~ $9x10^3$ s^{-1} or k_6 value ~ 2.3×10^3 s^{-1}. This gives $TOF_{app} = 4Y(d[[Ru(bpy)_3]^{3+}]/dt)_o/[Cat]_o = Yk_6$. Since Y ~ 0.7, then $TOF_{app} = 0.7\times k_6 \sim 1.6\times10^3$ s^{-1}, which is consistent with TOF_{app} value reported above. The fitting of kinetic curves in **Figure 3-8** to eqs **3-2** to **3-6** gives $k_6 \sim (2.4\pm0.1)\times10^3$ s^{-1} and $K_5 = 0.5$. The latter number indicates that the reaction in eq **3-5** is almost thermoneutral.

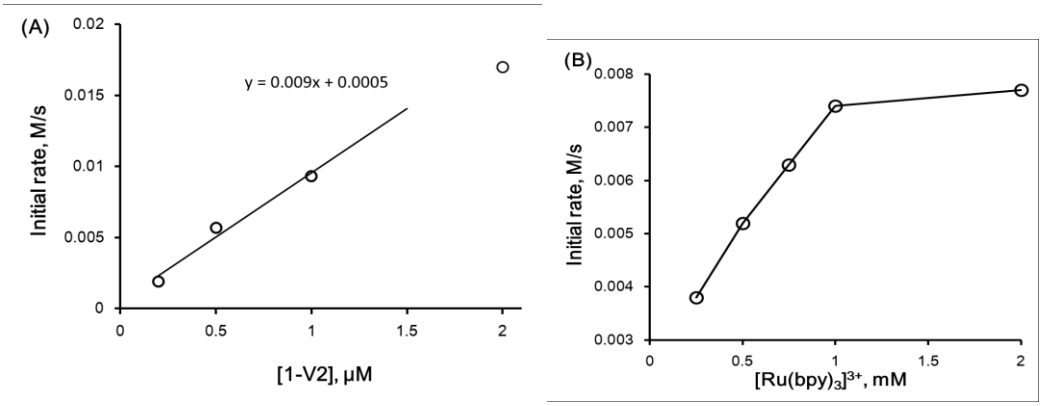

Figure 3-10 Dependence of initial rate of $[Ru(bpy)_3]^{3+}$ reduction on **1-V2** concentration at 1 mM $[Ru(bpy)_3]^{3+}$ (A) and on $[Ru(bpy)_3]^{3+}$ concentration at 1 μM **1-V2** (B). Conditions: 80 mM sodium borate buffer at pH 9.0, 298 K.

3.2.9. Light-Driven Catalytic Water Oxidation

The overall reaction of light-driven catalytic water oxidation is given in following equation:

$$2\ S_2O_8^{2-} + 2\ H_2O \rightarrow 4\ SO_4^{2-} + O_2 + 4\ H^+$$

The experiment was performed in a cylindrical cuvette (NSG, 32UV10) with a total volume of ~2.5 mL. The cell was filled with 2.0 mL of reaction solution with 1.0 mM $Ru(bpy)_3Cl_2 \cdot 6H_2O$, 5.0 mM $Na_2S_2O_8$, 0.2–6.0 μM catalysts in 80 mM sodium borate buffer and pH 9.0. The reaction cell was sealed with a rubber septum, carefully deaerated and filled with Ar. All procedures were performed with a minimum exposure to ambient light. The reaction was initiated by turning on the LED-light source (λ = 455 nm; light intensity 17 mW, beam diameter ~0.4 cm). A magnetically-coupled stirring system (SYS 114, SPECTROCELL) was used to mix reaction solutions (4×10^3 RPM). The O_2 concentration in the headspace was quantified by GC. The solution pH was measured after the reaction.

Analysis of dioxygen in the reaction headspace was performed using a computer controlled Agilent 6850 model gas chromatograph equipped with a thermal conductivity detector and a HP-MOLESIEVE capillary GC column (30m × 0.535 mm × 25.00 μm) Argon was used as a carrier gas. Typically, the O_2 yield was quantified by withdrawing a gas sample from the headspace without stopping the reaction. Contamination of the head-space with air was corrected by quantification of N_2 present in the head-space (from the N_2 peak in the GC traces).

3.2.10. Quantum Efficiency Measurements

The quantum efficiency of O_2 formation was defined as the number of O_2 molecules formed per two absorbed photons,>Huang, 2011 #4027;Huang, 2011 #4027< $\Phi = 2N(O_2)/[N(h\nu)]$, where $N(O_2)$ is the moles of O_2 formed, and $N(h\nu)$ is the moles of photons absorbed by the reaction solution. The quantum yield is defined for per two absorbed photons because the formation of one molecule of O_2 requires four oxidative

equivalents supplied by two molecules of persulfate after absorption of two photons. The total amount of photons absorbed for a given reaction time *t* was calculated from the irradiation power and the absorbance of the reaction solution. The irradiation power, 17 mW, was measured at the point right in front of the reaction cell using a laser power meter (Molectron, model Max 500A). Since the optical density of the reaction solution was high (A ≈ 14 at 455 nm in 1 cm long reaction cell), all light entering the reaction solution was considered to be fully absorbed. The amount of absorbed photons was corrected for the absorption loss (18%) by the optical glass (NSG cuvette manual, and by UV/Vis spectrometer) and reflection loss (4%) at the glass/air interface. All scattered photons due to the solvent (H_2O) are absorbed by the solution. **Table 3-3** summarizes the TONs, O_2 chemical yields, and quantum yields for homogeneous visible-light-driven water oxidation in the presence of **1-V2**.

Table 3-3 TONs, O_2 chemical yields, and quantum yields for homogeneous visible-light-driven water oxidation in the presence of **1-V2** [a].

[**1-V2**] *(μM)*	*TON* [b]	*Chemical Yield* [c]	*Quantum Yield* [d]
0.2	4210	0.337	0.477-
0.5	1840	0.368	0.484
1.0	1230	0.494	0.548
2.0	742	0.594	0.614
4.0	390	0.638	0.661
6.0	290	0.711	0.681

[a] Conditions: LED light (17 mW, 455 nm, beam diameter ~0.4 cm), $[Ru(bpy)_3]Cl_2$ (1.0 mM), $Na_2S_2O_8$ (5.0 mM), catalyst (0.2 - 6 μM), borate buffer (80 mM, initial pH 9.0). TON and chemical yields were evaluated at 11 minutes. The O_2 from the background (catalyst-free) reaction was subtracted. [b] (O_2 yield at 11 minutes) / (catalyst concentration) = $[O_2]_f/[catalyst]$; [c] $\Phi_{CY} = 2[O_2]_f/[Na_2S_2O_8]_0$ (per initial concentration of persulfate); [d] $\Phi_{QY}(0) = N(O_2)/[N(h\nu)/2] = 2(\Delta[O_2]/\Delta(h\nu))_0$, (initial O_2 formation rate) / (photon flux).

3.2.11. Dynamic Light Scattering Measurements

Dynamic light scattering (DLS) measurements were performed on a Brookhaven Instruments 90Plus particle size analyzer. Each sample was measured three times consecutively. The post-reaction solutions from both stoichiometric water oxidation and light-driven catalytic oxidation were evaluated by DLS. None of these post-reaction solutions showed the presence of any nanoparticles. For comparison, cobalt nitrate used as the catalyst, and in this case, CoO_x particles unequivocally formed during the reaction; they exhibited a maximum hydrodynamic radius centered at around 220 nm.

3.3 Results and Discussion

3.3.1. Synthesis, Crystal Structures and Characterization

The complex **1-V2** is prepared from a mixture of earth-abundant materials: cobalt ions, vanadate ($NaVO_3$), and tungstate (Na_2WO_4) in aqueous solution. Following an early report,[50] we have critically revisited and significantly improved the X-ray crystallographic and magnetic characterization of **1-V2** and confirmed that it is isostructural to the previously reported, $[Co_4(H_2O)_2(PW_9O_{34})_2]^{10-}$ (**1-P2**; **Figure 3-1**).[6,7] In both complexes, **1-V2** and **1-P2**, two tri-lacunary B-type $[XW_9O_{34}]^{9-}$ (X = V or P) ligands sandwich a tetra-cobalt cluster $[Co_4O_{14}]$. Two of the Co(II) centers on the outside positions in this central unit are solvent accessible and consequently bear one terminal aqua (water) ligand each. To our knowledge, the *R* value of 2.43% of our X-ray structure of K_{10}**1-V2** is one of the the lowest ever reported for a polyoxometalate so that the hydrogens on the cobalt terminal aqua ligands have been located (**Figure 3-1**, **Table 3-1**). The VO_4 unit in each $[VW_9O_{34}]^{9-}$ ligand has an approximately tetrahedral structure. Bond valence sum (BVS) calculations show that all the cobalt and the vanadium centers are in

the 2+ and 5+ oxidation states, respectively (**Table 3-4**). Extensive spectroscopic data on **1-V2** confirms the structure from the X-ray diffraction study. The ^{51}V NMR spectrum of **1-V2** shows only one peak at -506.8 ppm ($\Delta\nu_{1/2}$ = 30.5 Hz) for the central pseudo-tetrahedral V in the two symmetry-equivalent $[VW_9O_{34}]^{9-}$ ligands (**Figure 3-4**). The ESI-MS spectra for the TBA salt of **1-V2**, also confirm this structure: the assignments of the main peak envelopes indicate the presence of the **1-V2** polyanions in solution (**Figure 3-5** and **Table 3-2**).

Table 3-4 Bond Valence Sum (BVS) of the cobalt atoms and central vanadium atom.

Compound	Atom	BVS value
Na_{10}**1-V2**	Co1	1.99
	Co2	1.92
	V	5.17
K_{10}**1-V2**	Co1	2.06
	Co2	2.05
	V	5.23

Although both **1-V2** and **1-P2** have the same charge (10-) and very similar geometrical structures (metal-oxygen connectivity), they exhibit different electronic structures. First, the UV-Vis spectrum of **1-V2** reveals transitions involving orbitals with both cobalt and heteroatom (vanadium) character in aqueous solution or in 80 mM borate buffer, whereas, the spectrum of **1-P2** does not. The ligand-to-metal charge transfer (LMCT) and d-d transitions for **1-V2** are at 400 nm (ε_{400} = 1323 M^{-1} cm^{-1}) and 580 nm (ε_{580} = 158 M^{-1} cm^{-1}) respectively; whereas those for **1-P2** are at 580 nm (ε_{580} = 158 M^{-1} cm^{-1}) (**Figure 3-3**). Second, DFT calculations reveal that (a) the ground electronic state of **1-V2** is ^{13}A with four Co^{2+} centers, (b) its highest single occupied molecular orbitals (**Figure 3-11**) are primarily the d-orbitals of Co centers, with some mixing of oxygen orbitals of the

{VW_9O_{34}} units) followed by doubly occupied oxygen orbitals of {VW_9O_{34}} units and doubly occupied Co atomic orbitals, and (c) the lowest unoccupied orbital of **1-V2** contains mainly the VO_4 orbitals with some mixture from the Co_4O_x belt. This implicates the direct role of the d^0, V(V) centers in any redox chemistry of **1-V2**. No analogous orbital is found in **1-P2**. The calculated important bond distances are in good agreement with their X-ray crystallographic values (**Figure 3-12** and **Table 3-1**).

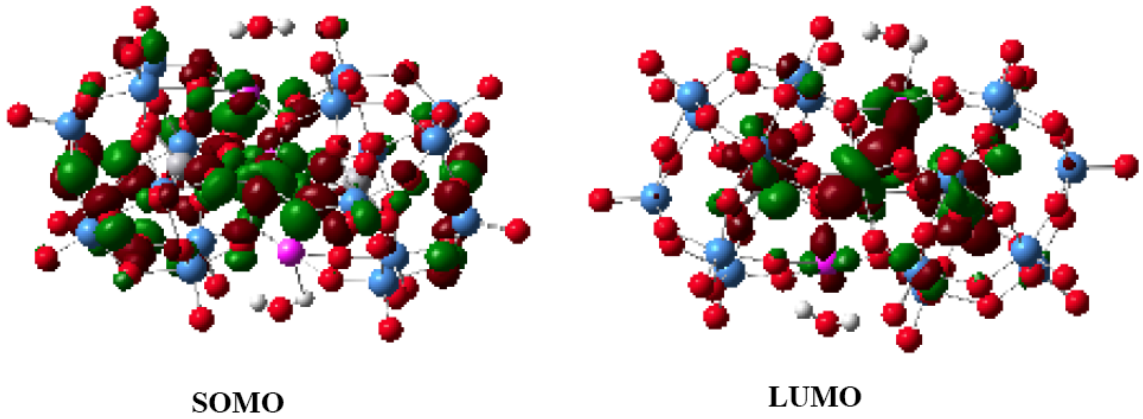

Figure 3-11 Calculated SOMO and LUMO orbitals of $[Co_4(H_2O)_2(VW_9O_{34})_2]^{10-}$, **1-V2**. The calculated (in water solution) SOMO-LUMO energy gap is 4.15 eV.

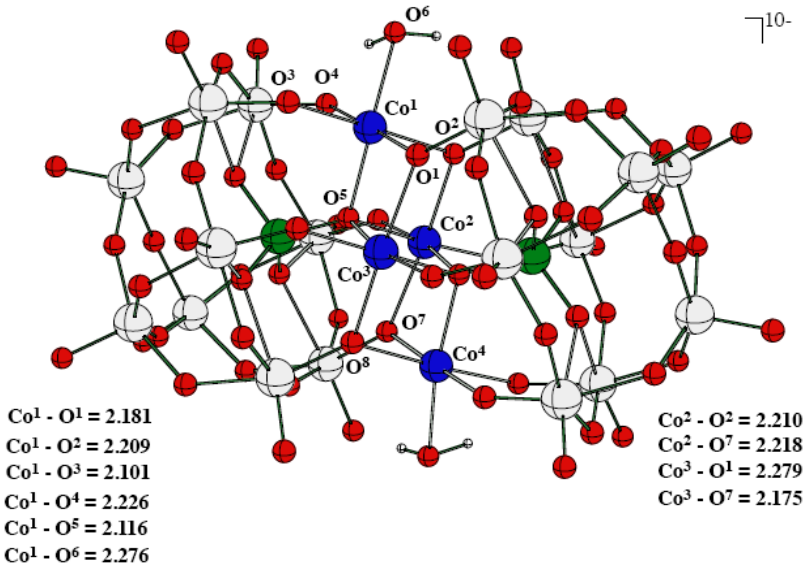

Figure 3-12 Calculated structure and important geometry parameters of $[Co_4(H_2O)_2(VW_9O_{34})_2]^{10-}$, **1-V2**.

Third, a full temperature-dependent magnetism study of **1-V2** and **1-P2** reveals significant differences in the two complexes (**Figure 3-6** and **Figure 3-7**), which reflect differences in the frontier orbitals involving the μ-O bridges linking the Co^{2+} spin centers that in turn translate into different coupling energies: whereas all nearest-neighbor interactions in **1-V2** are ferromagnetic, both ferromagnetic and weak antiferromagnetic coupling is found for **1-P2**. Overall, electronic structure data obtained from the full temperature-dependent magnetism study are consistent with aforementioned computational findings.

3.3.2. Water Oxidation Activity using Chemical Oxidant in Dark

The catalytic efficiency of **1-V2** and **1-P2** for water oxidation has been evaluated using $[Ru(bpy)_3]^{3+}$ as a stoichiometric oxidant in eq **3-1a** by following the kinetics of $[Ru(bpy)_3]^{3+}$ (ε_{670} = 420 M^{-1} cm^{-1})[52] consumption in 80 mM borate buffer at pH 9.0 using the stopped-flow technique (**Figure 3-8** and **Figure 3-13**).

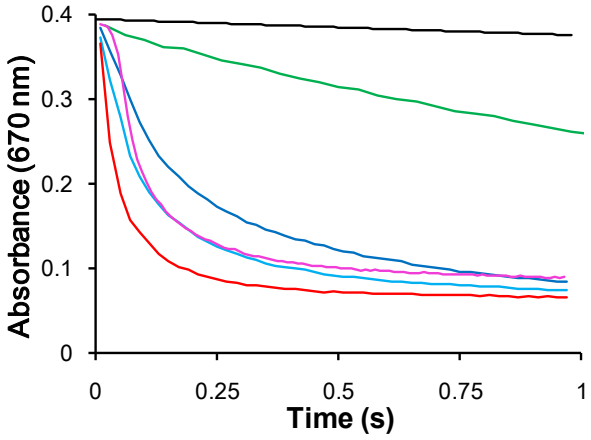

Figure 3-13 Kinetics of $[Ru(bpy)_3]^{3+}$ reduction to $[Ru(bpy)_3]^{2+}$ measured as the decrease in absorbance at 670 nm. No catalyst (black line), 1 μM **1-P2** (green curve), 0.5 μM **1-V2** (blue curve), 1 μM **1-V2** (light-blue curve), 2 μM **1-V2** (red curve) and 5 μM $Co(NO_3)_2$ (pink curve). Conditions: 1 mM $[Ru(bpy)_3]^{3+}$, 80 mM sodium borate buffer at pH 9.0, 298 K.

The kinetic curves for the catalytic process are not exponential; the reaction is inhibited by product $[Ru(bpy)_3]^{2+}$. In 80 mM sodium borate buffer at pH 9.0 the addition of 1 μM **1-V2** results in ~50% conversion of $[Ru(bpy)_3]^{3+}$ in 0.08 s, which is about 20 times faster than with 1 μM **1-P2**, and more than two orders of magnitude faster than the self-decomposition rate of $[Ru(bpy)_3]^{3+}$ (**Figure 3-13**). For comparison, we also obtained the kinetics of $[Ru(bpy)_3]^{3+}$ reduction catalyzed by 5 μM $Co(NO_3)_2$ (1.25 equivalents of cobalt relative to 1 μM **1-V2**), which exhibits a characteristic sigmoidal-shaped curve with an induction period (pink curve, **Figure 3-13**), indicating formation of catalytically active species from the initial $Co(NO_3)_2$.[66] The concentration of O_2 generated using 1 mM $[Ru(bpy)_3]^{3+}$ increases from about 0.15 to 0.18 mM with an increase of [**1-V2**] from 0.5 to 4.0 μM reaching the yield, $Y = 4[O_2]/[[Ru(bpy)_3]^{3+}]_0$ of 70 ± 5% (**Figure 3-9**). Based on the initial rate of $[Ru(bpy)_3]^{3+}$ consumption and the O_2 yields, the initial apparent turnover frequency, $TOF_{app} = \{0.7(d[Ru(bpy)_3^{3+}]/dt)\}/ (4\times[\mathbf{1\text{-}V2}])$, is in the range (1.6-2.2)$\times 10^3$ s^{-1} which is, to our knowledge, by far the fastest ever reported for a synthetic

water oxidation catalyst. This value is considerably higher than that of the Oxygen Evolving Center (OEC) in PSII (as high as 400 s^{-1}),[15] but direct comparison of the water oxidation rates of **1-V2** and the OEC is not highly meaningful because the overpotentials (driving forces) in these two systems are different. The kinetic and mechanistic analyses show that the initial reaction rate is close to first order with respect to $[\mathbf{1\text{-}V2}]_o$ and $[[Ru(bpy)_3]^{3+}]_o$ (at < 1.0 mM), and approaching zero order with respect to $[[Ru(bpy)_3]^{3+}]_o$ (at > 1.0 mM) (**Figure 3-10**).

3.3.3. Visible-Light-Driven Water Oxidation

Given the importance of visible-light-driven catalytic water oxidation, the activity of **1-V2** was also assessed by the standard approach using $[Ru(bpy)_3]^{2+}$ as a photosensitizer and persulfate as a sacrificial electron acceptor (**Figure 3-14**).>White, 1984 #4093;Geletii, 2009 #8526< The O_2 yield in the presence of **1-V2** is twice as high as that in the presence of **1-P2**[6,30] (**Figure 3-14**), indicating the higher selectivity for water oxidation versus *bpy* ligand oxidation for **1-V2**. The quantum efficiency of O_2 formation at 6.0 μM **1-V2** reaches the very high value of *ca*. 68% (**Table 3-3**).

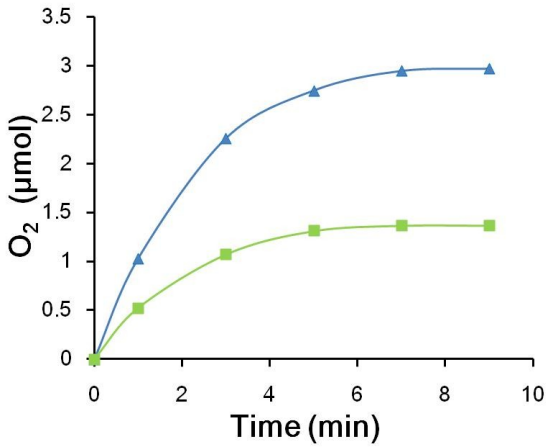

Figure 3-14 The time profile of light-driven O_2 evolution catalyzed by 2.0 μM **1-V2** (blue triangles) or 2.0 μM **1-P2** (green squares) with 1.0 mM $[Ru(bpy)_3]Cl_2$ and 5.0 mM $Na_2S_2O_8$.

Conditions: 455 nm LED light (17 mW, beam diameter ~0.4 cm), 80 mM sodium borate buffer initial pH 9.0, total solution volume 2.0 mL.

Note that the initial slopes (O_2 versus time) in the light-driven reactions are directly related to the quantum yield of these reactions; they are *not* the intrinsic catalytic turnover rates or TOF. Critically in light-driven reactions, the rate-limiting step in the great majority of cases (e.g. using the very popular $[Ru(bpy)_3]^{2+}$/light/persulfate system) is not the rate (TOF) of the catalyst. In contrast, the rate of oxidant, e.g. $[Ru(bpy)_3]^{3+}$, generation is rate-limiting. As a consequence, catalyst efficiencies (TOF, etc.) usually cannot be assessed in light-driven reactions, and in particular in light-driven multi-electron processes. The one rare exception for light-driven reactions in which the catalyst efficiency can be rate limiting or co-rate-limiting is where a very intense light source (not terrestrial sunlight) is used. To provide direct evidence for our case (**1-V2**/$[Ru(bpy)_3]^{2+}$/light/persulfate) that photogeneration of oxidant is rate limiting and catalyst turnover is not, we compare the accumulation of $[Ru(bpy)_3]^{3+}$ oxidant in both the presence and absence of **1-V2** by UV-Vis spectroscopy. **Figure 3-15** shows that the photogeneration of the $[Ru(bpy)_3]^{3+}$ oxidant in the absence of **1-V2** by UV-Vis spectra after 30 s of irradiation. Importantly, in the presence of **1-V2**, all the photogenerated $[Ru(bpy)_3]^{3+}$ oxidant is efficiently and almost completely consumed by **1-V2** for catalytic water oxidation/O_2 generation. The inserted photos clearly show the formation of O_2 bubbles in the presence of **1-V2** but no O_2 bubbles in the absence of **1-V2**. A central consequence of rate-limiting oxidant generation in photo-driven water oxidation processes is that the rate of O_2 generation does not reflect the TOF of the WOC.

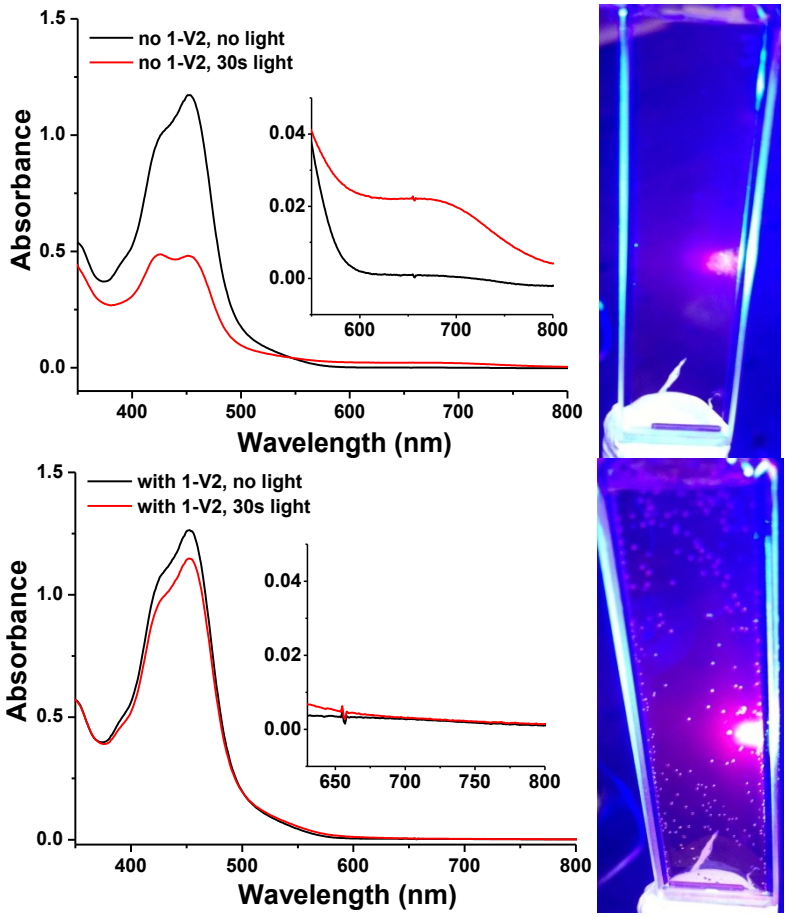

Figure 3-15 The UV-vis spectra of the reaction solution in the light-driven reaction. Above: no catalyst; Bottom: with 2 μM **1-V2** catalyst. The photographs in the right panel show the formation of oxygen bubbles catalyzed by **1-V2** after 2 min of irradiation. Conditions: 455 nm LED-light beam with OD = 0.4 cm and 17 mW was focused on the flat front wall of the reaction vessel (1 mm optical path length); 1.0 mM $[Ru(bpy)_3]^{2+}$, 5.0 mM $Na_2S_2O_8$, 80 mM borate buffer (pH 8).

3.3.4. Stability Studies

The stability of **1-V2** was studied by multiple experiments. After 24 hours no apparent changes in the UV-Vis spectra are observed in water or in borate buffer (**Figure 3-16**).

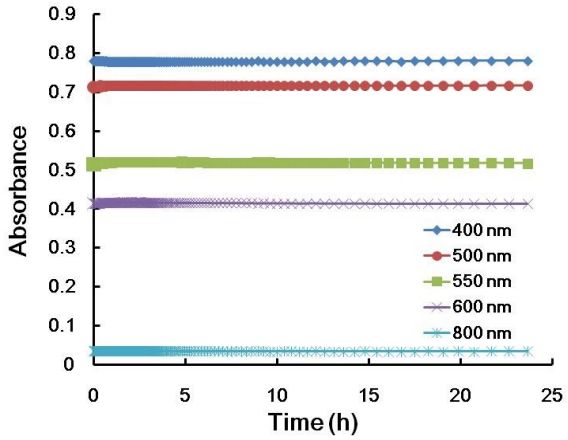

Figure 3-16 Changes in UV-vis spectra of 0.5 mM **1-V2** in 40 mM sodium borate buffer at pH 9.0 over a 24-hour period (less than 2% decrease).

^{51}V NMR spectra of **1-V2** in D_2O or in borate buffer at pH 9.0 exhibit only one peak at -506.8 ppm (**Figure 3-4**); no changes were noticed over a period of one month, confirming the stability of **1-V2** in borate buffer solution. Moreover, FT-IR (**Figure 3-17**) and ^{51}V NMR (**Figure 3-18**) spectra show no changes in **1-V2** before and after light-driven water oxidation catalysis.

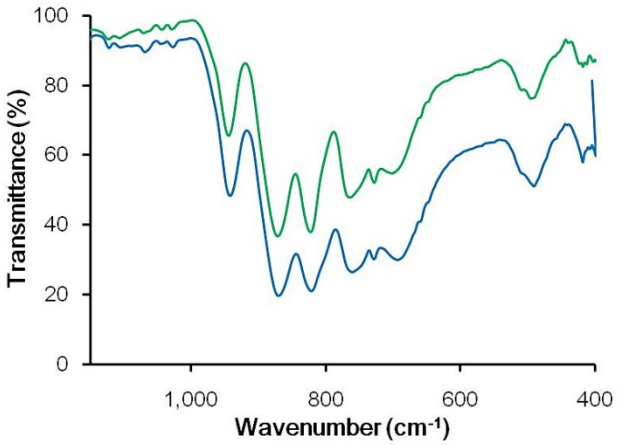

Figure 3-17 FT-IR spectra of the (**1-V2**$\cdots$[Ru(bpy)$_3$]$^{2+}$) precipitates from pre-reaction and post-reaction solutions (blue and green curves, respectively)

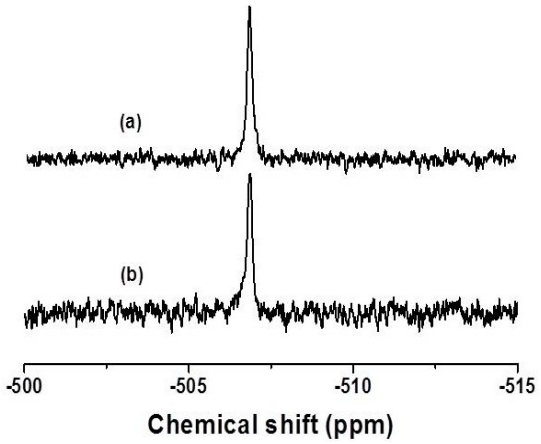

Figure 3-18 ^{51}V NMR for **1-V2** (a) before and (b) after the light-driven water oxidation reaction. Conditions: 455 nm LED light (17 mW, beam diameter ~0.4 cm), 3.3 mM $[Ru(bpy)_3]^{2+}$, 12.6 mM $Na_2S_2O_8$, 67 μM **1-V2**, 80 mM sodium borate buffer, initial pH 9.0, illumination time 50 min. TON ~ 35, chemical yield = $2\times(O_2)/(Na_2S_2O_8) \approx 37\%$. Chemical shifts are relative to neat $VOCl_3$ at 25 ^oC (0 ppm).

Also, water oxidation catalyzed by **1-V2** and $Co(NO_3)_2$ in separate reactions exhibit different overall kinetic profiles and different initial rates (**Figure 3-19**).

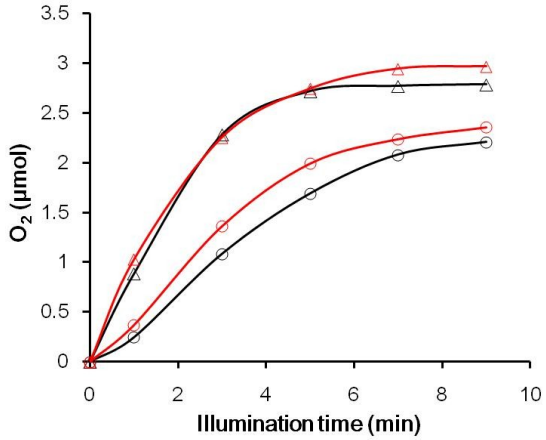

Figure 3-19 The kinetics of O_2 formation in the light-driven reaction catalyzed by 2 μM **1-V2** (Δ) or 2 μM $Co(NO_3)_2$ (○) in 80 mM borate buffers (black curves at pH 8 and red curves at pH 9). Conditions: 455 nm LED-light beam with OD = 0.4 cm and 17 mW was focused on the flat front wall of the reaction vessel; 1.0 mM $[Ru(bpy)_3]^{2+}$, 5.0 mM $Na_2S_2O_8$.

Table 3-5 gives many additional results from a range of stability experiments.[44,67,68] The catalytic water oxidation activity of 2 μM **1-V2** is higher than that of 8 μM Co^{2+}(aq) (same equivalents of Co species) under identical conditions (**Table 3-5**). Furthermore, the dependence of catalytic water oxidation activity as a function of pH, buffer and buffer concentration by **1-V2**, Co^{2+}(aq) and CoO_x are different (**Table 3-5**).

Table 3-5 Catalytic water oxidation activity of **1-V2**, Co^{2+}(aq) and amorphous CoO_x under various pH, buffer and buffer concentration conditions.

Entry	Complex	Complex concentration (μM)	pH	Buffer (mM)	TON	O_2 yield (%)
1	**1-V2**	2	9	80 NaB_i	742	59.4
2	**1-V2**	2	8	80 NaB_i	688	55.1
3	**1-V2** (aged 3 hrs) ‖	2	8	80 NaB_i	683	54.7
4	**1-V2**	2	8	120 NaB_i	690	55.2
5	**1-V2** (aged 3 hrs) ‖	2	8	120 NaB_i	687	55.0
6*	**1-V2**	2	7.5	120 NaB_i	231	18.5
7	**1-V2**	2	8	80 NaP_i	156	12.5
8	**1-V2** (aged 3 hrs) ‖	2	8	80 NaP_i	140	11.2
9	**1-V2**	2	8	100 NaP_i	127	10.2
10	**1-V2**	2	7.2	100 NaP_i	19	1.5
11	**1-V2**	2	6.2	100 NaP_i	0.7	0.06
12	$Co(NO_3)_2$	2	9	80 NaB_i	590	47.2
13	$Co(NO_3)_2$	2	8	80 NaB_i	505	40.4
14	$Co(NO_3)_2$	2	8	120 NaB_i	431	34.5
15*	$Co(NO_3)_2$	2	7.6	120 NaB_i	99	8.0
16	$Co(NO_3)_2$	8	8	120 NaB_i	607	48.6
17*	$Co(NO_3)_2$	8	7.6	120 NaB_i	168	13.5
18	$Co(NO_3)_2$	2	8	80 NaP_i	7.5	0.6
19	$Co(NO_3)_2$	2	8	100 NaP_i	6.1	0.48
20	$Co(NO_3)_2$	2	7.2	100 NaP_i	3.3	0.26

21	$Co(NO_3)_2$	2	6.2	100 NaP_i	0.47	0.03
22	CoO_x[†]	8[§]	9	80 NaB_i	42	3.3
23	CoO_x[†]	8[§]	8	80 NaB_i	142	11.4
24	CoO_x[†]	8[§]	8	80 NaP_i	2.1	0.18
25	CoO_x[†]	8[§]	7.2	100 NaP_i	0.73	0.06
26	CoO_x[†]	8[§]	6.2	100 NaP_i	0.74	0.06

*the reusability test of the catalyst, 2.38 mg NaS_2O_8 was added for the second run. [†]CoO_x was prepared by electrochemical deposition method.[18] [§]Not soluble; the suspension obtained after 10 min of sonication. [‖]Aged in the corresponding buffer solution.

In addition, a toluene solution of tetra-*n*-heptylammonium nitrate ($THpANO_3$) was used to quantitatively extract **1-V2** from the reaction (**Figure 3-20**).

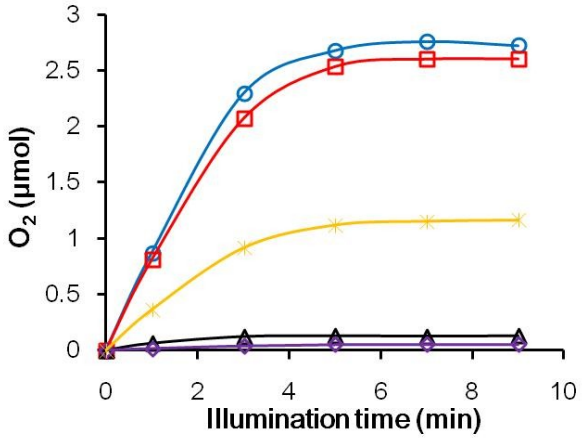

Figure 3-20 Kinetics of light-driven catalytic O_2 evolution from water catalyzed by **1-V2** in 0.12 M borate buffer at pH 8. Conditions: 455 nm LED light (17 mW, beam diameter ~0.4 cm), 5.0 mM $Na_2S_2O_8$, 1.0 mM $[Ru(bpy)_3]Cl_2$. Blue circles: 2 µM **1-V2** without extraction by $THpANO_3$-toluene solution; Red squares: extraction of the 2 µM **1-V2** in NaB_i buffer by $THpANO_3$-toluene solution, followed by addition of 2 µM **1-V2**, $[Ru(bpy)_3]Cl_2$ and $Na_2S_2O_8$; Orange stars: incomplete extraction of the **1-V2** in NaB_i buffer by $THpANO_3$-toluene solution, followed by addition of $[Ru(bpy)_3]Cl_2$ and $Na_2S_2O_8$; Black triangles: complete extraction of the 2 µM **1-V2** in NaB_i buffer with a $THpANO_3$-toluene solution, followed by addition of $[Ru(bpy)_3]Cl_2$ and $Na_2S_2O_8$ but no **1-V2**. Purple diamonds: the reaction solution after the first run followed by extraction using a $THpANO_3$-toluene solution and addition of 2.38 mg $Na_2S_2O_8$.

The extractive removal of **1-V2** from the solution after first catalytic run totally stops the reaction in the water layer (**Figure 3-20**). Similarly, control experiments show that the extraction of **1-V2** before catalytic reaction reduces the O_2 yield to almost zero. In contrast, neither CoO_x nor Co^{2+}(aq) is extracted into the toluene layer by $THpA^+$, and as a consequence, catalytic water oxidation is not affected significantly in these cases.[44] Finally, no particle formation is observed by dynamic light scattering (DLS) for reactions catalyzed by **1-V2**; in contrast, particles with a size around 220 nm are formed in reactions catalyzed by Co^{2+}(aq) (**Figure 3-21**).

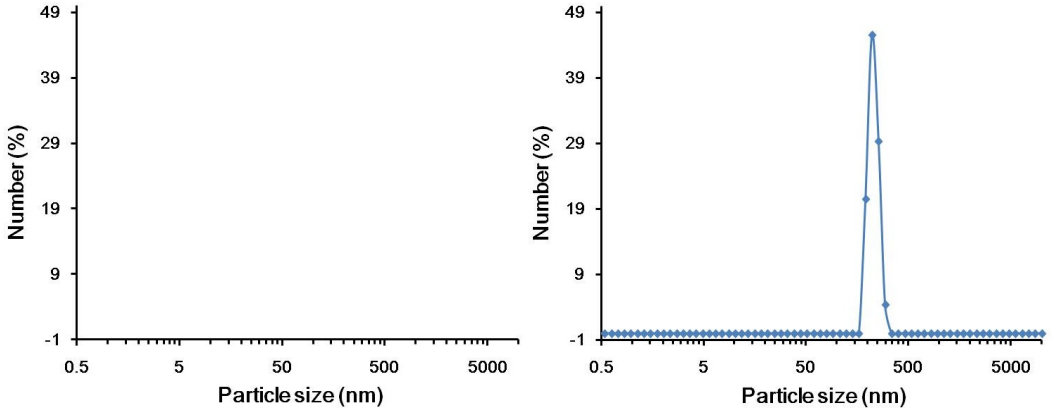

Figure 3-21 Particle size distribution (number %) obtained from dynamic light scattering (DLS) measurements for the post-reaction solution containing 2 μM **1-V2** (left panel) and 2 μM $Co(NO_3)_2$ (right panel) as catalyst, 1 mM $Ru(bpy)_3^{3+}$ in 80 mM borate buffer (pH 9.0).

3.4 Conclusions

In this section, we report a new molecular carbon-free water oxidation catalyst that exhibits high hydrolytic stability and is also by far the fastest synthetic WOC to date (TOF > 1×10^3 s^{-1}). Under light-driven conditions, **1-V2** exhibits higher selectivity for water oxidation versus *bpy* ligand oxidation, and the final O_2 yield using **1-V2** is twice as high as that using **1-P2**. In addition, the quantum efficiency of O_2 formation at 6.0 μM **1-**

V2 reaches the very high value of *ca*. 68%. Extensive studies confirm that the polyanion unit (**1-V2**) itself is the dominant active catalyst, and not Co^{2+}(aq) or cobalt oxide.

References

(1) Lewis, N. S.; Nocera, D. G. *Proc. Natl. Acad. Sci.* **2006**, *103(43)*, 15729.

(2) Eisenberg, R.; Gray, H. B. *Inorg. Chem.* **2008**, *47*, 1697.

(3) Barber, J. *Chem. Soc. Rev.* **2009**, *38*, 185.

(4) Shevchenko, D.; Anderlund, M. F.; Thapper, A.; Styring, S. *Energy Environ. Sci.* **2011**, *4*, 1284.

(5) Hammarstrom, L.; Hammes-Schiffer, S. *Acc. Chem. Res.* **2009**, *42*, 1859.

(6) Yin, Q.; Tan, J. M.; Besson, C.; Geletii, Y. V.; Musaev, D. G.; Kuznetsov, A. E.; Luo, Z.; Hardcastle, K. I.; Hill, C. L. *Science* **2010**, *328*, 342.

(7) Huang, Z.; Luo, Z.; Geletii, Y. V.; Vickers, J.; Yin, Q.; Wu, D.; Hou, Y.; Ding, Y.; Song, J.; Musaev, D. G.; Hill, C. L.; Lian, T. *J. Am. Chem. Soc.* **2011**, *133*, 2068.

(8) Roeser, S.; Fàrrs, P.; Bozoglian, F.; Martínez-Belmonte, M.; Benet-Buchholz, J.; Llobet, A. *ChemSusChem* **2011**, *4*, 197.

(9) Hurst, J. K. *Coord. Chem. Rev.* **2005**, *249*, 313.

(10) Concepcion, J. J.; Jurss, J. W.; Brennaman, M. K.; Hoertz, P. G.; Patrocinio, A. O. T.; Iha, N. Y. M.; Templeton, J. L.; Meyer, T. J. *Acc. Chem. Res.* **2009**, *42*, 1954.

(11) Hull, J. F.; Balcells, D.; Blakemore, J. D.; Incarvito, C. D.; Eisenstein, O.; Brudvig, G. W.; Crabtree, R. H. *J. Am. Chem. Soc.* **2009**, *131*, 8730.

(12) Zong, R.; Thummel, R. *J. Am. Chem. Soc.* **2005**, *127*, 12802.

(13) McCool, N. S.; Robinson, D. M.; Sheats, J. E.; Dismukes, G. C. *J. Am. Chem. Soc.* **2011**, *133*, 11446.

(14) McDaniel, N. D.; Coughlin, F. J.; Tinker, L. L.; Bernhard, S. *J. Am. Chem. Soc.* **2008**, *130*, 210.

(15) Duan, L.; Bozoglian, F.; Mandal, S.; Stewart, B.; Privalov, T.; Llobet, A.; Sun, L. *Nature Chem.* **2012**, *4*, 418.

(16) Muckerman, J. T.; Polyansky, D. E.; Wada, T.; Tanaka, K.; Fujita, E. *Inorg. Chem.* **2008**, *47*, 1787.

(17) Masaoka, S.; Sakai, K. *Chem. Lett.* **2009**, *38*, 182.

(18) Kanan, M. W.; Nocera, D. G. *Science* **2008**, *321*, 1072.

(19) Robinson, D. M.; Go, Y. B.; Greenblatt, M.; Dismukes, G. C. *J. Am. Chem. Soc.* **2010**, *132*, 11467.

(20) Youngblood, W. J.; Lee, S.-H. A.; Kobayashi, Y.; Hernandez-Pagan, E. A.; Hoertz, P. G.; Moore, T. A.; Moore, A. L.; Gust, D.; Mallouk, T. E. *J. Am. Chem. Soc.* **2009**, *131*, 926.

(21) Jiao, F.; Frei, H. *Angew. Chem. Int. Ed.* **2009**, *48*, 1841.

(22) Barnett, S. M.; Goldberg, K. I.; Mayer, J. M. *Nature Chem.* **2012**, *4*, 498.

(23) Zidki, T.; Zhang, L.; Shafirovich, V.; Lymar, S. V. *J. Am. Chem. Soc.* **2012**, *134*, 14275.

(24) Indra, A.; Menezes, P. W.; Zaharieva, I.; Baktash, E.; Pfrommer, J.; Schwarze, M.; Dau, H.; Driess, M. *Angew. Chem. Int. Ed.* **2013**, *52*, 13206.

(25) Smith, R. D. L.; Prévot, M. S.; Fagan, R. D.; Zhang, Z.; Sedach, P. A.; Siu, M. K. J.; Trudel, S.; Berlinguette, C. P. *Science* **2013**, *340*, 60.

(26) Liu, H.; Patzke, G. R. *Chem.- Asian J* **2014**, *9*, 2249.

(27) Kim, T. W.; Choi, K.-S. *Science* **2014**, *343*, 990.

(28) Vannucci, A. K.; Alibabaei, L.; Losego, M. D.; Concepcion, J. J.; Kalanyan, B.; Parsons, G. N.; Meyer, T. J. *Proc. Natl. Acad. Sci.* **2013**, *110*, 20918.

(29) Wang, D.; Groves, J. T. *Proc. Natl. Acad. Sci.* **2013**, *110*, 15579.

(30) Geletii, Y. V.; Botar, B.; Kögerler, P.; Hillesheim, D. A.; Musaev, D. G.; Hill, C. L. *Angew. Chem. Int. Ed.* **2008**, *47*, 3896.

(31) Sartorel, A.; Carraro, M.; Scorrano, G.; Zorzi, R. D.; Geremia, S.; McDaniel, N. D.; Bernhard, S.; Bonchio, M. *J. Am. Chem. Soc.* **2008**, *130*, 5006.

(32) Geletii, Y. V.; Huang, Z.; Hou, Y.; Musaev, D. G.; Lian, T.; Hill, C. L. *J. Am. Chem. Soc.* **2009**, *131*, 7522.

(33) Toma, F. M.; Sartorel, A.; Iurlo, M.; Carraro, M.; Parisse, P.; Maccato, C.; Rapino, S.; Gonzalez, B. R.; Amenitsch, H.; Ros, T. D.; Casalis, L.; Goldoni, A.; Marcaccio, M.; Scorrano, G.; Scoles, G.; Paolucci, F.; Prato, M.; Bonchio, M. *Nature Chem.* **2010**, *2*, 826.

(34) Besson, C.; Huang, Z.; Geletii, Y. V.; Lense, S.; Hardcastle, K. I.; Musaev, D. G.; Lian, T.; Proust, A.; Hill, C. L. *Chem. Commun.* **2010**, 2784.

(35) Murakami, M.; Hong, D.; Suenobu, T.; Yamaguchi, S.; Ogura, T.; Fukuzumi, S. *J. Am. Chem. Soc.* **2011**, *133*, 11605.

(36) Zhu, G.; Geletii, Y. V.; Kögerler, P.; Schilder, H.; Song, J.; Lense, S.; Zhao, C.; Hardcastle, K. I.; Musaev, D. G.; Hill, C. L. *Dalton Trans.* **2012**, *41*, 2084.

(37) Zhu, G.; Glass, E. N.; Zhao, C.; Lv, H.; Vickers, J. W.; Geletii, Y. V.; Musaev, D. G.; Song, J.; Hill, C. L. *Dalton Trans.* **2012**, *41*, 13043.

(38) Tanaka, S.; Annaka, M.; Sakai, K. *Chem. Commun.* **2012**, *48*, 1653.

(39) Car, P.-E.; Guttentag, M.; Baldridge, K. K.; Albertoa, R.; Patzke, G. R. *Green Chem.* **2012**, *14*, 1680.

(40) Lv, H.; Geletii, Y. V.; Zhao, C.; Vickers, J. W.; Zhu, G.; Luo, Z.; Song, J.; Lian, T.; Musaev, D. G.; Hill, C. L. *Chem. Soc. Rev.* **2012**, *41*, 7572.

(41) Goberna-Ferrón, S.; Vigara, L.; Soriano-López, J.; Galán-Mascarós, J. R. *Inorg. Chem.* **2012**, *51*, 11707.

(42) Soriano-López, J.; Goberna-Ferrón, S.; Vigara, L.; Carbó, J. J.; Poblet, J. M.; Galán-Mascarós, J. R. *Inorg. Chem.* **2013**, *52*, 4753.

(43) Song, F.; Ding, Y.; Ma, B.; Wang, C.; Wang, Q.; Du, X.; Fu, S.; Song, J. *Energy Environ. Sci.* **2013**, *6*, 1170.

(44) Vickers, J. W.; Lv, H.; Sumliner, J. M.; Zhu, G.; Luo, Z.; Musaev, D. G.; Geletii, Y. V.; Hill, C. L. *J. Am. Chem. Soc.* **2013**, *135*, 14110.

(45) Sumliner, J. M.; Lv, H.; Fielden, J.; Geletii, Y. V.; Hill, C. L. *Eur. J. Inorg. Chem.* **2014**, 635.

(46) Vickers, J. W.; Sumliner, J. M.; Lv, H.; Morris, M.; Geletii, Y. V.; Hill, C. L. *Phys. Chem. Chem. Phys.* **2014**, *16*, 11942.

(47) Han, X.-B.; Zhang, Z.-M.; Zhang, T.; Li, Y.-G.; Lin, W.; You, W.; Su, Z.-M.; Wang, E.-B. *J. Am. Chem. Soc.* **2014**, *136*, 5359.

(48) Guo, S.-X.; Liu, Y.; Lee, C.-Y.; Bond, A. M.; Zhang, J.; Geletii, Y. V.; Hill, C. L. *Energy Environ. Sci.* **2013**, *6*, 2654.

(49) Quintana, M.; López, A. M.; Rapino, S.; Toma, F. M.; Iurlo, M.; Carraro, M.; Sartorel, A.; Maccato, C.; Ke, X.; Bittencourt, C.; Da Ros, T.; Van Tendeloo, G.; Marcaccio, M.; Paolucci, F.; Prato, M.; Bonchio, M. *ACS Nano* **2013**, *7*, 811.

(50) Li, B.; Yan, Y.; Li, F.; Xu, L.; Bi, L.; Wu, L. *Inorg. Chim. Acta* **2009**, 2796.

(51) Katsoulis, D. E.; Pope, M. T. *J. Am. Chem. Soc.* **1984**, *106*, 2737.

(52) Ghosh, P. K.; Brunschwig, B. S.; Chou, M.; Creutz, C.; Sutin, N. *J. Am. Chem. Soc.* **1984**, *106*, 4772.

(53) Bruker AXS, I. Madison, WI., USA, 2012.

(54) Bruker AXS, I. Madison, WI, USA, 2009.

(55) Dolomanov, O. V.; Bourhis, L. J.; Gildea, R. J.; Howard, J. A. K.; Puschmann, H. *J. Appl. Crystallogr.* **2009**, *42*, 339.

(56) Sheldrick, G. *Acta Cryst. A* **2008**, *64*, 112.

(57) Frisch, M. J.; Trucks, G. W.; Schlegel, H. B.; Scuseria, G. E.; Robb, M. A.; Cheeseman, J. R.; Scalmani, G.; Barone, V.; Mennucci, B.; Petersson, G. A.; Nakatsuji, H.; Caricato, M.; Li, X.; Hratchian, H. P.; Izmaylov, A. F.; Bloino, J.; Zheng, G.; Sonnenberg, J. L.; Hada, M.; Ehara, M.; Toyota, K.; Fukuda, R.; Hasegawa, J.; Ishida, M.; Nakajima, T.; Honda, Y.; Kitao, O.; Nakai, H.; Vreven, T.; J. A. Montgomery, J.; Peralta, J. E.; Ogliaro, F.; Bearpark, M.; Heyd, J. J.; Brothers, E.; Kudin, K. N.; Staroverov, V. N.; Kobayashi, R.; Normand, J.; Raghavachari, K.; Rendell, A.; Burant, J. C.; Iyengar, S. S.; Tomasi, J.; Cossi, M.; N. Rega, J. M. M.; Klene, M.; Knox, J. E.; Cross, J. B.; Bakken, V.; Adamo, C.; Jaramillo, J.; Gomperts, R.; Stratmann, R. E.; Yazyev, O.; Austin, A. J.; Cammi, R.; Pomelli, C.; Ochterski, J. W.; Martin, R. L.; K. Morokuma, V. G. Z.; Voth, G. A.; Salvador, P.; Dannenberg, J. J.; Dapprich, S.; Daniels, A. D.; Ö. Farkas, J. B. F.; Ortiz, J. V.; Cioslowski, J.; Fox, D. J.; Revision A.1 ed.; Gaussian, I., Ed. Wallingford CT., 2009.

(58) Becke, A. D. *Phys. Rev. A* **1988**, *38*, 3098.

(59) Lee, C.; Yang, W.; Parr, R. G. *Phys. Rev. B* **1988**, *37*, 785.

(60) Becke, A. D. *J. Chem. Soc.* **1993**, *98*, 1372.

(61) Cances, E.; Mennucci, B.; Tomasi, J. *J. Chem. Phys.* **1997**, *107*, 3032.

(62) Hay, P. J.; Wadt, W. R. *J. Chem. Phys.* **1985**, *82*, 270.

(63) Wadt, W. R.; Hay, P. J. *J. Chem. Phys.* **1985**, *82*, 284.

(64) Hay, P. J.; Wadt, W. R. *J. Chem. Phys.* **1985**, *82*, 299.

(65) Speldrich, M.; Schilder, H.; Lueken, H.; Kögerler, P. *Isr. J. Chem.* **2011**, *51*, 215.

(66) Vickers, J.; Lv, H.; Zhuk, P. F.; Geletii, Y. V.; Hill, C. L. *MRS Proceedings* **2012**, *1387*, mrsf11.

(67) Schiwon, R.; Klingan, K.; Dau, H.; Limberg, C. *Chem. Commun.* **2014**, *50*, 100.

(68) Stracke, J. J.; Finke, R. G. *ACS Catal.* **2014**, *4*, 79.

Chapter 4

Bis(4'-(4-pyridyl)-2,2':6',2''-terpyridine)ruthenium(II) Complexes and Their N-alkylated Derivatives in Catalytic Light-Driven Water Oxidation

(Published in *RSC Advances* **2013***, 3,* 20647.) -- Reproduced by permission of The Royal Society of Chemistry.

With Jennifer A. Rudd, Petro F. Zhuk, JiYoung Lee, Edwin C. Constable, Catherine E. Housecroft,* Craig L. Hill, Djamaladdin G. Musaev, and Yurii V. Geletii*

4.1 Introduction

The world's fossil energy resources are rapidly diminishing and the search for renewable and sustainable sources to replace these is becoming paramount. It has become clear that water splitting to dihydrogen and dioxygen by artificial photosynthesis reactions would be an ideal way to convert solar energy into a renewable fuel.[1,2] This reaction is thermodynamically unfavorable by 1.23 V and requires the input of four photons with $\lambda <$ 1000 nm.[3-6] Overall, water oxidation is a 4-electron process, but the first step, 1-electron oxidation to hydroxyl radical, is prohibitively unfavorable, E = 2.85 V (vs NHE at pH 0). A highly efficient water oxidation catalyst (WOC) is required to form O_2 at a reasonable rate with low overpotential. Significant progress in the development of WOCs has been reported recently, and an all inorganic catalyst based on earth abundant Co-atoms embedded in a polyoxometalate framework, $Na_{10}[Co_4(H_2O)_2(\alpha\text{-}PW_9O_{34})_2]$ (**Co_4PPOM**), has been described.[7-9] For homogeneous light-driven water oxidation, a three-component system composed of a photosensitizer, a sacrificial electron acceptor and the WOC is generally used.[10-13] Salts of $[Ru(bpy)_3]^{2+}$ (bpy = 2,2'-bipyridine) are the most commonly used sensitizers because of an intense absorption band at 450 nm ($\varepsilon = 1.42 \times 10^4\ M^{-1}\ cm^{-1}$) and high oxidation potentials (E = 1.26 V vs. NHE). The photophysical and photochemical properties of $[Ru(bpy)_3]^{2+}$ derivatives have been a research focus for three decades,[14-17] and are central to photo-driven electron transfer in dye sensitized solar cells (DSSCs).[18-21] Recently two groups of researchers raised the question of whether **Co_4PPOM** is stable and a homogeneous WOC or, rather, functions as a precursor to cobalt oxide or another soluble species that is the actual WOC. These groups used quite different reaction conditions, including far higher **Co_4PPOM** concentrations, and

conducted different experiments than we did in our original (*Science*, 2010) work.[7] Specifically, Stracke and Finke showed that under electrocatalytic conditions and 0.5 mM **Co_4PPOM**, that a cobalt oxide film forms on the electrode surface and that is the dominant WOC under these conditions.[22] However, this group recently reported that at the **Co_4PPOM** concentrations used in our original work,[7] soluble **Co_4PPOM** could be a dominant catalyst, as all our experiments then and since have shown it to be.[23] The other group, demonstrated that the first electron removed from **Co_4PPOM** by photogenerated $[Ru(bpy)_3]^{3+}$ oxidant increases with aging time of **Co_4PPOM** in solution. However, this is not water oxidation, a four-electron-four-proton process, and these investigators actually did not monitor O_2 or study water oxidation. They also found no formation of cobalt oxide from **Co_4PPOM** under their homogeneous conditions. Thus this work, while reporting an interesting finding, is marginally relevant to the other studies by our group, Stracke-Finke, and others. Other groups have since confirmed that **Co_4PPOM** functions as a homogeneous catalyst under a range of conditions, or as a precursor to heterogeneous cobalt oxide under other conditions.[24]

In this work we explore the use of $[Ru(\mathbf{L})_2]^{4+}$ complexes (**Scheme 4-1**) which are *N*,*N*'-dialkylated derivatives of bis(4'-(4-pyridyl)-2,2':6',2''-terpyridine)ruthenium(II) as photosensitizers for water oxidation with long wavelength light. The *N*-substituents investigated are benzyl ($\mathbf{L}^+ = \mathbf{2}^+$), ethyl ($\mathbf{L}^+ = \mathbf{3}^+$), allyl ($\mathbf{L}^+ = \mathbf{4}^+$) and 4-cyanobenzyl ($\mathbf{L}^+ = \mathbf{5}^+$), **Scheme 4-1**. **$Co_4$PPOM** was used as a typical WOC to evaluate the efficiency of this family of photosensitizers as it has been comprehensively characterized in solution[7-9] and has a high WOC activity in light-driven conditions with prototype $[Ru(bpy)_3]^{2+}$ photosensitizers.

4.2 Experimental

4.2.1. General Methods and Materials

$[Ru(bpy)_3]Cl_2 \cdot H_2O$, sodium peroxydisulfate and all other purchased chemicals were of the highest purity available from commercial sources. $[Ru(bpy)_3]Cl_2 \cdot H_2O$ was recrystallized before use[8,10] and $[Ru(bpy)_3][ClO_4]_3$ was prepared as previously reported.[10,25] The borate buffer was prepared by mixing 0.16 M (based on B) $Na_2B_4O_7$ and H_3BO_3 solutions to achieve the desired pH. The compounds $[Ru(\mathbf{2})_2][HSO_4]_4$, $[Ru(\mathbf{3})_2][HSO_4]_4$, $[Ru(\mathbf{4})_2][HSO_4]_4$ and $[Ru(\mathbf{5})_2][HSO_4]_4$ were prepared as previously reported.[26]

Electronic absorption and emission spectra were recorded using an Agilent 8453 spectrophotometer and a Shimadzu RF-5301 PC spectrofluorometer, respectively. Lifetime measurements were made using a Mini-Tau spectrometer from Edinburgh Instruments (475 nm laser diode) in air-equilibrated water. ^1H and ^{13}C NMR spectra were recorded on a Bruker DRX-500 MHz NMR spectrometer with ^1H signals referenced to residual solvent peaks (TMS = δ 0 ppm); signals in the ^{13}C NMR spectrum were referenced with respect to $Na[Me_3Si(CH_2)_3SO_3]$ (DSS)[27] with the $SiMe_3$ signal at δ 0 ppm. Electrospray ionization mass spectra were recorded on a Bruker esquire 3000 plus mass spectrometer. Electrochemical data were obtained using i) a BAS CV-50W electrochemical analyzer at room temperature equipped with a glassy-carbon working, a Pt-wire auxiliary, and a Ag/AgCl (3 M NaCl) BAS reference electrodes; or ii) an Eco Chemie Autolab PGSTAT 20 system with glassy carbon working and platinum auxiliary electrodes. All redox potentials are reported relative to Ag/AgCl (3 M NaCl) reference electrode.

The fast reactions were studied using a Hi-Tech KinetAsyst Stopped Flow SF-61SX2 instrument equipped with a diode array detector operating in wavelength range 400-700 nm. Detailed analysis of kinetic data was performed using both Copasi 4.7 (Build 34)[28] and the Solver subprogram in Microsoft Excel.

4.2.2. Synthesis

$[Ru(\mathbf{1})_2][HSO_4]_2$. $[Ru(\mathbf{1})_2][PF_6]_2$ (150 mg, 0.164 mmol) and $[^nBu_4N][HSO_4]$ (300 mg, 0.884 mmol) were added to a mixture of MeCN and CH_2Cl_2 (6 mL, 9:1 by vol.) and the solution stirred for 30 min. A red precipitate formed and was separated by filtration. The solid was washed with Et_2O (30 mL) and $[Ru(\mathbf{1})_2][HSO_4]_2$ was isolated as a red solid (107 mg, 78.7%). ^{1}H NMR (500 MHz, D_2O) δ /ppm 9.30 (s, 4H, H^{B3}), 9.13 (d, J = 6.6 Hz, 4H, H^{C2}), 8.83 (d, J = 6.7 Hz, 4H, H^{C3}), 8.72 (d, J = 8.1 Hz, 4H, H^{A3}), 7.99 (td, J = 8.0, 1.2 Hz, 4H, H^{A4}), 7.46 (d, J = 5.4 Hz, 4H, H^{A6}), 7.22 (m, 4H, H^{A5}). ^{13}C NMR (126 MHz, D_2O) δ /ppm 160.1 (C^{A2}/C^{B2}), 158.8 (C^{A2}/C^{B2}), 156.9 (C^{C4}), 154.9 (C^{A6}), 145.2 (C^{C2}), 144.5 (C^{B4}), 141.2 (C^{A4}), 130.5 (C^{A5}), 128.4 (C^{C3}), 127.6 (C^{A3}), 124.7 (C^{B3}). ESI-MS *m/z* 361.0 $[M–2HSO_4]^{2+}$ (base peak, calc. 361.1). UV-vis (H_2O, 1.2×10^{-6} mol dm^{-3}) λ_{max} / nm (ε_{max} / dm^3 mol^{-1} cm^{-1}) 490 (33100), 313 (58100), 274 (75500), 239 (39600). Emission (H_2O, λ_{exc} = 490 nm) λ_{em} = 660 nm. Found C, 48.07; H, 3.63; N, 11.29; $C_{40}H_{30}N_8O_8RuS_2{\cdot}4.5H_2O$ requires C, 48.19; H, 3.94; N, 11.24.

4.2.3. Light-Driven Water Oxidation

Light-induced water oxidation was carried out in the cylindrical quartz optical cell (NSG, 32G10) with a 1 cm optical path length, an outer diameter 22 mm, and total volume ~ 2.8 mL equipped with standard joint. In a typical reaction, the vessel was filled with 2 mL of a solution with the desired concentrations of $[Ru(bpy)_3]Cl_2{\bullet}H_2O$, $Na_2S_2O_8$, catalyst, and

sodium borate buffer. The vessel was then sealed with a rubber septum and purged with Ar. The headspace was checked by gas chromatography (GC) to confirm the absence of O_2 before the experiment. All procedures were performed with a minimum exposure to ambient light. The reaction was initiated by turning on the LED light source (LLS) equipped with a 490 nm LED. A light beam with a diameter 0.4-0.5 cm and 7 mW power was focused on the flat front of the reaction vessel using two lenses. The power of the light source was measured using a laser power meter Molectron, model Max 500A. The solution was agitated by a magnetic stirring bar spinning vertically on the back side of the cell. After the desired illumination time, the reaction was temporarily stopped by blocking the light. The O_2-yield was quantified by GC as described earlier.[8,10,29]

4.3 Results and Discussion

4.3.1. Synthesis and characterization of $[Ru(1)_2][HSO_4]_2$

The water-soluble complex $[Ru(\mathbf{1})_2][HSO_4]_2$ was prepared via anion exchange by treating $[Ru(\mathbf{1})_2][PF_6]_2$[30,31] with $[^tBu_4N][HSO_4]$.[26] The red complex $[Ru(\mathbf{1})_2][HSO_4]_2$ is insoluble in most common organic solvents but readily soluble in water. The electrospray mass spectrum exhibited a peak at *m/z* 361.0 assigned to the $[M - 2HSO_4]^{2+}$ ion. ^1H and ^{13}C NMR spectra were recorded in D_2O and the latter were referenced to DSS (see experimental section). The spectra were assigned by use of COSY, DEPT, HMQC and HMBC methods and were consistent with a single ligand environment in the $[Ru(\mathbf{1})_2]^{2+}$ ion. Elemental analysis of the complex indicated the formation of the hydrate $[Ru(\mathbf{1})_2][HSO_4]_2 \cdot 4.5H_2O$. This was not unexpected in the light of data reported by us for a series of related complexes including $[Ru(\mathbf{2})_2][HSO_4]_4$, $[Ru(\mathbf{3})_2][HSO_4]_4$, $[Ru(\mathbf{4})_2][HSO_4]_4$ and $[Ru(\mathbf{5})_2][HSO_4]_4$.[26] The electronic absorption spectrum of an

aqueous solution of $[Ru(\mathbf{1})_2][HSO_4]_2$ is similar to that of $[Ru(\mathbf{1})_2][PF_6]_2$.[30] Three high-energy absorptions at 313, 274 and 239 nm are assigned to ligand-based $\pi^* \leftarrow \pi$ transitions, and the band at 490 nm responsible for the red colour of $[Ru(\mathbf{1})_2][HSO_4]_2$ arises from an MLCT transition. Excitation of $[Ru(\mathbf{1})_2][HSO_4]_2$ at 490 nm results in an emission at 690 nm with a lifetime of 73 ns. This is somewhat shorter than the emission lifetimes observed for $[Ru(\mathbf{L})_2][HSO_4]_4$ ($\mathbf{L}^+$ = $\mathbf{2}^+$, $\mathbf{3}^+$, $\mathbf{4}^+$ and $\mathbf{5}^+$). The quantum yield of 0.0018 for $[Ru(\mathbf{1})_2][HSO_4]_2$ is of the same order of magnitude as those observed for $[Ru(\mathbf{L})_2][HSO_4]_4$ ($\mathbf{L}^+$ = $\mathbf{2}^+$, $\mathbf{3}^+$, $\mathbf{4}^+$ and $\mathbf{5}^+$).[26] The UV-vis spectroscopic and electrochemical data of $[Ru(\mathbf{1})_2][HSO_4]_2$ were compared with those of $[Ru(\mathbf{L})_2][HSO_4]_4$ (L^+ = $\mathbf{2}^+$–$\mathbf{5}^+$) complexes in water and are summarized in **Table 4-1**.

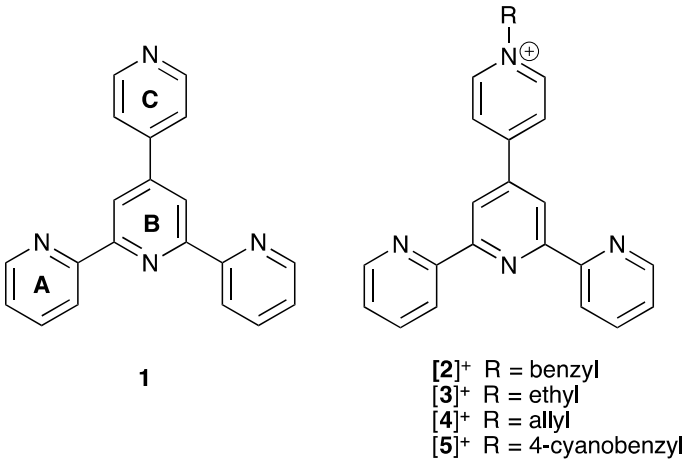

Scheme 4-1 Structures of ligands, and ring labelling in **1** for spectroscopic assignments.

Table 4-1 UV-vis spectroscopic and electrochemical data for ruthenium(II) complexes in water.

Complex	λ_{max} / nm	ε / $dm^3\ mol^{-1}\ cm^{-1}$	E^a/V	ΔE^b/V	τ_{em}/ns
$[Ru(bpy)_3]Cl_2$	450	14000	1.028	0	550[c]
$[Ru(\mathbf{1})_2][HSO_4]_2$	490	33000	1.21	0.182	73
$[Ru(\mathbf{2})_2][HSO_4]_4$	511	38000	1.24	0.212	135
$[Ru(\mathbf{3})_2][HSO_4]_4$	508	25000	1.21	0.192	146

$[Ru(\mathbf{4})_2][HSO_4]_4$	511	32000	1.21	0.182	137
$[Ru(\mathbf{5})_2][HSO_4]_4$	513	34000	1.24	0.212	108

[a] In the presence of 0.1 M $NaHSO_4$ electrolyte, vs Ag/AgCl reference electrode; [b] difference in potentials between $[Ru(\mathbf{L})_2]^{(n+1)+}/[Ru(\mathbf{L})_2]^{n+}$ (L = **1**, n = 2; L = **2-5**, n = 4) and $/[Ru(bpy)_3]^{3+}/[Ru(bpy)_3]^{2+}$ couples; [c] reference[32]

4.3.2. Mechanistic Evaluation of Catalytic Activity

Throughout the mechanistic discussions, we use the following abbreviated formulae for clarity: $[Ru^{II}(\mathbf{L})_2]$ stands for $[Ru(\mathbf{L})_2]^{n+}$ (L = **1**, n = 2; L^+ = $\mathbf{2}^+$–$\mathbf{5}^+$, n = 4); $[Ru^{III}(\mathbf{L})_2]$ stands for $[Ru(\mathbf{L})_2]^{(n+1)+}$ (L = **1**, n +1 = 3; L^+ = $\mathbf{2}^+$–$\mathbf{5}^+$, n + 1 = 5); $[Ru^{II}(bpy)_3]$ stands for $[Ru(bpy)_3]^{2+}$, and $[Ru^{III}(bpy)_3]$ stands for $[Ru(bpy)_3]^{3+}$.

The most common approaches for evaluating catalytic water oxidation activity in homogeneous systems are based on the use of strong oxidants such as Ce(IV) (E^o = 1.72 V vs. NHE[33]) or $[Ru(bpy)_3]^{3+}$ (E^o = 1.26 V vs. NHE[16]), or light induced generation of a strong oxidant such as $[Ru(bpy)_3]^{3+}$ in the presence of a sacrificial electron acceptor (often $S_2O_8^{2-}$). In the presence of light, the $[Ru^{II}(\mathbf{L})_2]$ or $[Ru^{II}(bpy)_3]$ driven water oxidation involves two key processes: i) photoinduced oxidation of $[Ru^{II}(\mathbf{L})_2]$ to $[Ru^{III}(\mathbf{L})_2]$ (or $[Ru^{II}(bpy)_3]$ to $[Ru^{III}(bpy)_3]$) by $Na_2S_2O_8$; ii) four sequential one-electron oxidation dark reactions of the catalyst to form O_2-releasing species by $[Ru^{III}(\mathbf{L})_2]$ or $[Ru^{III}(bpy)_3]$. This first photoinduced electron-transfer has been thoroughly studied for the reaction between $[Ru(mptpy)_2]^{4+}$ (mptpy$^+$ = 4'-(4-methylpyridinio)-2,2':6',2''-terpyridine) and $Na_2S_2O_8$.[34] The second process can be studied directly by observing the kinetics of $[Ru^{III}(\mathbf{L})_2]$ reduction in water in the presence of a catalyst. Attempts to synthesize $[Ru^{III}(\mathbf{L})_2]$ (**L** = **1** or $\mathbf{L}^+$ = $\mathbf{2}^+$ or $\mathbf{4}^+$) by oxidation with PbO_2 in 0.5-1.0 M aqueous H_2SO_4 in a manner analogous to the synthesis of $[Ru^{III}(bpy)_3]$ were unsuccessful

due to the instability of the higher oxidation states. After addition of PbO_2, the solution became dark green, but when the PbO_2 powder was filtered off, the solution again became red (i.e. the colour characteristic of $[Ru^{II}(\mathbf{L})_2]$).

To estimate the lifetime of $[Ru^{III}(\mathbf{L})_2]$ ($\mathbf{L}$ = **1** or $\mathbf{L}^+$ = $\mathbf{2}^+$ or $\mathbf{4}^+$) in acidic conditions (0.5 M H_2SO_4), we generated the compounds using $Ce(NH_4)_4(SO_4)_4 \bullet 2H_2O$ as a stoichiometric oxidant, eq. **4-1**.

$$[Ru^{II}(\mathbf{L})_2] + Ce(IV) \rightarrow [Ru^{III}(\mathbf{L})_2] + Ce(III) \qquad (\mathbf{4\text{-}1})$$

The reaction kinetics were followed by the formation of $[Ru^{III}(\mathbf{L})_2]$ as monitored by an increase in an absorbance at 670 nm. One of the feeding syringes was filled with aqueous $[Ru^{II}(\mathbf{L})_2]$ and the second with $Ce(NH_4)_4(SO_4)_4 \cdot 2H_2O$ in 0.5 M H_2SO_4. The concentration of $[Ru^{II}(\mathbf{L})_2]$ in the stock solutions was quantified using the absorbance at 510 nm. An example of the changes in absorbance is given in Figure 4-1.

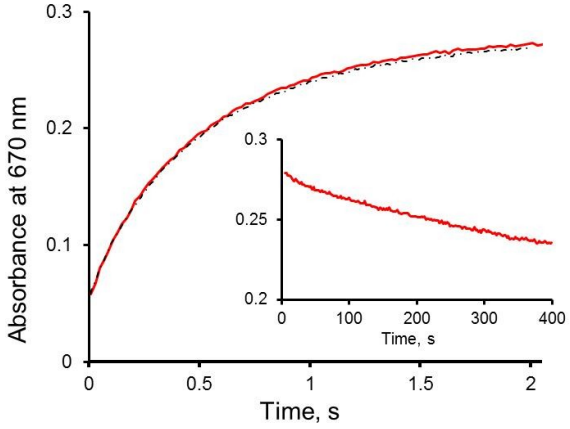

Figure 4-1 Kinetics of formation and decomposition of $[Ru^{III}(\mathbf{2})_2]$ (insert, longer time scale) in the reaction of 0.85 mM $[Ru^{II}(\mathbf{2})_2]$ with 0.62 mM $Ce(NH_4)_4(SO_4)_4 \cdot 2H_2O$ in 0.5 M H_2SO_4 (red line) following the change in absorbance at 670 nm. The fitting to eq. **4-12** with $k_{12} = 2.5 \times 10^8$ M^{-1} s^{-1} and $\varepsilon_4(670) = 430$ M^{-1} cm^{-1} is shown by the dashed black line.

The half-life of $[Ru^{III}(\mathbf{L})_2]$ was estimated from the slow decrease of absorbance at 670 nm, A(670), to be ~ 0.5 h. This is much shorter than for $[Ru^{III}(bpy)_3]$. This decomposition is thought to proceed via the reactions in eqs **4-2** and **4-3**, where **L′** is a one-electron oxidized ligand and P is the two-electron oxidized $[Ru^{II}(\mathbf{L})_2]$. The estimated rate constants k_d are in the range (0.5- 5) $\times 10^{-3}$ s^{-1} and are given in **Table 4-2**.

$$[Ru^{III}(\mathbf{L})_2] \xrightarrow{k_d} [Ru^{II}(\mathbf{LL'})] \qquad (\mathbf{4\text{-}2})$$

$$[Ru^{III}(\mathbf{L})_2] + [Ru^{II}(\mathbf{L})(\mathbf{L'})] \rightarrow P + [Ru^{II}(\mathbf{L})_2] \quad \text{fast} \quad (\mathbf{4\text{-}3})$$

Table 4-2 The reaction rate constants of $[Ru^{III}(L)_2]$ self-decomposition in 80 mM sodium borate buffer compared to that of $[Ru^{III}(bpy)_3]$.

Complex	pH 8	pH 9	0.5 M H_2SO_4
$[Ru^{III}(bpy)_3]$	0.0012	0.005	$<5\times10^{-5}$ [c]
$[Ru^{III}(\mathbf{1})_2]$	<5 [b]	n.d.	5×10^{-4}
$[Ru^{III}(\mathbf{2})_2]$	95±30	115±30	5×10^{-3}
$[Ru^{III}(\mathbf{2})_2]$	<1 [a]		
$[Ru^{III}(\mathbf{4})_2]$	20±7	90±30	5×10^{-4}
$[Ru^{III}(\mathbf{3})_2]$	<10 [b]	<10 [b]	n.d.
$[Ru^{III}(\mathbf{5})_2]$	<10 [b]	n.d.	n.d.

[a] In 80 mM sodium phosphate buffer at pH 8; [b] These complexes have a very weak effect on the rate of $[Ru^{III}(bpy)_3]$ decomposition. [c] References[25,35].

As noted earlier, the low stability of $[Ru^{III}(\mathbf{L})_2]$ (**L** = **1** or $\mathbf{L}^+$ = $\mathbf{2}^+$ or $\mathbf{4}^+$) does not permit their isolation. However, their solution spectra could be recorded (**Figure 4-2**). The solutions typically contain 1–3% of $[Ru^{II}(\mathbf{L})_2]$ and decomposition products, which strongly absorb light at λ <550 nm. Therefore, spectra were measured in the range 550-950 nm. Compared to $[Ru^{III}(bpy)_3]$, the absorbance maxima of $[Ru^{III}(\mathbf{L})_2]$ are shifted by about 90 nm to longer wavelength and extinction coefficients are about 50% higher.

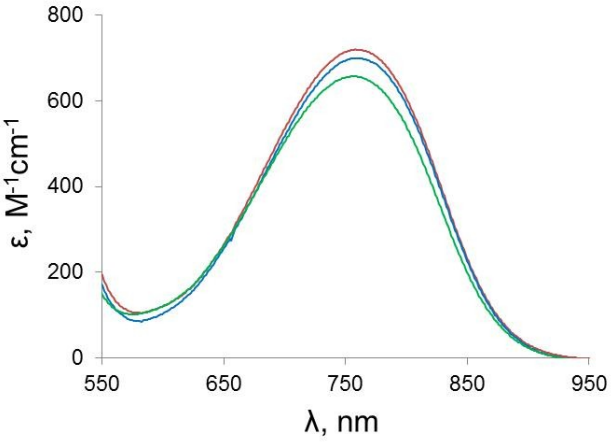

Figure 4-2 Part of the visible absorption spectrum of $[Ru^{III}(\mathbf{1})_2]$ (green), $[Ru^{III}(\mathbf{2})_2]$ (blue) and $[Ru^{III}(\mathbf{4})_2]$ (red) in 0.5 M aqueous H_2SO_4.

These experiments clearly indicate that $[Ru^{III}(\mathbf{L})_2]$ is unstable even at high acidity. The low stability and short life-time of $[Ru^{III}(\mathbf{L})_2]$ excited states could be prohibitive for use of these complexes as photosensitizers in light driven water oxidation reaction, although their higher oxidation potentials are advantageous.

To avoid precipitation of peroxydisulfate salts of $[Ru^{II}(\mathbf{L})_2]$, we have had to use relatively low concentrations in studies of the catalytic reactions. We have found that water is catalytically oxidized to O_2 in the light driven system with $S_2O_8^{2-}$ as a sacrificial electron acceptor in the presence of **Co_4PPOM** (catalyst) and $[Ru^{II}(\mathbf{L})_2]$ (photosensitizer) in borate buffer at pH 8 and 9 (**Figure 4-3**). The rates and O_2 yields are strongly dependent on the ligand. Complexes of **1** and $\mathbf{5}^+$ were almost inactive, those of $\mathbf{2}^+$, $\mathbf{3}^+$ and $\mathbf{4}^+$ showed a similar initial activity, with $[Ru^{II}(\mathbf{2})_2]$ being the most efficient over a longer time scale. The benchmark photosensitizer $[Ru^{II}(bpy)_3]$ had a similar activity to $[Ru^{II}(\mathbf{2})_2]$. The highest overall efficiency was obtained for $[Ru^{II}(\mathbf{2})_2]$ with O_2 yields per peroxydisulfate (yield = 2 $[O_2]/[Na_2S_2O_8]$) of up to 30% and TON = (0.7-1.0) × 10^2.

The yields were only weakly dependent on pH, although the rates were about double at pH 9. The turnover frequency, TOF, is commonly calculated as the ratio of the initial rate and the catalyst concentration, and $[Ru^{II}(\mathbf{L})_2]$ gave TOFs of up to ~ 0.15 s^{-1} at pH 9. However, in light driven systems, the initial rate is actually proportional to the quantum yield but not related to the TOF.

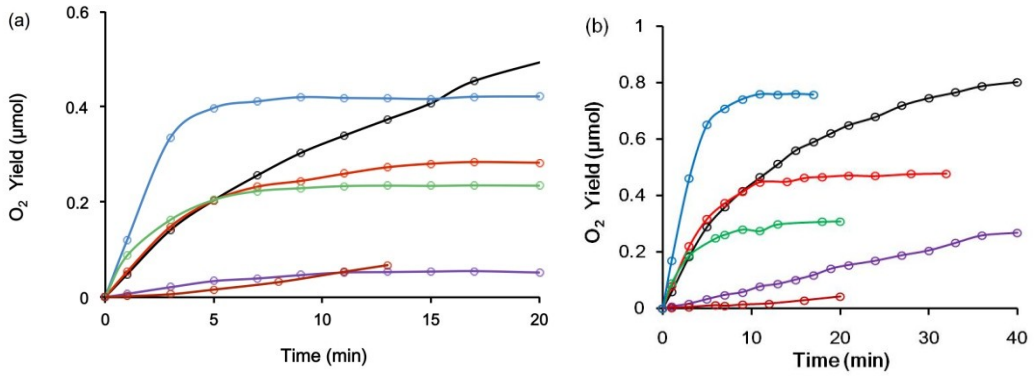

Figure 4-3 The time profile of O_2 formation in light driven water oxidation reaction. Conditions: LED light source with λ_{max} = 490 nm, 7 mW (photon flux 1.6 × 10^{16} photons s^{-1}), total solution volume 2 mL, 2.5 mM $Na_2S_2O_8$; 0.125 mM $[Ru^{II}(\mathbf{L})_2]$ or $[Ru^{II}(bpy)_3]$, 4 μM **Co_4PPOM**, 80 mM borate buffer: (a) pH 8.0, and (b) at pH 9.0. Blue curve is for $[Ru^{II}(bpy)_3]$, black for $[Ru^{II}(\mathbf{2})_2]$, red for $[Ru^{II}(\mathbf{4})_2]$, green for $[Ru^{II}(\mathbf{3})_2]$, purple for $[Ru^{II}(\mathbf{1})_2]$ and dark red for $[Ru^{II}(\mathbf{5})_2]$.

At constant light intensity or constant photon flux (q_p) and at high solution optical density, all light is absorbed and the total number of consumed photons during the time dt is $dN = q_p dt$. The apparent (incident) quantum yield Φ_{ap} is given by $d(O_2)/dN = (1/q_p)d(O_2)/dt$. For the LED light source with λ_{max} = 490 nm and power 7 mW, the photon flux q_p is ~1.6 × 10^{16} photon s^{-1}. The initial Φ_{ap} reaches up to 25% for $[Ru^{II}(bpy)_3]$ at pH 9. Of the new photosensitizers, $[Ru^{II}(\mathbf{1})_2]$ and $[Ru^{II}(\mathbf{5})_2]$ produce very low amounts of O_2. The initial quantum yields Φ_{ap} for $[Ru^{II}(\mathbf{2})_2]$, $[Ru^{II}(\mathbf{3})_2]$ and $[Ru^{II}(\mathbf{4})_2]$ are similar and fall in the range 3–6% and 8–12% at pH 8 and 9, respectively. However, the reaction

practically stops after about 10 minutes for $[Ru^{II}(\mathbf{3})_2]$ and $[Ru^{II}(\mathbf{4})_2]$, but continues longer for $[Ru^{II}(\mathbf{2})_2]$. Based on $[Ru^{II}(\mathbf{L})_2]$ ($\mathbf{L}$ = **1** or $\mathbf{L}^+$ = $\mathbf{2}^+$–$\mathbf{5}^+$), the turnover number TON_{Ru} = $4[O_2]/[Ru^{II}(\mathbf{L})_2]$, is about 10 for $\mathbf{L}$ = **2** at pH 9. There is no correlation of Φ_{ap} and O_2 yield with the oxidation potentials or excited state lifetimes of $[Ru^{II}(\mathbf{L})_2]$. It is likely that the performance of the dyes is related to their stability under turnover conditions. Hypothetically, the amount of degraded dye can be determined from the difference in solution absorbance before and after the reaction. However, the products of dye oxidation also absorb at similar wavelengths. In addition, decomposition of one molecule of dye may require large numbers of oxidative equivalents. As a result, UV-vis spectroscopy becomes uninformative. As seen from **Figure 4-4**, the absorbance after reaction for the most efficient dye $[Ru^{II}(\mathbf{2})_2]$ is smaller compared with much less efficient $[Ru^{II}(\mathbf{1})_2]$. Oxidation of the ligand $\mathbf{L}$ by Ru(III) may proceed through: i) an intramolecular pathway in $[Ru^{III}(\mathbf{L})_2]$ (self-decomposition) in eqs **4-2** and **4-3**; ii) an oxidation of $\mathbf{L}$ by the catalyst in high oxidation state(s). The first pathway, eqs **4-2** and **4-3**, is observed at neutral pH and is well known for $[Ru^{III}(bpy)_3]$.

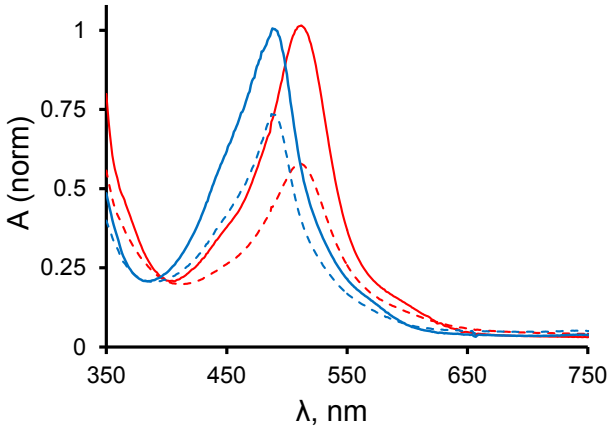

Figure 4-4 The normalized absorption spectra of $[Ru^{II}(3)_2]$ (solid red line) and $[Ru^{II}(1)_2]$ (solid blue) before and after the light driven water oxidation reaction (dashed lines) at pH 9. Conditions are given in the caption to **Figure 4-3**.

In order to oxidize water, the reaction in eq **4-2** should be slower than the rate of dioxygen formation $k_d[[Ru^{III}(\mathbf{L})_2]] << -4d[O_2]/dt$. Since the rate of O_2 formation at pH 9.0 is around 5×10^{-7} $M^{-1}s^{-1}$ and $[[Ru^{III}(\mathbf{L})_2]] < 1.25 \times 10^{-4}$ M, the self-decomposition might compete with water oxidation if $k_d > 10^{-3}$ s^{-1}. The latter number is close to that determined in 0.5 M H_2SO_4. Because k_d usually increases with pH, the reaction in eq **4-2** could significantly decrease the O_2 yield under turnover conditions at pH 8-9. The short life-times of $[Ru^{III}(\mathbf{L})_2]$ do not allow their isolation and the direct measurements of their self-decomposition rate constants.

4.3.3. Rate Constants of $[RuIII(L)_2]$ Self-Decomposition at Elevated pH

As shown in **Figure 4-4**, the concentration of ruthenium(II) species decreases in the course of the reaction as a result of self-decomposition of the photogenerated ruthenium(III) species. For all ligands, the rate constants of $[Ru^{III}(\mathbf{L})_2]$ self-decomposition under turnover conditions were measured indirectly using the kinetic model in eqs **4-4** to **4-8**. This model is based on an experimentally observed increase of the reaction rate

(measured as dOD/dt, where OD is the optical density at 670 nm, A_{670}) when a small amount of $[Ru^{III}(\mathbf{L})_2]$ was added to $[Ru^{III}(bpy)_3]$.

$$[Ru^{III}(bpy)_3] \rightarrow P1 \qquad (\mathbf{4\text{-}4})$$

$$[Ru^{III}(bpy)_3] + [Ru^{II}(\mathbf{L})_2] \rightleftharpoons [Ru^{II}(bpy)_3] + [Ru^{III}(\mathbf{L})_2] \qquad (\mathbf{4\text{-}5})$$

$$[Ru^{III}(\mathbf{L})_2] \rightarrow P2 \qquad (\mathbf{4\text{-}6})$$

$$[Ru^{III}(bpy)_3] + P1 \rightarrow [Ru^{II}(bpy)_3] + P \qquad (\mathbf{4\text{-}7})$$

$$[Ru^{III}(bpy)_3] + P2 \rightarrow [Ru^{II}(bpy)_3] + PP \qquad (\mathbf{4\text{-}8})$$

For simplicity we use abbreviations: $[Ru^{III}(bpy)_3] = A$, $[Ru^{II}(\mathbf{L})_2] = B$, $[Ru^{II}(bpy)_3] = C$, and $[Ru^{III}(\mathbf{L})_2] = D$. The D, P1 and P2 concentrations are considered as steady state. A thorough analysis of the data confirmed that the steady state concentration with respect to D is achieved in less than 1 ms. The reaction in eq **4-5** is thermodynamically unfavourable: $K_5 = k_5/k_{-5}$ is equal to 8.9×10^{-4} and 2.7×10^{-4} for $\Delta E = 0.182$ and 0.212 V, respectively (**Table 4-1**). The electron transfer reactions between ruthenium polypyridine complexes, such as in eq **4-5**, are very fast and of the order of 10^9 M^{-1} s^{-1}.>Creutz, 1980 #9878< Therefore under typical experimental conditions $k_{-5}C > 10^4$ s^{-1} and it is reasonable to assume that $k_{-5}C >> k_6$. The mass balance in the reaction is as follows: $A = A_0 - D - P1$, $C = C_0 + D$, $B = B_0 - D$; species P1 is a short lived intermediate and P1 << D. After simplification, one obtains eq. **4-9**.

$$D = K_5(A_0 + D)(B_0 - D) / (C_0 - D) \qquad (\mathbf{4\text{-}9})$$

After simplification, eq. **4-9** gives eq. **4-10**.

$$D^2+[C_0+K_5(A_0+B_0)]D-K_5A_0B_0=0 \qquad \textbf{(4-10)}$$

If: $p=C_0+K_5(A_0+B_0)$, $q=-K_5A_0B_0$

then eq. **4-10** becomes eq. **4-11** and D is found from eq. **4-12**.

$$D^2+pD+q=0 \qquad \textbf{(4-11)}$$

$$D=\frac{-p+\sqrt{p^2-4q}}{2} \qquad \textbf{(4-12)}$$

After reaching steady state conditions with respect to D, the decrease of optical density (OD) is described applying the Beer-Lambert law by eq **4-13** (where l = path length). For simplicity, it was assumed that the molar extinction coefficients for P and PP are close to those of $[Ru^{II}(bpy)_3]$ and $[Ru^{II}(\mathbf{L})_2]$, respectively.

$$d(OD)/dt=-d[(\varepsilon_1 A+\varepsilon_2 C+\varepsilon_2 P+\varepsilon_3 B+\varepsilon_3 PP+\varepsilon_4 D)l]/dt \qquad \textbf{(4-13)}$$

From the reaction mechanism in eqs **4–8**, and after several standard mathematical transformations, the initial rate R of optical density decrease can be expressed as eq **4-14**.

$$R=2(\varepsilon_1-\varepsilon_2)(k_4 A_0+k_6 D)l=R_0+2(\varepsilon_1-\varepsilon_2)k_6 Dl \qquad \textbf{(4-14)}$$

where $R_0=2(\varepsilon_1-\varepsilon_2)k_4A_0l$ is the initial rate of optical density decrease in the absence of $[Ru^{II}(\mathbf{L})_2]$ (the self-decomposition of $[Ru^{III}(bpy)_3]$). Eq. **4-14** with D calculated from eq **4-12** was used to fit experimental data with k_6 as a variable parameter. Examples of

the experimental and fitting data are presented in **Figure 4-5**, the values of k_6 are given in **Table 4-2**. In the following section, we consider the influence of the structure of the ruthenium complexes on these rate constants and on the overall water photocatalytic oxidation reaction.

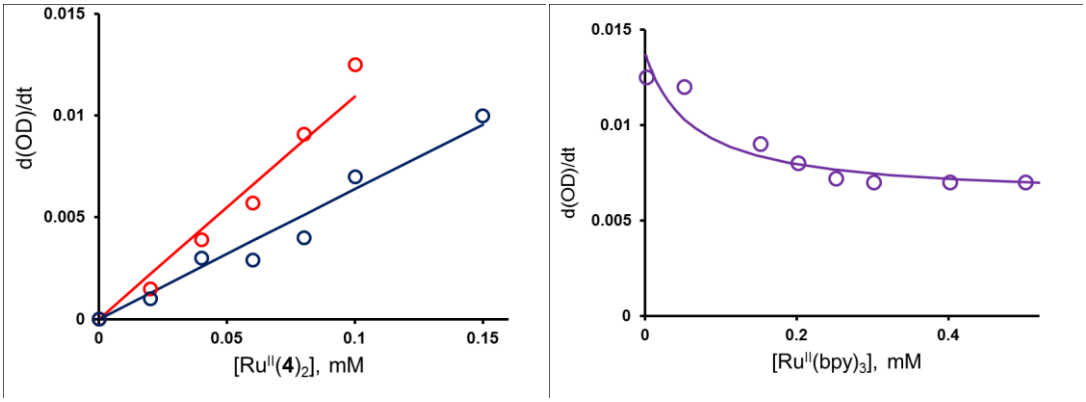

Figure 4-5 Effect of $[Ru^{II}(\mathbf{4})_2]$ (left) and $[Ru^{II}(bpy)_3]$ (right) on initial rate of $[Ru^{III}(bpy)_3]$ decomposition measured as the rate of decrease of absorbance at 670 nm, pH 9.0, 80 mM borate buffer. Initial conccentrations: 0.45 mM $[Ru^{III}(bpy)_3]$, 5.6×10^{-5} M $[Ru^{II}(bpy)_3]$ (red circle), 2×10^{-6} M $[Ru^{II}(bpy)_3]$ (blue circle), 0.08 mM $[Ru^{II}(\mathbf{4})_2]$ (purple).

4.3.4. Structure-Activity Correlation

As can be seen from **Table 4-2**, there is no simple correlation between the stability of the dyes (defined as the rate of self-decomposition, k_6) and the potentials of the $[Ru^{III}(\mathbf{L})_2]/[Ru^{II}(\mathbf{L})_2]$ couples. The effect of pH is small: ruthenium(II) polypyridyl complexes are less stable with increasing pH (**Table 4-2**). Changing borate to phosphate buffer has a dramatic effect on the relative stabilities of the dyes. The self-decomposition of $[Ru^{III}(bpy)_3]$ measured from the decrease of optical density at 670 nm obeys a simple exponential law at both pH 8 and 9. The reaction in phosphate buffer is faster but the kinetics are more complex.[25] The addition of $[Ru^{II}(\mathbf{2})_2]$ to $[Ru^{III}(bpy)_3]$ in phosphate buffer weakly affects the rate of $[Ru^{III}(bpy)_3]$ decomposition. The formal application of

eq **4-14** gives $k_6 < 0.5\ s^{-1}$, which is significantly lower than in borate buffer. Since the activity of **Co_4PPOM** in water oxidation is much lower in phosphate than in borate buffer, the stabilities of the $[Ru^{III}(\mathbf{L})_2]$ complexes were not studied in phosphate buffer.

The dioxygen yield in a light-driven system is strongly dependent on the nature of photosensitizer. Surprisingly, the most stable dye gave the lowest O_2 yield. This indicates that an intramolecular oxidation of the ligand **L** is much slower than intermolecular oxidation by strong oxidants present in solution under turnover conditions. The O_2 yield correlates to some extent with the lifetime of their excited states (**Table 4-1**). The quenching of the excited state $[Ru^{II}(\mathbf{L})_2]^*$ by $S_2O_8^{2-}$ proceeds through bimolecular and more efficient unimolecular pathways, eqs **4-15** to **4-17**.

$$[Ru^{II}(\mathbf{L})_2] + S_2O_8^{2-} \rightleftharpoons \{[Ru^{II}(\mathbf{L})_2]\ldots S_2O_8^{2-}\} \qquad (\mathbf{4\text{-}15})$$

$$[Ru^{II}(\mathbf{L})_2]^* + S_2O_8^{2-} \rightarrow [Ru^{III}(\mathbf{L})_2] + SO_4^{2-} + SO_4^{-\bullet} \qquad (\mathbf{4\text{-}16})$$

$$\{[Ru^{II}(\mathbf{L})_2]\ldots S_2O_8^{2-}\}^* \rightarrow [Ru^{III}(\mathbf{L})_2] + SO_4^{2-} + SO_4^{-\bullet} \qquad (\mathbf{4\text{-}17})$$

The lifetime of $[Ru^{II}(\mathbf{L})_2]^*$ is in the range 73–146 ns and significantly shorter than that of $[Ru^{II}(bpy)_3]^*$ (550 ns). The shorter lifetime results in lower quenching efficiency and lower quantum yield of O_2 formation (Φ_{CY}). In addition, the quenching efficiency for $[Ru^{II}(\mathbf{1})_2]^*$ is lower since the $\{[Ru^{II}(\mathbf{L})_2]\ldots S_2O_8^{2-}\}$ ion pair is less favourable. Consequently, the initial Φ_{CY} for **L** = **2**, **3** or **4** is higher than for **L** = **1**. Since the self-decomposition is slower under turnover conditions, the stability of $[Ru^{III}(\mathbf{L})_2]$ does not affect the final O_2 yield. Interestingly, that the reaction involving the most stable complex $[Ru^{III}(\mathbf{3})_2]$ stops much earlier compared with that involving the least stable

complex $[Ru^{III}(\mathbf{2})_2]$. The sulfate anion radical $SO_4^{-\bullet}$ formed in eqs **4-16** and **4-17** is believed to selectively oxidizes another $[Ru^{II}(\mathbf{L})_2]$ complex to $[Ru^{III}(\mathbf{L})_2]$ ($k = 5\times10^9$ $M^{-1}s^{-1}$ for **L** = bpy).[36] In our case this electron transfer pathway may compete with the reaction of $SO_4^{-\bullet}$ with a ligand **L**. For example, $SO_4^{-\bullet}$ quickly reacts with allylic alcohol and benzene, ~10^9 M^{-1} s^{-1}, but slower with pyridine, ~10^8 M^{-1} s^{-1}.[37] This would result to a faster degradation of $[Ru^{II}(\mathbf{2})_2]$ and $[Ru^{II}(\mathbf{4})_2]$ by $SO_4^{-\bullet}$ than that of $[Ru^{II}(\mathbf{1})_2]$. However, this is not consistent with the data in **Figure 4-3**. Such controversial behaviour is probably related to the oxidation of the ligand **L** by the water oxidation catalyst (WOC). In our system the WOC, namely **Co$_4$PPOM**, is negatively charged and forms strong ion-pairs with $[Ru^{II}(\mathbf{L})_2]$ or $[Ru^{III}(\mathbf{L})_2]$ (eq **4-18**).[38-40]

After removal of four electrons from **Co$_4$PPOM**, the reactive **Co$_4$PPOM**(–4e) intermediate oxidizes water as in eq **4-19**. Being a strong oxidant, this intermediate may also oxidize the ligand **L** as shown in eq **4-20**.

$$Ru(\mathbf{L})_2 + \mathbf{Co_4PPOM}(\text{-4e}) \rightleftharpoons \{Ru(\mathbf{L})_2\ \mathbf{Co_4PPOM}(\text{-4e})\} \qquad (\mathbf{4\text{-}18})$$

$$\{Ru(\mathbf{L})_2\mathbf{Co_4PPOM}(\text{-4e})\} + 2H_2O \rightarrow \{Ru(\mathbf{L})_2\mathbf{Co_4PPOM}\} + O_2 + 4H^+ \qquad (\mathbf{4\text{-}19})$$

$$\{Ru(\mathbf{L})_2\mathbf{Co_4PPOM}(\text{-4e})\} \rightarrow \{Ru(\mathbf{LL'})\mathbf{Co_4PPOM}\} \qquad (\mathbf{4\text{-}20})$$

where **L′** is a product of ligand oxidation. As a result, the O_2 yield is dependent on the competition between the two processes in eqs **4-19** and **4-20**. The factors controlling the ligand **L** by the catalyst are not well understood. Studies with different catalysts are in progress.

4.4 Conclusions

In conclusion, a family of *N*-alkylated derivatives of the complex $[Ru(\mathbf{1})_2]^{2+}$ (**1** = 4'-(4-pyridyl)-2,2':6',2''-terpyridine) has been investigated in conjunction with **Co_4PPOM** for their catalytic water oxidation activity. These $[Ru(\mathbf{L})_2]^{4+}$ complexes (abbreviated "$[Ru^{II}(\mathbf{L})_2]$") have two properties which argue for their use as photosensitizers, namely the longer wavelength absorption and higher oxidation potential, compared to the current standard, $[Ru(bpy)_3]^{2+}$ (abbreviated "$[Ru^{II}(bpy)_3]$"). In water oxidation experiments, complexes incorporating ligands **1** and $\mathbf{5}^+$ were almost inactive with low O_2 yields and a short reaction time. The activities of complexes incorporating ligands $\mathbf{2}^+$, $\mathbf{3}^+$ and $\mathbf{4}^+$ were similar, with $[Ru^{II}(\mathbf{2})_2]$ being the most efficient over a long time scale. $[Ru^{II}(\mathbf{2})_2]$ showed water oxidation activity that was comparable with the current standard photosensitizer, $[Ru^{II}(bpy)_3]$, with a TOF of up to 0.15 s^{-1}, TON of 1×10^2 and a 30% O_2 yield, based on the peroxydisulfate concentration. We propose that the performance of the dye is dependent on oxidizability of **L** by catalyst in high oxidation state. In order to confirm this, the rates of self-decomposition of $[Ru^{III}(\mathbf{L})_2]$ were determined indirectly using a kinetic model. The dye containing ligand **3** wis the most stable to self-decomposition but gives the lowest O_2 yield and the reaction stops much earlier compared with that involving the least stable complex (that with ligand **2**). While the series of complexes is promising in terms of light absorption and higher oxidation potentials, further work needs to be carried out to develop a $[Ru^{II}(\mathbf{L})_2]$ photosensitiser which can generate higher O_2 yields.

References

(1) Lewis, N. S.; Nocera, D. G. *Proc. Natl. Acad. Sci.* **2006**, *103(43)*, 15729.

(2) Chow, J.; Kopp, R. J.; Portney, P. R. *Science* **2003**, *302*, 1528.

(3) Eisenberg, R.; Gray, H. B. *Inorg. Chem.* **2008**, *47*, 1697.

(4) Betley, T. A.; Surendranath, Y.; Childress, M. V.; Alliger, G. E.; Fu, R.; Cummins, C. C.; Nocera, D. G. *Phil. Trans. R. Soc. B* **2008**, *363*, 1293.

(5) Barber, J. *Chem. Soc. Rev.* **2009**, *38*, 185.

(6) Young, K. J.; Martini, L. A.; Milot, R. L.; III, R. C. S.; Batista, V. S.; Schmuttenmaer, C. A.; Crabtree, R. H.; Brudvig, G. W. *Coord. Chem. Rev.* **2012**, *256*, 2503.

(7) Yin, Q.; Tan, J. M.; Besson, C.; Geletii, Y. V.; Musaev, D. G.; Kuznetsov, A. E.; Luo, Z.; Hardcastle, K. I.; Hill, C. L. *Science* **2010**, *328*, 342.

(8) Huang, Z.; Luo, Z.; Geletii, Y. V.; Vickers, J.; Yin, Q.; Wu, D.; Hou, Y.; Ding, Y.; Song, J.; Musaev, D. G.; Hill, C. L.; Lian, T. *J. Am. Chem. Soc.* **2011**, *133*, 2068.

(9) Lv, H.; Geletii, Y. V.; Zhao, C.; Vickers, J. W.; Zhu, G.; Luo, Z.; Song, J.; Lian, T.; Musaev, D. G.; Hill, C. L. *Chem. Soc. Rev.* **2012**, *41*, 7572.

(10) Geletii, Y. V.; Huang, Z.; Hou, Y.; Musaev, D. G.; Lian, T.; Hill, C. L. *J. Am. Chem. Soc.* **2009**, *131*, 7522.

(11) Jiao, F.; Frei, H. *Angew. Chem. Int. Ed.* **2009**, *48*, 1841.

(12) Besson, C.; Huang, Z.; Geletii, Y. V.; Lense, S.; Hardcastle, K. I.; Musaev, D. G.; Lian, T.; Proust, A.; Hill, C. L. *Chem. Commun.* **2010**, 2784.

(13) McCool, N. S.; Robinson, D. M.; Sheats, J. E.; Dismukes, G. C. *J. Am. Chem. Soc.* **2011**, *133*, 11446.

(14) Dressick, W. J.; Meyer, T. J.; Durham, B.; Rillema, D. P. *Inorg. Chem.* **1982**, *21*, 3451.

(15) Durham, B.; Caspar, J. V.; Nagle, J. K.; Meyer, T. J. *J. Am. Chem. Soc.* **1982**, *104*, 4803.

(16) Juris, A.; Balzani, V.; Barigelletti, F.; Campagna, S.; Belser, P.; Zelewsky, A. V. *Coord. Chem. Rev.* **1988**, *84*, 85.

(17) Yonemoto, E. H.; Riley, R. L.; Kim, Y. I.; Atherton, S. J.; Schmehl, R. H.; Mallouk, T. E. *J. Am. Chem. Soc.* **1992**, *114*, 8081.

(18) Nazeeruddin, M. K.; Kay, A.; Rodicio, I.; Humphry-Baker, R.; Müller, E.; Liska, P.; Vlachopoulos, N.; Grätzel, M. *J. Am. Chem. Soc.* **1993**, *115*, 6382.

(19) Grätzel, M. *Nature* **2001**, *414*, 338.

(20) Delgadillo, A.; Arias, M.; Leiva, A. M.; Loeb, B.; Meyer, G. J. *Inorg. Chem.* **2006**, *45*, 5721.

(21) Ardo, S.; Meyer, G. J. *Chem. Soc. Rev.* **2009**, *38*, 115.

(22) Stracke, J. J.; Finke, R. G. *J. Am. Chem. Soc.* **2011**, *133*, 14872.

(23) Stracke, J. J.; Finke, R. G. *ACS Catal.* **2013**, *3*, 1209.

(24) Goberna-Ferrón, S.; Vigara, L.; Soriano-López, J.; Galán-Mascarós, J. R. *Inorg. Chem.* **2012**, *51*, 11707.

(25) Ghosh, P. K.; Brunschwig, B. S.; Chou, M.; Creutz, C.; Sutin, N. *J. Am. Chem. Soc.* **1984**, *106*, 4772.

(26) Constable, E. C.; Devereux, M.; Dunphy, E. L.; Housecroft, C. E.; Rudd, J. A.; Zampese, J. A. *Dalton Trans.* **2011**, *40*, 5505.

(27) Harris Robin, K.; Becker Edwin, D.; Cabral de Menezes Sonia, M.; Goodfellow, R.; Granger, P. In *Pure Appl. Chem.* 2001; Vol. 73, p 1795.

(28) Hoops, S.; Sahle, S.; Gauges, R.; Lee, C.; Pahle, J.; Simus, N.; Singhal, M.; Xu, L.; Mendes, P.; Kummer, U. *Bioinformatics* **2006**, *22*, 3067.

(29) Lv, H.; Song, J.; Geletii, Y. V.; Vickers, J. W.; Sumliner, J. M.; Musaev, D. G.; Kögerler, P.; Zhuk, P. F.; Bacsa, J.; Zhu, G.; Hill, C. L. *J. Am. Chem. Soc.* **2014**, *136*, 9268.

(30) Constable, E. C.; Thompson, A. M. W. C. *J. Chem. Soc., Dalton Trans.* **1994**, 1409.

(31) Constable, E. C.; Dunphy, E. L.; Housecroft, C. E.; Kylberg, W.; Neuburger, M.; Schaffner, S.; Schofield, E. R.; Smith, C. B. *Chem.--Eur. J.* **2006**, *12*, 4600.

(32) White, H. S.; Becker, W. G.; Bard, A. J. *J. Phys. Chem.* **1984**, *88*, 1840.

(33) *CRC Handbook of Chemistry and Physics*; 81st. ed.; Lide, D. R., Ed.; CRC Press: Boca Raton, FL, 2000.

(34) Kaledin, A. L.; Huang, Z.; Yin, Q.; Dunphy, E. L.; Constable, E. C.; Housecroft, C. E.; Geletii, Y. V.; Lian, T.; Hill, C. L.; Musaev, D. G. *J. Phys. Chem. A* **2010**, *114*, 6284.

(35) Brunschwig, B. S.; Chou, M. H.; Creutz, C.; Ghosh, P.; Sutin, N. *J. Am. Chem. Soc.* **1983**, *105*, 4832.

(36) Henbest, K.; Douglas, P.; Garley, M. S.; Mills, A. *J. Photochem. Photobiol. A: Chem.* **1994**, *80*, 299.

(37) Neta, P.; Huie, R. E.; Ross, A. B. *J. Phys. Chem. Ref. Data* **1988**, *17*, 1027.

(38) Ballardini, R.; Gandolfi, M. T.; Balzani, V. *Inorg. Chem.* **1987**, *26*, 862.

(39) Natali, M.; Orlandi, M.; Berardi, S.; Campagna, S.; Bonchio, M.; Sartorel, A.; Scandola, F. *Inorg. Chem.* **2012**, *51*, 7324.

(40) Car, P.-E.; Guttentag, M.; Baldridge, K. K.; Albertoa, R.; Patzke, G. R. *Green Chem.* **2012**, *14*, 1680.

Chapter 5

Differentiating Homogeneous and Heterogeneous Water Oxidation Catalysis: Confirmation that $[Co_4(H_2O)_2(\alpha\text{-}PW_9O_{34})_2]^{10-}$ Is a Molecular Water Oxidation Catalyst

(Published in *J. Am. Chem. Soc.* **2013***, 135,* 14110−14118.)

With James W. Vickers, Jordan M. Sumliner, Guibo Zhu, Zhen Luo, Djamaladdin G. Musaev, Yurii V. Geletii, and Craig L. Hill*

5.1 Introduction

The production of solar fuel is a consensus goal of the research community based on the projected need for enormous quantities of high density energy in the coming decades.[1-3] Central to the production of solar fuels, either by water splitting ($H_2O + h\nu$ (sun) $\rightarrow H_2 + ½ O_2$) or carbon dioxide reduction ($2 CO_2 + 4 H_2O + h\nu$ (sun) $\rightarrow 2 CH_3OH + 3 O_2$) is the oxidation of water. This four-electron process ($2 H_2O \rightarrow O_2 + 4 H^+ + 4 e^-$) continues to be viewed as a central challenge in realizing solar fuel generating prototypes (electron-donor nanostructures, photoelectrochemical cells, etc.).[4-6] As a consequence, there continues to be exceptional research activity aimed at developing viable (fast, selective, stable) both homogeneous[7-25] and heterogeneous[26-41] water oxidation catalysts (WOCs).[31,40,42-49]

Pioneering work has provided criteria for distinguishing homogeneous catalysts from heterogeneous ones, largely for reactions under reducing conditions.[50-52] In continuation with this, we sought to develop a series of new experiments which can be used to not only differentiate a homogeneous catalyst from a heterogeneous one under oxidizing conditions, but also to distinguish particular molecular species generated in solution during turnover. Furthermore, these techniques can rule out activity from decomposition products which are known catalysts and show which species is responsible for the observed catalytic activity. These studies can be divided into two categories: (1) those quantifying the amount of catalyst decomposition during catalytic turnover or the amount of some decomposition product that could be involved in catalysis, and (2) those assessing the kinetic behavior of each catalytically competent species as a function of the reaction variables. For reactions in aqueous media, these variables include pH, buffer and buffer concentration. The combined knowledge of the quantities and kinetic behaviors of

potential catalytic species provides a complete picture of which species is responsible for observed catalytic activity, in this case, but not limited to water oxidation.

Table 5-1 Experimental conditions from various studies examining catalytic activity and stability of **Co_4PPOM**.

SF	SSB	HG Science	HG JACS	This Work
Electrochemical 1.1 V *versus* Ag/AgCl	Nanosecond Flash Photolysis	Dark(stoichiom -etric oxidant)	Photochemical 420-470 nm Xe lamp 16.8 mW	Photochemical 455 nm LED 17 mW
pH = 8.0 100 mM NaP_i 500 µM **Co_4PPOM**	pH = 8.0 80 mM NaP_i 50 µM **Co_4PPOM** 0.05 mM $[Ru(bpy)_3]^{2+}$ 5.0 mM $Na_2S_2O_8$	pH = 8.0 30 mM NaP_i 3.2 µM **Co_4PPOM** 1.5 mM $[Ru(bpy)_3]^{3+}$	pH = 8.0 80 mM NaB_i 5 µM **Co_4PPOM** 1.0 mM $[Ru(bpy)_3]^{2+}$ 5.0 mM $Na_2S_2O_8$	pH = 8.0 80 mM NaB_i 2 µM **Co_4PPOM** 1.0 mM $[Ru(bpy)_3]^{2+}$ 5.0 mM $Na_2S_2O_8$
TON calculated as 0.363	O_2 not measured	TON = 78.1	TON = 224	TON = 302 ± 1

One of the most promising classes of WOCs are polyoxometalates (POMs) because of their oxidative, thermal and tendency towards kinetic hydrolytic (over pH ranges dictated by the POM metal) stability. Some of these systems are among the fastest WOCs available to date.[53-55] Recently, several groups have reported POM WOCs based on abundant 3d elements (Co and Ni)[56-59] in addition to earlier Ru-containing POM WOCs.[60-64] After publication of the first precious-metal-free POM WOC, $[Co_4(H_2O)_2(PW_9O_{34})_2]^{10-}$ (**Co_4PPOM**) in 2010 (henceforth "HG"),[65-66] its stability, as well as the nature of the active species became the subject of multiple investigations under a range of experimental conditions (**Table 5-1**).

The initial claim of a fast, stable, molecular WOC was first brought into question by Stracke and Finke (Stracke and Finke, *J. Am. Chem. Soc.*, **2011**, *133*, 14872, henceforth "SF") who in electrochemical experiments, demonstrated that, the activity of **Co_4PPOM** could be explained by the formation of CoO_x films on the electrode surface. Another group (Scandola, Sartorel, Bonchio et al., *Chem. Commun*., **2012**, *48*, 8808, henceforth "SSB") studied **Co_4PPOM** by nanosecond flash photolysis experiments suggesting that the catalyst was a soluble molecular species, but that it was not **Co_4PPOM**. These three studies report on the WOC activity of **Co_4PPOM** in different systems using different techniques and draw conflicting conclusions. A follow-up paper by SF has revisited their previous work.[67] While **Co_4PPOM** has been well documented to be hydrolytically unstable above pH 7.5-8.0 in sodium phosphate buffer,[68-70] its kinetic stability under water oxidation conditions remains a subject of debate. A recent review noted a general need to address in detail the fate of **Co_4PPOM** under a variety of conditions.[71] Thus **Co_4PPOM** is a prime example of a system where there is need to differentiate an initial molecular catalyst from its various possible decomposition products which are also known catalysts.

5.2 Experimental

5.2.1. General Methods and Materials

$[Ru(bpy)_3]Cl_2.H_2O$, sodium peroxydisulfate, and all other chemicals were of the highest purity available from commercial sources. $[Ru(bpy)_3]Cl_2 \cdot H_2O$ was recrystallized from 5 mL DI-water before use and $[Ru(bpy)_3](ClO_4)_3$ was prepared as previously reported.[72] Electronic absorption spectra were recorded using Agilent 8453 spectrophotometer. Infrared spectra (2 % sample in KBr pellet) were recorded with a Nicolet TM 6700 FTIR

spectrometer. The fast reactions were studied using a Hi-Tech KinetAsyst Stopped Flow SF-61SX2 instrument equipped with a diode array detector operating in wavelength range 400-700 nm.

5.2.2. Synthesis of Co_4PPOM from Δ-PW_9O_{34} and Co^{2+} in Borate Buffer

An additional experiment was conducted to show that $[Co_4(H_2O)_2(PW_9O_{34})_2]^{10-}$ (**Co_4PPOM**) can form kinetically even under conditions where it is not fully stable hydrolytically. Specifically we successfully prepared **Co_4PPOM** in borate buffer solution as follows: $Na_9[A\text{-}PW_9O_{34}]\cdot 4H_2O$ was synthesized according to the published method.[73] The B-type or Δ-PW_9O_{34} was prepared by baking the dried solid of A-PW_9O_{34} at 140 °C for 6 hours.[66] A 116 mg sample of $Co(NO_3)_2\cdot 6H_2O$ was dissolved in 10 mL of borate buffer (0.1 M, pH 8) solution, and then 0.5 g of Δ-PW_9O_{34} was added in small portions with gentle stirring. The mixture was heated to 80 °C until a homogeneous purple solution was obtained, and then it was kept at 80 °C for an additional 10 min. Slow evaporation at room temperature resulted in 0.3 g (54.5% yield) of purple crystalline solid after about 5 days. X-ray crystallography was used to solve the crystal structure of the resulting product and its purity was checked by FT-IR and EA as in previous work.[65]

5.2.3. Electrochemical Synthesis of CoO_x

Authentic CoO_x was prepared by anodic deposition on fluorine doped tin oxide (FTO), (TEC-15 Hartford Glass Co.) at 1 V (vs Ag/AgCl, 3M NaCl) from 0.5 mM $Co(NO_3)_2 \cdot 6H_2O$ in 0.1 M pH 7 sodium phosphate buffer solution as previously described.[30] CoO_x was dried in air and then removed from the FTO electrode with a razor blade. Typically, 2-3 mg of CoO_x was formed during electrolysis. The CoO_x powder was suspended in water and sonicated for 10 minutess before doing a catalytic reaction.

5.2.4. Catalytic Light-Driven Water Oxidation

Light-induced water oxidation was carried out in the cylindrical quartz optical cell (NSG, 32G10) with a 1-cm optical path length, an outer diameter 22 mm, and total volume ~ 2.8 mL equipped with standard taper joint. In a typical reaction, the vessel was filled with 2 mL of a solution with the desired concentrations of $[Ru(bpy)_3]Cl_2$, $Na_2S_2O_8$, catalyst, and sodium borate or phosphate buffer. The vessel was then sealed with a rubber septum and carefully purged with Ar. The headspace was checked by gas chromatography (GC) to confirm the absence of O_2 before the experiment. All procedures were performed with a minimum exposure to ambient light. The reaction was initiated by turning on the LED light source (LLS) equipped with a 455-nm LED. A light beam with a diameter 0.4-0.5 cm and 17 mW power was focused on the flat front of the reaction vessel using two lenses. The power of the light source was measured using a laser power meter Molectron, model Max 500A. The solution was agitated by a magnetic stirring bar spinning vertically on the back side of the cell. After the desired illumination time, the reaction was temporarily stopped by blocking the light. The O_2-yield was quantified by GC as described previously.[74] The reusability test has been done as follows: after completion of the first reaction cycle, the same amount of NaS_2O_8, 2.38 mg, was added for the second run. The reaction was run with an initial buffer concentration of 120 mM such that the buffer capacity is not depleted over the second run but decreases O_2 yield.

5.2.5. Chemical Water Oxidation Kinetics Monitored by Stopped-Flow

One of the feeding syringes was filled with $[Ru(bpy)_3]^{3+}$ solution and the other with a freshly prepared solution of the catalyst in buffer. The $[Ru(bpy)_3]^{3+}$ solution was prepared in 0.1 mM HCl and filtered before use. Each data set included 200 spectra collected with

different timescales: from 0-0.4 s up to 0-400 s. Typically, the consumption of $[Ru(bpy)_3]^{3+}$ was followed by a decrease in absorbance at 670 nm ($\varepsilon_{670} = 4.2\times10^2$ $M^{-1}cm^{-1}$) with optical path length l = 10 mm. The data were acquired and treated using KinetAsyst™ 3.0 software.

5.2.6. Cathodic Adsorptive Stripping Voltammetry

Cathodic adsorptive stripping voltammetry was performed with slight modifications to the literature method.[75] A bismuth film glassy carbon electrode was prepared by applying a -0.25 V potential (vs Ag/AgCl (3M NaCl, BASi) for 45 s, using the clean electrode function in the software, while stirring, to a 1 M HCl solution containing 0.02 M $Bi(NO_3)_3$•$5H_2O$ and 0.5 M LiBr. The electrode was then rinsed with water and immediately immersed into a solution containing the desired buffer and 0.1 mM dimethylglyoxime (DMG). Differential pulse voltammetry (DPV) was then performed with the following parameters: Accumulation occurred at -0.7 V, for 60 s with stirring at 300 rpm, followed by a quiet period without stirring for 15 s. The voltammogram was then recorded from -0.7 V to -1.3 V at ν = 10 mV/s, a pulse potential = 50 mV and step potential = 2 mV. Calibration curves using $Co(NO_3)_2$•$6H_2O$ as the source of Co^{2+}(aq) were prepared for NaP_i (**Figure 5-1**) and borate (**Figure 5-2**) buffers to reduce possible interference effects from the buffer. In all cases, the peak current (i_p) was used to determine the concentration of Co^{2+}(aq) present. The dissociated Co^{2+}(aq) from **Co_4PPOM** was measured by the above differential pulse voltammetry (DPV) method. **Co_4PPOM** was aged in the desired buffer, and then a 1.5 mL aliquot of this solution was added to 1.5 mL of the same buffer containing 0.1 mM DMG. DPV was immediately performed as described above. The concentration determined from the calibration curve

was then multiplied by 2 to account for dilution. Complete results are presented below in **Table 5-2**.

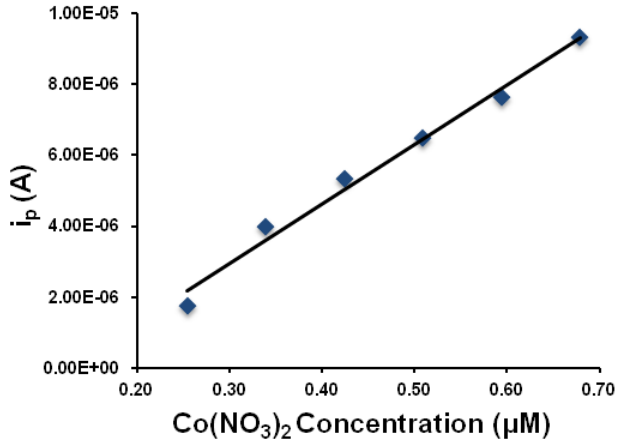

Figure 5-1 CAdSV NaP_i buffer calibration curve. Cathodic adsorptive stripping voltammetry with bismuth film glassy carbon electrode and 0.1 mM DMG. Voltammogram peak current (i_p) recorded from -0.7 V to -1.3 V at ν = 10 mV/s, pulse potential = 50 mV and step potential = 2 mV. With $Co(NO_3)_2$ in NaP_i buffer. $R^2 = 0.9871$.

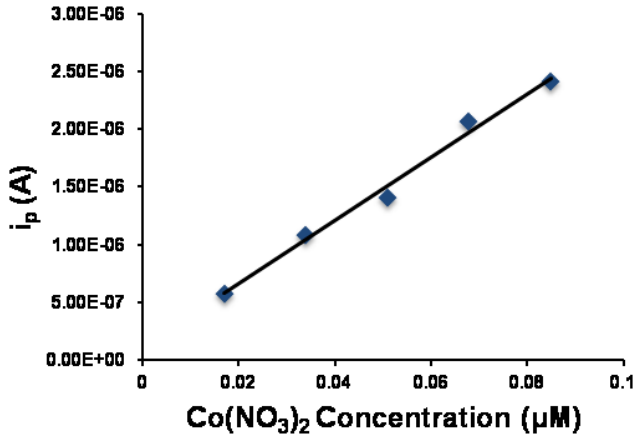

Figure 5-2 CAdSV borate buffer calibration curve. Cathodic adsorptive stripping voltammetry with bismuth film glassy carbon electrode and 0.1 mM DMG. Voltammogram peak current (i_p) recorded from -0.7 V to -1.3 V at ν = 10 mV/s, pulse potential = 50 mV and step potential = 2 mV. With $Co(NO_3)_2$ in borate buffer. $R^2 = 0.9899$.

Table 5-2 Cathodic adsorptive stripping voltammetry for quantification of Co^{2+}(aq) from aged **Co_4PPOM**, in buffer at pH 8.

Entry	[**Co_4PPOM**] (μM)	Buffer type, pH, concentration (mM)	Aging time in buffer (h)	[Co^{2+}(aq)], (μM)	Reference
1	2	NaB_i, 8, 80	3	0.07 ± 0.01	This work
2	2	NaP_i, 8, 80	3	0.54 ± 0.04	This work
3	2.5	NaP_i, 8, 100	1	0.25 ± 0.06	SF ACS Catalysis[67]
4	500	NaP_i, 8, 80	3	56 ± 2	SF JACS[76]

Conditions: Bismuth film glassy carbon electrode and 0.1 mM DMG. Voltammogram peak current (i_p) recorded from -0.7 V to -1.3 V at ν = 10 mV/s, pulse potential = 50 mV and step potential = 2 mV. With **Co_4PPOM** in buffer R^2 = 0.9899.

5.2.7. Synthesis of Tetraheptylammonium Nitrate ($THpANO_3$) and Extraction of Co_4PPOM from Post-Reaction Solution

The $THpANO_3$ was synthesized from the reaction of tetra-*n*-heptylammonium bromide (THpABr) with $AgNO_3$. Typically, an aqueous solution (10 mL of H_2O) of $AgNO_3$ (40 mg) was added to a solution of THpABr (110 mg) in toluene. The resulting mixture was shaken vigorously forming light yellow AgBr. The colorless organic layer was filtered to remove AgBr precipitate before use. The catalyst **Co_4PPOM** was extracted from the post-reaction solution using the resulting solution of $THpANO_3$ in toluene. The **Co_4PPOM**-free reaction solution was then recharged with 2.4 mg $Na_2S_2O_8$ before repeating the light-driven water oxidation reaction. A control experiment was conducted to ensure that the extraction did not in itself affect the O_2 yield. The extraction procedure was conducted to the buffer solution before the catalyst was added, solid **Co_4PPOM** was added and the reaction was conducted as normal.

5.2.8. Inductively Coupled Plasma Mass Spectrometry

Inductively coupled plasma mass spectrometry was performed by Galbraith Laboratories, Inc. (Knoxville, TN, USA) with a Perkin Elmer Sciex Elan 6100 ICP Mass Spectrometer. Samples were diluted as needed, then introduced to the instrument via peristaltic pump and cross flow II nebulizer. Samples were prepared as above for catalytic light-driven water oxidation. They were allowed to age for the desired time before the extraction procedure was performed as above. The remaining solution was then submitted for analysis. **Table 5-3** summarizes the complete results for these experiments.

Table 5-3 Inductively coupled plasma mass spectrometry for solution with **Co_4PPOM**, in buffer at pH 8 aged as noted.

Entry	**Co_4PPOM** (μM)	Aging time (h)	Buffer	Co after extraction (μM)
1	500	16	0.1 M NaB_i	18 ± 1
2	500	16	0.1 M NaP_i	93 ± 5
3	2	3	0.08 M NaB_i	0.07 ± 0.01
4	2	3	0.08 M NaP_i	0.44 ± 0.02

5.2.9. Dynamic Light Scattering

Reaction solutions were prepared as in standard catalytic light driven procedure. Buffer solution was filtered prior to addition of reagents. Spectra were collected on a Zetasizer Nano ZS 90 instrument (Malvern Instruments Ltd, UK) after one run. The particle sizes suitable for measurement by this instrument range from 0.3 to 5000 nm (diameter) with a limit of detection (LoD) of 0.1 ppm. As mentioned in previous work, the concentration of the catalyst and $[Ru(bpy)_3]Cl_2$ is limited by the formation of an insoluble adduct between **Co_4PPOM** and $[Ru(bpy)_3]^{2+}$. To quantify at what concentration an appreciable amount of this complex forms, DLS was used. To a solution containing 1.0 mM $[Ru(bpy)_3]^{2+}$, 5.0

mM $Na_2S_2O_8$ in 80 mM borate buffers filtered through a Millipore Millex-FX Phobic PTFE 0.45 μm syringe filter was added aliquots of 1.0 mM **Co_4PPOM** in water. Resulting solution was analyzed by DLS for particles above the limit of detection (**Figure 5-3**).

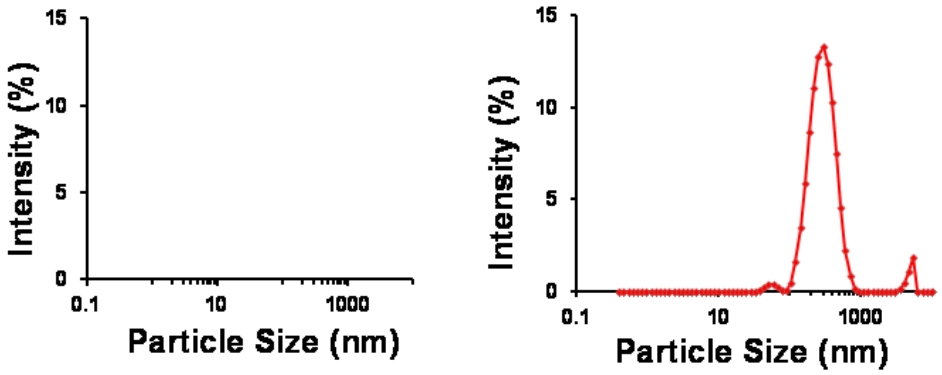

Figure 5-3 Particle size distribution (intensity %) obtained from dynamic light scattering measurement for solutions containing 1 mM $Ru(bpy)_3^{2+}$ in 80 mM NaB_i (pH = 8), 5.0 mM $Na_2S_2O_8$, with added **Co_4PPOM**. Amount added < 5.5 μM **Co_4PPOM** (left) or ≥ 5.5 μM **Co_4PPOM** (right).

5.2.10. Co_4PPOM Decomposition

Solutions of **Co_4PPOM** were dissolved in desired buffer solution and the electronic spectra were collected in a quartz cuvette (1 or 10 cm path length). Solutions were filtered prior to use. Absorbance at 579 nm was corrected by subtracting the absorbance at 800 nm. To correctly interpret the kinetics of decomposition of **Co_4PPOM** (measured as the decrease in absorbance at 580 nm, **Figure 5-4**), it is necessary to take into account the spectra of decomposition products which may overlap with the **Co_4PPOM** spectrum, and change the observed spectral shape. No such changes were observed (**Figure 5-5**) after aging for 10 minutes under conditions in **Figure 5-4**. To increase the reaction conversion in order to obtain sufficient decomposition for quantification by UV-Vis we aged the solutions of 0.5 mM **Co_4PPOM** in 80 mM borate buffer (pH 8) at 60 °C for 10

hours. The initial and final spectra (after correction for the base line) are presented in **Figure 5-6**. The analysis of these spectra showed that decomposition products absorb light in the range 450-550 nm and the contribution of Co^{2+}(aq) is negligibly small. Thus, the decrease in absorbance at 580 nm can be safely assigned to the decrease of **Co_4PPOM** concentration (ε_{580} = 170±10 $M^{-1}cm^{-1}$).

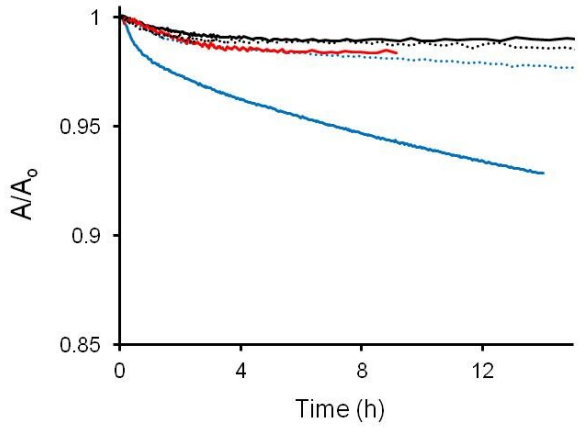

Figure 5-4 Normalized peak absorbance at 580 nm of **Co_4PPOM** as a function of time. Conditions: 0.5 mM **Co_4PPOM** in 0.03 and 0.1 M NaP_i (blue dotted and solid lines, respectively), in 0.1 M sodium borate buffer 0.45 and 0.8 mM **Co_4PPOM** at pH 8 and 9 (black solid and dotted lines, respectively); 1.15 mM **Co_4PPOM** in 0.05 M CAPS buffer at pH 10 (red); 25 ºC.

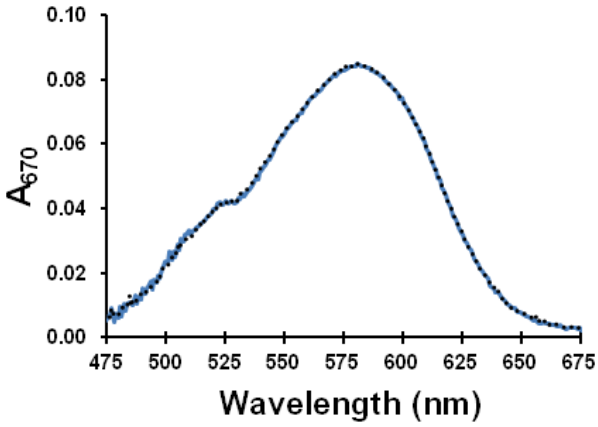

Figure 5-5 Stopped flow mixing of 80 mM sodium phosphate buffer at pH 8.0 (final concentration 40 mM), and 1000 µM **Co_4PPOM** in water (final concentration 500 µM) at 25 °C. Blue, initial spectrum; black dashed, after 10 minutes.

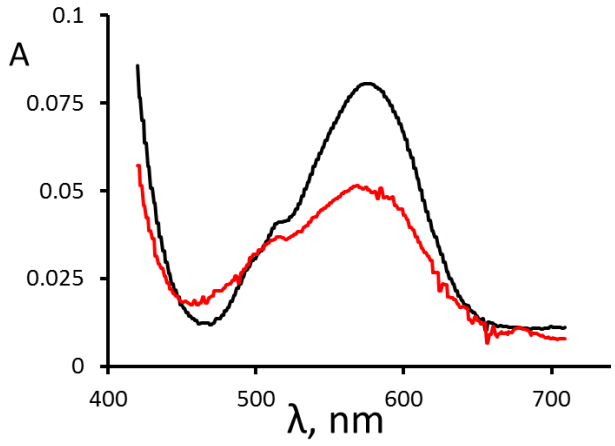

Figure 5-6 The spectra of 0.5 mM **Co_4PPOM** in 80 mM borate buffer at pH 8.0 before (black) and after 10 hours aging (red) at 60 °C.

5.3 Results and Discussion

5.3.1. Quantification of Active Species Leached from the Initial Molecular Catalyst

Cobalt oxides (henceforth "CoO_x") and aqueous cobalt ions are the simplest and most likely decomposition products of **Co_4PPOM** and are known WOCs.[29,30,72] Thus it was important to test the hypothesis that some cobalt containing species (henceforth "Co_{app}") or cobalt oxides, in amounts that have been shown to be present, might be able to account for the O_2 yields we observe. The results herein show that they cannot.

The first step in examining whether decomposition products of **Co_4PPOM** are able to account for the observed catalysis is quantifying the amount of decomposition and the decomposition products formed. To this end two techniques have been developed. We conducted an analysis showing quantitatively that the maximum amount of Co_{app} present in solutions of **Co_4PPOM** and the equivalent quantity of CoO_x formed from this Co_{app} do not account for the observed catalytic water oxidation rates. Previous work[76] estimated

decomposition based on the decrease in absorbance at 580 nm from a solution of **Co_4PPOM**. Due to the low molar absorptivity of **Co_4PPOM**, high concentrations (≥500 μM) are required to obtain a sufficient absorbance. However, these experimental conditions do not convincingly reflect conditions where **Co_4PPOM** was reported to be catalytically active (~5 μM; a complete listing of the vary different studies are given in **Table 5-1**). To more accurately quantify the amount of Co_{app} present in solution when **Co_4PPOM** is aged in catalytic conditions (low concentrations), cathodic adsorptive stripping voltammetry (CAdSV), a technique first applied to these systems by SF,[76] was used (see Experimental section). This technique has been reported to determine the amount of Co_{app} in a high **Co_4PPOM** concentration sodium phosphate buffered (NaP_i) system,[76] as well as at 2.5 μM in the same buffer,[67] released as a function of aging time. After aging 2 μM of **Co_4PPOM** in 80 mM pH 8 borate buffer for 3 h, the concentration of Co_{app} was found to be 0.07 ± 0.01 μM. Complete results are listed in **Table 5-2**.

A second new and general method to address catalysis by soluble molecular species (POMs or otherwise) versus insoluble metal oxides or soluble hydrated metal cations as catalysts for reactions in aqueous solution has been devised and is reported here for the first time. This method is a two-step process where a soluble, anionic catalyst is separated from solution containing all species present during turnover, then the remaining cobalt containing species (Co_{app}) in solution are quantified. Here, a toluene solution of tetra-*n*-heptylammonium nitrate ($THpANO_3$) is used to extract **Co_4PPOM** from the aqueous layer. $THpA^+$ is well known to quantitatively extract most POMs from the aqueous phase to a second toluene phase.[77] This extraction technique was applied to the aqueous solution of **Co_4PPOM** after light-driven catalytic water oxidation and this removal of

Co_4PPOM effectively stops catalysis decreasing catalytic water oxidation by ~ 98 %, (**Figure 5-7**, green triangles). Control experiments show that neither the extraction method nor the presence of residual toluene or $THpA^+$ significantly affect catalysis by Co^{2+}(aq), or CoO_x (**Figure 5-8**). Catalysis of **Co_4PPOM** is also not significantly affected by residual toluene or $THpA^+$ (**Figure 5-7**, red open squares). Extraction of **Co_4PPOM** before catalytic reaction reduces the O_2 yield to effectively zero.

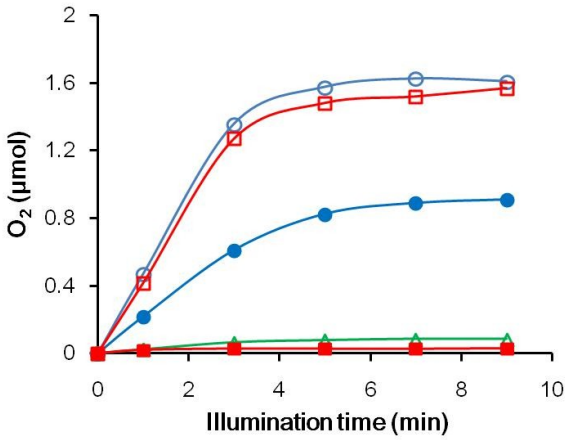

Figure 5-7 Kinetics of light-driven catalytic O_2 evolution from water catalyzed by **Co_4PPOM** in 0.12 M borate buffer at pH 8. Conditions: 455 nm LED light (17 mW, beam diameter ~ 0.5 cm), 5.0 mM $Na_2S_2O_8$, 1.0 mM $[Ru(bpy)_3]Cl_2$. Blue open circles, 2 µM **Co_4PPOM** initial run; blue solid circles, 2 µM **Co_4PPOM** second run; red solid squares, extraction of the 2 µM **Co_4PPOM** solution in borate buffer with a toluene solution of $THpANO_3$, followed by addition of $[Ru(bpy)_3]Cl_2$ and $Na_2S_2O_8$; green triangles, the aqueous catalyst solution after the first run followed by extraction using a toluene solution of $THpANO_3$; red open squares, control reaction where 2 µM **Co_4PPOM** solution in borate buffer extracted by a toluene solution of $THpANO_3$, followed by addition of 2 µM **Co_4PPOM**, $[Ru(bpy)_3]Cl_2$ and $Na_2S_2O_8$.

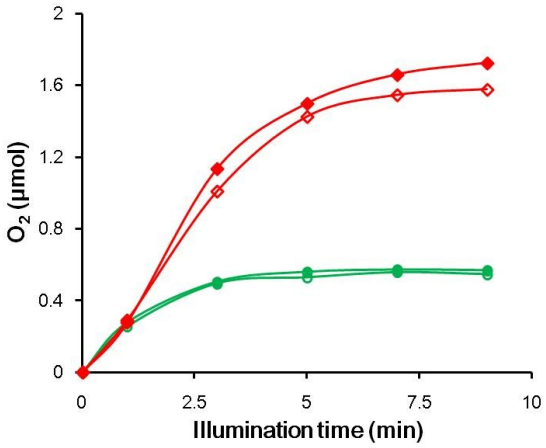

Figure 5-8 Kinetics of light-driven catalytic O_2 evolution from water catalyzed by CoO_x and $Co(NO_3)_2$ in 0.12 M borate buffer at pH 8. Conditions: 455 nm LED light (17 mW, beam diameter ~0.5 cm), 5.0 mM $Na_2S_2O_8$, 1.0 mM $[Ru(bpy)_3]Cl_2$. Red solid diamonds: 2 µM $Co(NO_3)_2$ initial run. Red empty diamonds: control reaction where 2 µM $Co(NO_3)_2$ solution in borate buffer extracted by a toluene solution of $THpANO_3$, followed by addition of $[Ru(bpy)_3]Cl_2$ and $Na_2S_2O_8$; Green solid circles: CoO_x (containing 8 µM equivalents of Co^{2+}) initial run. Green empty circles: control reaction where CoO_x suspension in borate buffer extracted by a toluene solution of $THpANO_3$, followed by addition of 2 µM **Co_4PPOM**, $[Ru(bpy)_3]Cl_2$ and $Na_2S_2O_8$.

After extraction of **Co_4PPOM** from solutions aged in buffer, inductively coupled plasma mass spectrometry (ICP-MS) was performed to quantify the amount of Co_{app}. Aging 2 µM of **Co_4PPOM** in 80 mM pH 8 sodium borate buffer (NaB_i) for 3 h, followed by the extraction technique, yielded a concentration of Co_{app} at 0.07 ± 0.01 µM remaining in the reaction solution, exactly as was found by CAdSV above. Complete results and the procedure is reported in **Table 5-3**.

In order to gauge the catalytic role of the quantified cobalt containing species, water oxidation was conducted either by a dark reaction where the reaction kinetics are monitored by a decrease in absorbance of the sacrificial oxidant tris(bipyridine)ruthenium(III) perchlorate ($[Ru(bpy)_3](ClO_4)_3$), or a photochemical method whereby O_2 is monitored by gas chromatography (GC) using $[Ru(bpy)_3]Cl_2$ as a

photosensitizer and $Na_2S_2O_8$ as a sacrificial electron acceptor with visible light. Both methods were previously reported[65,74] and are fully elaborated in the Experimental section. To show that ~ 0.07 μM Co_{app} could not account for the observed catalytic activity, several control experiments were conducted. Addition of 0.10 μM $Co(NO_3)_2$ (approximating Co_{app} as in SF, more than doubling the amount) to a buffered solution of 2 μM **Co_4PPOM** (more than doubling the amount of Co_{app}) produces less than 5 % increase in the overall rate of $[Ru(bpy)_3]^{3+}$ reduction (dark reaction): compare the blue dashed curve in **Figure 5-9** and the red solid curve which has no added $Co(NO_3)_2$.

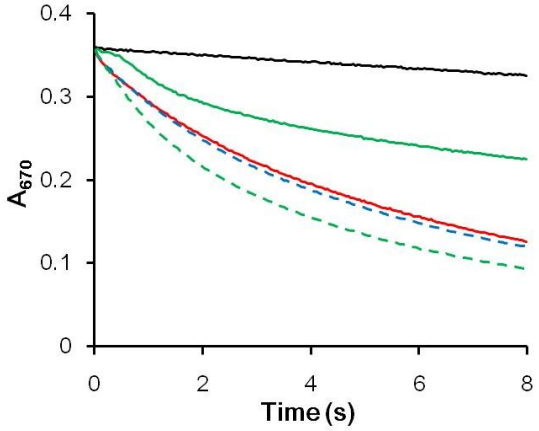

Figure 5-9 Kinetics of $[Ru(bpy)_3]^{3+}$ reduction in 80 mM sodium borate buffer at pH 8.0 and 25 °C, measured as the decrease in absorbance at 670 nm: No catalyst (black), 2.0 μM **Co_4PPOM** (red), 0.5 μM $Co(NO_3)_2$ (green), 2.0 μM **Co_4PPOM** in the presence of 0.10 μM $Co(NO_3)_2$ (blue dashed), 2.0 μM **Co_4PPOM** in the presence of 0.50 μM $Co(NO_3)_2$ (green dashed).

Similar results were obtained under photochemical conditions, where water oxidation by 0.15 μM $Co(NO_3)_2$, twice the amount found to be present by both techniques, gives a negligible O_2 yield and addition of 0.15 μM $Co(NO_3)_2$ to 2 μM **Co_4PPOM** shows no effect on the kinetics or yield of oxygen evolution (**Figure 5-10**). Furthermore, increasing the concentration of the added $Co(NO_3)_2$ to 0.5 μM (green dashed curve) increases the overall rate of the reaction by ~ 15 %. Thus, the concentration of $Co(NO_3)_2$ can be made

so great that it effects the catalysis, but even at this elevated level, seven times higher than what is found to exist, the majority of catalysis still derives from **Co_4PPOM**.

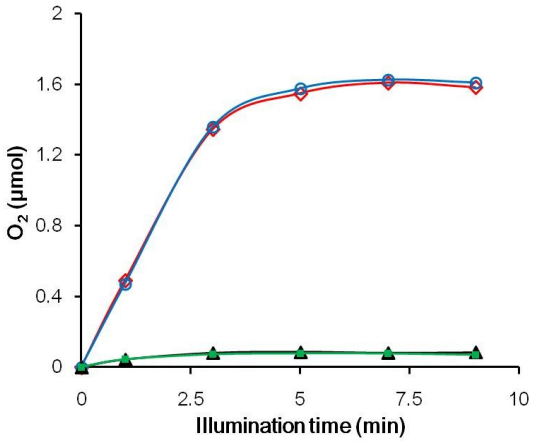

Figure 5-10 Kinetics of light-driven catalytic O_2 evolution from water catalyzed by **Co_4PPOM** and $Co(NO_3)_2$. Conditions: 455 nm LED light (17 mW, beam diameter ~ 0.5 cm), 5.0 mM $Na_2S_2O_8$, 1.0 mM $[Ru(bpy)_3]Cl_2$. 2.0 µM **Co_4PPOM** (blue) , 2.0 µM **Co_4PPOM** + 0.15 µM $Co(NO_3)_2$ (red), 0.15 µM $Co(NO_3)_2$ (black) all in 120 mM borate buffer, and 0.15 µM $Co(NO_3)_2$ (green) in 80 mM borate buffer. Initial pH = 8.0, total volume 2.0 mL.

5.3.2. Behavioral Distinction Between A Molecular Catalyst and Decomposition Product Catalysts

Examining behavioral differences between each catalytically competent species under specific conditions provides further evidence to differentiate **Co_4PPOM** from Co_{app}, CoO_x, or other possible decomposition products. By analyzing differences in the kinetics of the dark reaction or the yields of the photochemical reaction, when changing only a single variable of the conditions, we can determine the identity of the catalytically active species. Several additional control experiments to compare the catalytic behavior of freshly prepared and aged solutions of **Co_4PPOM** and $Co(NO_3)_2$ were performed. First, it has been established that these two species have quite different time profiles for O_2 formation *and* $[Ru(bpy)_3]^{3+}$ reduction. Similar findings were reported for the kinetics of Co^{2+}(aq) as a WOC.[78] Second, it was confirmed, that water oxidation by $Co(NO_3)_2$

exhibits an induction period, as observed by a characteristic sigmoidal-shape (green curve, **Figure 5-9**), indicating that the initial $Co(NO_3)_2$ is a precursor of a catalytically active species. In contrast **Co_4PPOM** shows no induction period (red solid and blue dashed curve **Figure 5-9**, **Figure 5-11**, and **Figure 5-12**).

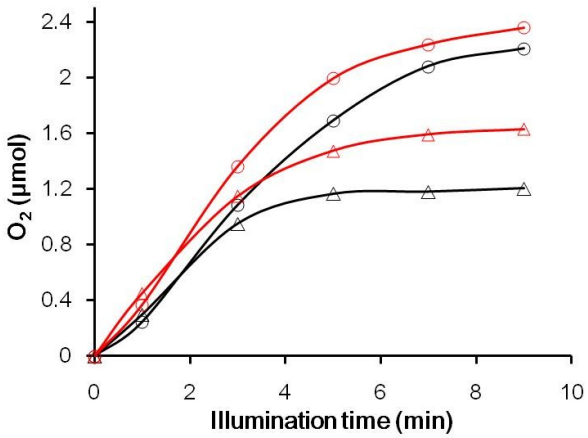

Figure 5-11 The kinetics of O_2 formation catalyzed by 2 µM **Co_4PPOM** (Δ) or 2 µM $Co(NO_3)_2$ (○) in 80 mM borate buffers (black curves at pH 8 and red curves at pH 9). Conditions: 455 nm LED-light beam with OD ≈ 0.4-0.5 cm and 17 mW was focused on the flat front wall of the reaction vessel; 1.0 mM $[Ru(bpy)_3]^{2+}$, 5.0 mM $Na_2S_2O_8$.

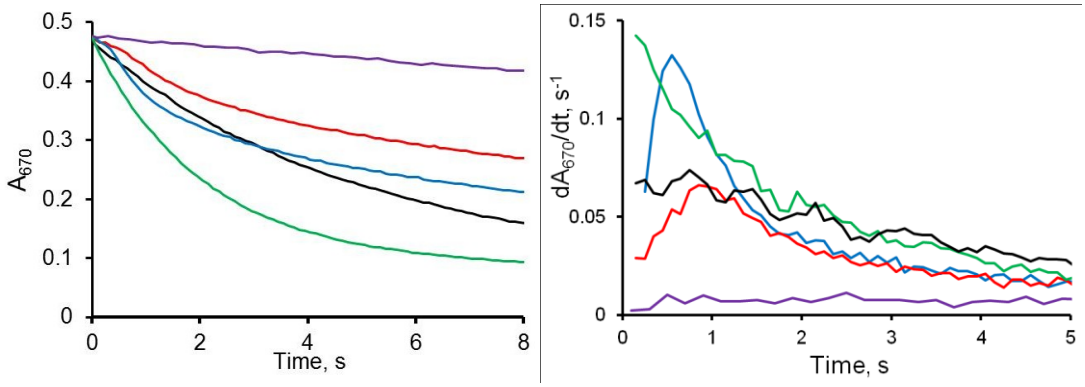

Figure 5-12 Left panel: stopped flow kinetics of catalytic $[Ru(bpy)_3]^{3+}$ reduction in 80 mM sodium borate buffer at pH 8.0 and 25 °C: No catalyst (magenta), 1 and 3 µM **Co_4PPOM** (black and green, respectively), 0.5 and 1.0 µM $Co(NO_3)_2$ (red and blue, respectively). Right panel: the rate of catalytic $[Ru(bpy)_3]^{3+}$ reduction as a function of time in 80 mM sodium borate buffer at pH 8.0 and 25 °C: No catalyst (magenta), 1 and 3 µM **Co_4PPOM** (black and green respectively), 0.5 and 1.0 µM $Co(NO_3)_2$ (red and blue, respectively).

Third, the pH dependence of **Co_4PPOM** and other species were compared. In general, different pH dependencies of O_2 yields are consistent with the presence of different catalytically active species during turnover. Therefore, the response of a catalytic system to pH change can and should be used to probe the nature of the catalyst in aqueous media. Here, the pH dependence of O_2 yields for **Co_4PPOM**, Co^{2+}(aq) and CoO_x catalysts were compared. As seen in **Table 5-4**, the activity of **Co_4PPOM** strongly depends on pH: lines 10 and 11 show that when the pH is increased from 7.2 to 8.0, with all other conditions held constant, the yield increases by over an order of magnitude. In contrast, the O_2 yield from both $Co(NO_3)_2$ and CoO_x is weakly dependent on pH: under the same conditions the yields increase only about two- and three-fold respectively. The different dependences on pH provide further evidence that the catalytic activity observed from **Co_4PPOM** is not due to either Co^{2+}(aq) or CoO_x.

Fourth, the behavioral dependence in different buffers was studied. The overall rate of **Co_4PPOM** loss is faster in phosphate buffer than in borate as seen in high concentrations quantified by UV-Vis (**Figure 5-4**). The decrease in absorbance is also slower in the presence of CAPS buffer, where **Co_4PPOM** shows only slight decomposition even at pH 10.[69] The amount of Co_{app} quantified by ICP-MS and CAdSV at lower, catalytic conditions corroborates this relationship (over six-fold greater [Co_{app}] for both techniques in NaP_i over NaB_i, **Tables 5-2** and **5-3**). The effect of aging **Co_4PPOM** solutions in buffer on the catalytic activity under HG conditions was also examined. Data show that the kinetic curves for reduction of 0.83 mM $[Ru(bpy)_3]^{3+}$ by 2 μM **Co_4PPOM** are nearly identical for both freshly prepared and 1.5 h-aged solutions in 0.1 M phosphate or borate buffer at pH 8.0 suggesting that any Co_{app} has little effect on catalytic activity (**Figure 5-**

13). The photochemical reactions give similar results where the catalytic solutions in both NaB_i and NaP_i show only a minimal decrease in turnover number (TON) after several hours aging (entries 2 and 3, 6 and 7 respectively).

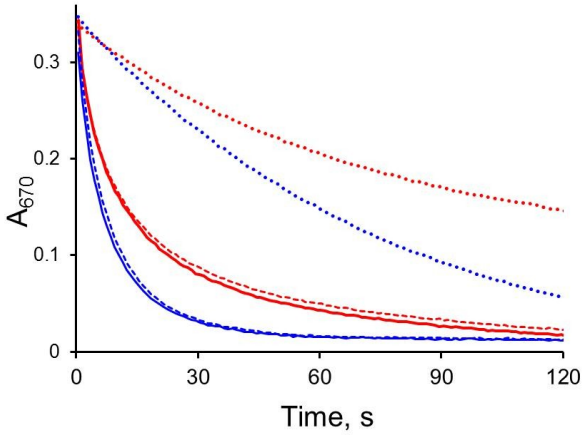

Figure 5-13 The reduction of 0.83 mM $[Ru(bpy)_3]^{3+}$ catalyzed by 5 μM **Co_4PPOM** freshly prepared (solid lines) and aged in buffer solutions for 1.5 h (dashed lines): 0.1 M sodium phosphate (red lines) or borate buffer (blue lines) at pH 8. The self-decomposition of $[Ru(bpy)_3]^{3+}$ in the absence of the **Co_4PPOM** is in phosphate and borate (red and blue dotted lines respectively).

In addition to the depen[79]dence on the nature of the buffer, the concentration of the buffer was also investigated as a fifth behavioral test. If the concentration of NaP_i is that in HG, the decrease in absorbance for **Co_4PPOM** is ~ 2.5 % compared to ~ 7.5 % when the concentration of NaP_i is increased to that used in SF (after 16 h of aging). A similar trend is observed in catalytic water oxidation activities; when the concentration of NaP_i is increased from 80 mM to 100 mM, the TON decreases from 125 ± 1 to 44 ± 3 (entries 6 and 10, **Table 5-4**). Importantly, **Co_4PPOM** and Co^{2+}(aq) show the opposite buffer-concentration dependence when NaB_i is used. When the concentration of NaB_i is increased from 80 mM to 120 mM with all other conditions held constant, the TON increases from 302 ± 1 to 399 ± 4 for **Co_4PPOM** (entries 2 and 4, **Table 5-4**), and

decreases from 509 ± 5 to 423 ± 11 for Co^{2+}(aq) (entries 14 and 15, **Table 5-4**). Thus, the nature of buffer, its concentration, and pH of the solution are all critical parameters in the decomposition of **Co_4PPOM** and, in general, POM-metal oxide equilibria.

Table 5-4 Light-driven water oxidation activity of **Co_4PPOM**, Co^{2+}(aq) and amorphous CoO_x as a function of pH, buffer and buffer concentration.

Entry	Complex	Complex concentration (μM)	pH	Buffer (mM)	TON	O_2 yield (%)
1	**Co_4PPOM**	2	9	80 NaB_i	410 ± 4	32.8 ± 0.3
2	**Co_4PPOM**	2	8	80 NaB_i	302 ± 1	24.2 ± 0.1
3	**Co_4PPOM** (aged 3 h) ‖	2	8	80 NaB_i	290 ± 4	23.2 ± 0.2
4	**Co_4PPOM**	2	8	120 NaB_i	399 ± 4	31.9 ± 0.4
5*	**Co_4PPOM**	2	7.6	120 NaB_i	226 ± 4	18 ± 0.3
6	**Co_4PPOM**	2	8	80 NaP_i	125 ± 1	9.9 ± 0.1
7	**Co_4PPOM** (aged 3 h) ‖	2	8	80 NaP_i	130 ±2	10.4 ± 0.2
8‡	**Co_4PPOM**	50	8	80 NaP_i	0.35 ± 0.11	0.71± 0.22
9‡	**Co_4PPOM** (aged 3 h) ‖	50	8	80 NaP_i	0.38 ± 0.02	0.75 ± 0.04
10	**Co_4PPOM**	2	8	100 NaP_i	44 ± 3	3.6 ± 0.2
11	**Co_4PPOM**	2	7.2	100 NaP_i	4.3 ± 0.1	0.34 ± 0.01
12	**Co_4PPOM**	2	6.2	100 NaP_i	2.8 ± 0.2	0.23 ± 0.02
13	$Co(NO_3)_2$	2	9	80 NaB_i	596 ± 8	47.7 ± 0.6
14	$Co(NO_3)_2$	2	8	80 NaB_i	509 ± 5	40.8 ± 0.5
15	$Co(NO_3)_2$	2	8	120 NaB_i	423 ± 11	33.9 ± 0.9
16*	$Co(NO_3)_2$	2	7.6	120 NaB_i	100 ± 1	8.1 ± 0.1
17	$Co(NO_3)_2$	8	8	120 NaB_i	600 ± 11	48 ± 1
18*	$Co(NO_3)_2$	8	7.6	120 NaB_i	160 ± 11	12.8 ± 1.1
19	$Co(NO_3)_2$	2	8	80 NaP_i	7.7 ± 0.2	0.61 ± 0.01
20	$Co(NO_3)_2$	2	8	100 NaP_i	6.4 ± 0.4	0.51 ± 0.04

21	$Co(NO_3)_2$	2	7.2	100 NaP_i	3.4 ± 0.1	0.27 ± 0.01
22	$Co(NO_3)_2$	2	6.2	100 NaP_i	0.5 ± 0.04	0.04 ± 0.01
23	CoO_x[†]	8[§]	9	80 NaB_i	40 ± 3	3.2 ± 0.1
24	CoO_x[†]	8[§]	8	80 NaB_i	144 ± 2	11.5 ± 0.1
25	CoO_x[†]	8[§]	8	100 NaP_i	2.6 ± 0.6	0.19 ± 0.02
26	CoO_x[†]	8[§]	7.2	100 NaP_i	0.78 ± 0.08	0.07 ± 0.01
27	CoO_x[†]	8[§]	6.2	100 NaP_i	0.25 ± 0.01	0.02 ± 0.001

Conditions unless otherwise noted: 1mM $Ru(bpy)_3^{2+}$, 5 mM $Na_2S_2O_8$, 455 nm LED light (17 mW, beam diameter ~0.5 cm), 2 mL total solution volume, all stock solutions prepared in DI water. [‖]Aged in the corresponding buffer solution. [*]Catalyst reusability test: 2.38 mg $Na_2S_2O_8$ was added for the second run. [‡]SSB conditions (50 μM $[Ru(bpy)_3]Cl_2$ and 50 μM **Co_4PPOM**). [†]CoO_x was prepared by electrochemical deposition as described in the Experimental section. [§]Not soluble, the suspension obtained after 10 min of sonication, 8 μM equivalents of Co^{2+} was used for catalytic reaction. The errors are calculated as the standard deviation from multiple experiments.

As a sixth behavioral metric, when the photochemical reactions were completed, a second identical molar amount of $Na_2S_2O_8$ was added. This provides a test of the reusability of the entire catalytic system (buffer, $[Ru(bpy)_3]Cl_2$, etc.) and not solely the catalyst. The addition of a second aliquot of $Na_2S_2O_8$ to the **Co_4PPOM** solution results in a 43.6 ± 2 % drop in O_2 yield relative to the first run (entries 4-5 in **Table 5-4** and **Figure 5-14**). The lower O_2 yield in the second runs results primarily from partial decomposition of the $[Ru(bpy)_3]Cl_2$ photosensitizer (**Figure 5-15**), and a slight decrease of pH from the water oxidation reaction itself. In contrast, $Co(NO_3)_2$ shows a dramatically deceased O_2 yield in the second run (76.1 ± 0.9 % drop relative to the first run, entries 15-16 in **Table 5-4** and **Figure 5-14**). Although 8 μM $Co(NO_3)_2$ (same Co equivalents as that of 2 μM **Co_4PPOM**) gives a higher O_2 yield in the first run; the second run produces far less O_2 than for the **Co_4PPOM**-catalyzed reactions (75 ± 3 % drop relative to the first run, entries 17-18 in **Table 5-4** and **Figure 5-14**).

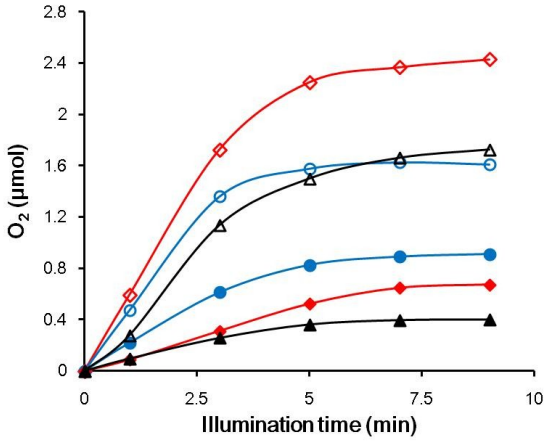

Figure 5-14 Kinetics of light-driven catalytic O_2 evolution from water catalyzed by **Co_4PPOM** and $Co(NO_3)_2$ in 0.12 M borate buffer at pH 8. Conditions: 455 nm LED light (17 mW, beam diameter ~0.5 cm), 5.0 mM $Na_2S_2O_8$, 1.0 mM $[Ru(bpy)_3]Cl_2$, 2.0 µM **Co_4PPOM** (blue) or 2.0 µM (black) or 8 µM $Co(NO_3)_2$ (red). Initial pH = 8.0, total volume 2.0 mL, 120 mM borate buffer. The curves with solid icons are for the second run after addition of another portion of 5.0 mM $Na_2S_2O_8$ to bring the solution to its original concentration.

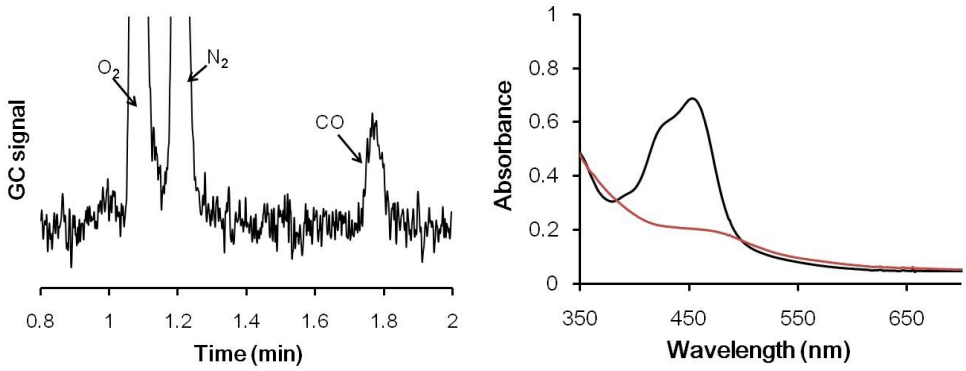

Figure 5-15 Left: the GC/TCD signal of gas products at the end of reaction. Right: the UV-vis absorbance of the reaction solution before (black) and after (red) photocatalytic water oxidation. Conditions: 455 nm LED light (17 mW, beam diameter ~0.5 cm), 5.0 mM $Na_2S_2O_8$, 50 µM $[Ru(bpy)_3]Cl_2$, 50 µM **Co_4PPOM** in 80 mM NaP_i pH = 8.0 buffer, reaction time: 11 mins.

A seventh probe addresses particle formation during water oxidation catalyzed by **Co_4PPOM**, and Co_{app} in separate reactions. Detecting the formation of nanoparticles has been well established as a crucial component in distinguishing homogeneous species from heterogeneous ones.[80] Dynamic light scattering (DLS) studies of the post-water-

oxidation catalytic solutions, confirm that no CoO_x particles result from water oxidation catalyzed by **Co_4PPOM** above the limit of detection (LoD), while those catalyzed by Co^{2+}(aq) do produce particles which are presumably CoO_x (**Figure 5-16**). This finding is consistent with the observation of others,[81] indicating that CoO_x is not the actual catalyst under HG turnover conditions.

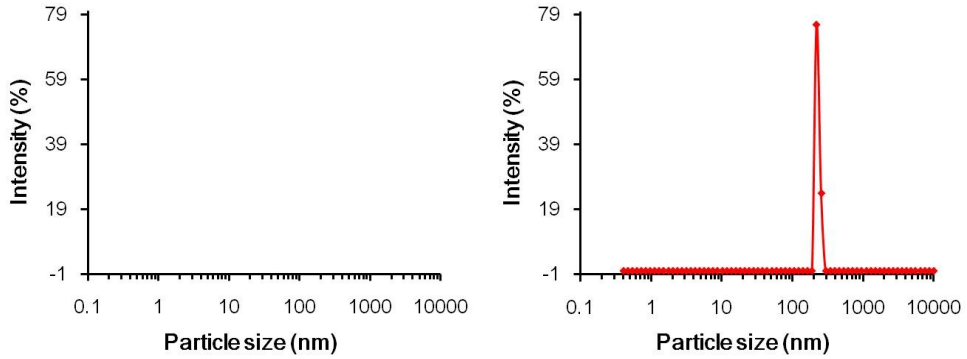

Figure 5-16 Particle size distribution (intensity %) obtained from dynamic light scattering measurement for post-reaction solutions containing 2 μM **Co_4PPOM** (left) or $Co(NO_3)_2$ (right) as catalyst, 1 mM $Ru(bpy)_3^{2+}$ in 80 mM borate buffer (pH = 8), 5.0 mM $Na_2S_2O_8$.

In summary, these collective experiments establish that when both Co_{app} and **Co_4PPOM** are present in solution, the vast majority of catalytic activity -- assessed either by $[Ru(bpy)_3]^{3+}$ reduction, or by photochemical O_2 production, is accounted for by **Co_4PPOM**. Furthermore each catalyst exhibits unique kinetic behavior as a function of pH, buffer identity, and buffer concentration. These experiments should be helpful in many other investigations of POM catalysis, particularly in water, to identify the active catalyst. These include but are not limited to other WOC systems.

5.3.3. Equilibrium Aspects of POM Systems

While molecular WOCs have been and are now typically coordination complexes or organometallic compounds with one or more transition metals, many POM WOCs have

been reported recently.[59] POMs, metal oxides, and soluble hydrated metal cations constitute equilibrium systems; under some conditions (pH, ionic strength, buffer and buffer concentration) the metal oxides are more stable, and the POMs convert to metal oxides; under other conditions, the POMs are more stable and metal oxides and hydroxides convert to the POMs.[82] There are examples over the full pH range (0 – 14) where metal oxides convert to POMs and thus the former are less stable thermodynamically than the latter: at pH 14, the oxide Nb_2O_5 converts fully to the POM, $[Nb_6O_{19}]^{8-}$,[83] and at pH 0, many metal oxides will dissolve and form POMs.[84,85] Thus a POM system is ideal for the rigorous analysis presented in this paper as it is likely that species other than the initial POM will exist in solution. It has been well established that **Co_4PPOM** is hydrolytically unstable above pH 7.5-8.0 in NaP_i buffer.[68-70] As a consequence we conducted seven control experiments in our original study (HG Science) demonstrating that the catalytic water oxidation derives form **Co_4PPOM** and not from Co^{2+}(aq) or metal oxide CoO_x. The present work further affirms that despite some decomposition, **Co_4PPOM** is absolutely the dominant species in solution under HG conditions, including the time scale of the reactions.[65] Experiments reproduced by others,[86] involve the chelation of Co^{2+}(aq) leading to quantitative formation of $[Co(bpy)_3]^{2+}$, where bpy = 2,2'-bipyridine (($\log\beta_3 = 16.02$[87]) and complete suppression of CoO_x formation provided strong evidence that Co^{2+}(aq) is not the WOC under the HG conditions.[65]

5.3.4. Analysis of Previous Co_4PPOM Studies

A series of studies examining the same catalyst, **Co_4PPOM** arrive at apparently different conclusions. The first of these studies by Hill reported homogeneous water oxidation

activity of the compound in both dark[65] and light-driven[74] systems, and provided seven lines of evidence for a soluble catalyst under their conditions (these and all relevant conditions of the various studies are listed in **Table 5-1**). Since then, multiple other groups have analyzed these works,[48,56,58,88-96] reported additional stability studies,[69,70] or used **Co_4PPOM** for water oxidation.[86,90] Thus further analysis of this catalyst and the various systems it has been reported in was required.

A subsequent publication, SF, demonstrated convincingly that **Co_4PPOM**, in an electrochemical system, decomposes into a heterogeneous Co-containing film responsible for the water oxidation activity.[76] However, these were electrocatalytic, rather than homogeneous chemically driven experiments. This difference, coupled with a 156-fold higher **Co_4PPOM** concentration and longer aging times, are most likely key factors that lead to formation of CoO_x in catalytically significant quantities. Additionally, it was observed that **Co_4PPOM** aged in sodium phosphate buffer decomposes to release Co^{2+}(aq) in amounts that quantitatively account for all of the observed water oxidation activity in their study within the standard error. As stated in SF, the conditions used in the SF and HG studies differ and conclusions from one work might not apply to the other.[76]

While all the catalytic water oxidation studies by **Co_4PPOM** and other multi-cobalt POM WOCs,[86,97] use NaP_i or NaB_i buffers, the most detailed thermodynamic hydrolytic (speciation) studies use either no buffer[70] or HEPES, PIPES and CAPS buffers.[69] Potential confusion in catalytic water oxidation by POMs very often arises from neglecting the specific effects of the buffer molecule(s) on both POM speciation in water and POM-catalyzed water oxidation. Both the buffer and the buffer concentration must

be kept relatively constant in POM studies if meaningful comparisons are to be made, particularly near the pH where the POM becomes hydrolytically unstable with respect to metal oxide. As discussed above, the equilibria involving a POM, soluble hydrated metal cations, and metal oxides, is dependent on concentrations of all soluble species present in the equilibrium, and these are frequently perturbed by the buffer.[69] The SF study brought this home in the case of **Co_4PPOM**, by showing that at a concentration of 500 μM, the absorbance at 580 nm (λ_{max}) in pH 8.0 NaP_i decreases by ~ 5 % over 3 h. In NaB_i, we observe a decrease of 1.7 % over 16 h in agreement with SF (**Figure 5-4**), and as described above, we also find that in both buffers the concentration of Co_{app} under photocatalytic conditions is extremely small. Thus, while it has been shown that **Co_4PPOM** releases some Co_{app}/CoO_x, these sub-micromolar quantities of Co species formed by **Co_4PPOM** equilibria cannot account for the O_2 yields observed.

A third group, SSB, studied this system by nanosecond flash photolysis and concluded that Co^{2+}(aq) was not involved in the catalysis either as a catalyst or as a precursor to CoO_x. These nanosecond flash photolysis experiments dictate that quite different experimental conditions ($[Ru(bpy)_3]^{2+}$:**Co_4PPOM** = 1:1[81,98]) than those of HG ($[Ru(bpy)_3]^{n+}$:**Co_4PPOM** = 470:1[65] or 200:1[74]) are used. Under SSB conditions, it was reported that scavenging of the photogenerated $[Ru(bpy)_3]^{3+}$ (or hole scavenging) by **Co_4PPOM** in NaP_i buffer increases with aging time (rapidly in the first 1-8 minutes and continuing to 90 min) of **Co_4PPOM** solutions. From this experiment it was concluded that **Co_4PPOM** is not the true WOC and that no CoO_x forms under these water oxidation conditions, therefore another decomposition product of **Co_4PPOM** must be the active catalyst. Certainly it appears that a new species must form, but our stopped flow data

show that there is no significant change in the UV-vis spectra of **Co_4PPOM** in NaP_i buffer from 2 s to 8 minutes (**Figure 5-5**). Thus, the effect of **Co_4PPOM** aging seen by SSB is too fast to be the process observed in this work or the work of SF. Additionally almost no effect of aging **Co_4PPOM** in NaB_i buffer was observed up to 22 h in SSB.[81] If the hypothesis in SSB (i.e. some **Co_4PPOM** decomposition product and not **Co_4PPOM** itself is the actual WOC) is correct, then one should see higher O_2 yields in NaP_i buffer than in NaB_i buffer, unless the decomposition products exhibit drastically different activity in the two buffers. However, the exact opposite trend is observed experimentally: water oxidation activity in the presence of 2 μM **Co_4PPOM** is threefold higher in NaB_i buffer than that in NaP_i buffer (**Figure 5-17** and entries 2-3, 6-7 in **Table 5-4**).

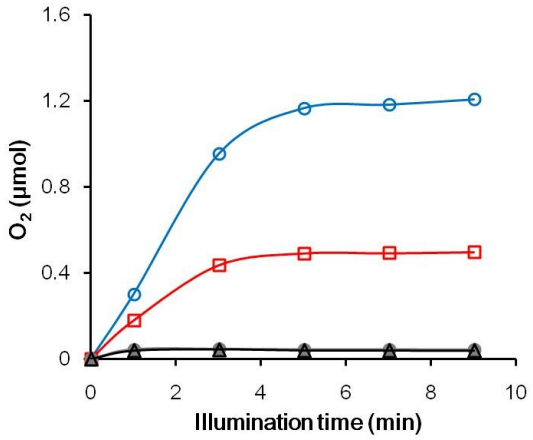

Figure 5-17 Kinetics of light-driven catalytic O_2 evolution as function of buffer and reactant concentration ratio. Conditions: 455 nm LED light (17 mW, beam diameter ~0.5 cm), and 5.0 mM $Na_2S_2O_8$. With 1.0 mM $[Ru(bpy)_3]Cl_2$, 2.0 μM **Co_4PPOM** in 80 mM NaB_i (blue) or 80 mM NaP_i (red), and 50 μM $[Ru(bpy)_3]Cl_2$, 50 μM **Co_4PPOM**, 80 mM NaP_i fresh solution (black) and aged for 3 h (grey) all pH = 8.0. Note: black and grey curves are obtained under the SSB conditions.

This study by SSB did not actually involve measuring water oxidation (O_2 evolution). New experimental evidence in this work comparing O_2 formation under SSB and HG conditions show that there is no effect within experimental error of **Co_4PPOM** solution

aging on catalytic water oxidation activity (entries 6-9 in **Table 5-4**, black and grey curves in **Figure 5-17**). As noted above, the possible decomposition products proposed by SSB[99] could not account for observed catalytic activity in the amounts they are produced. Interestingly, we find that the O_2 yield under SSB experimental conditions is negligible with a ~ 96 % decrease in O_2 yield from HG to SSB conditions, and is independent of aging time (entries 2, 8-9 in **Table 5-4** and **Figure 5-17**). Thus, the conditions required for nanosecond flash photolysis cannot accurately probe those required for successful catalytic water oxidation. As a possible explanation, we reproducibly see an increase in carbon monoxide from *bpy* ligand oxidation under SSB conditions by gas chromatography, indicating that the bleach recovery observed by SSB is not solely from the hole-scavenging process, i.e. oxidation of **Co_4PPOM** (left panel in **Figure 5-15**). The UV-Vis spectra show that the photosensitizer, $[Ru(bpy)_3]^{2+}$, has been almost completely degraded after 11 minutes of irradiation (right panel in **Figure 5-15**).

It was also reported that $[Ru(bpy)_3]^{3+}$ does not have sufficient potential to oxidize **Co_4PPOM**, or to promote water oxidation catalyzed by **Co_4PPOM**, thus **Co_4PPOM** itself could not be the active catalyst. Electrochemical studies in SSB show an increase in anodic current at ca. 1.3 V (vs. Ag/AgCl) with aging time, data similar to that of SF and their later work.[67] However, the electrochemical work of SF and HG makes a strong case that the catalytic current observed at ca. 1.1 V results from CoO_x films, not from **Co_4PPOM**. Recently, SF also explored the electrochemical activity of 2.5 μM **Co_4PPOM** at 1.4 V but concluded that the observed O_2 evolution could not be distinguished as originating from **Co_4PPOM** or decomposition products.[67] Compounding the difficulty in electrochemical studies of **Co_4PPOM**, as shown by HG, SF and others[100]

is that the cobalt-based redox processes in molecular **Co_4PPOM** are voltammetrically silent in aqueous media.>Balula, 2004 #9968< As such, the driving forces for redox processes involving $[Ru(bpy)_3]^{3+}$ and other soluble species in **Co_4PPOM**-catalyzed water oxidation studies conditions, are not accessible by voltammetry and remain unknown.

5.4 Conclusions

It is frequently challenging to determine whether a given complex or material acts as a heterogeneous or homogeneous catalyst, particularly under oxidizing conditions where POMs or metal oxides are frequently the thermodynamic products. The situation is further complicated when possible catalyst decomposition products are soluble species and known catalysts. Pinpointing all species that may result due to dissociation or other decomposition of a dissolved WOC can be problematical. Based on conflicting reports in the literature, and the nature of POM systems, the WOC **Co_4PPOM** was chosen as an ideal system for rigorous study using new techniques to determine the nature of the catalytically active species, and to quantify decomposition products. Supplementing the techniques reported in the initial HG studies, several additional experiments are reported here that distinguish homogeneous WOCs, from their corresponding WOC hydrolysis products (Co^{2+}(aq) and CoO_x in this case). Some of these experiments are of general use in distinguishing these three types of WOCs. A new procedure entails extracting the catalyst from the aqueous phase where water oxidation takes place with a hydrophobic organic solvent containing a hydrophobic quaternary ammonium cation (tetra-*n*-heptylammonium nitrate, "THpA", in toluene). POMs are extracted quantitatively from the water into toluene; whereas, hydrated metal cations and metal oxides are not extracted

at all. This procedure clearly distinguishes the initial catalyst from its possible hydrolysis products.

The amount of Co_{app} present in a range of experiments involving **Co_4PPOM** was quantified at micromolar concentrations using two complementary techniques, cathodic adsorptive stripping voltammetry (CAdSV) and $THpA^+$/toluene extraction followed by ICP-MS. Both techniques found the amount of Co_{app} to be 0.07 ± 0.01 μM under catalytic conditions with 2 μM **Co_4PPOM**. Control experiments show that this amount of Co_{app}, approximated by $Co(NO_3)_2$, results in a negligible increase either in catalytic reduction of $[Ru(bpy)_3]^{3+}$ (dark reactions) or O_2 production (light-driven reactions). Thus the amount of Co_{app} or CoO_x formed from **Co_4PPOM**, cannot account for the observed O_2 yields.

While the POM-metal oxide equilibrium can lie on the side of POM or the metal oxide, for all the studies of **Co_4PPOM** as a WOC thus far (basic buffered aqueous solutions), this POM is thermodynamically unstable towards hydrolysis. As a consequence, we have systematically examined the kinetic stability (specifically Co^{2+} (aq) loss from **Co_4PPOM** and CoO_x particle formation) as a function of time and the four main variables that also impact thermodynamic stability (pH, ionic strength, buffer, and buffer concentration). In addition, the WOC activity was assessed by altering the above four variables over a wide range, including the experimental conditions in HG, SF and SSB. These collective studies establish the crucial role of these four variables in POM stability and reactivity. More importantly, the nature of the oxidation: a soluble oxidant versus applied potential (electrochemical) is paramount in addressing stability. A central corollary here is that catalytic studies of molecular species, especially POM WOCs, under one set of

experimental conditions should be compared only with extreme caution, if at all, to those under other conditions.

References

(1) Chow, J.; Kopp, R. J.; Portney, P. R. *Science* **2003**, *302*, 1528.

(2) Lewis, N. S.; Nocera, D. G. *Proc. Natl. Acad. Sci.* **2006**, *103(43)*, 15729.

(3) Gray, H. B. *Nature Chem.* **2009**, *1*, 7.

(4) Eisenberg, R.; Gray, H. B. *Inorg. Chem.* **2008**, *47*, 1697.

(5) Young, K. J.; Martini, L. A.; Milot, R. L.; III, R. C. S.; Batista, V. S.; Schmuttenmaer, C. A.; Crabtree, R. H.; Brudvig, G. W. *Coord. Chem. Rev.* **2012**, *256*, 2503.

(6) Kanan, M. W.; Surendranath, Y.; Nocera, D. G. *Chem. Soc. Rev.* **2009**, *38*, 109.

(7) Concepcion, J. J.; Jurss, J. W.; Brennaman, M. K.; Hoertz, P. G.; Patrocinio, A. O. T.; Iha, N. Y. M.; Templeton, J. L.; Meyer, T. J. *Acc. Chem. Res.* **2009**, *42*, 1954.

(8) Gersten, S. W.; Samuels, G. J.; Meyer, T. J. *J. Am. Chem. Soc.* **1982**, *104*, 4029.

(9) Hurst, J. K. *Coord. Chem. Rev.* **2005**, *249*, 313.

(10) McDaniel, N. D.; Coughlin, F. J.; Tinker, L. L.; Bernhard, S. *J. Am. Chem. Soc.* **2008**, *130*, 210.

(11) Muckerman, J. T.; Polyansky, D. E.; Wada, T.; Tanaka, K.; Fujita, E. *Inorg. Chem.* **2008**, *47*, 1787.

(12) Hull, J. F.; Balcells, D.; Blakemore, J. D.; Incarvito, C. D.; Eisenstein, O.; Brudvig, G. W.; Crabtree, R. H. *J. Am. Chem. Soc.* **2009**, *131*, 8730.

(13) Masaoka, S.; Sakai, K. *Chem. Lett.* **2009**, *38*, 182.

(14) McCool, N. S.; Robinson, D. M.; Sheats, J. E.; Dismukes, G. C. *J. Am. Chem. Soc.* **2011**, *133*, 11446.

(15) Bernet, L.; Lalrempuia, R.; Ghattas, W.; Mueller-Bunz, H.; Vigara, L.; Llobet, A.; Albrecht, M. *Chem. Commun.* **2011**, *47*, 8058.

(16) Chen, Z.; Concepcion, J. J.; Meyer, T. J. *Dalton Trans.* **2011**, *40*, 3789.

(17) Fillol, J. L.; Codolà, Z.; Garcia-Bosch, I.; Gómez, L.; Pla, J. J.; Costas, M. *Nature Chem.* **2011**, *3*, 807.

(18) Murakami, M.; Hong, D.; Suenobu, T.; Yamaguchi, S.; Ogura, T.; Fukuzumi, S. *J. Am. Chem. Soc.* **2011**, *133*, 11605.

(19) Wasylenko, D. J.; Ganesamoorthy, C.; Borau-Garcia, J.; Berlinguette, C. P. *Chem. Commun.* **2011**, *47*, 4249.

(20) Roeser, S.; Fàrrs, P.; Bozoglian, F.; Martínez-Belmonte, M.; Benet-Buchholz, J.; Llobet, A. *ChemSusChem* **2011**, *4*, 197.

(21) An, J.; Duana, L.; Sun, L. *Faraday Discuss.* **2012**, *155*, 267.

(22) Kaveevivitchai, N.; Zong, R.; Tseng, H.-W.; Chitta, R.; Thummel, R. P. *Inorg. Chem.* **2012**, *51*, 2930.

(23) Hong, D.; Jung, J.; Park, J.; Yamada, Y.; Suenobu, T.; Lee, Y.-M.; Nam, W.; Fukuzumi, S. *Energy Environ. Sci.* **2012**, *5*, 7606.

(24) Bernardini, G.; Wedd, A. G.; Zhao, C.; Bond, A. M. *Proc. Natl. Acad. Sci.* **2012**, *109*, 11552.

(25) Zhang, M.-T.; Chen, Z.; Kang, P.; Meyer, T. J. *J. Amer. Chem. Soc.* **2013**, *135*, 2048.

(26) Joya, K. S.; Subbaiyan, N. K.; D'Souza, F.; Groot, H. J. M. d. *Angew. Chem. Int. Ed.* **2012**, *51*, 9601.

(27) Youngblood, W. J.; Lee, S.-H. A.; Maeda, K.; Mallouk, T. E. *Acc. Chem. Res.* **2009**, *42*, 1966.

(28) Shafirovich, V. Y.; Khannanov, N. K.; Strelets, V. V. *Nouveau J. Chim.* **1980**, *4*, 81.

(29) Harriman, A.; Pickering, I. J.; Thomas, J. M.; Christensen, P. A. *J. Chem. Soc., Faraday Trans. 1 F* **1988**, *84*, 2795.

(30) Kanan, M. W.; Nocera, D. G. *Science* **2008**, *321*, 1072.

(31) Jiao, F.; Frei, H. *Angew. Chem. Int. Ed.* **2009**, *48*, 1841.

(32) Robinson, D. M.; Go, Y. B.; Greenblatt, M.; Dismukes, G. C. *J. Am. Chem. Soc.* **2010**, *132*, 11467.

(33) Carraro, M.; Sartorel, A.; Toma, F. M.; Puntoriero, F.; Scandola, F.; Campagna, S.; Prato, M.; Bonchio, M. *Top. Curr. Chem.* **2011**, *303*, 121.

(34) Gerken, J. B.; McAlpin, J. G.; Chen, J. Y. C.; Rigsby, M. L.; Casey, W. H.; Britt, R. D.; Stahl, S. S. *J. Am. Chem. Soc.* **2011**, *133*, 14431.

(35) Pijpers, J. J. H.; Winkler, M. T.; Surendranath, Y.; Buonassisi, T.; Nocera, D. G. *Proc. Natl. Acad. Sci.* **2011**, *108*, 10056.

(36) Sivasankar, N.; Weare, W. W.; Frei, H. *J. Am. Chem. Soc.* **2011**, *133*, 12976.

(37) Wang, C.; Xie, Z.; deKrafft, K. E.; Lin, W. *J. Am. Chem. Soc.* **2011**, *133*, 13445.

(38) Wang, D.; Jiang, H.; Zong, X.; Xu, Q.; Ma, Y.; Li, G.; Li, C. *Chem. Eur. J.* **2011**, *17*, 1275.

(39) Steinmiller, E. M. P.; Choi, K.-S. *Proc. Natl. Acad. Sci.* **2009**, *106*, 20633.

(40) Zidki, T.; Zhang, L.; Shafirovich, V.; Lymar, S. V. *J. Am. Chem. Soc.* **2012**, *134*, 14275.

(41) Higashi, M.; Domen, K.; Abe, R. *J. Am. Chem. Soc.* **2012**, *134*, 6968.

(42) Youngblood, W. J.; Lee, S.-H. A.; Kobayashi, Y.; Hernandez-Pagan, E. A.; Hoertz, P. G.; Moore, T. A.; Moore, A. L.; Gust, D.; Mallouk, T. E. *J. Am. Chem. Soc.* **2009**, *131*, 926.

(43) Chen, Z.; Concepcion, J. J.; Hull, J. F.; Hoertz, P. G.; Meyer, T. J. *Dalton Trans.* **2010**, *39*, 6950.

(44) Shevchenko, D.; Anderlund, M. F.; Thapper, A.; Styring, S. *Energy Environ. Sci.* **2011**, *4*, 1284.

(45) Barnett, S. M.; Goldberg, K. I.; Mayer, J. M. *Nature Chem.* **2012**, *4*, 498.

(46) Gonçalves, R. H.; Leite, L. D. T.; Leite, E. R. *ChemSusChem* **2012**, *5*, 2341.

(47) Toma, F. M.; Sartorel, A.; Iurlo, M.; Carraro, M.; Parisse, P.; Maccato, C.; Rapino, S.; Gonzalez, B. R.; Amenitsch, H.; Ros, T. D.; Casalis, L.; Goldoni, A.; Marcaccio, M.; Scorrano, G.; Scoles, G.; Paolucci, F.; Prato, M.; Bonchio, M. *Nature Chem.* **2010**, *2*, 826.

(48) Yamada, Y.; Yano, K.; Hong, D.; Fukuzumi, S. *Phys. Chem. Chem. Phys.* **2012**, *14*, 5753.

(49) Risch, M.; Klingan, K.; Ringleb, F.; Chernev, P.; Zaharieva, I.; Fischer, A.; Dau, H. *ChemSusChem* **2012**, *5*, 542.

(50) Anton, D. R.; Crabtree, R. H. *Organometallics* **1983**, *2*, 855.

(51) Widegren, J. A.; Finke, R. G. *J. Mol. Catal. A: Chem.* **2003**, *198*, 317.

(52) Whitesides, G. M.; Hackett, M.; Brainard, R. L.; Lavalleye, J.-P. P. M.; Sowinski, A. F.; Izumi, A. N.; Moore, S. S.; Brown, D. W.; Staudt, E. M. *Organometallics* **1985**, *4*, 1819.

(53) Kuznetsov, A. E.; Geletii, Y. V.; Hill, C. L.; Morokuma, K.; Musaev, D. G. *J. Am. Chem. Soc.* **2009**, *131*, 6844.

(54) Quiñonero, D.; Kaledin, A. L.; Kuznetsov, A. E.; Geletii, Y. V.; Besson, C.; Hill, C. L.; Musaev, D. G. *J. Phys. Chem. A* **2010**, *114*, 535.

(55) Sartorel, A.; Miro, P.; Salvadori, E.; Romain, S.; Carraro, M.; Scorrano, G.; Valentin, M. D.; Llobet, A.; Bo, C.; Bonchio, M. *J. Am. Chem. Soc.* **2009**, *131*, 16051.

(56) Car, P.-E.; Guttentag, M.; Baldridge, K. K.; Albertoa, R.; Patzke, G. R. *Green Chem.* **2012**, *14*, 1680.

(57) Zhu, G.; Glass, E. N.; Zhao, C.; Lv, H.; Vickers, J. W.; Geletii, Y. V.; Musaev, D. G.; Song, J.; Hill, C. L. *Dalton Trans.* **2012**, *41*, 13043.

(58) Tanaka, S.; Annaka, M.; Sakai, K. *Chem. Commun.* **2012**, *48*, 1653.

(59) Lv, H.; Geletii, Y. V.; Zhao, C.; Vickers, J. W.; Zhu, G.; Luo, Z.; Song, J.; Lian, T.; Musaev, D. G.; Hill, C. L. *Chem. Soc. Rev.* **2012**, *41*, 7572.

(60) Geletii, Y. V.; Botar, B.; Kögerler, P.; Hillesheim, D. A.; Musaev, D. G.; Hill, C. L. *Angew. Chem. Int. Ed.* **2008**, *47*, 3896.

(61) Geletii, Y. V.; Huang, Z.; Hou, Y.; Musaev, D. G.; Lian, T.; Hill, C. L. *J. Am. Chem. Soc.* **2009**, *131*, 7522.

(62) Besson, C.; Musaev, D. G.; Lahootun, V.; Cao, R.; Chamoreau, L.-M.; Villanneau, R.; Villain, F.; Thouvenot, R.; Geletii, Y. V.; Hill, C. L.; Proust, A. *Chem. Eur. J.* **2009**, *15*, 10233.

(63) Besson, C.; Huang, Z.; Geletii, Y. V.; Lense, S.; Hardcastle, K. I.; Musaev, D. G.; Lian, T.; Proust, A.; Hill, C. L. *Chem. Commun.* **2010**, 2784.

(64) Sartorel, A.; Carraro, M.; Scorrano, G.; Zorzi, R. D.; Geremia, S.; McDaniel, N. D.; Bernhard, S.; Bonchio, M. *J. Am. Chem. Soc.* **2008**, *130*, 5006.

(65) Yin, Q.; Tan, J. M.; Besson, C.; Geletii, Y. V.; Musaev, D. G.; Kuznetsov, A. E.; Luo, Z.; Hardcastle, K. I.; Hill, C. L. *Science* **2010**, *328*, 342.

(66) Finke, R. G.; Droege, M. W.; Domaille, P. J. *Inorg. Chem.* **1987**, *26*, 3886.

(67) Stracke, J. J.; Finke, R. G. *ACS Catal.* **2013**, *3*, 1209.

(68) Finke, R. G.; Droege, M.; Hutchinson, J. R.; Gansow, O. *J. Am. Chem. Soc.* **1981**, *103*, 1587.

(69) Lieb, D.; Zahl, A.; Wilson, E. F.; Streb, C.; Nye, L. C.; Meyer, K.; Ivanović-Burmazović, I. *Inorg. Chem.* **2011**, *50*, 9053.

(70) Ohlin, C. A.; Harley, S. J.; McAlpin, J. G.; Hocking, R. K.; Mercado, B. Q.; Johnson, R. L.; Villa, E. M.; Fidler, M. K.; Olmstead, M. M.; Spiccia, L.; Britt, R. D.; Casey, W. H. *Chem. Eur. J.* **2011**, *17*, 4408.

(71) Swierk, J. R.; Mallouk, T. E. *Chem. Soc. Rev.* **2013**, *42*, 2357.

(72) Ghosh, P. K.; Brunschwig, B. S.; Chou, M.; Creutz, C.; Sutin, N. *J. Am. Chem. Soc.* **1984**, *106*, 4772.

(73) Klemperer, W. G. In *Inorg. Synth.*; Ginsberg, A. P., Ed.; John Wiley and Sons, Inc.: New York, 1990; Vol. 27, p 71.

(74) Huang, Z.; Luo, Z.; Geletii, Y. V.; Vickers, J.; Yin, Q.; Wu, D.; Hou, Y.; Ding, Y.; Song, J.; Musaev, D. G.; Hill, C. L.; Lian, T. *J. Am. Chem. Soc.* **2011**, *133*, 2068.

(75) Krolicka, A.; Bobrowski, A.; Kalcher, K.; Mocak, J.; Svancara, I.; Vytras, K. *Electroanalysis* **2003**, *15*, 1859.

(76) Stracke, J. J.; Finke, R. G. *J. Am. Chem. Soc.* **2011**, *133*, 14872.

(77) Katsoulis, D. E.; Pope, M. T. *J. Am. Chem. Soc.* **1984**, *106*, 2737.

(78) Vickers, J.; Lv, H.; Zhuk, P. F.; Geletii, Y. V.; Hill, C. L. *MRS Proceedings* **2012**, *1387*, mrsf11.

(79) Balula, Maria S.; Gamelas, José A.; Carapuça, Helena M.; Cavaleiro, Ana M. V.; Schlindwein, W. *Eur. J. Inorg. Chem.* **2004**, *2004*, 619.

(80) Schley, N. D.; Blakemore, J. D.; Subbaiyan, N. K.; Incarvito, C. D.; D'Souza, F.; Crabtree, R. H.; Brudvig, G. W. *J. Am. Chem. Soc.* **2011**, *133*, 10473.

(81) Natali, M.; Berardi, S.; Sartorel, A.; Bonchio, M.; Campagna, S.; Scandola, F. *Chem. Commun.* **2012**, *48*, 8808.

(82) Weinstock, I. A.; Barbuzzi, E. M. G.; Wemple, M. W.; Cowan, J. J.; Reiner, R. S.; Sonnen, D. M.; Heintz, R. A.; Bond, J. S.; Hill, C. L. *Nature* **2001**, *414*, 191.

(83) 5x *5x* **5x**, *5x*.

(84) Hill, C. L. In *Comprehensive Coordination Chemistry-II: From Biology to Nanotechnology*; Wedd, A. G., Ed.; Elsevier Ltd.: Oxford, UK, 2004; Vol. 4, p 679.

(85) Pope, M. T. In *Comprehensive Coordination Chemistry II: From Biology to Nanotechnology*; Wedd, A. G., Ed.; Elsevier Ltd.: Oxford, UK, 2004; Vol. 4, p 635.

(86) Goberna-Ferrón, S.; Vigara, L.; Soriano-López, J.; Galán-Mascarós, J. R. *Inorg. Chem.* **2012**, *51*, 11707.

(87) Del Piero, S.; Di Bernardo, P.; Fedele, R.; Melchior, A.; Polese, P.; Tolazzi, M. *Eur. J. Inorg. Chem.* **2006**, *2006*, 3738.

(88) Joya, K. S.; Vallés-Pardo, J. L.; Joya, Y. F.; Eisenmayer, T.; Thomas, B.; Buda, F.; de Groot, H. J. M. *ChemPlusChem* **2013**, *78*, 35.

(89) Wasylenko, D. J.; Palmer, R. D.; Schott, E.; Berlinguette, C. P. *Chem. Commun.* **2012**, *48*, 2107.

(90) Wu, J.; Liao, L.; Yan, W.; Xue, Y.; Sun, Y.; Yan, X.; Chen, Y.; Xie, Y. *ChemSusChem* **2012**, *5*, 1207.

(91) Woolerton, T. W.; Sheard, S.; Chaudhary, Y. S.; Armstrong, F. A. *Energy Environ. Sci.* **2012**, *5*, 7470.

(92) Limburg, B.; Bouwman, E.; Bonnet, S. *Coord. Chem. Rev.* **2012**, *256*, 1451.

(93) Anxolabéhère-Mallart, E.; Costentin, C.; Fournier, M.; Nowak, S.; Robert, M.; Savéant, J.-M. *J. Am. Chem. Soc.* **2012**, *134*, 6104.

(94) Du, P.; Eisenberg, R. *Energy Environ. Sci.* **2012**, *5*, 6012.

(95) Crabtree, R. H. *Chem. Rev.* **2012**, *112*, 1536.

(96) Soriano-López, J.; Goberna-Ferrón, S.; Vigara, L.; Carbó, J. J.; Poblet, J. M.; Galán-Mascarós, J. R. *Inorg. Chem.* **2013**, *52*, 4753.

(97) Zhu, G.; Geletii, Y. V.; Song, J.; Zhao, C.; Glass, E. N.; Bacsa, J.; Hill, C. L. *Inorg. Chem.* **2012**, *52*, 1018.

(98) Sartorel, A.; Bonchio, M.; Campagna, S.; Scandola, F. *Chem. Soc. Rev.* **2013**, *42*, 2262.

(99) Quoting SSB: "As to the nature of such an active product, free aqueous Co^{2+} (an obvious candidate on the way to cobalt oxide formation) is ruled out by control experiments performed with $Co(NO_3)_2$, where no appreciable $Ru(bpy)_3^{3+}$ reduction takes place in this time scale. Therefore, the most likely hypothesis is that of an earlier decomposition product, possibly a fragment of the original [**Co_4PPOM**] anion of 2:1 Co:POM stoichiometry."

(100) Gao, S.; Li, T.; Li, X.; Cao, R. *Mater. Lett.* **2006**, *60*, 3622.

Chapter 6

Visible-Light-Driven Hydrogen Evolution from Water Using a Noble-Metal-Free Polyoxometalate Catalyst

(Published in *J. Catal.* **2013***, 307,* 48-54.) -- Reproduced by permission of Elsevier, License number: 3693230846355.

With James W. Vickers, Jordan M. Sumliner, Guibo Zhu, Zhen Luo, Djamaladdin G. Musaev, Yurii V. Geletii, and Craig L. Hill*

6.1 Introduction

Currently the conversion of sunlight energy into chemical energy in the form of convenient, sustainable and non-fossil-based fuels such as dihydrogen is the focus of numerous studies.[1,2] The general principle of water splitting into H_2 and O_2 is adapted from Nature, where reductive equivalents are generated in Photosystems I and II producing O_2 as a by-product. The promise of a low-cost, sustainable, environmentally benign fuel using sunlight as the energy source and water as the reducing agent is motivating a large international community to develop novel and effective heterogeneous[3-8] or homogeneous[5,9-13] structures or devices to facilitate water splitting.

Photocatalysis based on dispersion of heterogeneous semiconductor particles is one promising approach for solar water splitting because such particles are robust under some conditions and readily prepared at low cost.[3,5,14,15] To fully understand the structures and dynamics of solar-driven water splitting architectures as well as optimizing their performance, it is valuable to have molecular systems that facilitate detailed experimental and computational studies.[16,17] Most of systems employ noble metals as the catalyst,[11,12,18-20] with a separate chromophore[21-25]; systems based exclusively on earth-abundant elements are very rare.[26-28] In this context, the development of catalysts that exhibit the advantages of both heterogeneous semiconductor catalysts and homogeneous molecular catalysts are of clear and growing interest. Polyoxometalates (POMs), showing similar compositions to semiconductor metal oxides, are a large family of transition metal oxygen anion clusters with d^0 electronic configurations. POMs combine the stability advantages of heterogeneous catalysts with the tractability and other advantages of homogeneous catalysts. While there are many very recent reports of

transition-metal-substituted POMs catalyzing the efficient oxidation of water under thermal and photochemical conditions,[29-36] there are very few reports of such complexes catalyzing the reduction of water.[37-41] We and others have studied hydrogen evolution from reduced POMs, usually in context with UV-light-driven photooxidation of organic substrates (alcohols, alkanes, others) but all these studies involve conventional (non-d-metal-containing) POMs.[42-46] Many of these H_2 evolution studies required the presence of Pt(0) as a co-catalyst to achieve rates amenable to detailed studies. Recently, Artero and coworkers[47] developed a covalent-linked Ir(III)-photosensitized polyoxometalate complex, which shows very efficient photoreduction of polyoxometalate in the presence of sacrificial electron donor upon visible light irradiation. This system performs photocatalytic H_2 production without obvious loss of activity over more than one week; however, a TON of only 41 is obtained after 7 days of irradiation.[47] Clearly, the development of an inexpensive and efficient WRC that is also water compatible would be a breakthrough in artificial photosynthesis. In this context, we report a Mn-substituted polyoxometalate, $[Mn_4(H_2O)_2(VW_9O_{34})_2]^{10-}$ (**1**), that is isostructural to the efficient water oxidation catalyst, $[Co_4(H_2O)_2(PW_9O_{34})_2]^{10-}$. While **1** is inactive as a water oxidation catalyst, it is catalytically active for water reduction. We describe the reduction of water catalyzed by **1** under visible light irradiation using $[Ru(bpy)_3]^{2+}$ as photosensitizer with TEOA as a sacrificial electron donor.

6.2 Experimental

6.2.1. Materials and Instrumentation

All reagents and solvents were purchased from commercial sources unless otherwise noted. $[Ru(bpy)_3]Cl_2 \cdot 6H_2O$ was purified before use by recrystallizing from 5 mL of warm

water; This $[Ru(bpy)_3](ClO_4)_3$ was prepared by literature procedure with minor modifications.[48] All other chemicals and salts were used as received without further purification unless otherwise noted. Water for the preparation of solutions was obtained from a Barnstead Nanopure® water-purification system. D_2O and $CDCl_3$ for isotope labeling experiment or NMR studies were obtained from Cambridge Isotope Inc.

The FT-IR spectra were measured on a Thermo Nicolet 6700 spectrometer. UV-Vis spectra were acquired using Agilent 8453 spectrophotometer equipped with a diode-array detector and an Agilent 89090A cell temperature controller unit. ^{51}V NMR (151.6 MHz) spectra were obtained at 298 K in 5 mm O.D. NMR tubes on a Unity Plus 600 spectrometer equipped with a Varian 600 SW/PF6 probe head. All the chemical shifts were referenced to neat $VOCl_3$ (reference as 0 ppm at 25^oC). Elemental analyses were performed by Galbraith Lab Inc., Knoxville, TN, 37921. Thermogravimetric data were collected on Instrument Specialists Incorporated TGA 1000 instruments. Analysis of hydrogen in the reaction headspace was performed using a HP7890A model gas chromatograph equipped with thermal conductivity detector (TCD) and a GC column packed with 5Å molecular sieves. The steady-state luminescence quenching spectra were recorded on a FluoroMax 3 spectrofluorimeter. For time-resolved fluorescence decay measurements, femtosecond laser pulses (~100 fs, 80 MHz repetition rate) were generated with a mode-locked Ti:sapphire laser (Tsunami oscillator pumped by 10 W Millennia Pro, Spectra-Physics). Excitation pulses at 400 nm were generated by second harmonic generation of the 800 nm pulses in a BBO crystal. The repetition rate of output pulse centered at 800 nm was reduced to 1.6 MHz using a pulse picker (Conoptics, USA). The 580-620 nm emissions of $Ru(bpy)_3^{2+}$ were detected by a microchannel plate

photomultiplier tube (Hamamatsu R3809U-51), whose output was amplified and analyzed by a TCSPC board (Becker & Hickel SPC 600).

6.2.2. Synthesis

$Na_{10}[Mn_4(H_2O)_2(VW_9O_{34})_2]\cdot 26H_2O$ **(**Na**1)** was synthesized according to modified literature method[49] as follows: $Mn(NO_3)_2\cdot 4H_2O$ (1.0 g) and $Na_2WO_4\cdot 2H_2O$ (5.8 g) were dissolved in 0.5 M sodium acetate buffer (120 mL, pH 4.8) and vigorously stirred for several minutes before $NaVO_3$ (0.27g) was added in small portions. The resulting turbid mixture was then heated to 80 °C for 1.5 hours. The hot brown mixture was filtered to remove any precipitate and left to crystallize for around one week to give dark block crystals of Na**1** (yield 2.45 g; ca. 70 % based on tungstate). One single crystal was submitted to structural analysis by X-ray crystallography and the bulk sample was analyzed by elemental analysis. Elemental Analysis, Calcd (Found %) for Na_{10}**1**: calc for Mn, 4.03; V, 1.87; W, 60.68; found for Mn, 4.01; V, 1.81; W, 59.89. FT-IR (2% KBr pellet, 1000 - 400 cm^{-1}): 951(m), 874(s), 825(s), 752(m), 698(s), 490(m). ^{51}V NMR: -505.2 ppm, $\Delta\nu_{1/2}$ = 73.7 Hz. Thermogravimetric analysis (TGA): weight loss 8.5%, corresponding to 26 water molecules. Molecular weight: 5453.04 g mol^{-1}.

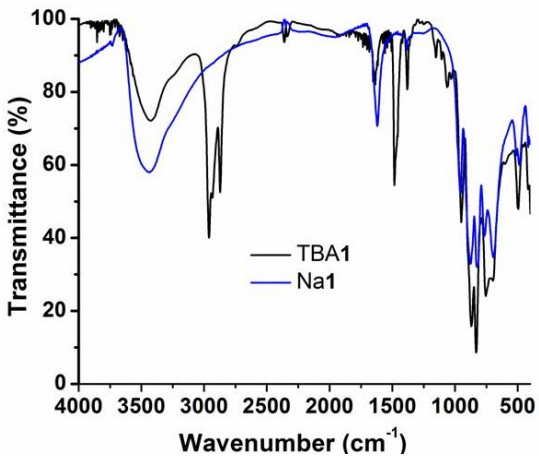

Figure 6-1 FT-IR spectra of Na**1** (black line) and TBA**1** (grey line). The spectra show all the characteristic bands of polyanion 1 confirming that the cation exchange (TBA^+ for Na^+) does not change the structure of **1**.

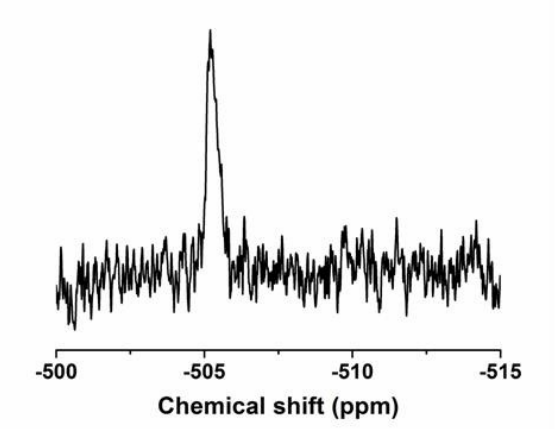

Figure 6-2 ^{51}V NMR spectrum of **1** in D_2O. Chemical shifts relative to neat $VOCl_3$ at 25 ^oC (0 ppm). The ^{51}V NMR spectrum shows only one broad peak at -505.2 ppm ($\Delta\nu_{1/2}$ = 73.7 Hz) for the central pseudo-tetrahedral V in the two symmetry-equivalent $[VW_9O_{34}]^{9-}$ ligands which is consistent with a solution structure for **1** that is identical to the X-ray structure.

The tetrabutylammonium (TBA) salt was prepared according to general literature procedure of Katsoulis and Pope with some modifications.[50] Typically, an aqueous solution of Na**1** (0.1 mmol, 0.545 g) in 10 mL H_2O was added to a solution of tetrabutylammonium bromide (15 mmol, 0.483 g) in CH_2Cl_2. The mixture was then shaken heavily to transfer the polyanions to the organic layer. The dark brown organic

layer was separated and washed with deionized water (15 mL × 6 times) to remove excess TBA bromide. Crystalline material was obtained by dissolving the TBA salt in 10 mL acetonitrile and allowing diethyl ether vapor to diffuse into the solution. The product was then dried *in vacuo*. The purity was confirmed by FT-IR, ^{51}V NMR and EA.

6.2.3. X-ray crystallography

The title compound Na_{10}**1** was isolated as orange-brown crystals. A complete set of diffraction intensities was collected at the X-ray Crystallography facility at Emory University. A single crystal 0.23 x 0.14 x 0.1 mm^3 with high order faces was used. Single crystal X-ray data were collected at 173(2) K on a Bruker APEX2 diffractometer with graphite-monochromated Mo-K_α (0.71073 Å) radiation. The data were collected using ω scans with different φ values and optimal frame exposure times and widths yielding 43235 reflections in the θ range 1.37 - 29.15°, of which 12472 were unique. The strategy for the data collection, cell parameters and symmetry were evaluated using APEXII software.[51] The frames were integrated with the SAINT v7.68a.[52] The distances of the faces from the center of the crystal were measured for a numerical absorption correction. A combination of a numerical and a multi-scan absorption correction was carried out using the program SADABS V2008-1.[53] The structure was solved with SHELXS and refined with Olex2,[54] a graphical interface to SHELXL.[55] The results are summarized in **Table 6-1**.

Table 6-1 Crystallographic data and structure refinement for Na_{10}**1**.

	Na_{10}**1**
Empirical formula	$Na_{10}H_{64}Mn_4V_2W_{18}O_{100}$
Formula weight	5541.31
Temperature	173(2) K

Wavelength	0.71073 Å
Crystal system	Triclinic
Space group	$P\bar{1}$
Unit cell dimensions	a = 12.9416(15) Å α= 93.041(2)°
	b = 13.4134(16) Å β= 105.580(2)°
	c = 15.7553(19) Å γ= 115.808(2)°
Volume	2325.7(5) $Å^3$
Z	1
Density (calculated)	4.006 Mg/m^3
Absorption coefficient	23.076 mm^{-1}
F(000)	2458
Crystal size	0.23 x 0.14 x 0.10 mm^3
Reflections collected	43235
Independent reflections	12472 [R(int) = 0.0382]
Refinement method	Full-matrix least-squares on F^2
Data / restraints / parameters	12472 / 0 / 394
Goodness-of-fit on F^2	1.058
Final R indices [I>2sigma(I)]	[a]R1 = 0.0331, [b]wR2 = 0.0824
R indices (all data)	R1 = 0.0400, wR2 = 0.0882

[a] $R_1 = \Sigma||F_0| - |F_c|| / \Sigma|F_0|$; [b] $wR_2 = \Sigma[w(F_0^2 - F_c^2)^2]/ \Sigma[w(F_0^2)^2]^{1/2}$

6.2.4. General Procedure for Light-Driven Catalytic Experiments

The light-driven water reduction experiment was performed in a cylindrical cuvette (NSG, 32UV10) with a total volume of ~2.5 mL. In a typical experiment, the cell was filled with 2.0 mL DMF/H_2O (1.86/1 v/v) solution containing 0.67 mM $Ru(bpy)_3Cl_2$, 0.25 M TEOA and 22.9 μM catalyst. The pH of the reaction solution was adjusted using 6 M HCl. The reaction cell was sealed with a rubber septum, carefully degassed and filled with Ar. All procedures were performed with a minimum exposure to ambient light. The reaction samples were irradiated by a LED-light source (λ = 455 nm; light intensity 30 mW, beam

diameter ~0.4 cm) at room temperature with constant stirring (4×10^3 RPM) using a magnetically-coupled stirring system (SYS 114, SPECTROCELL). The post-reaction solution was collected and left for a few days in order for crystals to grow. Needle-like crystals were isolated by centrifugation and used in the FT-IR stability evaluations (2.0 wt% samples in KBr) for comparison with complex **1** before catalysis.

Control experiments were carried out under the same conditions in the absence of each component (e.g. TEOA, $Ru(bpy)_3Cl_2$) of the hydrogen generating samples as described above. More control experiments were performed by replacing complex **1** with $TBA_3[VW_{12}O_{40}]$,[56] freshly prepared MnO_2, VO_2 and WO_3 nanopowders under otherwise the identical conditions.

6.2.5. Isotope Labeling Experiment

Isotope labeling experiments were conducted under the same conditions as described in *section 2.4* using D_2O instead of H_2O to verify the source of H_2 production. The gas produced in the headspace was analyzed by GC-TCD with helium as the carrier gas.

6.2.6. Steady-State and Time-Resolved Fluorescence Decay Measurement of $[Ru(bpy)_3]^{2+}$ in the Presence of 1 or TEOA

The mixed solvent of DMF/H_2O (1.86/1) was used for fluorescence decay measurements. Before each experiment, the samples with different concentrations of either **1** or TEOA were purged with argon for 10 min to remove soluble oxygen. The strong emission band of $[Ru(bpy)_3]^{2+*}$ at 500 - 800 nm with λ_{max} = 612 nm ($\lambda_{excitation}$ = 455 nm) was measured using the instruments described in **section 6.2.1.**

6.2.7. Computational Procedure

Calculations were performed using the Gaussian 09 program.[57] The geometries of the $[Mn_4(H_2O)_2(VW_9O_{34})_2]^{10-}$ (**1**) polyoxoanion were optimized without any symmetry constraint at the density functional (M06L) level of theory.[58] In these calculations we used Hay-Wadt effective core potentials (ECPs) with the associated Lanl2dz basis set for transition metals[59-61] and the standard 6-31G* split-valence-polarization basis set for all other atoms. The solvent effects were estimated by using the self-consistent reaction field IEF-PCM method[62] with water as a solvent (dielectric constant $\varepsilon = 78.39$).

6.2.8. Kinetics of Stoichiometric Reduction $[Ru(bpy)_3]^{3+}$ by TEOA

The rapid kinetics for stoichiometric reduction of $[Ru(bpy)_3]^{3+}$ by TEOA was monitored using a Hi-Tech Stopped Flow SF-61SX2 instrument equipped with a diode array detector (400-700 nm). Two feeding syringes were filled with an aqueous solution of either $[Ru(bpy)_3]^{3+}$ or TEOA. The consumption of $[Ru(bpy)_3]^{3+}$ was followed by a decrease in absorbance at 670 nm ($\varepsilon_{670} = 4.2 \times 10^2\ M^{-1}\ cm^{-1}$) with optical path length l = 1 cm. The data were acquired and treated using KinetAsyst^{TM} 3.0 software.

6.3 Results and Discussion

6.3.1. Preparation and Characterization of Complex 1

Complex **1** was synthesized using a one-pot method in acidic buffer solution starting from salts of earth abundant elements (Co, W and V) by a modification of the literature method.[49] It was characterized by X-ray crystallography (**Figure 6-3**), FT-IR (**Figure 6-1**), ^{51}V NMR (**Figure 6-2**), UV-Vis (**Figure 6-4**), TGA, and elemental analysis (**Section 6.2.1**).

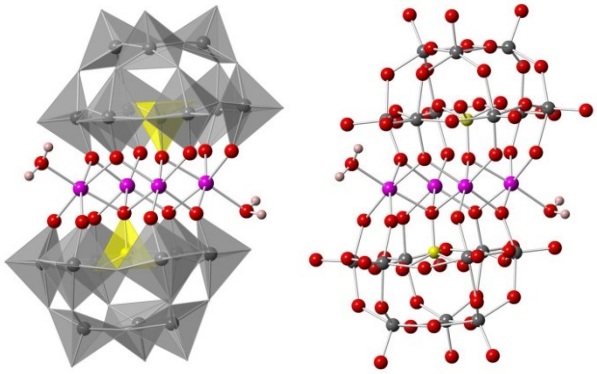

Figure 6-3 X-ray crystal structure of **1**. Left: a combined ball-and-stick (central unit) and polyhedral (POM ligands) representation; Right: ball-and-stick representation. Red: oxygen; Pink: hydrogen; Magenta: manganese; Yellow: VO_4; Grey: WO_6.

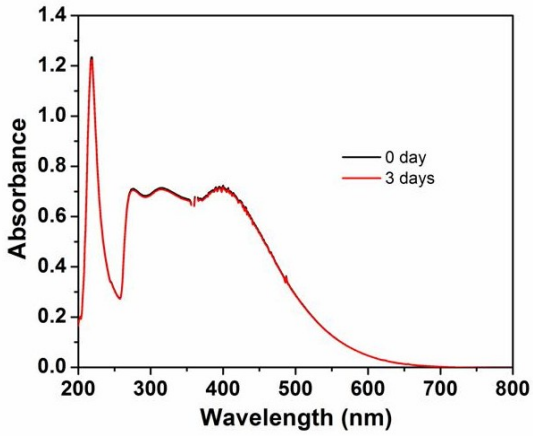

Figure 6-4 UV-vis spectrum of 0.38 mM TBA**1** in mixed solvent of DMF/H_2O (3/1) containing 0.25 M TEOA, the time profile of this UV-Vis spectrum is shown in **Figure 6-12**.

The sodium salt of **1** crystallizes in the triclinic space group $P\bar{1}$ (**Table 6-1**). The sandwich type cluster, $[Mn_4(H_2O)_2(VW_9O_{34})_2]^{10-}$, consists of two $[VW_9O_{34}]^{9-}$ trivacant subunits which derive from the Keggin structure ($[VW_{12}O_{40}]^{3-}$) by removal of three adjacent edge-sharing octahedral WO_6 units. A tetra-manganese core is stabilized in the central belt position by two heptadentate $[VW_9O_{34}]^{9-}$ units (**Figure 6-3**). Two of the Mn(II) centers reside in distorted octahedra with one solvent accessible site and thus one

terminal labile water ligand each. The vanadium atoms occupying the center of each POM ligand reside in an approximately tetrahedral O_4 coordination environment.

Computational studies of the electronic structure of **1** provide additional support for the nature of Mn-centers. It was shown that **1** has several lower-lying electronic states among which the high-spin ferromagnetically coupled ^{21}A and the antiferromagnetically coupled ^{11}A and ^{1}A states are the lowest in energy and degenerate: the ^{11}A and ^{1}A states are calculated to be only 0.10 and 0.21 kcal/mol higher in energy than the ^{21}A state. In the other words, the antiferromagnetic interaction between the Mn-centers is insignificant. Spin density analyses indicates that in the ^{21}A electronic state of **1** its Mn^1, Mn^2, Mn^3 and Mn^4 centers have 4.82, 4.82, 4.78 and 4.78 |e| unpaired α-spins, respectively (see **Figure 6-5** for notation of atoms in **1**). In its ^{11}A state, the Mn^1, Mn^3 and Mn^4 centers are high-spin Mn(II) centers with 4.82, 4.79 and 4.79 |e| α-spins, respectively, while Mn^2 has 4.83 |e| b-spins. In the fully antiferromagnetically coupled ^{1}A state of **1**, the Mn^1 and Mn^3 centers are high-spin Mn(II) centers with 4.82 and 4.79 |e| α-spins, respectively, while the Mn^2 and Mn^4 centers have 4.83 and 4.79 |e| β-spins. We should mention that almost 0.80 |e| spins are located on the O-centers coordinated to Mn centers. The frontier orbital analysis (HOMOs and LUMOs) is consistent with the above electronic state analyses. The several top singly occupied MOs of the high-spin ground state of **1** are mostly Mn core orbitals, and there is small involvement of tungstate orbitals.

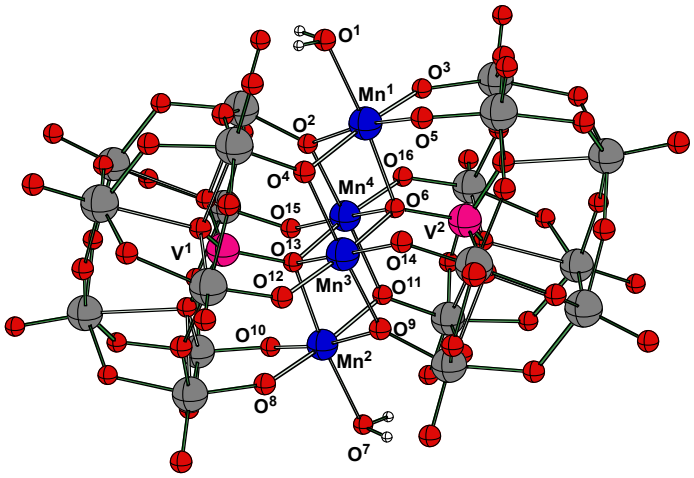

$[Mn_4(H_2O)_2(VW_9O_{34})_2]^{10-}$

Mn^1-O^1 = 2.263	Mn^2-O^7 = 2.263	Mn^3-O^4 = 2.144	Mn^4-O^2 = 2.144
Mn^1-O^2 = 2.178	Mn^2-O^8 = 2.083	Mn^3-O^6 = 2.237	Mn^4-O^6 = 2.236
Mn^1-O^3 = 2.083	Mn^2-O^9 = 2.178	Mn^3-O^9 = 2.144	Mn^4-O^{11} = 2.144
Mn^1-O^4 = 2.176	Mn^2-O^{10} = 2.084	Mn^3-O^{12} = 2.046	Mn^4-O^{13} = 2.236
Mn^1-O^5 = 2.084	Mn^2-O^{11} = 2.176	Mn^3-O^{13} = 2.236	Mn^4-O^{15} = 2.046
Mn^1-O^6 = 2.191	Mn^2-O^{12} = 2.191	Mn^3-O^{14} = 2.046	Mn^4-O^{16} = 2.046

V^1-O^{13} = 1.712 V^2-O^6 = 1.712

Figure 6-5 Notation of atoms and calculated important distances (in Å) of the polyoxoanion $[Mn_4(H_2O)_2(VW_9O_{34})_2]^{10-}$.

6.3.2. Photocatalytic H_2 Formation

The catalytic activity was initially studied by the commonly used system comprising $[Ru(bpy)_3]^{2+}$ (photosensitizer), methyl viologen (MV^{2+}; electron relay), and a H_2-evolution catalyst.[5,20,25,63] However, only small amount of H_2 was produced with **1** as a catalyst under such experimental conditions. Interestingly, in the absence of MV^{2+}, the yield of H_2 increases. The low activity of **1** with MV^{2+} as a relay is related to the low reduction potential of the $MV^{2+}/MV^{+\bullet}$ couple, -450 mV vs NHE relative to the reduction potential of the primary reducing agent, $[Ru(bpy)_3]^{2+*}$: $[Ru(bpy)_3]^{3+/2+*}$ = -840 mV vs NHE. As a consequence, the reduced methyl viologen, unlike the photoexcited $[Ru(bpy)_3]^{2+*}$, isn't sufficiently reducing to reduce complex **1** in the present system. Therefore, all the studies reported here involve a methyl viologen-free, three-component

system: $[Ru(bpy)_3]^{2+}$ as photosensitizer, TEOA as sacrificial electron donor and complex **1** as catalyst. In this system the catalyst is directly and readily reduced by $[Ru(bpy)_3]^{2+*}$.

As shown in **Figure 6-6**, no H_2 is formed in dark. After exposure to light for 0.5 h, a peak at 0.98 min was observed, corresponding to the formation of H_2. The contamination of the reaction vessel with air is seen as an increase in the N_2 peak at 1.2 min. Residual amounts of dioxygen give a peak at 1.08 min; however, O_2 is hard to detect because it is consumed under the reducing experimental conditions. Under minimally optimized conditions, 1.92 μmol H_2 gas per 0.046 μmol **1**, corresponding to a turnover number (TON) of 42, was obtained after 5.5 hrs of irradiation.

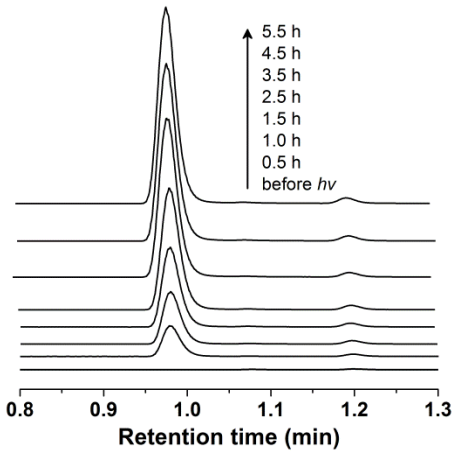

Figure 6-6 GC/TCD signal of H_2 production over time. Conditions: LED light (30 mW, 455 nm, beam diameter ~0.4 cm), TEOA (0.25 M), **1** (22.9 μM), $[Ru(bpy)_3]^{2+}$ (0.67 mM), 2 mL DMF/H_2O (1.86/ 1). The peak at 1.2 min is N_2.

Control experiments revealed that the presence of **1**, TEOA and $[Ru(bpy)_3]^{2+}$ are all essential for H_2 evolution: the absence of any one of these species results in only a trace of H_2 formation (**Figure 6-7A**). Additional control experiments using $TBA_3[VW_{12}O_{40}]$, freshly prepared MnO_2, VO_2 and WO_3 nanopowders (as possible products of catalyst decomposition) gave only negligible amounts of H_2 (**Figure 6-7A**).

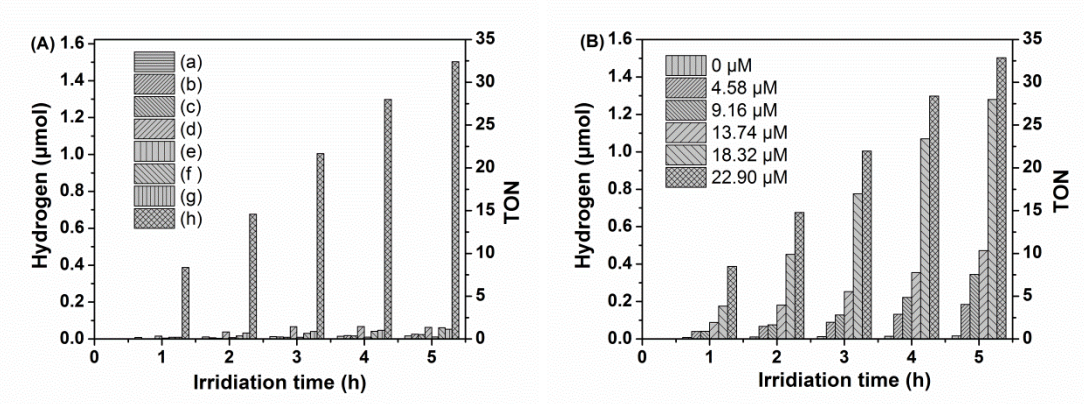

Figure 6-7 (A) Photocatalytic H_2 evolution with a) no catalyst; b) no $[Ru(bpy)_3]^{2+}$; c) no TEOA; d) 0.5 mg freshly prepared MnO_2; e) 3 mg WO_3; f) 0.8 mg VO_2; g) 55 μM $TBA_3[VW_{12}O_{40}]$; h) 22.9 μM **1** and (B) photocatalytic H_2 evolution with different concentrations of 1. Conditions: LED light (30 mW, 455 nm, beam diameter ~0.4 cm), $[Ru(bpy)_3]^{2+}$ (0.67 mM), TEOA (0.25 M), catalyst **1** (0 - 22.9 μM), 2 mL DMF/H_2O (1.86/ 1).

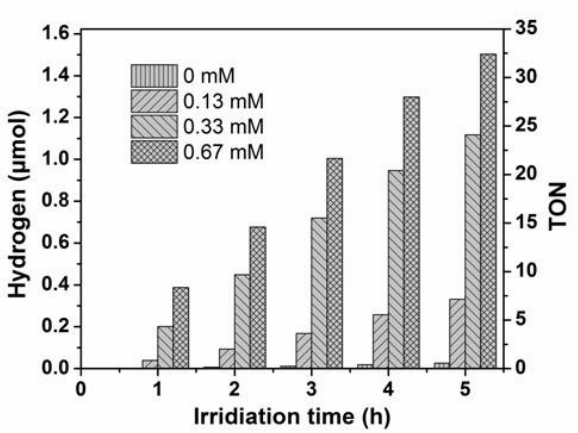

Figure 6-8 Photocatalytic H_2 evolution with different concentrations of $[Ru(bpy)_3]^{2+}$ under otherwise identical conditions: LED light (30 mW, 455 nm, beam diameter ~0.4 cm), TEOA (0.25 M), 22.9 μM **1**, 2 mL DMF/H_2O (1.86/ 1).

The H_2 yield also depends on pH and the concentrations of $[Ru(bpy)_3]^{2+}$, TEOA and **1**. As shown in **Figure 6-7B**, increasing the concentration of **1** from 4.6 to 23 μM at pH 9.5 (0.25 M TEOA and 0.67 mM $[Ru(bpy)_3]^{2+}$) results in an increase in the H_2 yield from 0.18 to 1.51 μmol after 5 hrs of illumination. The concentration of the photosensitizer, $[Ru(bpy)_3]^{2+}$, strongly affects the rate and final yield of H_2 (**Figure 6-8**). The amount of

H_2 formed increases with an increase of $[Ru(bpy)_3]^{2+}$ concentration from 0.13 mM to 0.67 mM.

In contrast, the concentration of TEOA has a minor effect on final H_2 yield (**Figure 6-9**). The rate of photocatalytic H_2 production is pH dependent. The maximum rate of H_2 evolution and the final yield of H_2 is observed at higher pH (**Figure 6-10**), despite that H^+ reduction becomes less thermodynamically favorable at higher pH. H_2 production rates and yields maximize when TEOA is fully deprotonated (the pK_a of $TEOAH^+$ is 7.74).[10,25,64]

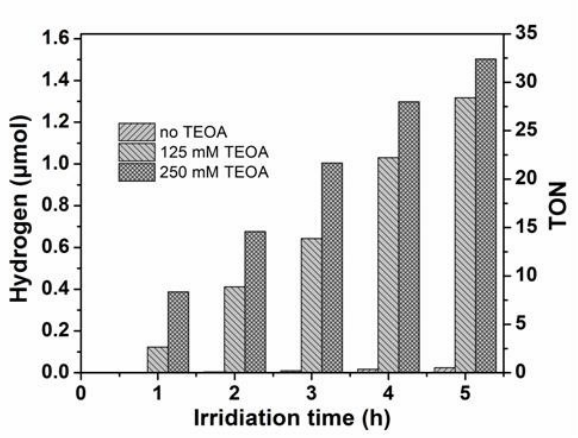

Figure 6-9 Photocatalytic H_2 evolution with different TEOA concentrations at parity of other conditions: LED light (30 mW, 455 nm, beam diameter ~0.4 cm), $[Ru(bpy)_3]^{2+}$ (0.67 mM), 22.9 μM **1**, 2 mL DMF/H_2O (1.86/ 1).

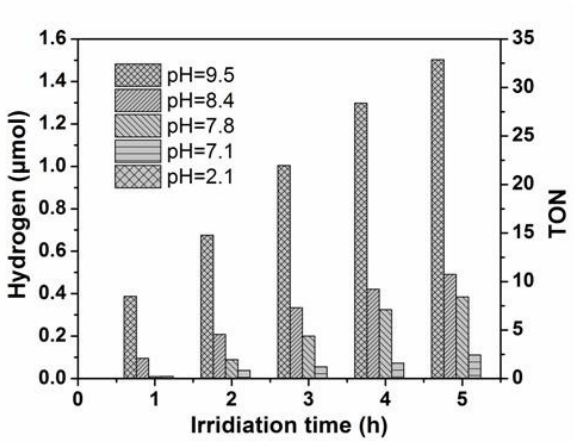

Figure 6-10 Photocatalytic H_2 evolution at different pH values. Conditions: LED light (30 mW, 455 nm, beam diameter ~0.4 cm), $[Ru(bpy)_3]^{2+}$ (0.67 mM), TEOA (0.25 M), catalyst **1** (22.9 μM), 2 mL DMF/H_2O (1.86/ 1).

6.3.3. Determination of the Origin of H_2

To determine the source of H_2, isotope labeling experiments with either H_2O or D_2O as solvent were conducted. The formation of H_2 and D_2 can be distinguished by GC-TCD if helium is used as a carrier gas due to their thermal conductivity difference.[65-67]

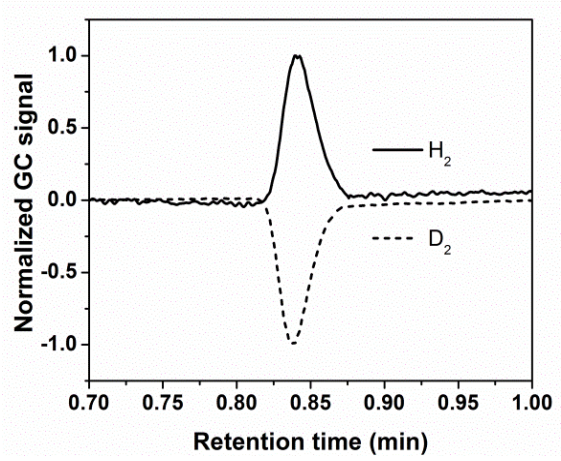

Figure 6-11 Normalized GC signal of H_2 and D_2 evolved as monitored by GC-TCD using helium as carrier gas. Conditions: LED light (30 mW, 455 nm, beam diameter ~0.4 cm), $[Ru(bpy)_3]Cl_2$ (0.67 mM), TEOA (0.25 M), **1** (22.9 μM), 2 mL DMF/H_2O (or DMF/D_2O) (1.86/ 1).

Figure 6-11 shows the normalized GC signal of H_2 and D_2 generated in the full photocatalytic system. Specifically, H_2, indicated by a positive peak at ~0.84 min, forms when H_2O is the proton source, and D_2, indicated by a negative peak at ~0.84 min, forms when D_2O is the proton source. These results clearly demonstrate that water is the source of hydrogen during the photocatalytic reaction.

6.3.4. Catalyst Stability Tests

A central point of this study is to address the possibility of formulating a homogeneous WRC or family of WRCs that are thermodynamically stable to hydrolytic decomposition under turnover conditions, a challenge not met by nearly all known homogeneous WRCs. In this context we have examined the stability of **1** using multiple spectroscopic methods under aqueous catalytic turnover conditions. First, the electronic absorption spectrum of **1** under these conditions shows less than 1% change after three days (**Figure 6-4**). **Figure 6-12** gives the time-dependent data of the UV-vis absorbance in first 21 hours. Second, the FT-IR spectra (**Figure 6-13**) confirm the integrity of **1** before and after catalysis. As shown in **Figure 6-13**, the characteristic IR bands of **1** are basically retained after 24 hours of irradiation. Control experiment (**Figure 6-13c**) shows that the other IR bands result from TEOA and bpy oxidation products.

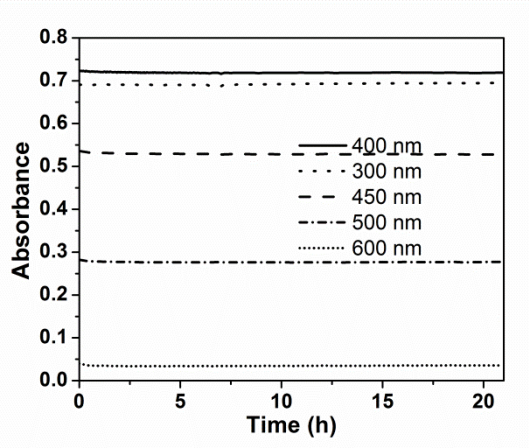

Figure 6-12 Time-dependent data of UV-vis absorbance of 0.38 mM TBA**1** in the mixed solvent of DMF/H_2O (3/1) containing 0.25 M TEOA.

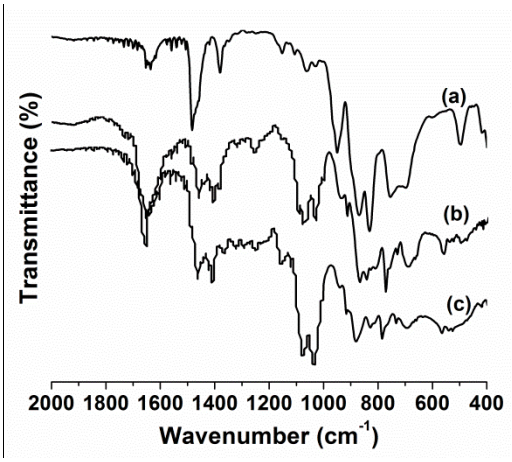

Figure 6-13 FT-IR spectra of (a) TBA**1** before light-driven reaction; (b) the same sample after reaction (re-isolated from post-catalytic reaction solution, illumination time 24 hrs, TON ~ 87) and (c) isolated sample before light-driven reaction from the solution containing $[Ru(bpy)_3]^{3+}$ and TEOA. Control experiments show that the additional peaks in the "after catalysis" reaction derive from bpy and TEOA oxidation products. All FT-IR spectra were 2 wt% samples in KBr.

6.3.5. Mechanistic Studies

The direct reduction of **1** by $[Ru(bpy)_3]^{2+*}$ was first confirmed by steady-state fluorescence spectroscopy. Excitation of $[Ru(bpy)_3]^{2+}$ at λ_{max} = 455 nm results in a luminescence at λ_{max} = 612 nm with emission quantum yield of 0.062.[68] The excited state can be either reductively or oxidatively quenched by an electron donor or acceptor,[69-72]

resulting in a decrease of the fluorescence intensity.[69-72] **Figure 6-14** shows the luminescence spectra of deairated solutions of $[Ru(bpy)_3]^{2+}$ (DMF/H_2O = 1.86/1, v/v).

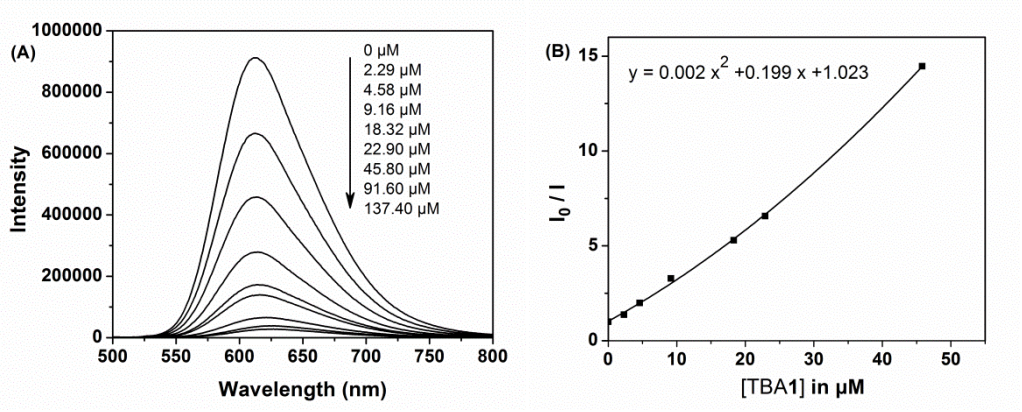

Figure 6-14 (A) Emission spectra of $[Ru(bpy)_3]^{2+}$ as a function of added **1** and (B) Stern-Volmer plot for emission quenching of $[Ru(bpy)_3]^{2+}$ by **1**. The concentration of $[Ru(bpy)_3]^{2+}$ was 2×10^{-5} M.

The excited state $[Ru(bpy)_3]^{2+*}$ is dramatically quenched by **1**. The Stern-Volmer plot deviates from linearity (**Figure 6-14B**), indicating the presence of static as well as dynamic quenching. Approximate fitting of the Stern-Volmer plot by linear function gives an apparent quenching rate constant of 2.8×10^{11} M^{-1} s^{-1}. This is faster than diffusion control ($\sim 10^{10}$ M^{-1} s^{-1}) consistent with a contribution of static quenching via formation of a $\{\mathbf{1}\ldots[Ru(bpy)_3]^{2+*}\}$[17] complex.[73-75] Although the efficient quenching of excited states may also happen by energy transfer,[72,76,77] the small spectral overlap between the absorption of the catalyst, **1**, (**Figure 6-4**) and the emission of $[Ru(bpy)_3]^{2+}$ (**Figure 6-14A**) makes this pathway unimportant.[78] Importantly, at $[\mathbf{1}] < [Ru(bpy)_3]^{2+}$ the drop of emission intensity, $(1 - I/I_o)$ is about twice higher than $(1 - [\mathbf{1}]/[Ru(bpy)_3]^{2+})$. This is consistent with reduction of **1** by more than one electron. The reductive quenching of $[Ru(bpy)_3]^{2+*}$ by TEOA is ruled out because the addition of TEOA in concentrations up to 0.25 M does not affect the luminescence intensity (**Figure 6-15**).[69] The reduction of

$[Ru(bpy)_3]^{3+}$ by TEOA proceeds very rapidly, confirming the ability of TEOA to serve as an efficient sacrificial electron donor (**Figure 6-16**).

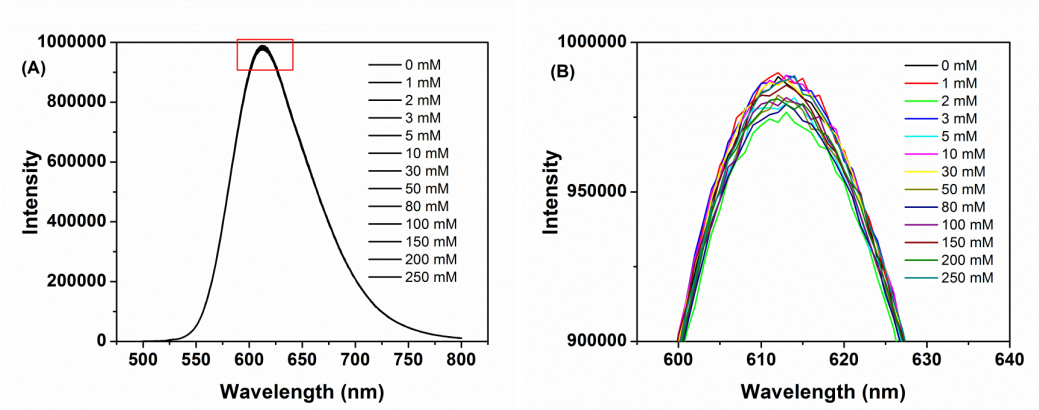

Figure 6-15 (A) Emission spectra of $[Ru(bpy)_3]^{2+}$ at different concentrations of added TEOA and (B) magnification of the red rectangular region in (A). The concentration of $[Ru(bpy)_3]^{2+}$ was 2×10^{-5} M.

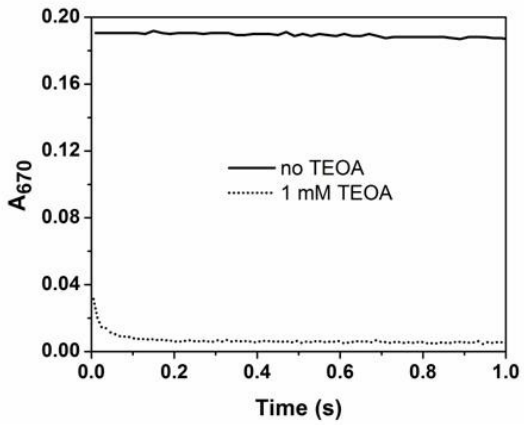

Figure 6-16 Stoichiometric reduction of $[Ru(bpy)_3]^{3+}$ by TEOA. Conditions: 0.454 mM $[Ru(bpy)_3]^{3+}$ (final), 1 mM TEOA in water, 298 K.

To further investigate the reaction mechanism, we used time-resolved fluorescence spectroscopy to follow the kinetics of fluorescence decay of $[Ru(bpy)_3]^{2+}$ ($\lambda_{excitation}$ = 400 nm). **Figure 6-17** clearly shows that TEOA does not affect the fluorescence decay ($\tau_{1/2}$ values are 0.60 and 0.57 μs in the absence and presence of TEOA, respectively) in

agreement with the steady state fluorescence quenching results. The kinetics of fluorescence decay in the presence of **1** is bi-exponential with life-times of 21 and 540 ns. The slower component is assigned to the light emission by $[Ru(bpy)_3]^{2+*}$, while the faster component (21 ns) is attributed to the efficient electron transfer process from excited $[Ru(bpy)_3]^{2+}$ to the proximal catalyst **1**. This electron transfer rate (4.7×10^7 s^{-1}) is much faster than the diffusion-limited bimolecular quenching rate (estimated to be 2.7×10^5 s^{-1} based on approximated rate constant of $\sim 10^{10}$ M^{-1} s^{-1} with the catalyst, **1**, at a concentration of 27 μM). These data, together with the bi-exponential decay behavior, suggest that electron transfer occurs within a $\{\mathbf{1}\ldots[Ru(bpy)_3]^{2+*}\}$ complex present in DMF/H_2O solutions.

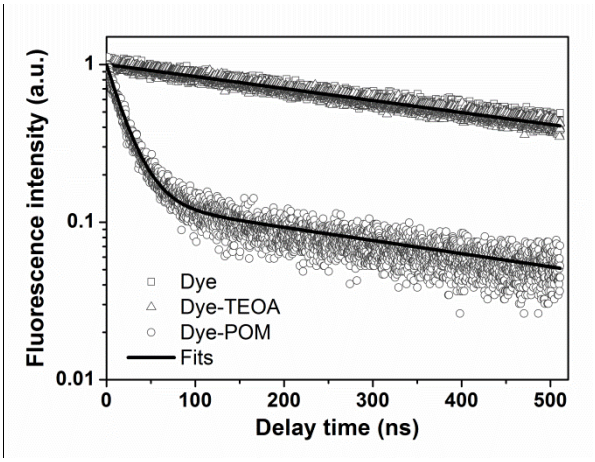

Figure 6-17 Normalized fluorescence decay of $[Ru(bpy)_3]^{2+}$ (dark grey rectangles) and $[Ru(bpy)_3]^{2+}$ with TEOA (grey triangles) and $[Ru(bpy)_3]^{2+}$ with catalyst **1** (light grey circles). Conditions: 20 μM $[Ru(bpy)_3]^{2+}$, 20 mM TEOA and 27 μM catalyst **1**. The black solid lines are best fits according to single exponential decay (for the former two) and biexponential decay (for the latter). The y-axis is in log scale.

A proposed qualitative mechanism for this visible-light-induced, aqueous-medium catalytic H_2 evolution is shown in **Scheme 6-1**.

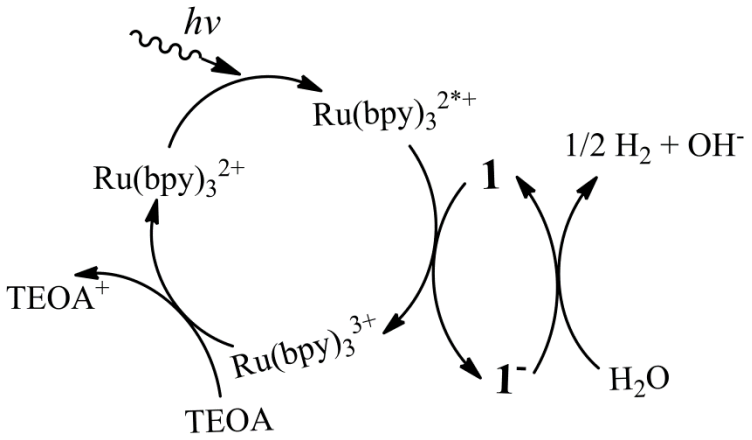

Scheme 6-1 Proposed mechanism for light-driven hydrogen evolution catalyzed by **1**.

Upon visible light irradiation, the excited state $[Ru(bpy)_3]^{2+*}$ is oxidatively quenched by catalyst **1** through oxidative electron transfer, producing $[Ru(bpy)_3]^{3+}$ which is rapidly reduced by the sacrificial electron donor, TEOA, to regenerate the photosensitizer $[Ru(bpy)_3]^{2+}$. In the second cycle the catalyst gains one more electron and then reduces water to produce H_2. Optimization of the catalytic system and further investigation of the reaction mechanism are in progress.

6.4 Conclusions

In conclusion, we have successfully prepared a tetra-manganese-containing V-centered polyoxotungstate, $Na_{10}[Mn_4(H_2O)_2(VW_9O_{34})_2]$ (**1**). The electronic structure of **1** was elucidated using the DFT approach. Complex **1** is readily prepared by a one-pot procedure in aqueous solution and catalyzes the reduction of water using visible light irradiation (λ = 455 nm) with $[Ru(bpy)_3]^{2+}$ and triethanolamine (TEOA) as a photosensitizer and sacrificial electron donor, respectively. Upon irradiation, the excited state $[Ru(bpy)_3]^{2+*}$ is oxidatively quenched by **1**, as confirmed by steady-state and time-resolved fluorescence decay studies, to form $[Ru(bpy)_3]^{3+}$ and a reduced form of the

catalyst. The $[Ru(bpy)_3]^{2+}$ is rapidly regenerated by reaction with TEOA. The reduced form of the catalyst, **1**, reacts with water to generate hydrogen. Isotope labeling experiments demonstrate that the hydrogen comes from water. Multiple spectroscopic methods confirm the integrity of **1** before and after catalysis.

References

(1) Lewis, N. S.; Nocera, D. G. *Proc. Natl. Acad. Sci. USA* **2006**, *103*, 15729.

(2) Fujita, E.; Muckerman, J. T.; Domen, K. *ChemSusChem* **2011**, *4*, 155157.

(3) Kudo, A.; Miseki, Y. *Chem. Soc. Rev.* **2009**, *38*, 253.

(4) Bard, A. J.; Fox, M. A. *Acc. Chem. Res.* **1995**, *28*, 141.

(5) Kirch, M.; Lehn, J.-M.; Sauvage, J.-P. *Helv. Chim. Acta* **1979**, *62*, 1345.

(6) Zhu, H.; Song, N.; Lv, H.; Hill, C. L.; Lian, T. *J. Am. Chem. Soc.* **2012**, *134*, 11701.

(7) Lv, H. J.; Ma, L.; Zeng, P.; Ke, D. N.; Peng, T. Y. *J. Mater. Chem.* **2010**, *20*, 3665.

(8) Han, Z.; Qiu, F.; Eisenberg, R.; Holland, P. L.; Krauss, T. D. *Science* **2012**, *338*, 1321.

(9) Keller, P.; Moradpour, A. *J. Am. Chem. Soc.* **1980**, *102*, 7193.

(10) Kalyanasundaram, K.; Kiwi, J.; Grätzel, M. *Helv. Chim. Acta* **1978**, *61*, 2720.

(11) Cline, E. D.; Adamson, S. E.; Bernhard, S. *Inorg. Chem.* **2008**, *47*, 10378.

(12) Du, P.; Knowles, K.; Eisenberg, R. *J. Am. Chem. Soc.* **2008**, *130*, 12576.

(13) Kunkely, H.; Vogler, A. *Angew. Chem. Int. Ed.* **2009**, *48*, 1685.

(14) Zou, Z.; Ye, J.; Sayama, K.; Arakawa, H. *Nature* **2001**, *414*, 625.

(15) Peng, T.; Zhang, X.; Lv, H.; Zan, L. *Catal. Commun.* **2012**, *28*, 116.

(16) Esswein, A. J.; Nocera, D. G. *Chem. Rev. (Washington, DC, U. S.)* **2007**, *107*, 4022.

(17) Muckerman, J. T.; Fujita, E. *Chem. Commun. (Cambridge, U. K.)* **2011**, *47*.

(18) Singh Bindra, G.; Schulz, M.; Paul, A.; Soman, S.; Groarke, R.; Inglis, J.; Pryce, M. T.; Browne, W. R.; Rau, S.; Maclean, B. J.; Vos, J. G. *Dalton Trans.* **2011**, *40*, 10812.

(19) Heyduk, A. F.; Nocera, D. G. *Science* **2001**, *293*, 1639.

(20) Yamauchi, K.; Masaoka, S.; Sakai, K. *J. Am. Chem. Soc.* **2009**, *131*, 8404.

(21) Ozawa, H.; Haga, M.-a.; Sakai, K. *J. Am. Chem. Soc.* **2006**, *128*, 4926.

(22) Nielsen, M.; Kammer, A.; Cozzula, D.; Junge, H.; Gladiali, S.; Beller, M. *Angew. Chem. Int. Ed.* **2011**, *50*, 9593.

(23) Singh, W. M.; Pegram, D.; Duan, H.; Kalita, D.; Simone, P.; Emmert, G. L.; Zhao, X. *Angew. Chem. Int. Ed.* **2012**, *51*, 1653.

(24) Zhang, J.; Du, P.; Schneider, J.; Jarosz, P.; Eisenberg, R. *J. Am. Chem. Soc.* **2007**, *129*, 7726.

(25) Du, P.; Schneider, J.; Jarosz, P.; Eisenberg, R. *J. Am. Chem. Soc.* **2006**, *128*, 7726.

(26) Wang, F.; Wang, W.-G.; Wang, H.-Y.; Si, G.; Tung, C.-H.; Wu, L.-Z. *ACS Catalysis* **2012**, *2*, 407.

(27) Nocera, D. G. *Acc. Chem. Res.* **2012**, *45*, 767.

(28) Artero, V.; Chavarot-Kerlidou, M.; Fontecave, M. *Angew. Chem. Int. Ed.* **2011**, *50*, 7238.

(29) Geletii, Y. V.; Botar, B.; Kögerler, P.; Hillesheim, D. A.; Musaev, D. G.; Hill, C. L. *Angew. Chem. Int. Ed.* **2008**, *47*, 3896.

(30) Sartorel, A.; Carraro, M.; Scorrano, G.; Zorzi, R. D.; Geremia, S.; McDaniel, N. D.; Bernhard, S.; Bonchio, M. *J. Am. Chem. Soc.* **2008**, *130*, 5006.

(31) Yin, Q.; Tan, J. M.; Besson, C.; Geletii, Y. V.; Musaev, D. G.; Kuznetsov, A. E.; Luo, Z.; Hardcastle, K. I.; Hill, C. L. *Science* **2010**, *328*, 342.

(32) Car, P.-E.; Guttentag, M.; Baldridge, K. K.; Alberto, R.; Patzke, G. R. *Green Chem.* **2012**.

(33) Tanaka, S.; Annaka, M.; Sakai, K. *Chem. Commun. (Cambridge, U. K.)* **2012**, *48*, 1653.

(34) Zhu, G.; Geletii, Y. V.; Kogerler, P.; Schilder, H.; Song, J.; Lense, S.; Zhao, C.; Hardcastle, K. I.; Musaev, D. G.; Hill, C. L. *Dalton Trans.* **2012**, *41*, 2084.

(35) Zhu, G.; Glass, E. N.; Zhao, C.; Lv, H.; Vickers, J. W.; Geletii, Y. V.; Musaev, D. G.; Song, J.; Hill, C. L. *Dalton Trans.* **2012**, *41*, 13043.

(36) Lv, H.; Geletii, Y. V.; Zhao, C.; Vickers, J. W.; Zhu, G.; Luo, Z.; Song, J.; Lian, T.; Musaev, D. G.; Hill, C. L. *Chem. Soc. Rev.* **2012**, *41*, 7572.

(37) Papaconstantinou, E. *J. Chem. Soc., Chem. Commun.* **1982**.

(38) Papaconstantinou, E.; Pope, M. T. *Inorg. Chem.* **1970**, *9*, 667.

(39) Papaconstantinou, E.; Pope, M. T. *Inorg. Chem.* **1967**, *6*, 1152.

(40) Papaconstantinou, E.; Dimoticali, D.; Ioannidis, A.; Argitis, P. *Journal of Photochemistry* **1981**, *17*, 171.

(41) Savinov, E. N.; Saidkhanov, S. S.; Parmon, V. N.; Zamaraev, K. I. *React. Kinet. Catal. Lett.* **1981**, *17*, 407.

(42) Hill, C. L.; Bouchard, D. A. *J. Am. Chem. Soc.* **1985**, *107*, 5148.

(43) Renneke, R. F.; Hill, C. L. *J. Am. Chem. Soc.* **1986**, *108*, 3528.

(44) Hill, C. L.; Renneke, R. F.; Combs, L. *Tetrahedron* **1988**, *44*, 7499.

(45) Renneke, R. F.; Hill, C. L. *Angew. Chem. Int. Ed.* **1988**, *27*, 1526.

(46) Renneke, R. F.; Hill, C. L. *J. Am. Chem. Soc.* **1988**, *110*, 5461.

(47) Matt, B.; Fize, J.; Moussa, J.; Amouri, H.; Pereira, A.; Artero, V.; Izzet, G.; Proust, A. *Energy Environ. Sci.* **2013**, *6*, 1504.

(48) Ghosh, P. K.; Brunschwig, B. S.; Chou, M.; Creutz, C.; Sutin, N. *J. Am. Chem. Soc.* **1984**, *106*, 4772.

(49) Li, B.; Yan, Y.; Li, F.; Xu, L.; Bi, L.; Wu, L. *Inorg. Chim. Acta* **2009**, *362*, 2796.

(50) Katsoulis, D. E.; Pope, M. T. *J. Am. Chem. Soc.* **1984**, *106*, 2737.

(51) Bruker; BRUKER AXS Inc.: Madison, WI, USA, 2012.

(52) Bruker; BRUKER AXS Inc.: Madison, WI, USA., 2009.

(53) Bruker; BRUKER AXS Inc.: Madison, WI, USA., 2008.

(54) Dolomanov, O. V.; Bourhis, L. J.; Gildea, R. J.; Howard, J. A. K.; Puschmann, H. *J. Appl. Crystallogr.* **2009**, *42*, 339.

(55) Sheldrick, G. *Acta Cryst. A* **2008**, *64*, 112.

(56) Himeno, S.; Takamoto, M.; Higuchi, A.; Maekawa, M. *Inorg. Chim. Acta* **2003**, *348*, 57.

(57) Frisch, M. J.; Trucks, G. W.; Schlegel, H. B.; Scuseria, G. E.; Robb, M. A.; Cheeseman, J. R.; Scalmani, G.; Barone, V.; Mennucci, B.; Petersson, G. A.; Nakatsuji, H.; Caricato, M.; Li, X.; Hratchian, H. P.; Izmaylov, A. F.; Bloino, J.; Zheng, G.; Sonnenberg, J. L.; Hada, M.; Ehara, M.; Toyota, K.; Fukuda, R.; Hasegawa, J.; Ishida, M.; Nakajima, T.; Honda, Y.; Kitao, O.; Nakai, H.; Vreven, T.; J. A. Montgomery, J.; Peralta, J. E.; Ogliaro, F.; Bearpark, M.; Heyd, J. J.; Brothers, E.; Kudin, K. N.; Staroverov, V. N.; Kobayashi, R.; Normand, J.; Raghavachari, K.; Rendell, A.; Burant, J. C.; Iyengar, S. S.; Tomasi, J.; Cossi, M.; N. Rega, J. M. M.; Klene, M.; Knox, J. E.; Cross, J. B.; Bakken, V.; Adamo, C.; Jaramillo, J.; Gomperts, R.; Stratmann, R. E.; Yazyev, O.; Austin, A. J.; Cammi, R.; Pomelli, C.; Ochterski, J. W.; Martin, R. L.; K. Morokuma, V. G. Z.; Voth, G. A.; Salvador, P.; Dannenberg, J. J.; Dapprich, S.; Daniels, A. D.; Ö. Farkas, J. B. F.; Ortiz, J. V.; Cioslowski, J.; Fox, D. J.; Revision A.1 ed.; Gaussian, I., Ed. Wallingford CT., 2009.

(58) Zhao, Y.; Truhlar, D. G. *J. Chem. Phys.* **2006**, *125*, 194101.

(59) Hay, P. J.; Wadt, W. R. *J. Chem. Phys.* **1985**, *82*, 270.

(60) Wadt, W. R.; Hay, P. J. *J. Chem. Phys.* **1985**, *82*, 284.

(61) Hay, P. J.; Wadt, W. R. *J. Chem. Phys.* **1985**, *82*, 299.

(62) Cances, E.; Mennucci, B.; Tomasi, J. *J. Chem. Phys.* **1997**, *107*, 3032.

(63) Borgarello, E.; Kiwi, J.; Pelizzetti, E.; Visca, M.; Graetzel, M. *J. Am. Chem. Soc.* **1981**, *103*, 6324.

(64) Miller, D. S.; McLendon, G. *J. Am. Chem. Soc.* **1981**, *103*, 6791.

(65) Snavely, K.; Subramaniam, B. *J. Chromatogr. Sci.* **1998**, *36*, 191.

(66) Garwin, E. L.; Roder, A. *J. Chromatogr. Sci.* **1976**, *14*, 541.

(67) Degtyareva, O. F.; Bondareva, L. T. *J. Anal. Chem.* **2004**, *59*, 442.

(68) Calvert, J. M.; Caspar, J. V.; Binstead, R. A.; Westmoreland, T. D.; Meyer, T. J. *J. Am. Chem. Soc.* **1982**, *104*, 6620.

(69) Sun, H.; Hoffman, M. Z. *J. Phys. Chem.* **1994**, *98*, 11719.

(70) Geletii, Y. V.; Huang, Z.; Hou, Y.; Musaev, D. G.; Lian, T.; Hill, C. L. *J. Am. Chem. Soc.* **2009**, *131*, 7522.

(71) Juris, A.; Balzani, V.; Barigelletti, F.; Campagna, S.; Belser, P.; von Zelewsky, A. *Coord. Chem. Rev.* **1988**, *84*, 85.

(72) Sutin, N. *Journal of Photochemistry* **1979**, *10*, 19.

(73) Walsh, J. J.; Long, D.-L.; Cronin, L.; Bond, A. M.; Forster, R. J.; Keyes, T. E. *Dalton Trans.* **2011**, *40*, 2038.

(74) Dung, D.; Ramsden, J.; Graetzel, M. *J. Am. Chem. Soc.* **1982**, *104*, 2977.

(75) Ballardini, R.; Gandolfi, M. T.; Balzani, V. *Inorg. Chem.* **1987**, *26*, 862.

(76) Sutin, N.; Creutz, C. *Pure Appl. Chem.* **1980**, *52*, 2717.

(77) Whitten, D. G. *Acc. Chem. Res.* **1980**, *13*, 83.

(78) Symes, M. D.; Lutterman, D. A.; Teets, T. S.; Anderson, B. L.; Breen, J. J.; Nocera, D. G. *ChemSusChem* **2013**, *6*, 65.

Chapter 7

A Noble-Metal-Free, Tetra-nickel Polyoxotungstate Catalyst for Efficient Photocatalytic Hydrogen Evolution

(Published in *J. Am. Chem. Soc.* **2014***, 136,* 14015-14018.)

With Weiwei Guo, Kaifeng Wu, Zheyuan Chen, John Bacsa, Djamaladdin G. Musaev, Yurii V. Geletii, Sarah M. Lauinger, Tianquan Lian, Craig L. Hill*

7.1 Introduction

The photocatalytic splitting of water into dihydrogen and dioxygen utilizing solar energy has become a very active research area recently.[1-7] Current research endeavors focus on developing efficient, robust, inexpensive, sustainable, and environmentally-benign catalytic systems for each half reaction, i.e. water oxidation or water reduction. Since early reports on molecular photocatalytic water-reducing systems in the late 1970s,[8,9] many organometallic complexes of several earth-abundant metals including iron,[10-12] cobalt,[13-18] nickel,[19-23] and molybdenum[24,25] have been used as molecular catalysts for photochemically- and electrochemically-driven hydrogen production. Although some of these systems are sufficiently robust to achieve high turnover numbers (TON higher than 10^3),[15,17-19,21-23] many others have the problems of either low efficiency, limited solubility in aqueous media, instability towards strong acidic environments, or they deactivate by ligand dissociation, decomposition and/or hydrogenation.[26-28] Therefore, the development of new transition-metal-based catalysts that are highly efficient, very stable, structurally and geometrically tunable remains a substantial challenge.

Polyoxometalates (POMs), a large family of transition-metal oxygen-anion clusters with d^0 electronic configurations, are attractive candidates for catalysis of multi-electron processes because of their extensive tunability, rich redox chemistry and high stability towards hydrolysis in water or hydrogenation under reducing conditions.[29-33] Recently, transition-metal-substituted POMs have been extensively investigated as water oxidation catalysts (WOCs) under thermal,[34-41] photochemical[42-52] and electrochemical[53-57] conditions; however, this is not the case for POM-based water reduction catalysts (WRCs). There are early studies that show reduced POMs evolve H_2 *via* photochemical[58-

[62] or electrochemical[63,64] processes, but all these studies involve either strong UV-light irradiation or the use of Pt(0) as a co-catalyst.

To date, there are only few reports on visible-light-driven H_2 evolution by POM WRCs,[65-69] and only two of them are Pt(0) free.[67,68] The first example by Artero, Izzet, and coworkers involves a covalently-linked Ir(III)-photosensitized polyoxometalate complex, which catalyzes H_2 production with a TON of 41 after 7 days of visible light irradiation.[67] The second example, recently reported by our group, is a tetramanganese-containing POM, $[Mn_4(H_2O)_2(VW_9O_{34})_2]^{10-}$ (**Mn_4V_2**) that catalyzes hydrogen evolution from water with a TON of 42 after 5.5 h of visible light irradiation. Although the efficiency of the **Mn_4V_2** system is higher than that of the Ir^{III}-photosensitized POM catalyst,[67] there is still much room for improvement. In an effort to develop more viable (fast, selective and stable), more efficient, and noble-metal-free molecular WRCs, we report here a tetra-nickel-substituted polyoxometalate, $[Ni_4(H_2O)_2(PW_9O_{34})_2]^{10-}$ (Na_6K_4-**Ni_4P_2**), that works as an efficient and robust molecular catalyst for H_2 production in a three-component system upon visible light irradiation.

7.2 Experimental

7.2.1. Materials and Instrumentation

All reagents and solvents were purchased from commercial sources unless otherwise noted, which were used as received without further purification unless otherwise noted. Water for the preparation of solutions was obtained from a Barnstead Nanopure® water-purification system.

The FT-IR spectra were measured on a Thermo Nicolet 6700 spectrometer. UV-Vis spectra were acquired using Agilent 8453 spectrophotometer equipped with a diode-array detector and an Agilent 89090A cell temperature controller unit. Elemental analyses were performed by Galbraith Lab Inc., Knoxville, TN, 37921. Thermogravimetric data were collected on Instrument Specialists Incorporated TGA 1000 instruments. Cyclic voltammograms were recorded using a WaveDriver 20 Bipotentiostat (Pine Research Instrumentation) and a three-electrode setup, with glassy carbon disk (working), Pt-wire (auxiliary), and Ag/Ag^+ (in acetonitrile with 0.01 M $AgNO_3$ and 0.1 M $TBAPF_6$ reference) electrodes. The ferrocene/ferrocenium couple was used as an internal standard for calibration. Mass spectrometry determinations were carried out on a Thermo Finnigan LTQ-FTMS spectrometer with electrospray (ESI) ionization. Analysis of hydrogen in the reaction headspace was performed using a HP7890A model gas chromatograph equipped with thermal conductivity detector (TCD) and a 5Å molecular sieve capillary column. The steady-state luminescence quenching spectra were recorded on a FluoroMax 3 spectrofluorimeter. For time-resolved fluorescence decay measurements, femtosecond laser pulses (~100 fs, 80 MHz repetition rate) were generated with a mode-locked Ti:sapphire laser (Tsunami oscillator pumped by 10 W Millennia Pro, Spectra-Physics). Excitation pulses at 400 nm were generated by second harmonic generation of the 800 nm pulses in a BBO crystal. The repetition rate of output pulse centered at 800 nm was reduced to 1.6 MHz using a pulse picker (Conoptics, USA). The emissions of $[Ir(ppy)_2(dtbbpy)]^+$ were detected by a microchannel plate photomultiplier tube (Hamamatsu R3809U-51), whose output was amplified and analyzed by a TCSPC board (Becker & Hickel SPC 600). Nanosecond (0.5 ns to 50 μs) transient absorption

measurement was performed with the EOS spectrometer (Ultrafast Systems LLC). The pump pulses at 400 nm were generated in the regeneratively amplified Ti:sapphire laser system described above. The white light continuum probe pulse (380 to 1700 nm, 0.5 ns pulse width, 20 kHz repetition rate) was generated by focusing a Nd:YAG laser into a photonic crystal fiber. The probe pulses were synchronized with the femtosecond amplifier, and the delay time was controlled by a digital delay generator (CNT-90, Pendulum Instruments). The probe light was detected in fiberoptics coupled multichannel spectrometers with CMOS sensors.

7.2.2. Synthesis of polyanion $[Ni_4(H_2O)_2(PW_9O_{34})_2]^{10-}$ (Ni_4P_2)

$Na_6K_4[Ni_4(H_2O)_2(PW_9O_{34})_2]\cdot 32H_2O$ (Na_6K_4-**Ni_4P_2**) was synthesized according to modified literature method[70] as follows: $Na_2WO_4\cdot 2H_2O$ (33 g, 100 mmol) and Na_2HPO_4 (1.57 g, 11 mmol) were dissolved in 100 mL Nanopure® water with the pH adjusted to 7.0 using concentrated acetic acid. To this was added slowly with vigorously stirring a solution of $Ni(OOCCH_3)_2\cdot 4H_2O$ (5.5 g, 22 mmol) in 50 mL Nanopure® water. The resulting mixture was refluxed for 2.5 hrs and filtered hot to remove any precipitate, then 4 g of $K(OOCCH_3)$ was added and the hot yellow solution left for crystallization. A mixture of small yellow high quality crystals and crystalline powder of the desired products was collected by filtration with high yield (22.1 g, 73%). One single crystal was submitted to structural analysis by X-ray crystallography and the bulk sample was analyzed by elemental analysis. Elemental analysis for Na_6K_4-**Ni_4P_2**: calcd. For Na, 2.46; K, 2.79; Ni, 4.19; P, 1.11; W, 59.08%; found for Na, 2.39; K, 2.81; Ni, 4.23; P, 1.18; W, 60.01%. FT-IR (2% KBr pellet, cm^{-1}, **Figure 7-1**): 1044(s), 1017 (s), 963(sh), 940(s), 891(m), 778(sh), 721 (s), and 500 (w).

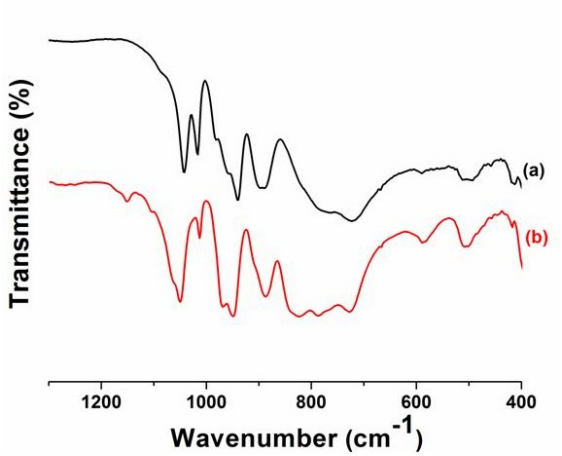

Figure 7-1 FT-IR spectra of (a) Na_6K_4-**Ni_4P_2** (black) and (b) TBA-**Ni_4P_2** (red), ~ 2 wt % in KBr. The spectra show all the characteristic bands of polyanion **Ni_4P_2** confirming that the cation exchange (TBA^+ for Na^+ and K^+) does not change the structure of **Ni_4P_2**.

The tetrabutylammonium (TBA^+) salt of **Ni_4P_2** (TBA-**Ni_4P_2**) was prepared using following procedure: typically, Na_6K_4-**Ni_4P_2** (5 g, 1 mmol) was dissolved in 40 mL H_2O, to which a solution of tetrabutylammonium bromide (TBABr, 5 g, 15 mmol) dissolved in 10 mL 0.5 M sodium acetate buffer (pH 4.8) was added. A lot of pale yellow precipitates were formed immediately and collected by centrifugation. The resulting solid was washed with water (twice) and ethanol (once) to removed any additional TBABr and dried under air. The dried solid was then redissolved in 5 mL CH_3CN and the mixture centrifuged to separate any undissolved precipitate. The final products in high purity were obtained by adding anhydrous diether to a clear CH_3CN solution. The FT-IR spectrum of TBA-**Ni_4P_2** is shown in **Figure 7-1**.

7.2.3. X-ray Crystallography

Complete data for Na_6K_4-**Ni_4P_2** were collected at Emory University. A suitable crystal (0.43 × 0.17 × 0.10 mm^3) was selected and mounted on a loop with paratone oil and placed under a nitrogen gas stream at 110(2) K on a Bruker D8 APEX II CCD sealed

tube diffractometer. Data were measured using ω scans of 1° per frame for 20s using MoK_λ radiation (fine-focus sealed tube, 45 kV, 30 mA). The total number of runs and images was based on the strategy calculation from the program **APEXII**.[71] A resolution of λ = 30.029° was achieved.[71] Data reduction was performed using the **SAINT** (Bruker, V8.34A, 2013)[72] software. The final completeness is 100.00% out to 30.029°in θ. The absorption coefficient (μ) of this material is 24.786 mm^{-1} and the minimum and maximum transmissions are 0.0074 and 0.2249. Cell parameters were retrieved using the **SAINT**[72] software and refined using **SAINT**[72] on 9974 reflections, 36% of the observed reflections. The results are summarized in **Table 7-1**. The structure was solved using **Olex2**[73] by Charge Flipping using the **Superflip**[74] structure solution program and refined by Least Squares using version 2013-4 of ShelXL.[75] The structure was solved in the space group $P\bar{1}$ (#2). All non-hydrogen atoms were refined anisotropically. The value of Z' is 0.5. This means that only half of the formula unit is present in the asymmetric unit, with the other half consisting of symmetry equivalent atoms.

Table 7-1 Crystallographic data and structure refinement for Na_6K_4-Ni_4P_2.

	Na_6K_4-$\mathbf{Ni_4P_2}$
Formula	$H_{68}K_4Na_6Ni_4O_{102}P_2W_{18}$
Formula weight	5600.96 g mol^{-1}
μ/mm^{-1}	24.786
$D_{calc.}$/ g cm^{-3}	4.252
Crystal System	triclinic
Space Group	$P\bar{1}$
Colour	green
T/K	110(2)
a/Å	11.5861(16)
b/Å	12.2589(17)
c/Å	16.041(2)

$\alpha/^{\circ}$	82.4668(16)
$\beta/^{\circ}$	88.9589(16)
$\gamma/^{\circ}$	75.5820(15)
V/Å^3	2187.3(5)
Z	1
$\Theta_{min}/^{\circ}$	1.815
$\Theta_{max}/^{\circ}$	30.029
Measured Refl.	27964
Independent Refl.	12611
Reflections Used	10917
R_{int}	0.0382
Parameters	677
Restraints	17
GooF	1.042
wR_2 (all data) [b]	0.0938
wR_2	0.0893
R_1 (all data) [a]	0.0444
R_1	0.0362

[a] $R_1 = \Sigma||F_0| - |F_c|| / \Sigma|F_0|$; [b] $wR_2 = \Sigma[w(F_0^2 - F_c^2)^2]/ \Sigma[w(F_0^2)^2]^{1/2}$

Difference electron-density maps revealed disorder for the WO_3 groups belonging to the (PW_9O_{34}) units of the $\{Ni_4O_{70}P_2W_{18}H_4\}$ cluster. Large peaks (5-8 eÅ^3) in the difference syntheses indicated that a W_3O_3 group occupies two or more positions with the largest residual peaks corresponding to the W atoms from the second component. These large peaks were used to add W atoms and then the site occupancies were refined. The site occupancies of the W atoms of the initial W_3O_3 group were also refined with the sum of the occupancies of the W atoms set to one. The population of the major component refined to 0.9465(9) and the minor component to 0.0535(9). Since the O atoms belonging to the second component of the disordered W_3O_3 group contribute to a very small portion

of the scattering, their positions could not be determined and were not included in the scattering model. Plots of the disorder are shown in **Figure 7-2**.

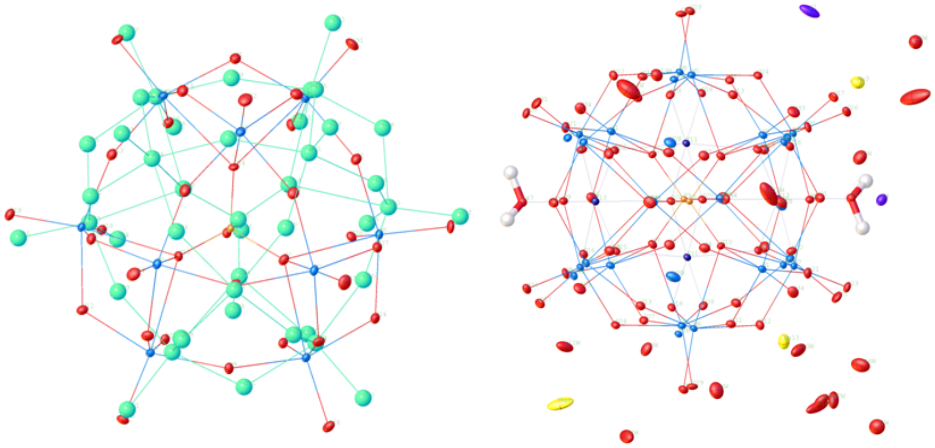

Figure 7-2 Plots of the $\mathbf{Ni_4P_2}$ structure with the disorder model. The left hand plot shows the disordered, symmetry independent (PW_9O_{34}) unit with the minor component shown in green and the right hand plot shows the scattering model with symmetry generated atoms for the cluster.

7.2.4. ESI Mass Spectrometry and Peak Assignments

Mass spectrometry determinations were carried out on a Thermo Finnigan LTQ-FTMS spectrometer with electrospray (ESI) ionization. For ESI-MS experiments, the solution of TBA-$\mathbf{Ni_4P_2}$ in acetonitrile has been used because TBA^+ cations have a higher mass than Na^+ or K^+ and thus give a large separation between signals with different charges or protonated states. The spectra are given in **Figure 7-3**. **Table 7-2** listed the main peak assignments of the ESI-MS spectra of TBA-$\mathbf{Ni_4P_2}$, which proves the integrity of $\mathbf{Ni_4P_2}$ polyanions in solution.

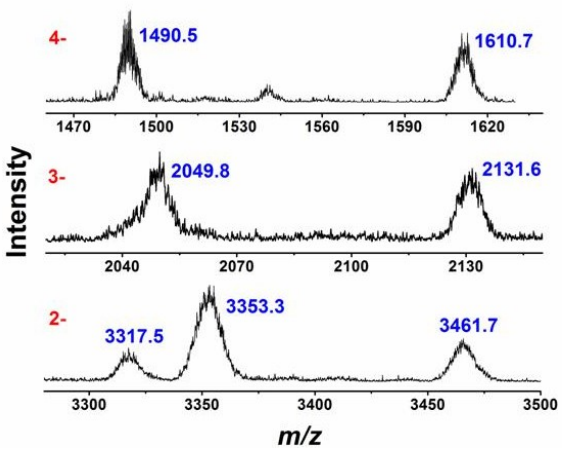

Figure 7-3 ESI-MS spectra obtained for TBA-$\mathbf{Ni_4P_2}$ in acetonitrile. The main peak envelopes with –4, –3 and –2 charges are marked with numbers.

Table 7-2 List of *m/z* peak assignments in the ESI-MS spectra of the TBA salt of $\mathbf{Ni_4P_2}$.

Peak assignments	Observed m/z	Calculated m/z
$\{(C_{16}H_{36}N)_4(CH_3CN)_6H_2[Ni_4(H_2O)_2(PW_9O_{34})_2]\}^{4-}$	1490.5	1487.1
$\{(C_{16}H_{36}N)_6(CH_3CN)_6[Ni_4(H_2O)_2(PW_9O_{34})_2]\}^{4-}$	1610.7	1607.7
$\{(C_{16}H_{36}N)_5(CH_3CN)_5H_2[Ni_4(H_2O)_2(PW_9O_{34})_2]\}^{3-}$	2049.8	2049.8
$\{(C_{16}H_{36}N)_6(CH_3CN)_5H[Ni_4(H_2O)_2(PW_9O_{34})_2]\}^{3-}$	2131.6	2130.3
$\{(C_{16}H_{36}N)_7(CH_3CN)_5H[Ni_4(H_2O)_2(PW_9O_{34})_2]\}^{2-}$	3317.5	3316.7
$\{(C_{16}H_{36}N)_8(CH_3CN)[Ni_4(H_2O)_2(PW_9O_{34})_2]\}^{2-}$	3353.3	3355.3
$\{(C_{16}H_{36}N)_8(CH_3CN)_6[Ni_4(H_2O)_2(PW_9O_{34})_2]\}^{2-}$	3461.7	3458.0

7.2.5. Visible-Light-Driven Catalytic Experiments and Characterization of the Post-Catalysis Solution

The light-driven water reduction experiment was performed in a cylindrical cuvette (NSG, 32UV10) with a total volume of ~2.5 mL. In a typical experiment, the cell was filled with 2.0 mL CH_3CN/DMF (1/3) solution containing 0.2 mM $[Ir(ppy)_2(dtbbpy)]^+$, 0.25 M TEOA and 4 - 30 μM catalyst. The reaction cell was sealed with a rubber septum, carefully degassed and filled with Ar. All procedures were performed with a minimum exposure to ambient light. The reaction samples were irradiated by a LED-light source (λ = 455 nm; light intensity 20 mW, beam diameter ~0.4 cm) at room temperature with

constant stirring (3×10^3 RPM) using a magnetically-coupled stirring system (SYS 114, SPECTROCELL). The post-reaction solution was collected, to which a saturated solution of $[Ru(bpy)_3]^{2+}$ in CH_3CN was added to precipitate the polyanion **Ni_4P_2**. The precipitate was isolated by centrifugation and used in the FT-IR stability evaluations (2.0 wt% samples in KBr) for comparison with the sample prepared using same procedures before catalysis. Control experiments were carried out under the same conditions in the absence of each component (e.g. $[Ir(ppy)_2(dtbbpy)]^+$, TEOA, or catalyst **Ni_4P_2**) of the hydrogen generating samples as described above. More control experiments were performed by replacing complex **Ni_4P_2** with $TBA_6[P_2W_{18}O_{62}]$ (TBA-**P_2W_{18}**), $TBA_{10}[Mn_4(H_2O)_2(VW_9O_{34})_2]$ (TBA-**Mn_4V_2**) or $NiCl_2$ under otherwise the identical conditions.

7.2.6. Steady-State and Time-Resolved Luminescence Decay and Nanosecond Transient Absorption Measurements of $[Ir(ppy)_2(dtbbpy)]^+$ in the Presence of Catalyst Ni_4P_2 or TEOA

The mixed solvent of CH_3CN/DMF (1/3) was used for fluorescence decay measurements. Before each experiment, the samples with different concentrations of either **Ni_4P_2** or TEOA were purged with argon for 10 min to remove soluble oxygen. The strong emission band of $[Ir(ppy)_2(dtbbpy)]^+$ at 500 - 750 nm with λ_{max} = 581 nm ($\lambda_{excitation}$ = 455 nm) was measured using the instruments described in **Section 7.2.1**.

7.2.7. Dynamic Light Scattering Measurements

Dynamic light scattering (DLS) measurements were performed on a Brookhaven Instruments 90Plus particle size analyzer. Each sample was measured three times consecutively. The post-reaction solutions from light-driven catalytic reaction using either catalyst **Ni_4P_2** or $NiCl_2$ were evaluated by DLS. None of these post-reaction solutions catalyzed by **Ni_4P_2** showed the presence of any nanoparticles. In contrast,

nanoparticles with maximum hydrodynamic sizes centered at 1.5 and 220 nm are formed in reactions catalyzed by $NiCl_2$.

7.2.8. TEM, SEM and EDS Measurements

Morphologies of the materials were characterized by Variable Pressure Scanning Electron Microscope-SU6600 instrument along with Energy Dispersive Spectroscopy (EDS) analysis. The TEM images were obtained using Scanning Transmission Electron Microscope-HD2000 operating at 30 kV. The samples for TEM/SEM measurements were isolated from the post-reaction solution by centrifugation at 10,000 RPM. The resulting particles were redispersed in ethanol by ultrasonication for 10 min, followed by drop coating on carbon-coated copper grid and dried under ambient conditions.

7.3 Results and Discussion

7.3.1. Synthesis, Crystal Structures and Characterization

Polyoxoanion **Ni_4P_2** was prepared from salts of earth-abundant elements (nickel acetate, sodium tungstate, and Na_2HPO_4) following a modification of the procedure by Coronado, Galán-Mascaros and co-workers[70] and systematically characterized. This **Ni_4P_2** complex shows a 10.9 % of weight loss, corresponding to 32 hydration water molecules per polyanion; the FT-IR spectra exhibit all the characteristic bands of sandwich-type POMs (**Figure 7-1**);[70] the cation exchange (tetrabutylammonium cation or TBA^+ for Na^+ and K^+) following modified literature procedures[76] does not change the structure of **Ni_4P_2**; elemental analysis confirmed the percentage of each element in **Ni_4P_2** in agreement with the formula obtained from the X-ray crystal structure. This diffraction study confirmed that the salt of **Ni_4P_2** crystallizes in the triclinic space group $P\bar{1}$ (R = 3.6%; **Table 7-1**)

and is isostructural to the POM-based WOCs, $[Co_4(H_2O)_2(PW_9O_{34})_2]^{10-}$ and $[Co_4(H_2O)_2(VW_9O_{34})_2]^{10-}$.[36,44,48,50] As noted in the previous work, **Ni_4P_2** contains a tetra-nickel cluster core $[Ni_4O_{14}]$ sandwiched by two tri-lacunary, heptadentate $[PW_9O_{34}]^{9-}$ POM ligands (**Figure 7-4**). The thermal ellipsoid plot indicates that the molecular structure refined well with good data quality (right, **Figure 7-4**). Three WO_3 groups belonging to the (PW_9O_{34}) units of the $\{Ni_4O_{70}P_2W_{18}H_4\}$ cluster are disordered, with a major (95%) and a minor component (5%) and only the major component of this disorder is shown in **Figure 7-4**.

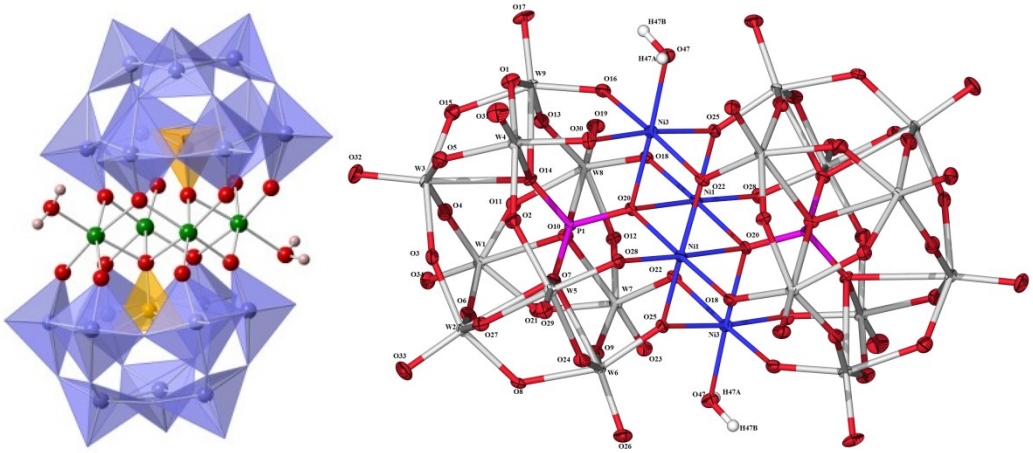

Figure 7-4 Left: Polyhedral and ball-and-stick representation of **Ni_4P_2**. Green: Ni; Red: Oxygen; Pink: H; Light blue: WO_6; Orange: PO_4. **Right:** A displacement ellipsoid plot of the **Ni_4P_2** polyanion. Three WO_3 groups belonging to the (PW_9O_{34}) units are disordered, but only one component of each disordered group is shown. Non-H atoms are represented by ellipsoids at the 50% probability.

Each of the two outside Ni(II) centers lies in a distorted octahedron of one oxygen atom from a labile aqua (water) ligand and five oxygen atoms from the heptadentate $[PW_9O_{34}]^{9-}$ ligands. The central PO_4 of each POM ligand has approximately tetrahedral symmetry. Bond valence sum (BVS) calculations indicate that all the Ni, P, and W atoms are in the 2+, 5+, and 6+ oxidation states, respectively. The solution structure of **Ni_4P_2**

has also been studied by ESI Mass Spectrometry (ESI-MS); the TBA^+ salt of **Ni_4P_2** in acetonitrile solution was used because TBA^+ cations have a higher mass than Na^+ or K^+ and thus give a larger separation between peaks with different charges or protonation states. The ESI-MS spectra of complex TBA-**Ni_4P_2** confirm the presence of the **Ni_4P_2** polyanions in solution based on the assignments of the peak envelopes (**Figure 7-3**, **Table 7-2**), in agreement with the solid state structure from X-ray diffraction.

7.3.2. Computational Studies

Geometries of the anions **Ni_4P_2** and $[\mathbf{Ni_4P_2}]^{2-}$ were optimized at their several lower-lying electronic states in the gas phase with no geometry constraints. Vibrational analyses were performed to ensure that all converged structures are true minima. In these calculations we used the spin-unrestricted DFT method (the hybrid M06L functional)[77] in conjunction with the split-valence 6-31G(d) basis sets for H, O, P atoms, and the lanl2dz basis with the associated Hay-Wadt ECPs[78-80] for the W and Ni atoms, which below will be referred to as "UM06L/lanl2dz". All calculations were carried out with the Gaussian 09 software package.[81]

The ground state electronic state and geometrical structure of the **Ni_4P_2** and its 2-electron reduced form **$[Ni_4P_2]^{2-}$** were calculated using the DFT method. Ongoing studies in our group will focus on describing the mechanism of the H_2 formation steps. The first tasks reported here address the electronic and geometric structures of the **Ni_4P_2** polyanion and its two-electron reduced form $[\mathbf{Ni_4P_2}]^{2-}$. The important bond lengths are summarized in **Table 7-3**, and compared with their available X-ray values. The structures of these species, as well as notation of atoms, are shown in **Figure 7-5** and their fully optimized geometries are provided in **Table 7-4**.

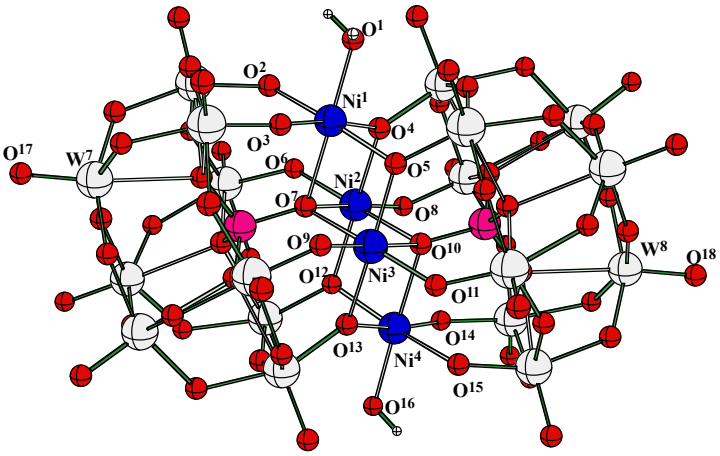

Figure 7-5 Calculated structures of $\mathbf{Ni_4P_2}$ and $[\mathbf{Ni_4P_2}]^{2-}$ (two-electron-reduced state) as well as notation of atoms.

Table 7-3 Experimental (crystallographic) with estimated standard deviations and calculated bond lengths (Å) in the cluster anions $\mathbf{Ni_4P_2}$ and $[\mathbf{Ni_4P_2}]^{2-}$.

Parameters	Computational		Experimental
	$\mathbf{Ni_4P_2}$	$\mathbf{[Ni_4P_2]^{2-}}$	$\mathbf{Ni_4P_2}$
Ni^1-O^1	2.24	2.23	2.060(6)
Ni^1-O^2	2.11	2.02	2.002(6)
Ni^1-O^3	2.03	2.03	2.019(6)
Ni^1-O^4	2.11	2.12	2.054(6)
Ni^1-O^5	2.09	2.09	2.066(6)
Ni^1-O^7	2.11	2.11	2.164(6)
Ni^2-O^6	2.03	2.02	1.986(6)
Ni^2-O^7	2.22	2.21	2.164(6)
Ni^2-O^8	2.03	2.02	1.981(6)
Ni^2-O^{10}	2.22	2.21	2.155(5)
Ni^2-O^4	2.08	2.13	2.045(5)
Ni^2-O^{12}	2.08	2.14	2.049(5)
Ni^3-O^9	2.03	2.02	1.981(6)
Ni^3-O^7	2.23	2.22	2.155(5)
Ni^3-O^{11}	2.03	2.02	1.986(6)

Ni^3-O^{10}	2.23	2.22	2.164(6)
Ni^3-O^5	2.09	2.14	2.049(5)
Ni^3-O^{13}	2.09	2.11	2.045(5)
Ni^4-O^{12}	2.11	2.12	2.066(6)
Ni^4-O^{13}	2.09	2.09	2.054(6)
Ni^4-O^{14}	2.11	2.02	2.019(6)
Ni^4-O^{15}	2.03	2.02	2.002(6)
Ni^4-O^{10}	2.11	2.11	2.158(5)
Ni^4-O^{16}	2.24	2.23	2.060(6)

Table 7-4 Calculated Cartesian coordinates (in Å) of $\mathbf{Ni_4P_2}$ and $[\mathbf{Ni_4P_2}]^{2-}$ anions at their high-spin ground states.

$\mathbf{Ni_4P_2}$	x	y	z	$\mathbf{[Ni_4P_2]^{2-}}$	x	y	z
P	-2.93356	0.054012	0.011083	P	-2.94001	0.030005	-0.030763
P	2.933445	-0.05393	0.010167	P	2.927934	-0.02749	0.025184
Ni	0.868349	-2.5368	0.038775	Ni	0.930388	-1.61697	1.852182
Ni	-0.86872	2.536548	0.031272	Ni	-0.93486	1.602884	-1.853169
Ni	-0.00025	-0.00255	-1.621766	Ni	0.000371	-1.25624	-1.076228
Ni	0.000726	0.003165	1.67181	Ni	0.003709	1.26618	1.073524
W	-6.49102	1.206118	-0.000348	W	-6.5896	0.818687	-0.939628
W	6.490684	-1.20621	0.00226	W	6.590211	-0.81379	0.943711
W	-5.5039	-1.91196	1.894193	W	-5.5344	0.18762	2.658812
W	5.4988	1.905519	-1.885622	W	5.533668	-0.18445	-2.653075
W	-4.00419	3.062844	1.685794	W	-4.02534	3.278928	-1.200328
W	4.036635	-3.02841	-1.740312	W	4.025283	-3.2811	1.171593
W	-3.04328	-0.00796	3.57633	W	-3.03694	2.68396	2.356307
W	3.004788	0.048317	-3.577689	W	3.027764	-2.67206	-2.377458
W	-2.12354	-2.90134	1.915261	W	-2.13844	-0.48905	3.438288
W	2.136866	2.898538	-1.838119	W	2.142272	0.509654	-3.433574
O	-6.89274	-2.74618	-2.550225	O	-6.90594	-3.74238	0.40328
O	6.915324	2.734732	2.546119	O	6.912637	3.742747	-0.393904
O	-4.35171	4.356953	-2.847396	O	-4.31796	0.723075	-5.145172

O	4.34114	-4.39448	2.781235	O	4.321763	-0.75933	5.146203
O	-2.99448	0.178143	-5.312929	O	-3.03511	-3.8851	-3.62938
O	3.064507	-0.2437	5.308559	O	3.053357	3.858982	3.649993
O	-1.5358	-4.4689	-2.36733	O	-1.63799	-4.80744	1.776245
O	1.61622	4.449949	2.526754	O	1.640203	4.82148	-1.744496
O	-5.61475	-2.3606	0.004389	O	-5.64291	-1.53322	1.777441
O	5.615124	2.36039	-0.003143	O	5.643387	1.539998	-1.77231
W	-5.49897	-1.91089	-1.879661	W	-5.53792	-2.65319	0.195689
W	5.504326	1.917565	1.888288	W	5.539425	2.658731	-0.194371
W	-4.03741	3.022042	-1.749579	W	-4.0248	0.688896	-3.411233
W	4.004528	-3.05676	1.695466	W	4.023358	-0.72146	3.413325
W	-3.00468	-0.0597	-3.577564	W	-3.02876	-2.73506	-2.299934
W	3.043753	0.019111	3.576888	W	3.043141	2.71636	2.31416
W	-2.13757	-2.90499	-1.828916	W	-2.1473	-3.32723	0.999165
W	2.124459	2.907821	1.906159	W	2.144267	3.333657	-0.977673
O	-8.23436	1.435185	-0.016334	O	-8.2893	0.9668	-1.123876
O	8.23402	-1.43532	-0.01326	O	8.289858	-0.97532	1.114517
O	-6.91433	-2.72751	2.555305	O	-6.90654	0.146987	3.761733
O	6.892262	2.738594	-2.559605	O	6.900555	-0.13622	-3.761935
O	-4.34143	4.403389	2.767869	O	-4.32684	4.98765	-1.488672
O	4.350789	-4.36665	-2.834128	O	4.324583	-4.99152	1.450179
O	-3.06433	0.260376	5.307149	O	-3.05001	4.165389	3.302948
O	2.9947	-0.19453	-5.312359	O	3.03891	-4.14955	-3.330002
O	-1.61494	-4.4414	2.540815	O	-1.63419	-1.03336	5.021189
O	1.53543	4.461023	-2.380881	O	1.632576	1.066063	-5.0105
O	-6.23506	-0.22132	-1.311248	O	-6.30964	-1.12845	-0.687924
O	6.249133	0.211747	1.279829	O	6.314116	1.115968	0.684869
O	-6.25069	-0.20826	1.281715	O	-6.31435	0.837582	1.006781
O	6.236292	0.217373	-1.313338	O	6.305902	-0.84228	-1.018002
O	-2.39822	-3.31379	0.040486	O	-2.41053	-2.18281	2.543736
O	2.398554	3.312989	0.030555	O	2.410975	2.202356	-2.525113
O	-3.93407	1.517051	-2.974171	O	-3.92739	-1.22372	-3.077785
O	3.948997	-1.5538	2.930819	O	3.92857	1.19667	3.082894

O	-3.94739	1.563043	2.924689	O	-3.92761	3.230215	0.746811
O	3.932757	-1.52676	-2.969009	O	3.927996	-3.22368	-0.77179
O	-5.91879	2.400576	-1.367292	O	-5.93187	0.57359	-2.708092
O	5.933355	-2.43224	1.310483	O	5.942953	-0.59099	2.710434
O	-5.93301	2.435874	1.303704	O	-5.94282	2.599924	-0.967959
O	5.91774	-2.40493	-1.360475	O	5.932153	-2.59815	0.952496
O	-4.78817	-1.04283	-3.399527	O	-4.82097	-3.22511	-1.463675
O	4.835408	0.998689	3.392599	O	4.835336	3.205814	1.478623
O	-4.8344	-0.98816	3.395553	O	-4.82777	1.92153	2.959221
O	4.787093	1.031985	-3.402447	O	4.815897	-1.90819	-2.981966
O	-4.1215	-3.21349	-2.023249	O	-4.15135	-3.62089	1.080347
O	4.154987	3.205348	2.063637	O	4.163394	3.635381	-1.06186
O	-4.15414	-3.19888	2.073365	O	-4.15866	-0.52945	3.750232
O	4.1215	3.20719	-2.033206	O	4.147226	0.550725	-3.736611
O	-4.28977	3.935268	-0.040526	O	-4.3211	2.571672	-2.98583
O	4.288844	-3.93542	-0.028378	O	4.325256	-2.58995	2.973014
O	-2.34025	-1.94124	-3.45515	O	-2.36724	-3.88884	-0.809923
O	2.391025	1.905752	3.499069	O	2.385091	3.886309	0.83019
O	-2.38971	-1.89483	3.504989	O	-2.37808	1.380163	3.722802
O	2.33949	1.930966	-3.461283	O	2.360873	-1.36164	-3.728791
O	-3.89084	1.291483	-0.00604	O	-3.87385	0.85055	-0.968984
O	3.891375	-1.2908	-0.003118	O	3.873986	-0.83581	0.961839
O	-3.23503	-0.81139	-1.25616	O	-3.2445	-1.48721	-0.215112
O	3.249759	0.806487	1.273934	O	3.219858	1.494022	0.197598
O	-3.24977	-0.80173	1.278194	O	-3.24279	0.41561	1.448209
O	3.234435	0.806998	-1.260352	O	3.224908	-0.42239	-1.452763
O	-1.41073	0.49552	0.022689	O	-1.40069	0.301229	-0.348397
O	1.410529	-0.49544	0.023228	O	1.391438	-0.30735	0.351934
O	-2.24921	3.027794	-1.483662	O	-2.23939	0.917525	-3.236638
O	2.235208	-3.06497	1.442594	O	2.238752	-0.94415	3.247975
O	-2.23473	3.072223	1.432884	O	-2.23942	3.08557	-1.399114
O	2.248289	-3.03298	-1.474664	O	2.240496	-3.08584	1.381478
O	-1.40807	0.48327	-2.995116	O	-1.41803	-1.95966	-2.329334

O	1.427033	-0.49521	3.022199	O	1.423789	1.957179	2.331453
O	-1.42642	0.504244	3.020049	O	-1.41926	2.60196	1.596534
O	1.407563	-0.49155	-2.993765	O	1.416132	-2.59532	-1.607139
O	-0.59272	-1.98309	-1.374039	O	-0.57583	-2.39527	0.620018
O	0.571245	2.004774	1.455406	O	0.57394	2.409339	-0.602064
O	-0.57123	-1.99932	1.460449	O	-0.56895	-0.26015	2.466782
O	0.591833	1.978891	-1.379571	O	0.571332	0.278683	-2.456445
O	0.515793	-4.71103	-0.383802				
O	-0.51732	4.710766	-0.398418				
H	-1.32189	4.536645	-0.938406				
H	0.20889	4.684617	-1.063841				
H	-0.21086	-4.68748	-1.048925				
H	1.320004	-4.53896	-0.925211				

Calculations show that the ground electronic state of **Ni_4P_2** is a nintet, ^{9}A, state with 1.67, 1.68, 1.68, and 1.67 |e| un-paired α-spins localized on the Ni^1, Ni^2, Ni^3 and Ni^4 centers, respectively, and residual 1.30 |e| α-spins delocalized over the O-centers of the (PW_9O_{34}) fragments. This spin distribution data is consistent with Ni centers being of d^8 Ni(II) cations. The antiferromagnetically coupled singlet state of **Ni_4P_2** with 1.68 and 1.67|e| un-paired α-spins on Ni^2 and Ni^4, and 1.67 and 1.68|e| un-paired β spins on Ni^1 and Ni^3, is energetically degenerate with its ferromagnetic ^{9}A counterpart. Therefore, below, for sake of accuracy of our calculations and discussions, we only report properties of the high-spin ferromagnetic **Ni_4P_2** and **$[Ni_4P_2]^{2-}$** species.

As noted, reduction of the catalyst **Ni_4P_2** occurs before the H_2 formation from protons. Therefore, we also computationally analyzed the electronic state of **$[Ni_4P_2]^{2-}$**. Our studies show that the ground electronic state of **$[Ni_4P_2]^{2-}$** is a high-spin ^{11}A state, with

1.63, 1.71, 1.71, and 1.63 |e| un-paired α-spins localized on the Ni^1, Ni^2, Ni^3 and Ni^4 centers, respectively. The two additional electrons in $\mathbf{[Ni_4P_2]^{2-}}$ result in a residual 1.32 |e| α-spins which are delocalized over the (PW_9O_{34}) fragments consistent with reduction of these ligands (**Figure 7-6**). Consistent with these electronic structure findings, the two-electron reduction of $\mathbf{Ni_4P_2}$ only slightly impacts the Ni-O bond distances. All calculated bond distances are in good agreement with their crystallographically determined bond distances: the small differences are within expectations for crystallographic and gas phase calculated structures (**Table 7-3**). The crystal structure has significantly shorter Ni-O(H_2O) bond than that from the calculations. The experimentally determined Ni-O(H_2O) bond distance is 2.060(6) Å. *i.e.* this Ni - O distance for the water molecule is 2.05-2.07 Å within experimental error. The X-ray structure has suitable hydrogen bonds to water molecules of crystallization whereas the theoretical structure is in the gas-phase. The additional valence and shorter bond distances are likely to be due to hydrogen bonding to additional water molecules in the crystal lattice.

Figure 7-6 Photographs of the photocatalytic reaction solution before (left) and after (right) illumination. Conditions: LED light (20 mW, 455 nm, beam diameter ~0.4 cm), $[Ir(ppy)_2(dtbbpy)]^+$ (0.2 mM), TEOA (0.25 M), catalyst $\mathbf{Ni_4P_2}$ (20 μM) in 2 mL CH_3CN/DMF (1/3) deaerated with Ar.

7.3.3. Cyclic Voltammetry

Cyclic voltammograms of 2.0 mM **Ni_4P_2** in deairated CH_3CN/DMF (1/3) solution show quasi-reversible, poorly resolved redox waves in the range of 0 to −1.65 V. The width and low current of the CV peaks are consistent with slow electron transfer rates likely due to high reorganization energies associated with **Ni_4P_2**-based redox processes. The negative-domain peaks contain both the reductions of W(VI) to W(V), W(V) to W(IV) and Ni(II) to Ni(I), which are very difficult to distinguish due to the substantial overlap of these peaks. This heavily overlap of redox peaks is common in most CVs of POM systems.[82,83] The peak current is linearly dependent on the square root of the scan rates ($R^2 \sim 0.998$, **Figure 7-7**) consistent with diffusion-controlled interfacial redox processes.

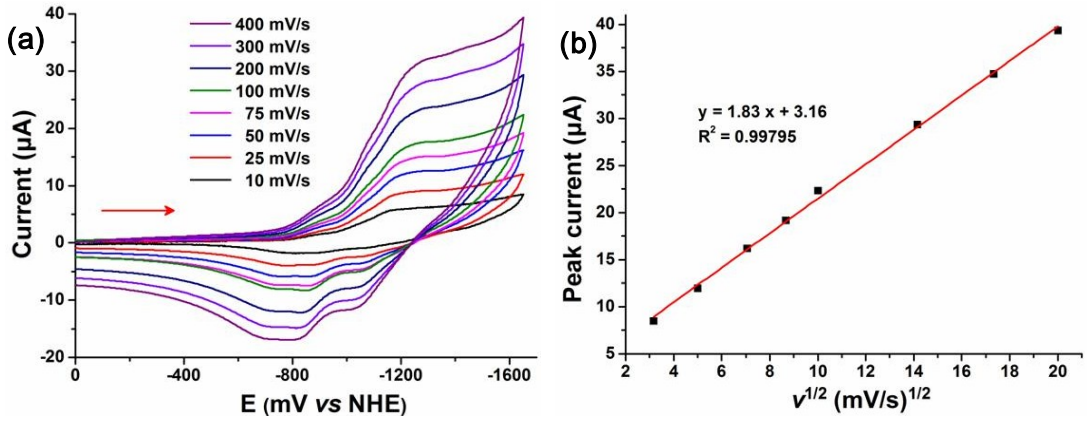

Figure 7-7 (a): cyclic voltammograms of 2.0 mM TBA-**Ni_4P_2** at different scan rates in the range of 0 to −1.65 V; (b): the plot of maximum anodic peak currents versus the square root of scan rates. Conditions: 0.2 M tetrabutylammonium hexafluorophosphate ($TBAPF_6$) electrolyte in 5 mL of CH_3CN/DMF (1/3) deairated with Ar; glassy carbon working electrode, Pt wire auxiliary electrode, non-aqueous Ag^+/Ag reference electrode (0.1 M $TBAPF_6$ and 0.01 M $AgNO_3$) calibrated with ferrocene/ferrocenium redox couple, T = 25 ^oC.

To examine the potential activity of **Ni_4P_2** for electrocatalytic H_2 production, varying equivalents of acetic acid were added to the solution of **Ni_4P_2** in deairated CH_3CN/DMF (1/3). There is clear and substantial current starting at -1.06 V, indicating onset of

electrocatalysis (**Figure 7-8a**). Addition of 3 M water with 60 mM acetic acid to the CV solution further increases the catalytic current (**Figure 7-8b**). A control experiment in the absence of $\mathbf{Ni_4P_2}$ but with the same concentration of acetic acid in deairated CH_3CN/DMF solvent shows a much lower current enhancement at more negative potential, indicating that $\mathbf{Ni_4P_2}$ complex is the electroactive species (**Figure 7-8c**).

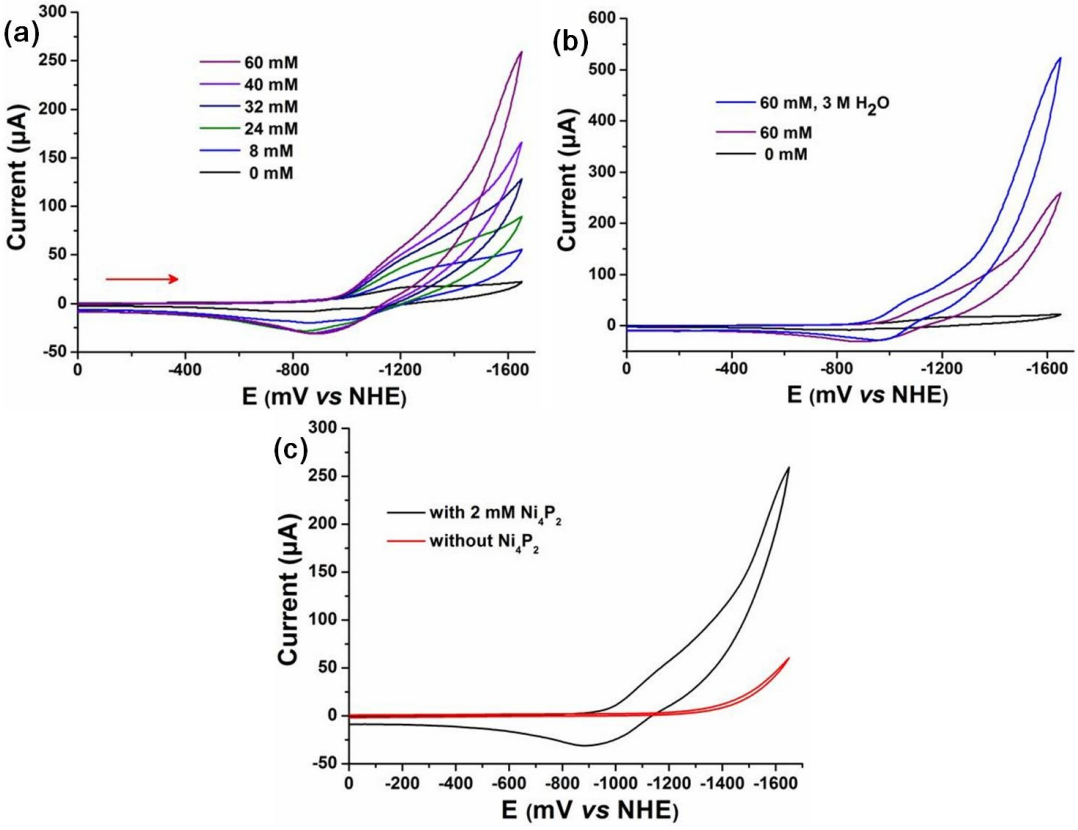

Figure 7-8 Successive cyclic voltammograms of 2.0 mM TBA-$\mathbf{Ni_4P_2}$ with (a) varying concentrations of acetic acid, (b) in the presence of 3 M water; (c) CVs of 60 mM acetic acid in the presence/absence of TBA-$\mathbf{Ni_4P_2}$. Conditions are the same as Figure S7, scan rate: 100 mV/s, scan range: 0 to -1.65V.

7.3.4. Visible-Light-Driven Catalytic Activity of Ni_4P_2

The visible-light-driven catalytic activity of $\mathbf{Ni_4P_2}$ for hydrogen evolution was examined using a three-component system: $[Ir(ppy)_2(dtbbpy)]^+$ as photosensitizer, triethanol-amine

(TEOA) as sacrificial electron donor, and **Ni_4P_2** as a WRC. We chose the iridium photosensitizer, $[Ir(ppy)_2(dtbbpy)]^+$, rather than $[Ru(bpy)_3]^{2+}$ used in our recent work,[68] because its excited state provides more driving force ($[Ir(ppy)_2(dtbbpy)]^{2+/+*}$ ~ -0.96 V vs SCE; $[Ir(ppy)_2(dtbbpy)]^{+/0}$ ~ -1.51 V vs SCE in CH_3CN) for successive reduction of the **Ni_4P_2** catalyst.[84,85] Photolysis of a solution of 0.2 mM $[Ir(ppy)_2(dtbbpy)]^+$, 0.25 M TEOA and catalyst **Ni_4P_2** in deaerated CH_3CN/DMF (1/3) using a blue-light-emitting diode (LED) (λ = 455 nm, 20 mW) at 25 ℃ results in the reduction of **Ni_4P_2** (change in solution color from yellow to green; **Figure 7-6**) in agreement with DFT calculations (see above discussion) and the production of hydrogen. No such color change is observed in the absence of **Ni_4P_2**. H_2 production increases linearly with time after exposure to the 455-nm visible light (**Figure 7-9**), and no H_2 forms in the dark. A TON of ~290 (~11.6 μmol H_2 gas per 0.04 μmol catalyst **Ni_4P_2**) is obtained after 2.5 hrs of irradiation. This is more than 20 times higher than the **Mn_4V_2** WRC.[68]

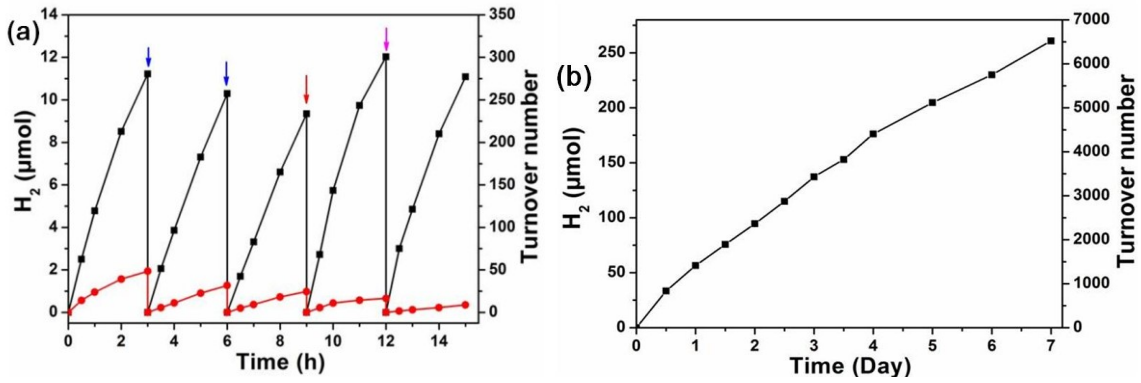

Figure 7-9 (a): photocatalytic H_2 evolution using 20 μM **Ni_4P_2** (black curve) and 20 μM $NiCl_2$ (red curve); conditions: LED light (20 mW, 455 nm), $[Ir(ppy)_2(dtbbpy)]^+$ (0.2 mM), TEOA (0.25 M), 2 mL CH_3CN/DMF (1/3) deaerated with Ar. (b): long-term photocatalytic H_2 evolution using **Ni_4P_2** (10 μM) conditions: LED light (20 mW, 455 nm), $[Ir(ppy)_2(dtbbpy)]^+$ (0.2 mM), TEOA (0.25 M), H_2O (1.4 M), 4 mL CH_3CN/DMF (1/3) deaerated with Ar. Note: the blue arrow means the reaction solution was degassed; the red arrow indicates 0.1 mL dye (0.8 mM) was added; the pink arrow represents the reaction was centrifuged.

Control experiments revealed that all 3 components, i.e. the catalyst **Ni_4P_2**, TEOA and $[Ir(ppy)_2(dtbbpy)]^+$ are essential for efficient H_2 evolution; the absence of any one of these species results in little or no H_2 (**Figure 7-10**). An additional control experiment using $TBA_6[P_2W_{18}O_{62}]$ (TBA-**P_2W_{18}**) in place of **Ni_4P_2** gives very little H_2 (TON = 1; **Figure 7-10**). A Ni^{2+} salt (e.g. $NiCl_2$), a potential dissociation product of **Ni_4P_2**, under otherwise identical conditions gives much less H_2 (**Figure 7-10**).

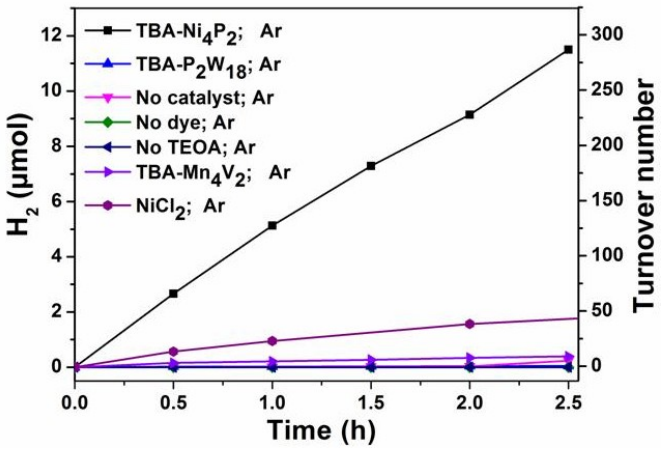

Figure 7-10 Photochemical H_2 evolution by different catalysts (WRCs) under otherwise identical conditions: LED light (20 mW, 455 nm, beam diameter ~0.4 cm), $[Ir(ppy)_2(dtbbpy)]^+$ (0.2 mM), TEOA (0.25 M), catalyst (20 μM), 2 mL CH_3CN/DMF (1/3) deaerated with Ar.

Figure 7-9 illustrates the reusability of the **Ni_4P_2** and $NiCl_2$ catalysts. The **Ni_4P_2**-catalyzed system shows much higher H_2 evolution rates and final yields. A slight decrease of H_2 yield is observed in three successive runs. However, the addition of fresh $[Ir(ppy)_2(dtbbpy)]^+$ stock solution (0.1 mL of 0.8 mM) fully restores the H_2 evolution activity. The kinetics of H_2 production in the $NiCl_2$-catalyzed system shows quickly diminishing yields of H_2 with time. After 12 hours of irradiation, the total TON is 1,100 and 110 for **Ni_4P_2** and $NiCl_2$, respectively. Centrifugation of the $NiCl_2$-containing solution almost completely removes its photocatalytic activity, indicating the heterogeneity of the system (**Figure 7-9a**, red line, pink arrow). This phenomenon is not

seen in the **Ni_4P_2**-catalyzed system. A scale-up experiment was used to evaluate the long-term robustness of the **Ni_4P_2**-catalyzed system. **Figure 7-9b** shows that **Ni_4P_2** catalyzes H_2 production over one week, reaching a TON of 6,500 (corresponding to 260 μmol H_2 per 0.04 μmol **Ni_4P_2**), with little or no loss of catalytic activity, which is, to our knowledge, the highest value for a noble-metal-free POM-catalyzed H_2 evolution system.

The rate of H_2 evolution depends on the concentrations of catalyst **Ni_4P_2**, $[Ir(ppy)_2(dtbbpy)]^+$ photosensitizer and TEOA sacrificial donor. At constant concentration of $[Ir(ppy)_2(dtbbpy)]^+$ and TEOA, increasing [**Ni_4P_2**] from 4 to 30 μM results in an increase in the H_2 yield from 1.33 to 15.5 μmol after 2.5 hours of irradiation (**Figure 7-11a**). **Figure 7-11b** gives dependences of the rate and final yield of H_2 on the photosensitizer concentration. The amount of H_2 generated increases from 8.5 to 14.1 μmol (corresponding to a TON of ~ 210 to 350, respectively) when varying the $[Ir(ppy)_2(dtbbpy)]^+$ concentration from 0.1 mM to 0.4 mM. The H_2 yield increases as [TEOA] increases from 0.05 to 0.25 M (TON increases from 160 to 290; **Figure 7-11c**).

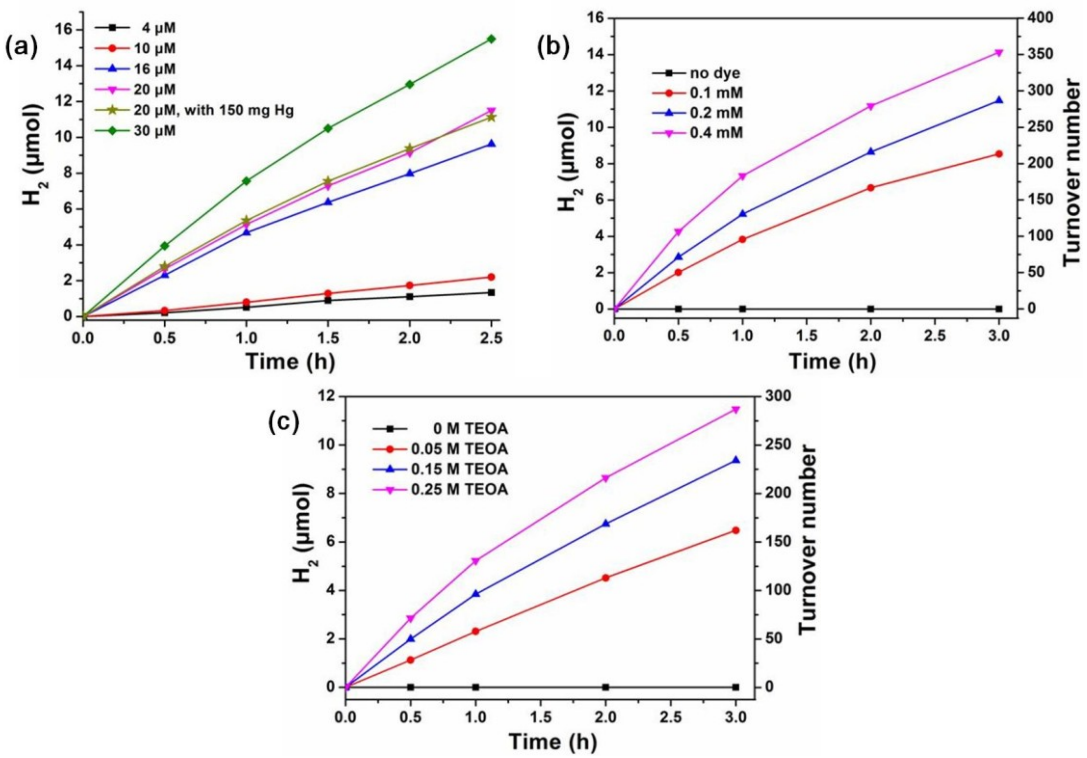

Figure 7-11 (a) Photocatalytic H_2 evolution as a function of **Ni_4P_2** concentration. Conditions: $[Ir(ppy)_2(dtbbpy)]^+$ (0.2 mM), TEOA (0.25 M), catalyst **Ni_4P_2** (4 - 30 μM), 150 mg mercury (Hg); (b) Photocatalytic H_2 evolution as a function of $[Ir(ppy)_2(dtbbpy)]^+$ concentration. Conditions: $[Ir(ppy)_2(dtbbpy)]^+$ (0.1 - 0.4 mM), TEOA (0.25 M), catalyst **Ni_4P_2** (20 μM); (c) Photocatalytic H_2 evolution as a function of sacrificial reductant (TEOA) concentration at parity of other conditions: $[Ir(ppy)_2(dtbbpy)]^+$ (0.2 mM), TEOA (0 - 0.25 M), TBA-**Ni_4P_2** (20 μM). Light source: LED light (20 mW, 455 nm, beam diameter ~0.4 cm), solvent: 2 mL CH_3CN/DMF (1/3) deaerated with Ar.

7.3.5. Mechanistic Studies

In photo-driven catalytic systems, the photosensitizer excited state can function as either an oxidant or reductant, and thus can be quenched by an electron donor or an acceptor.[22,68,85,86] To assess the quenching mechanism of our system, the luminescence of the excited photosensitizer, $[Ir(ppy)_2(dtbbpy)]^{+*}$, in deaerated CH_3CN/DMF (1/3) was measured as function of both TEOA (**Figure 7-12**) and separately, **Ni_4P_2** concentration (**Figure 7-13**). The Stern-Volmer analysis of the reductive quenching by TEOA yields a

quenching rate constant of 3.3×10^7 M^{-1} s^{-1} (**Figure 7-12**). The linear fitting of a Stern-Volmer plot gives an apparent rate constant of 2.7×10^{10} M^{-1} s^{-1} for oxidative quenching by **Ni_4P_2** (**Figure 7-13**). Although the rate constant for oxidative quenching is about three orders of magnitude higher than that of reductive quenching, the reductive process is still dominant given the much higher concentration of TEOA (0.25 M) relative to **Ni_4P_2** (20 μM).

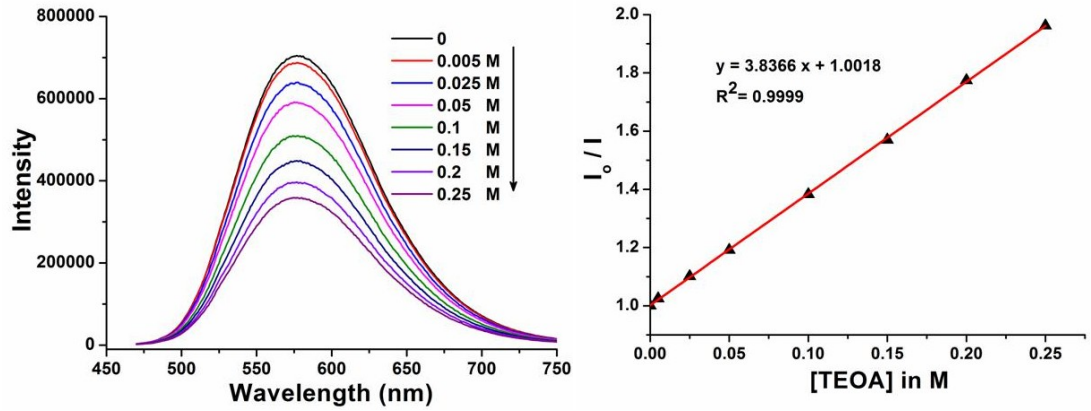

Figure 7-12 Emission spectra of $[Ir(ppy)_2(dtbbpy)]^+$ (0.2 mM) as a function of added TEOA and the corresponding linear Stern-Volmer plot.

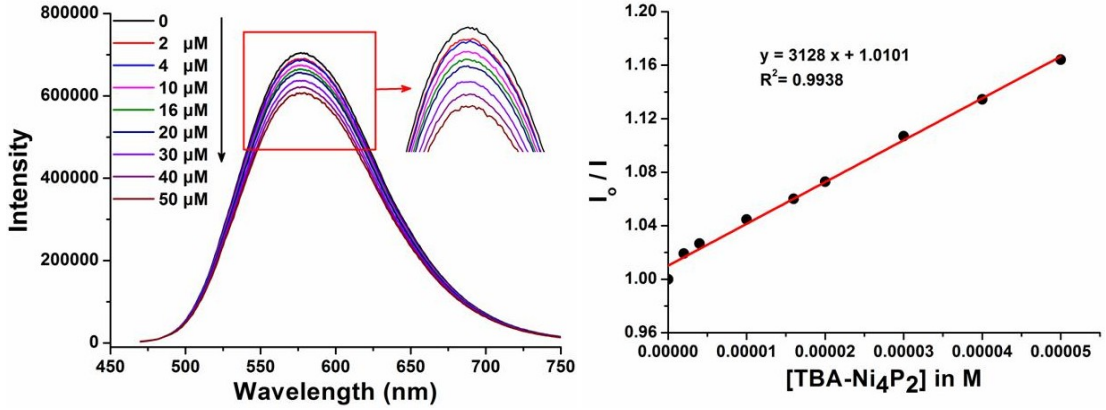

Figure 7-13 Emission spectra of $[Ir(ppy)_2(dtbbpy)]^+$ (0.2 mM) as a function of added **Ni_4P_2** and the corresponding linear Stern-Volmer plot.

To further investigate the electron-transfer steps, time-resolved fluorescence spectroscopy was used to follow the $[Ir(ppy)_2(dtbbpy)]^{+*}$ luminescence decay kinetics.

Figure 7-14 shows that both **Ni_4P_2** and TEOA can accelerate the $[Ir(ppy)_2(dtbbpy)]^{+*}$ luminescence decay. Single exponential fitting of these kinetics in the presence of **Ni_4P_2** and TEOA gives lifetimes of ~96 and ~52 ns, respectively; however, in the absence of quenchers, the luminescence decay kinetics slow down (lifetime = 103 ns). These data further confirm that catalyst **Ni_4P_2** and TEOA can oxidatively and reductively quench the excited state of $[Ir(ppy)_2(dtbbpy)]^{+*}$ and that the reductive quenching pathway is dominant in agreement with the steady state luminescence quenching results.

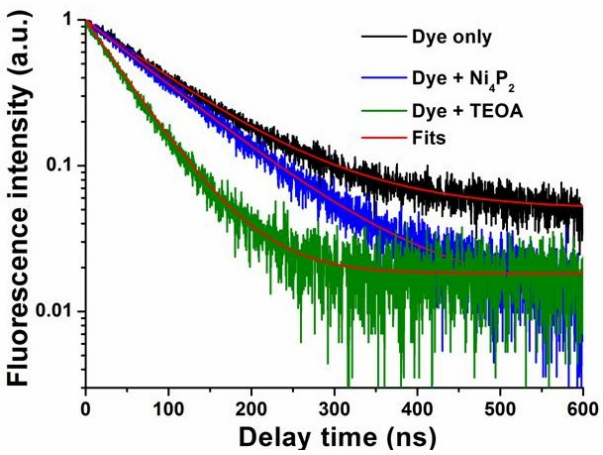

Figure 7-14 Normalized fluorescence decay kinetics of $[Ir(ppy)_2(dtbbpy)]^+$ (black curve) and $[Ir(ppy)_2(dtbbpy)]^+$ with **Ni_4P_2** (blue curve) and $[Ir(ppy)_2(dtbbpy)]^+$ with TEOA (green curve). Conditions: 400 nm excitation, 0.2 mM $[Ir(ppy)_2(dtbbpy)]^+$, 0.25 M TEOA and 50 μM catalyst **Ni_4P_2**. The red curves are best fits according to single exponential decay. The y-axis is in log scale.

Transient absorption measurements have also been used to determine the rates of electron-transfer processes. The decay kinetics of $[Ir(ppy)_2(dtbbpy)]^{+*}$ only is single-exponential with lifetime of ~115 ns (**Figure 7-15a** and **Table 7-5**). In contrast, the lifetime of $[Ir(ppy)_2(dtbbpy)]^{+*}$ shortens to ~98 ns through oxidative quenching by **Ni_4P_2** (**Figure 7-15b**, **Table 7-5**). In addition, $[Ir(ppy)_2(dtbbpy)]^{+*}$ is also reductively quenched by TEOA with the lifetime of ~78 ns (**Figure 7-15c**, **Table 7-5**), resulting in the

formation of one-electron-reduced dye (λ_{max} = 500 nm) that further reduces catalyst **Ni_4P_2** (**Figure 7-15d**, red dash-line circle). Based on the above experimental data, we propose the mechanism in **Scheme 7-1** for this visible-light-induced photocatalytic H_2 evolution.

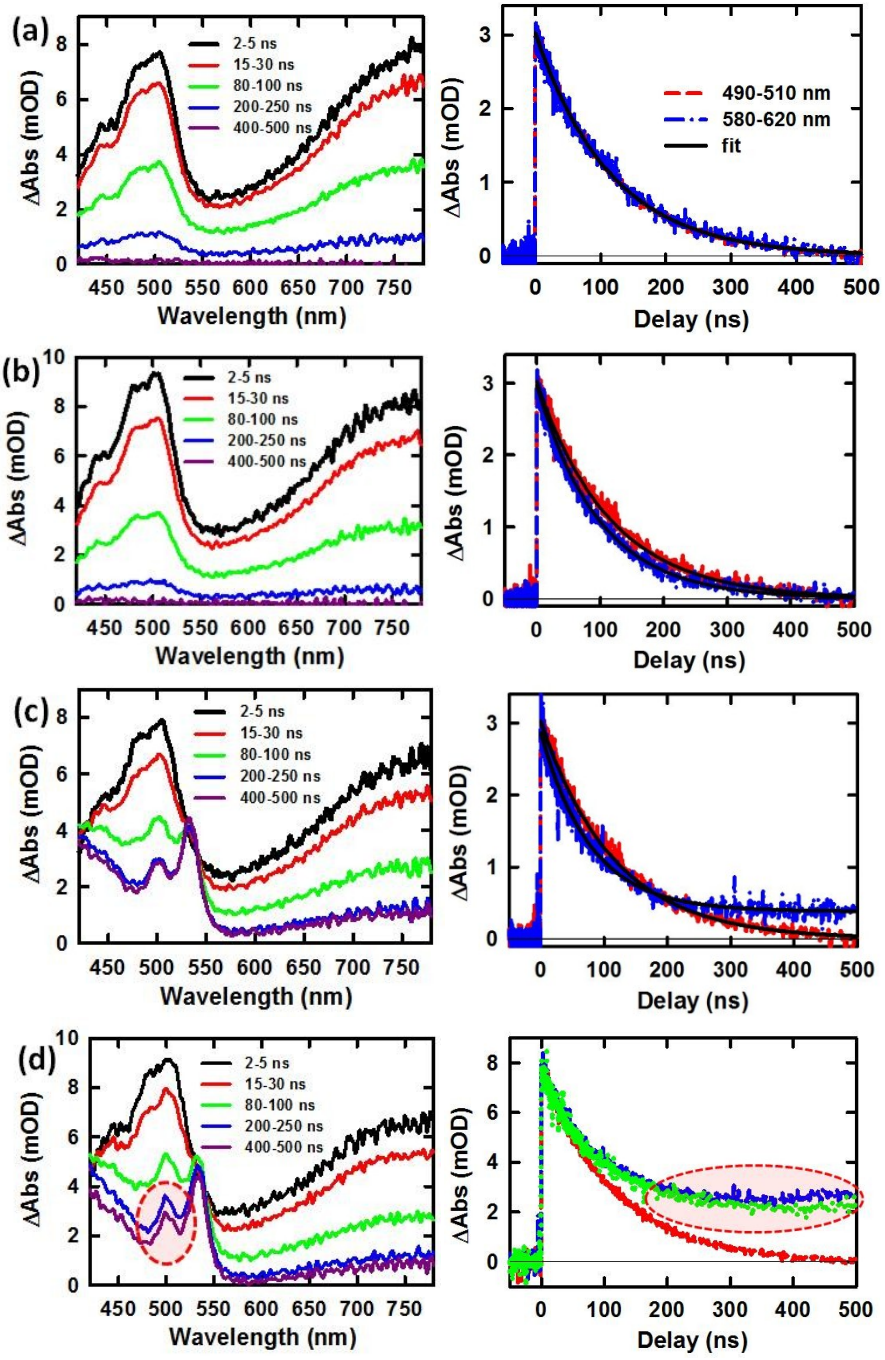

Figure 7-15 Transient absorption spectra (left panels) and kinetics (right panels) excited at 400 nm and probed at the indicated wavelength ranging from 0 to 500 ns. (a) free $[Ir(ppy)_2(dtbbpy)]^+$

dye probed at 490-510 nm and 580-620 nm wavelengths, (b) $[Ir(ppy)_2(dtbbpy)]^+$ dye in the presence of TBA-**Ni_4P_2** probed at 580-620 nm wavelengths (red line: free dye; blue line: dye + TBA-**Ni_4P_2**), (c) $[Ir(ppy)_2(dtbbpy)]^+$ dye in the presence of TEOA probed at 580-620 nm wavelengths (red line: free dye; blue line: dye + TEOA), and (d) $[Ir(ppy)_2(dtbbpy)]^+$ dye in the presence of TBA-**Ni_4P_2** and TEOA probed at 490-510 nm wavelength (red line: free dye; blue line: dye + TEOA; green line: dye + TEOA + TBA-**Ni_4P_2**). Conditions: $[Ir(ppy)_2(dtbbpy)]^+$ (0.4 mM), TEOA (0.25 M), TBA-**Ni_4P_2** (0.1 mM), 1 mL CH_3CN/DMF (1/3), 2 mm pathlength cuvette. All the kinetics data are fitted by single-exponential decays (black lines).

Table 7-5 Comparison of lifetimes of excited state $[Ir(ppy)_2(dtbbpy)]^+$ dye from the data in **Figure 7-15**.

Sample	Lifetime (ns)
Free $[Ir(ppy)_2(dtbbpy)]^+$ dye	115.0±0.5
Dye + TBA-**Ni_4P_2**, CH_3CN/DMF (1/3)	98.1±0.5
Dye + TEOA, CH_3CN/DMF (1/3)	78.3±1.0

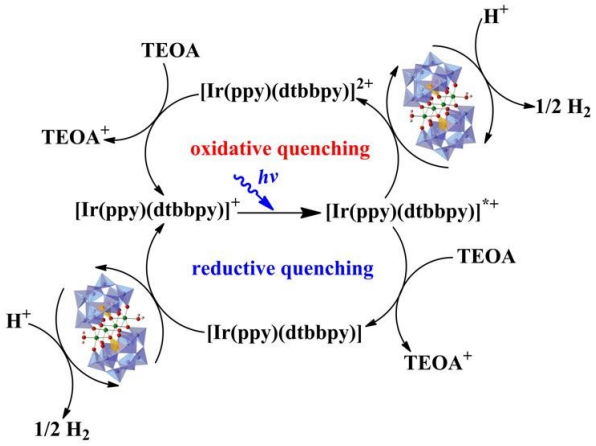

Scheme 7-1 Proposed mechanism for visible-light-driven hydrogen evolution catalyzed by **Ni_4P_2**.

7.3.6. Stability Studies

The stability of molecular WRCs under turnover conditions is a general concern. In this context, the photostability of **Ni_4P_2** in our system has been examined using multiple physicochemical methods. First, under non-turnover conditions, the UV-Vis spectrum of **Ni_4P_2** shows no significant change after 24 hours (**Figure 7-16**).

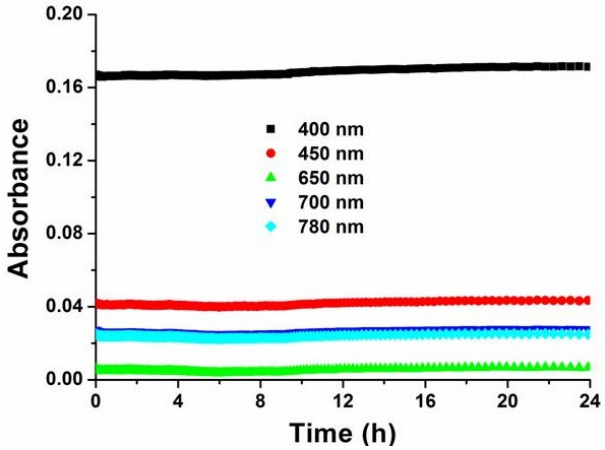

Figure 7-16 Time profile of UV-vis spectra of TBA-$\mathbf{Ni_4P_2}$ in CH_3CN/DMF (1/3) containing 0.25 M TEOA, over a 24-hour period (less than 1% decrease).

Second, the FT-IR spectra of $\mathbf{Ni_4P_2}$ isolated from post-reaction solution after 2.5 hrs or 7 days remain unchanged relative to the spectrum before photocatalytic reaction (**Figure 7-17**).

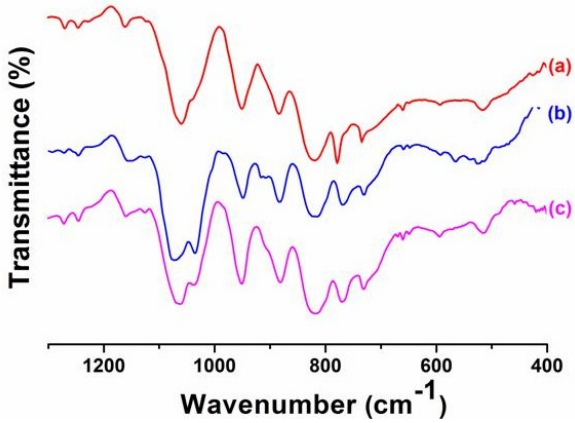

Figure 7-17 FT-IR spectra of (a) TBA-$\mathbf{Ni_4P_2}$ before light-driven reaction isolated from the solution containing $[Ir(ppy)_2(dtbbpy)]^+$ and TEOA using $[Ru(bpy)_3]^{2+}$; (b) the sample after light-driven reaction (isolated from post-catalytic reaction solution, illumination time: 2.5 hrs, TON ~ 300) and (c) the sample after light-driven reaction (isolated from post-catalytic reaction solution, illumination time: 7 days, TON ~6500). All FT-IR spectra were ~2 wt% samples in KBr.

Third, no decrease of photocatalytic activity by **Ni_4P_2** is observed in a mercury-poison test (using up to 150 mg Hg, **Figure 7-11**). Forth, no detectable formation of nanoparticles is observed by either DLS or TEM in the **Ni_4P_2**-catalyzed post-reaction solution. In contrast, nanoparticles with hydrodynamic sizes centered at 1.5 and 220 nm are observed by DLS in $NiCl_2$-catalyzed reactions (**Figure 7-18**), consistent with the size distribution (centered at around 2 nm) shown in TEM image (**Figure 7-19**). Elemental mapping of these nanoparticles show the presence of both Ni and O, where the O might come from surface oxidation of the Ni nanoparticles upon exposure to air (**Figure 7-19**).

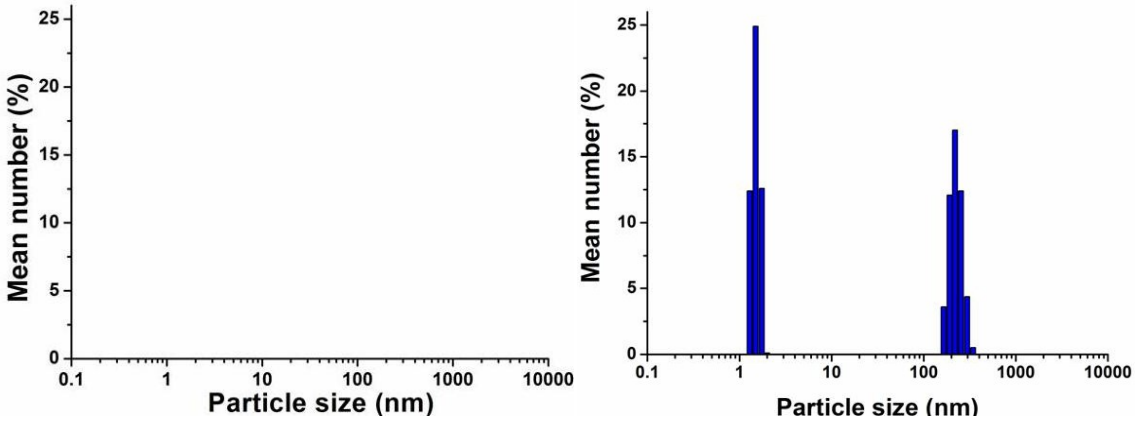

Figure 7-18 Particle size distribution (mean number %) obtained from dynamic light scattering (DLS) measurements for the post-reaction solution using 20 μM **Ni_4P_2** (left panel; the counts are below the detectable limit) and 20 μM $NiCl_2$ (right panel) as catalyst.

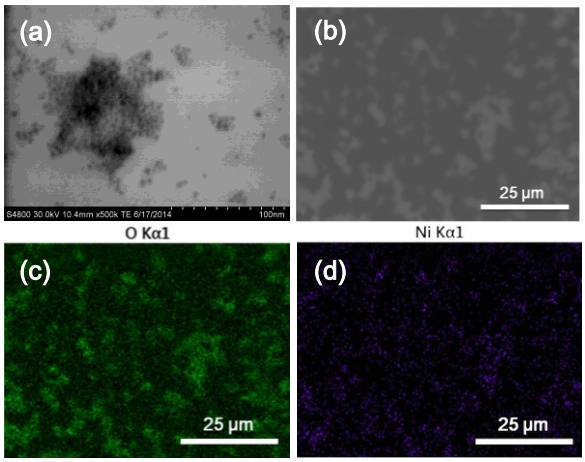

Figure 7-19 (a) TEM image and (b) SEM image of the nanoparticles isolated from the post-reaction solution using $NiCl_2$ as catalysts; (c) and (d) are the corresponding elemental mapping of the O and Ni, respectively.

7.4 Conclusions

In this section, we report an efficient, robust, and noble-metal-free molecular POM-based WRC, **Ni_4P_2** that catalyzes H_2 production upon visible-light irradiation over one week. It achieves the highest TON value (~6,500) for a POM-catalyzed H_2 evolution system with no significant loss in activity.

References

(1) Meyer, T. J. *Acc. Chem. Res.* **1989**, *22*, 163.

(2) Gratzel, M. *Nature* **2001**, *414*, 338.

(3) Lewis, N. S.; Nocera, D. G. *Proc. Natl. Acad. Sci. USA* **2006**, *103*, 15729.

(4) Esswein, A. J.; Nocera, D. G. *Chem. Rev. (Washington, DC, U. S.)* **2007**, *107*, 4022.

(5) Gray, H. B. *Nat. Chem.* **2009**, *1*, 7.

(6) Eisenberg, R. *Science* **2009**, *324*, 44.

(7) Faunce, T.; Styring, S.; Wasielewski, M. R.; Brudvig, G. W.; Rutherford, A. W.; Messinger, J.; Lee, A. F.; Hill, C. L.; Fontecave, M.; MacFarlane, D. R. *Energy Environ. Sci.* **2013**, *6*, 1074.

(8) Brown, G. M.; Brunschwig, B. S.; Creutz, C.; Endicott, J. F.; Sutin, N. *J. Am. Chem. Soc.* **1979**, *101*, 1298.

(9) DeLaive, P. J.; Sullivan, B. P.; Meyer, T. J.; Whitten, D. G. *J. Am. Chem. Soc.* **1979**, *101*, 4007.

(10) Streich, D.; Astuti, Y.; Orlandi, M.; Schwartz, L.; Lomoth, R.; Hammarstroem, L.; Ott, S. *Chem.--Eur. J.* **2010**, *16*, 60.

(11) Li, X.; Wang, M.; Chen, L.; Wang, X.; Dong, J.; Sun, L. *ChemSusChem* **2012**, *5*, 913.

(12) Berggren, G.; Adamska, A.; Lambertz, C.; Simmons, T. R.; Esselborn, J.; Atta, M.; Gambarelli, S.; Mouesca, J. M.; Reijerse, E.; Lubitz, W.; Happe, T.; Artero, V.; Fontecave, M. *Nature* **2013**, *499*, 66.

(13) Fihri, A.; Artero, V.; Razavet, M.; Baffert, C.; Leibl, W.; Fontecave, M. *Angew. Chem. Int. Ed.* **2008**, *47*, 564.

(14) Lazarides, T.; McCormick, T.; Du, P.; Luo, G.; Lindley, B.; Eisenberg, R. *J. Am. Chem. Soc.* **2009**, *131*, 9192.

(15) McNamara, W. R.; Han, Z.; Alperin, P. J.; Brennessel, W. W.; Holland, P. L.; Eisenberg, R. *J. Am. Chem. Soc.* **2011**, *133*, 15368.

(16) Zhang, P.; Jacques, P.-A.; Chavarot-Kerlidou, M.; Wang, M.; Sun, L.; Fontecave, M.; Artero, V. *Inorg. Chem.* **2012**, *51*, 2115.

(17) Singh, W. M.; Baine, T.; Kudo, S.; Tian, S.; Ma, X. A. N.; Zhou, H.; DeYonker, N. J.; Pham, T. C.; Bollinger, J. C.; Baker, D. L.; Yan, B.; Webster, C. E.; Zhao, X. *Angew. Chem. Int. Ed.* **2012**, *51*, 5941.

(18) Khnayzer, R. S.; Thoi, V. S.; Nippe, M.; King, A. E.; Jurss, J. W.; El Roz, K. A.; Long, J. R.; Chang, C. J.; Castellano, F. N. *Energy Environ. Sci.* **2014**, *7*, 1477.

(19) Helm, M. L.; Stewart, M. P.; Bullock, R. M.; DuBois, M. R.; DuBois, D. L. *Science* **2011**, *333*, 863.

(20) Small, Y. A.; DuBois, D. L.; Fujita, E.; Muckerman, J. T. *Energy Environ. Sci.* **2011**, *4*, 3008.

(21) Han, Z.; Qiu, F.; Eisenberg, R.; Holland, P. L.; Krauss, T. D. *Science* **2012**, *338*, 1321.

(22) Han, Z.; McNamara, W. R.; Eum, M.-S.; Holland, P. L.; Eisenberg, R. *Angew. Chem. Int. Ed.* **2012**, *51*, 1667.

(23) Han, Z.; Shen, L.; Brennessel, W. W.; Holland, P. L.; Eisenberg, R. *J. Am. Chem. Soc.* **2013**, *135*, 14659.

(24) Karunadasa, H. I.; Chang, C. J.; Long, J. R. *Nature* **2010**, *464*, 1329.

(25) Karunadasa, H. I.; Montalvo, E.; Sun, Y.; Majda, M.; Long, J. R.; Chang, C. J. *Science* **2012**, *335*, 698.

(26) Hawecker, J.; Lehn, J. M.; Ziessel, R. *Nouv. J. Chim.* **1983**, *7*, 271.

(27) Collin, J. P.; Sauvage, J. P. *Coord. Chem. Rev.* **1989**, *93*, 245.

(28) McCormick, T. M.; Han, Z.; Weinberg, D. J.; Brennessel, W. W.; Holland, P. L.; Eisenberg, R. *Inorg. Chem.* **2011**, *50*, 10660.

(29) Hill, C. L. *Chem. Rev.* **1998**, *98*, 1.

(30) Hiskia, A.; Mylonas, A.; Papaconstantinou, E. *Chem. Soc. Rev.* **2001**, *30*, 62.

(31) Lv, H.; Geletii, Y. V.; Zhao, C.; Vickers, J. W.; Zhu, G.; Luo, Z.; Song, J.; Lian, T.; Musaev, D. G.; Hill, C. L. *Chem. Soc. Rev.* **2012**, *41*, 7572.

(32) Cronin, L.; Muller, A. *Chem. Soc. Rev.* **2012**, *41*, 7333.

(33) Sumliner, J. M.; Lv, H.; Fielden, J.; Geletii, Y. V.; Hill, C. L. *Eur. J. Inorg. Chem.* **2014**, *2014*, 635.

(34) Geletii, Y. V.; Botar, B.; Kögerler, P.; Hillesheim, D. A.; Musaev, D. G.; Hill, C. L. *Angew. Chem. Int. Ed.* **2008**, *47*, 3896.

(35) Sartorel, A.; Carraro, M.; Scorrano, G.; Zorzi, R. D.; Geremia, S.; McDaniel, N. D.; Bernhard, S.; Bonchio, M. *J. Am. Chem. Soc.* **2008**, *130*, 5006.

(36) Yin, Q.; Tan, J. M.; Besson, C.; Geletii, Y. V.; Musaev, D. G.; Kuznetsov, A. E.; Luo, Z.; Hardcastle, K. I.; Hill, C. L. *Science* **2010**, *328*, 342.

(37) Murakami, M.; Hong, D.; Suenobu, T.; Yamaguchi, S.; Ogura, T.; Fukuzumi, S. *J. Am. Chem. Soc.* **2011**, *133*, 11605.

(38) Vickers, J.; Lv, H.; Zhuk, P. F.; Geletii, Y. V.; Hill, C. L. *MRS Proceedings* **2012**, *1387*, mrsf11.

(39) Goberna-Ferrón, S.; Vigara, L.; Soriano-López, J.; Galán-Mascarós, J. R. *Inorg. Chem.* **2012**, *51*, 11707.

(40) Stracke, J. J.; Finke, R. G. *ACS Catalysis* **2013**, *4*, 79.

(41) Schiwon, R.; Klingan, K.; Dau, H.; Limberg, C. *Chem. Commun.* **2014**, *50*, 100.

(42) Geletii, Y. V.; Huang, Z.; Hou, Y.; Musaev, D. G.; Lian, T.; Hill, C. L. *J. Am. Chem. Soc.* **2009**, *131*, 7522.

(43) Besson, C.; Huang, Z. Q.; Geletii, Y. V.; Lense, S.; Hardcastle, K. I.; Musaev, D. G.; Lian, T. Q.; Proust, A.; Hill, C. L. *Chem. Commun.* **2010**, *46*, 2784.

(44) Huang, Z.; Luo, Z.; Geletii, Y. V.; Vickers, J. W.; Yin, Q.; Wu, D.; Hou, Y.; Ding, Y.; Song, J.; Musaev, D. G.; Hill, C. L.; Lian, T. *J. Am. Chem. Soc.* **2011**, *133*, 2068.

(45) Car, P.-E.; Guttentag, M.; Baldridge, K. K.; Alberto, R.; Patzke, G. R. *Green Chem.* **2012**, *14*, 1680.

(46) Tanaka, S.; Annaka, M.; Sakai, K. *Chem. Commun. (Cambridge, U. K.)* **2012**, *48*, 1653.

(47) Zhu, G.; Glass, E. N.; Zhao, C.; Lv, H.; Vickers, J. W.; Geletii, Y. V.; Musaev, D. G.; Song, J.; Hill, C. L. *Dalton Trans.* **2012**, *41*, 13043.

(48) Vickers, J. W.; Lv, H.; Sumliner, J. M.; Zhu, G.; Luo, Z.; Musaev, D. G.; Geletii, Y. V.; Hill, C. L. *J. Am. Chem. Soc.* **2013**, *135*, 14110.

(49) Song, F.; Ding, Y.; Ma, B.; Wang, C.; Wang, Q.; Du, X.; Fu, S.; Song, J. *Energy Environ. Sci.* **2013**, *6*, 1170.

(50) Lv, H.; Song, J.; Geletii, Y. V.; Vickers, J. W.; Sumliner, J. M.; Musaev, D. G.; Kögerler, P.; Zhuk, P. F.; Bacsa, J.; Zhu, G.; Hill, C. L. *J. Am. Chem. Soc.* **2014**, *136*, 9268.

(51) Vickers, J. W.; Sumliner, J. M.; Lv, H.; Morris, M.; Geletii, Y. V.; Hill, C. L. *Phys. Chem. Chem. Phys.* **2014**, *16*, 11942.

(52) Han, X.-B.; Zhang, Z.-M.; Zhang, T.; Li, Y.-G.; Lin, W.; You, W.; Su, Z.-M.; Wang, E.-B. *J. Am. Chem. Soc.* **2014**, *136*, 5359.

(53) Toma, F. M.; Sartorel, A.; Iurlo, M.; Carraro, M.; Parisse, P.; Maccato, C.; Rapino, S.; Gonzalez, B. R.; Amenitsch, H.; Da Ros, T.; Casalis, L.; Goldoni, A.; Marcaccio, M.; Scorrano, G.; Scoles, G.; Paolucci, F.; Prato, M.; Bonchio, M. *Nat Chem* **2010**, *2*, 826.

(54) Quintana, M.; López, A. M.; Rapino, S.; Toma, F. M.; Iurlo, M.; Carraro, M.; Sartorel, A.; Maccato, C.; Ke, X.; Bittencourt, C.; Da Ros, T.; Van Tendeloo, G.; Marcaccio, M.; Paolucci, F.; Prato, M.; Bonchio, M. *ACS Nano* **2013**, *7*, 811.

(55) Soriano-López, J.; Goberna-Ferrón, S.; Vigara, L.; Carbó, J. J.; Poblet, J. M.; Galán-Mascarós, J. R. *Inorg. Chem.* **2013**, *52*, 4753.

(56) Guo, S.-X.; Liu, Y.; Lee, C.-Y.; Bond, A. M.; Zhang, J.; Geletii, Y. V.; Hill, C. L. *Energy Environ. Sci.* **2013**, *6*, 2654.

(57) Liu, Y.; Guo, S.-X.; Bond, A. M.; Zhang, J.; Geletii, Y. V.; Hill, C. L. *Inorg. Chem.* **2013**, *52*, 11986.

(58) Papaconstantinou, E.; Pope, M. T. *Inorg. Chem.* **1967**, *6*, 1152.

(59) Savinov, E. N.; Saidkhanov, S. S.; Parmon, V. N.; Zamaraev, K. I. *React. Kinet. Catal. Lett.* **1981**, *17*, 407.

(60) Ioannidis, A.; Papaconstantinou, E. *Inorg. Chem.* **1985**, *24*, 439.

(61) Hill, C. L.; Bouchard, D. A. *J. Am. Chem. Soc.* **1985**, *107*, 5148.

(62) Yamase, T.; Cao, X.; Yazaki, S. *J. Mol. Catal. A: Chem.* **2007**, *262*, 119.

(63) Keita, B.; Nadjo, L. *J. Electroanal. Chem. Interfacial Electrochem.* **1987**, *217*, 287.

(64) Keita, B.; Kortz, U.; Holzle, L. R. B.; Brown, S.; Nadjo, L. *Langmuir* **2007**, *23*, 9531.

(65) Liu, X.; Li, Y.; Peng, S.; Lu, G.; Li, S. *Int. J. Hydrogen Energy* **2012**, *37*, 12150.

(66) Zhang, Z.; Lin, Q.; Zheng, S.-T.; Bu, X.; Feng, P. *Chem. Commun. (Cambridge, U. K.)* **2011**, *47*, 3918.

(67) Matt, B.; Fize, J.; Moussa, J.; Amouri, H.; Pereira, A.; Artero, V.; Izzet, G.; Proust, A. *Energy Environ. Sci.* **2013**, *6*, 1504.

(68) Lv, H.; Song, J.; Zhu, H.; Geletii, Y. V.; Bacsa, J.; Zhao, C.; Lian, T.; Musaev, D. G.; Hill, C. L. *J. Catal.* **2013**, *307*, 48.

(69) Suzuki, K.; Tang, F.; Kikukawa, Y.; Yamaguchi, K.; Mizuno, N. *Chem. Lett.* **2014**, *43*, 1429.

(70) Clemente-Juan, J. M.; Coronado, E.; Galan-Mascaros, J. R.; Gomez-Garcia, C. J. *Inorg. Chem.* **1999**, *38*, 55.

(71) Bruker In *APEXII v2014.1-1*; Bruker AXS Inc.: Madison, WI., 2014.

(72) Bruker In *SAINT v8.34A*; Bruker AXS Inc.: Madison, WI., 2013.

(73) Dolomanov, O. V.; Bourhis, L. J.; Gildea, R. J.; Howard, J. A. K.; Puschmann, H. *J. Appl. Crystallogr.* **2009**, *42*, 339.

(74) Palatinus, L.; Chapuis, G. *J. Appl. Crystallogr.* **2007**, *40*, 786.

(75) Sheldrick, G. *Acta Cryst. A* **2008**, *64*, 112.

(76) Katsoulis, D. E.; Pope, M. T. *J. Am. Chem. Soc.* **1984**, *106*, 2737.

(77) Zhao, Y.; Truhlar, D. G. *J. Chem. Phys.* **2006**, *125*, 194101.

(78) Hay, P. J.; Wadt, W. R. *J. Chem. Phys.* **1985**, *82*, 270.

(79) Wadt, W. R.; Hay, P. J. *J. Chem. Phys.* **1985**, *82*, 284.

(80) Hay, P. J.; Wadt, W. R. *J. Chem. Phys.* **1985**, *82*, 299.

(81) Frisch, M. J.; Trucks, G. W.; Schlegel, H. B.; Scuseria, G. E.; Robb, M. A.; Cheeseman, J. R.; Scalmani, G.; Barone, V.; Mennucci, B.; Petersson, G. A.; Nakatsuji, H.; Caricato, M.; Li, X.; Hratchian, H. P.; Izmaylov, A. F.; Bloino, J.; Zheng, G.; Sonnenberg, J. L.; Hada, M.; Ehara, M.; Toyota, K.; Fukuda, R.; Hasegawa, J.; Ishida, M.; Nakajima, T.; Honda, Y.; Kitao, O.; Nakai, H.; Vreven, T.; J. A. Montgomery, J.; Peralta, J. E.; Ogliaro, F.; Bearpark, M.; Heyd, J. J.; Brothers, E.; Kudin, K. N.; Staroverov, V. N.; Kobayashi, R.; Normand, J.; Raghavachari, K.; Rendell, A.; Burant, J. C.; Iyengar, S. S.; Tomasi, J.; Cossi, M.; N. Rega, J. M. M.; Klene, M.; Knox, J. E.; Cross, J. B.; Bakken, V.; Adamo, C.; Jaramillo, J.; Gomperts, R.;

Stratmann, R. E.; Yazyev, O.; Austin, A. J.; Cammi, R.; Pomelli, C.; Ochterski, J. W.; Martin, R. L.; K. Morokuma, V. G. Z.; Voth, G. A.; Salvador, P.; Dannenberg, J. J.; Dapprich, S.; Daniels, A. D.; Ö. Farkas, J. B. F.; Ortiz, J. V.; Cioslowski, J.; Fox, D. J.; Revision A.1 ed.; Gaussian, I., Ed. Wallingford CT., 2009.

(82) Mbomekalle, I. M.; Keita, B.; Nierlich, M.; Kortz, U.; Berthet, P.; Nadjo, L. *Inorg. Chem.* **2003**, *42*, 5143.

(83) Ibrahim, M.; Xiang, Y.; Bassil, B. S.; Lan, Y.; Powell, A. K.; de Oliveira, P.; Keita, B.; Kortz, U. *Inorg. Chem.* **2013**, *52*, 8399.

(84) Cline, E. D.; Adamson, S. E.; Bernhard, S. *Inorg. Chem.* **2008**, *47*, 10378.

(85) Prier, C. K.; Rankic, D. A.; MacMillan, D. W. C. *Chem. Rev. (Washington, DC, U. S.)* **2013**, *113*, 5322.

(86) Sun, H.; Hoffman, M. Z. *J. Phys. Chem.* **1994**, *98*, 11719.

Chapter 8

$[\{Ni_4(OH)_3AsO_4\}_4(\textit{B}\text{-}\alpha\text{-}PW_9O_{34})_4]^{28-}$ a New Polyoxometalate Structural Family with Catalytic Hydrogen Evolution Activity

(Accepted by *Chem.-a Eur. J.* **2015**, chem.201503010) -- Reproduced by permission of John Wiley and Sons.

With Hongjin Lv, Yingnan Chi, Jan van Leusen, Paul Kögerler, Zheyuan Chen, John Bacsa, Weiwei Guo, Tianquan Lian, Craig L. Hill*

8.1 Introduction

Polyoxometalates (POMs) have attracted considerable recent attention due to their structural and compositional diversity as well as their applications in catalysis, medicine, electrochromism, materials science, photochemistry, analytical chemistry, and molecular magnetism.[1-17] Lacunary POMs generated by removing one or several MO_6 (M = Mo, W) units from prototypal architectures such as the Keggin or Wells-Dawson types, in particular, are strong inorganic, diamagnetic, multidentate O-donor ligands allowing for construction of various mono- or multinuclear transition-metal-substituted POMs (TMSPOMs). TMSPOMs have been effective models to study superexchange interactions between paramagnetic transition metal clusters and several of them exhibit single-molecule magnet behavior.[18-20] They are also attractive candidates for catalysis of multi-electron-transfer processes because of their unusually rich redox chemistry yet stability to oxidative degradation.[10,11,21-23] Recently, TMSPOMs have been extensively investigated for solar energy conversion as both water oxidation catalysts (WOCs) under thermal,[24-31] photochemical[32-42] and electrochemical[43-46] conditions and water reduction catalysts (WRCs)[47-52] under visible light irradiation. To date, many multinuclear TMSPOMs have been synthesized by reaction of lacunary POMs with transition metal ions using conventional solution-based[18-20,41,53-76] or hydrothermal[77-79] methods. Representative examples of these structurally, catalytically, and magnetically interesting multinuclear ($n \geq 6$) TMSPOMs include $\{Mn_6W_{18}\}$,[18] $\{Mn_6W_{24}\}$,[53] $\{Mn_{14}W_{36}\}$,[54] $\{Mn_{14}W_{48}\}$,[55] $\{Fe_6W_{24}\}$,[56] $\{Fe_9W_{12}\}$,[57] $\{Fe_9W_{24}\}$,[19] $\{Fe_{13}W_{36}\}$,[58,59] $\{Fe_{16}W_{48}\}$,[60] $\{Fe_{28}W_{48}\}$,[61] $\{Co_6W_{24}\}$,[62-64] $\{Co_7W_{25}\}$,[65] $\{Co_9W_{27}\}$,[66] $\{Co_{16}W_{36}\}$,[20,41,67] $\{Cu_6W_{18}\}$,[68] $\{Cu_{14}W_{36}\}$,[69] and $\{Cu_{20}W_{48}\}$.[70] Multi-nickel clusters stabilized by POMs have also been

studied (e.g. $\{Ni_6W_{24}\}$ [71] $\{Ni_7W_{19}\}$,[72] $\{Ni_8W_{18}\}$,[73] $\{Ni_9W_{18}\}$,[73] $\{Ni_9W_{27}\}$,[74] $\{Ni_{12}W_{35}\}$,[75] $\{Ni_{14}W_{60}\}$,[76]). To date, the largest number of Ni ions incorporated into a single POM cluster was 14.[76] Yang's group reported a series of $\{Ni_{20}\}$ to $\{Ni_{40}\}$-containing POMs,[77-79] prepared under hydrothermal conditions using organic amines, that contain organic ligands. Thus the design and synthesis of high-nuclearity Ni-containing POMs under mild solution-based conditions with interesting magnetic and/or catalytic properties remains a significant challenge. Herein, we report the straightforward, one-pot synthesis of a structurally unprecedented POM, the multi-nickel carbon-free complex, $[\{Ni_4(OH)_3AsO_4\}_4(\textit{B}\text{-}\alpha\text{-}PW_9O_{34})_4]^{28-}$ (**$Ni_{16}As_4P_4$**), along with its magnetic, spectroscopic and catalytic properties.

8.2 Experimental

8.2.1. Materials and Instrumentation

All chemicals and solvents for syntheses, characterization, and catalytic studies were purchased from commercial sources, which were used as received without further purification unless otherwise noted. A Barnstead Nanopure® water-purification system was used to produce Nanopure H_2O for solution preparation. The FT-IR spectra were measured on a Thermo Nicolet 6700 spectrometer. UV-Vis spectra were acquired using Agilent 8453 spectrophotometer equipped with a diode-array detector and an Agilent 89090A cell temperature controller unit. Elemental analyses were performed by Galbraith Lab Inc., Knoxville, TN, 37921. Thermogravimetric data were collected on Simultaneous Thermal analysis STA 6000 (PerkinElmer). Magnetic ac and dc susceptibility data were recorded using a Quantum Design MPMS-5XL SQUID magnetometer. Analysis of hydrogen was conducted using a HP7890A model gas chromatograph equipped with

thermal conductivity detector (TCD) and a 5Å molecular sieve capillary column. Dynamic light scattering (DLS) measurements were performed on a Brookhaven Instruments 90Plus particle size analyzer; each sample was measured three times consecutively. The emission quenching spectra were recorded on a FluoroMax 3 spectrofluorimeter; the strong emission band of $[Ir(ppy)_2(dtbbpy)]^+$ at 470 - 750 nm with λ_{max} = 577 nm ($\lambda_{excitation}$ = 455 nm) was recorded. For time-resolved fluorescence decay measurements, femtosecond laser pulses (~100 fs, 80 MHz repetition rate) were generated with a mode-locked Ti:sapphire laser (Tsunami oscillator pumped by 10 W Millennia Pro, Spectra-Physics). Excitation pulses at 400 nm were produced by second harmonic generation of the 800 nm pulses in a BBO crystal. The repetition rate of output pulse centered at 800 nm was reduced to 1.6 MHz using a pulse picker (Conoptics, USA). The emissions of $[Ir(ppy)_2(dtbbpy)]^+$ were detected by a microchannel plate photomultiplier tube (Hamamatsu R3809U-51), whose output was amplified and analyzed by a TCSPC board (Becker & Hickel SPC 600).

8.2.2. Synthesis

Synthesis of polyanion $[\{Ni_4(OH)_3AsO_4\}_4(\textit{B}\text{-}\alpha\text{-}PW_9O_{34})_4]^{28-}$ ($Ni_{16}As_4P_4$). $Na_{28}[\{Ni_4(OH)_3AsO_4\}_4(\textit{B}\text{-}\alpha\text{-}PW_9O_{34})_4]\cdot 120H_2O$ (Na_{28}-**$Ni_{16}As_4P_4$**) was synthesized via the following two methods: **Method I:** $Na_2WO_4\cdot 2H_2O$ (16.5 g, 50 mmol) and $Na_2HAsO_4\cdot 7H_2O$ (1.716 g, 5.5 mmol) were dissolved in 80 mL Nanopure® water and the pH adjusted to 8.10 using concentrated acetic acid. To this was added slowly with vigorously stirring a solution of $Ni(OOCCH_3)_2\cdot 4H_2O$ (4.1 g, 16 mmol) in 35 mL Nanopure® water. The resulting green solution was refluxed for 2 hrs. Then, a 4-g amount of Na_2HPO_4 was added and the resulting mixture was refluxed again for 9 h and

filtered hot to remove any precipitate. The hot green solution was allowed to cool at room temperature and left for crystallization. After 8 days, millimeter-long green needle-shaped crystals of the desired products were collected by filtration and dried under ambient conditions (yield = 2.7 g, 20.1% based on Ni). **Method II:** $Na_2WO_4{\cdot}2H_2O$ (16.5 g, 50 mmol) and Na_2HPO_4 (0.78 g, 5.5 mmol) were dissolved in 80 mL Nanopure® water and the pH adjusted to 8.10 using concentrated acetic acid. To this was added slowly with vigorously stirring a solution of $Ni(OOCCH_3)_2{\cdot}4H_2O$ (4.1 g, 16 mmol) in 35 mL Nanopure® water. The resulting green solution was refluxed for 2 hrs. Subsequently, a mixture of 3 g Na_2HPO_4 and 1.7 g $Na_2HAsO_4{\cdot}7H_2O$ were added and the resulting mixture was refluxed again for 9 h and filtered hot to remove any precipitate. The hot green solution was allowed to cool at room temperature and left for crystallization. After three days millimeter-long green needle-shaped crystals of the desired products were collected by filtration and dried under ambient conditions (yield = 6.2 g, 46.2% based on Ni). Elemental analysis for $Na_{28}[\{Ni_4(OH)_3AsO_4\}_4(\textit{B}\text{-}\alpha\text{-}PW_9O_{34})_4]{\cdot}120H_2O$: Calcd for Na, 4.80; Ni, 7.00; P, 0.92; As, 2.23; W, 49.31%; found for Na, 4.78; Ni, 7.02; P, 0.93; As, 2.19; W, 49.80%. FT-IR (2% KBr pellet, 1100–400 cm^{-1}, **Figure 8-1**): 1081(s), 1028(s), 954(sh), 935(m), 886(m), 798(m), 720(m), 585(w) and 483(w). CCDC 1050850 (**$Ni_{16}As_4P_4$**) contains the supplementary crystallographic data for this work. These data can be obtained free of charge from The Cambridge Crystallographic Data Centre via www.ccdc.cam.ac.uk/ data_request/cif.

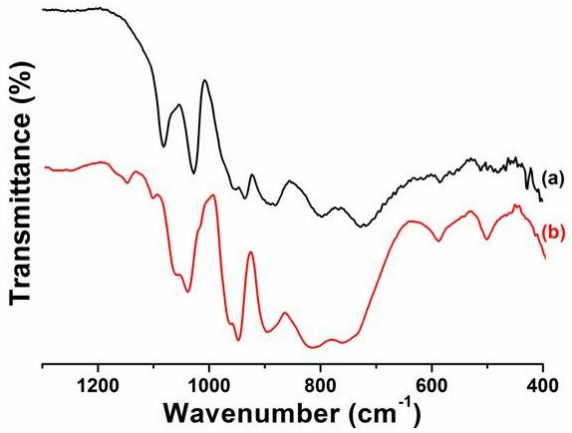

Figure 8-1 FT-IR spectra of (a) Na_{28}-$\mathbf{Ni_{16}As_4P_4}$ (black) and (b) TBA-$\mathbf{Ni_{16}As_4P_4}$ (red), ~2 wt % in KBr. The spectra show all the characteristic bands of polyanion $\mathbf{Ni_{16}As_4P_4}$ confirming that the cation exchange (TBA^+ for Na^+ and K^+) does not change the structure of $\mathbf{Ni_{16}As_4P_4}$.

The tetrabutylammonium (TBA^+) salt of $\mathbf{Ni_{16}As_4P_4}$ (TBA-$\mathbf{Ni_{16}As_4P_4}$) was prepared following a modified literature procedure[80]: typically, Na_{28}-$\mathbf{Ni_{16}As_4P_4}$ (1.34 g, 0.1 mmol) was dissolved in 30 mL H_2O, to which a solution of tetrabutylammonium bromide (TBABr, 5 g, 15 mmol) dissolved in 20 mL 0.25 M sodium acetate buffer (pH 4.8) was added. The pale green precipitate formed immediately and was collected by centrifugation. The resulting solid was washed with water (twice) and ethanol (once) to remove any additional TBABr and dried under air. The dried solid was then redissolved in 5 mL CH_3CN and the mixture centrifuged to isolate any undissolved precipitate. The final products were obtained in high purity by adding anhydrous diethyl ether to the clear CH_3CN solution. The FT-IR spectrum of TBA-$\mathbf{Ni_{16}As_4P_4}$ is shown in **Figure 8-1**; the cation exchange does not change the structure of $\mathbf{Ni_{16}As_4P_4}$.

Synthesis of $\mathbf{Na_{18}K_{10}[\{Ni_4(OH)_3PO_4\}_4(\mathit{A}\text{-}\alpha\text{-}PW_9O_{34})_4]\cdot 75H_2O}$ ($\mathbf{Na_{18}K_{10}}$-$\mathbf{Ni_{16}P_4P_4}$). $Na_2WO_4{\cdot}2H_2O$ (16.5 g, 50 mmol) and Na_2HPO_4 (0.78 g, 5.5 mmol) were dissolved in 90 mL of Nanopure® water and the pH adjusted to 8.10 using concentrated acetic acid. The

solution was heated to boiling with vigorous stirring, to which was added slowly a solution of $Ni(OOCCH_3)_2 \cdot 4H_2O$ (4.1 g, 16 mmol) in 30 mL Nanopure® water. The resulting greenish solution was refluxed for 2 hrs. Subsequently, 4 g of Na_2HPO_4 was added and the resulting mixture was continuously refluxed for another 9 hrs. The hot turbid solution was centrifuged to remove any precipitate. Solid potassium acetate (5 g) was added to the clear green solution, inducing an instantaneous precipitation of pale green solid and formation of a greenish oil in the bottom of the beaker. The oily green precipitate was collected by decanting off the pale green mixture. The residue was re-dissolved in 15 mL of warm water, which was cooled down to room temperature and left for crystallization. After about 1 week well-formed green block crystals of the desired products were collected by filtration and dried under ambient conditions (yield = 0.92 g, 7.3% based on Ni). Elemental analysis for $Na_{18}K_{10}[\{Ni_4(OH)_3PO_4\}_4(A\text{-}\alpha\text{-}PW_9O_{34})_4] \cdot 75H_2O$: calcd for Na, 3.28; K, 3.10; Ni, 7.45; P, 1.97; W, 52.54%; found for Na, 3.48; K, 3.02 Ni, 7.54; P, 1.90; W, 53.01%. FT-IR (2% KBr pellet, 1200 – 400 cm^{-1}, **Figure 8-1**): 1090(sh), 1055(s), 1030(s), 940(s), 877(m), 824(s), 703(m), 580(w) and 505(w). CCDC 1055749 (**$Ni_{16}P_4P_4$**) contains the supplementary crystallographic data for this work. These data can be obtained free of charge from The Cambridge Crystallographic Data Centre via www.ccdc.cam.ac.uk/ data_request/cif.

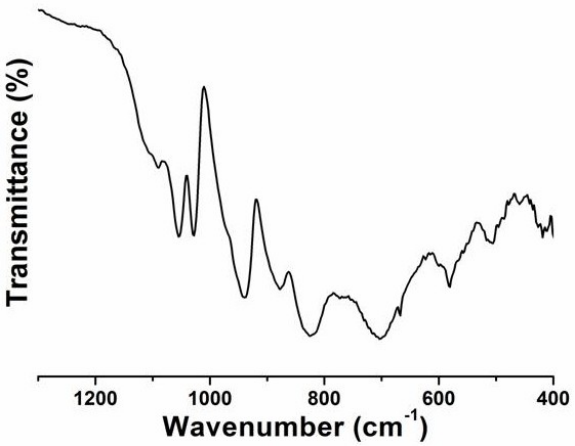

Figure 8-2 FT-IR spectrum of $Na_{18}K_{10}$-$\mathbf{Ni_{16}P_4P_4}$, ~2 wt % in KBr.

8.2.3. X-ray Crystallography

Complete data for Na_{28}-$\mathbf{Ni_{16}As_4P_4}$ were collected at Emory. A suitable crystal (0.45 × 0.23 × 0.20 mm^3, **Figure 8-3**) was selected and mounted on a loop with paratone oil and placed under a nitrogen gas stream at 110(2) K on a Bruker D8 APEX II CCD sealed tube diffractometer. Data were measured using MoK_λ radiation (fine-focus sealed tube, 45 kV, 30 mA). The total number of runs and images was based on the strategy calculation from the program **APEXII**.[81] A resolution of λ = 30.029° was achieved.[81] Data reduction was performed using the **SAINT** (Bruker, V8.34A, 2013)[82] software. The final completeness is 100.00% out to 30.029°in θ. The absorption coefficient (μ) of this material is 24.786 mm^{-1} and the minimum and maximum transmissions are 0.0074 and 0.2249. Cell parameters were refined using **SAINT**[82] on 34376 reflections, 22% of the observed reflections. The results are summarized in **Table 8-1**. The structure was solved using **Olex2**[83] by Charge Flipping using the **Superflip**[84] structure solution program and refined by Least Squares using version 2013-4 of ShelXL.[85] The structure was solved in the space group $P\bar{1}$ (# 2). All non-hydrogen atoms were refined anisotropically.

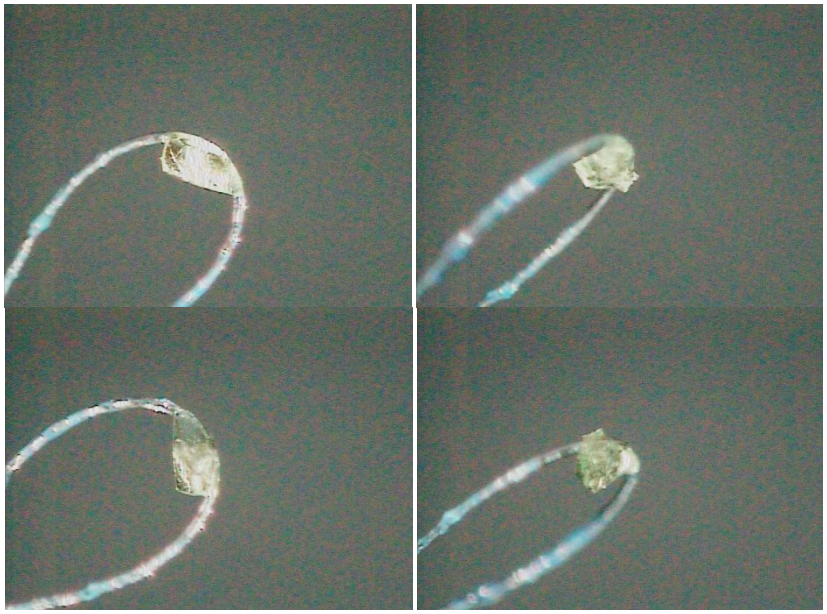

Figure 8-3 Images of the Na_{28}-$\mathbf{Ni_{16}As_4P_4}$ crystal on the diffractometer.

The atomic displacement parameters of the As and the P atoms belonging to the (XO_4) groups were unreasonably large and small respectively compared to the rest of the model, especially in comparison to their neighboring atoms. Because the intensity of Bragg diffraction corresponds to the electron density at the atom sites, the least-squares refinement will expand the thermal ellipsoid to increase the volume of an atom if too much electron density has been assigned to that atom. The most likely explanation is that small amounts of P contaminate the As sites and *vice versa*. Chemically these two atoms are sufficiently similar for this to be possible. These atom sites were split into two parts corresponding to two atoms sharing the same site. The *x,y* and *z* and thermal displacement parameters of the two parts were set to be equal. The partial occupancies were refined freely (by using free variables) but with the sum to be constant (1.0). There are 4 PO_4 and 4 AsO_4 sites. Interestingly the refined occupancies balanced to give the integer formula: 4 PO_4 and 4 AsO_4. The average refined occupancies were approximately 0.85As:0.15P for the AsO_4 sites and 0.85P:0.15As for the PO_4 sites; these values were

used in the final refinements. In other words the (XO_4) sites originally assigned as X=As contain approximately 85% As and 15%P (**Figure 8-4**).

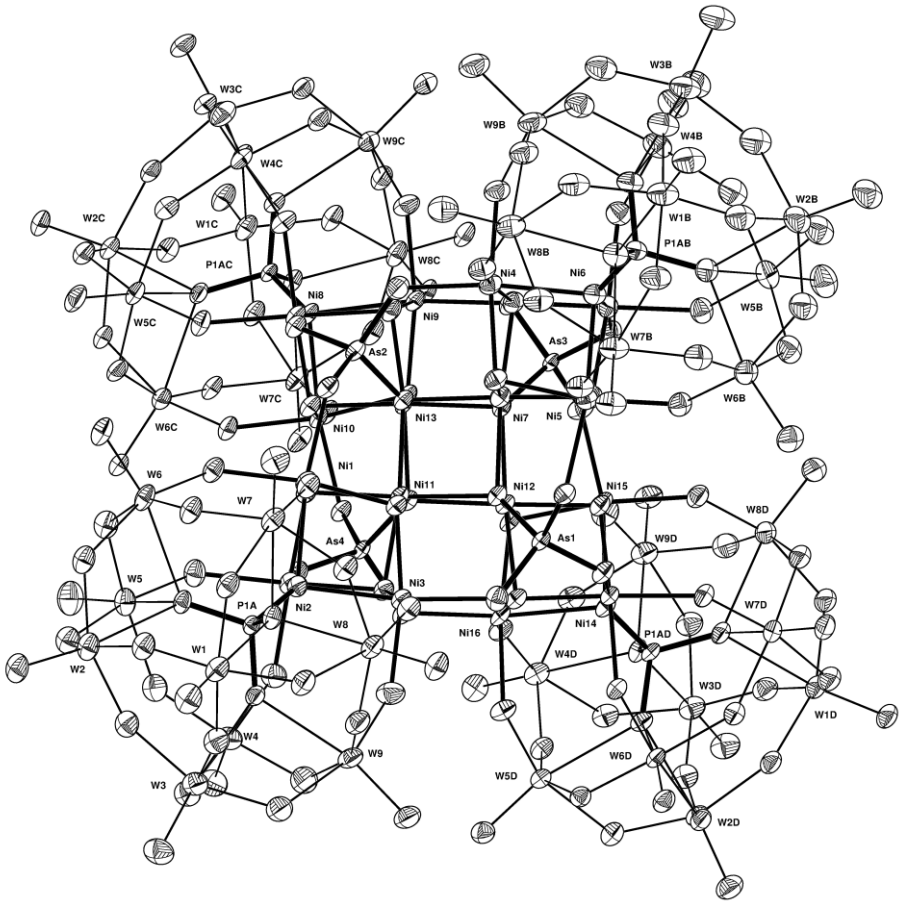

Figure 8-4 A displacement ellipsoid plot of the $\mathbf{Ni_{16}As_4P_4}$ polyanion. Atoms are represented by ellipsoids at the 50% probability level. In cases where two atoms share the same site, the dominant chemical species (P or As) is shown.

Similarly, complete data for $Na_{18}K_{10}$-$\mathbf{Ni_{16}P_4P_4}$ were also collected at the Emory. A suitable green crystal (0.45 × 0.36 × 0.30 mm^3) was mounted on a loop with paratone oil and placed on a Bruker D8 APEX II CCD sealed tube diffractometer equipped with an Oxford Cryosystems low-temperature apparatus operating at T = 110(2) K. Data were measured using ϕ and ω scans scans of 0.5° per frame for 30 s using MoK_α radiation (fine-focus sealed tube, 45 kV, 30 mA). The total number of runs and images was based

on the strategy calculation using the program APEX2 (Bruker).[81] The maximum resolution that was achieved was Θ = 27.5°. Data reduction was performed using the SAINT[82] software. The final completeness is 100.00% out to 27.5°in θ. The absorption coefficient (μ) of this material is 21.159 mm^{-1} and the minimum and maximum transmissions are 0.0087 and 0.1386. Unit cell indexing were performed by using the APEX2[81] software and cell parameters were refined using SAINT[82] on 28147 reflections, 18.6% of the observed reflections. The structure was solved using Olex2[83] by Charge Flipping using the Superflip[84] structure solution program and refined by Least Squares minimization using version 2013-4 of ShelXL.[85] The structure was solved in the space group $P2_1/c$ (#14, **Table 8-1**). All non-hydrogen atoms were refined anisotropically.

Table 8-1 Crystallographic data and structure refinement for Na_{28}-**$Ni_{16}As_4P_4$** and $Na_{18}K_{10}$-**$Ni_{16}P_4P_4$**.

	Na_{28}-$Ni_{16}As_4P_4$	**$Na_{18}K_{10}$-$Ni_{16}P_4P_4$**
Formula	$As_4Na_{26}Ni_{16}O_{230}P_4W_{36}$	$Na_{18}K_{10}Ni_{16}O_{239}P_8W_{36}H_{162}$
Formula weight	12259.26 g mol^{-1}	12597.07 g mol^{-1}
μ/mm^{-1}	20.880	21.159
$D_{calc.}$/ g cm^{-3}	3.703	3.769
Crystal System	triclinic	monoclinic
Space Group	$P\bar{1}$	$P2_1/c$
Colour	green	green
T/K	110(2)	110(2)
a/Å	22.582(7)	25.498(2)
b/Å	23.243(7)	26.339(2)
c/Å	23.584(7)	31.519(3)
α/°	92.346(5)	90
β/°	94.403(5)	91.761(14)
γ/°	116.628(4)	90
V/$Å^3$	10994(6)	21157(3)

Z	2	4
Θ_{min}/°	1.703	0.799
Θ_{max}/°	29.728	27.504
Measured Refl.	155317	150962
Independent Refl.	61059	48417
Reflections Used	34376	28147
R_{int}	0.1093	0.1227
Parameters	2856	2643
Restraints	4779	4878
GooF	1.072	1.032
R_1	0.0892	0.0787
R_1 (all data)[a]	0.1769	0.1303
wR_2	0.1904	0.1977
wR_2 (all data)[b]	0.2347	0.2191

[a] $R_1 = \Sigma||F_0| - |F_c||/ \Sigma|F_0|$; [b] $wR_2 = \Sigma[w(F_0^2 - F_c^2)^2]/ \Sigma[w(F_0^2)^2]^{1/2}$

8.2.4. Magnetochemical Characterization.

Magnetic dc susceptibility data of Na_{28}-**$Ni_{16}As_4P_4$** were recorded between 2.0 and 290 K at 0.1 Tesla using a Quantum Design MPMS-5XL SQUID magnetometer. For alternating current (ac) measurements, the data were collected between 2.0 and 50.0 K in the frequency range 3−938 s^{-1} with an amplitude of B_{ac} = 3 Gauss in absence of a static bias field. The polycrystalline sample was compacted and immobilized into a cylindrical PTFE sample holder. The data were corrected for diamagnetic contributions from the sample holder and the compound (χ_{dia}(Na_{28}-**$Ni_{16}As_4P_4$**) = -6.66×10^{-3} cm^3 mol^{-1}).

8.2.5. Visible-light-driven Catalytic Hydrogen Evolution Experiments

The light-driven water reduction experiment was performed in a cylindrical cuvette (NSG, 32UV10) with a total volume of ~2.5 mL. In a typical experiment, the cell was filled with 2.0 mL CH_3CN/DMF (1/3) solution containing 0.2 mM $[Ir(ppy)_2(dtbbpy)]^+$, 0.25 M

triethanolamine (TEOA) or triethylamine (TEA), 1.4 M H_2O and 4 - 20 μM catalyst. The reaction cell was sealed with a rubber septum, carefully deaerated and filled with Ar. The reaction samples were irradiated by a LED-light source (λ = 455 nm; light intensity 20 mW, beam diameter ~0.4 cm) at room temperature with constant stirring (3×10^3 RPM) using a magnetically-coupled stirring system (SYS 114, SPECTROCELL). Control experiments were carried out under the same conditions in the absence of each component (e.g. $[Ir(ppy)_2(dtbbpy)]^+$, TEOA or TEA, or catalyst **$Ni_{16}As_4P_4$**) of the hydrogen generating samples as described above. More control experiments were performed by replacing complex **$Ni_{16}As_4P_4$** with $TBA_6[P_2W_{18}O_{62}]$ (TBA-**P_2W_{18}**) or $NiCl_2$ under otherwise the identical conditions. The mercury-poison test has been conducted under similar experimental conditions as regular catalytic H_2 evolution run but adding 150 mg Hg into the reaction solution. Typically, the cell was filled with 2.0 mL CH_3CN/DMF (1/3) solution containing 0.2 mM $[Ir(ppy)_2(dtbbpy)]^+$, 0.25 M triethanolamine (TEOA), 1.4 M H_2O, 20 μM catalyst and 150 mg Hg. The reaction cell was sealed with a rubber septum, carefully deaerated and filled with Ar. The reaction samples were irradiated by a LED-light source (λ = 455 nm; light intensity 20 mW, beam diameter ~0.4 cm) at room temperature with constant stirring (3×10^3 RPM) using a magnetically-coupled stirring system (SYS 114, SPECTROCELL). The headspace gases has been analyzed by a HP7890A model gas chromatograph equipped with thermal conductivity detector (TCD) and a 5Å molecular sieve capillary column.

8.3 Results and Discussion

8.3.1. Synthesis, Crystal Structures and Characterization

Polyoxoanion **$Ni_{16}As_4P_4$** was prepared using a facile method by refluxing nickel acetate, sodium tungstate, Na_2HPO_4, and Na_2HAsO_4 in basic conditions. The highest yield is obtained when Na_2HAsO_4 is added last (see **section 8.2.2**). This polyoxoanion crystallizes as an extensively hydrated sodium salt, $Na_{28}[\{Ni_4(OH)_3AsO_4\}_4(B\text{-}\alpha\text{-}PW_9O_{34})_4]\cdot 120H_2O$ (Na_{28}-**$Ni_{16}As_4P_4$**), in triclinic space group $P\bar{1}$ (**Table 8-1**). The thermogravimetric analysis confirmed 120 water molecules per formula unit corresponding to 16.1% weight loss. The composition and number of counter cations was determined by elemental analysis in good agreement with the results obtained from single crystal X-ray diffraction. The FT-IR spectrum of **$Ni_{16}As_4P_4$** in 2 wt% KBr pellet shows all the characteristic bands in the range of 1100–400 cm^{-1} (**Figure 8-1**). The structure of **$Ni_{16}As_4P_4$** can be regarded as a tetramer comprising four tetra-nickel-substituted Keggin fragments, $\{Ni_4(OH)_3(B\text{-}\alpha\text{-}PW_9O_{34})\}$ (**Figure 8-5a**), and four $\{AsO_4\}$ linkers (**Figure 8-5b**) with idealized T_d symmetry (**Figure 8-6**). Alternatively, **$Ni_{16}As_4P_4$** can also be structurally interpreted as a tetrahedral $\{Ni_4(AsO_4)_4\}$ core capped by four tri-nickel-substituted $[\{Ni(OH)\}_3(B\text{-}\alpha\text{-}PW_9O_{34})]$ units. The high-nuclearity Ni_{16} cluster in **$Ni_{16}As_4P_4$** is formed through the condensation of four distorted $\{Ni_4O(OH)_3\}$ cubane units linked by four $\{AsO_4\}$ moieties (**Figure 8-5d-e**).

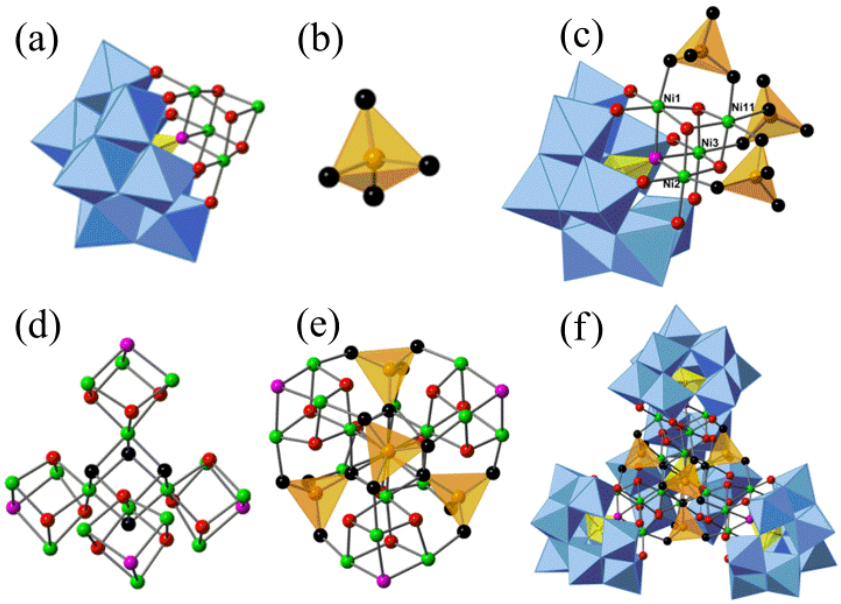

Figure 8-5 Polyhedral and ball-and-stick representations of the building blocks of polyoxoanion **$Ni_{16}As_4P_4$**: (a) $\{Ni_4(OH)_3(B\text{-}\alpha\text{-}PW_9O_{34})\}$, (b) $\{AsO_4\}$, (c) $\{Ni_4(OH)_3(AsO_4)_3(B\text{-}\alpha\text{-}PW_9O_{34})\}$, (d) $\{Ni_{16}(OH)_{12}O_8\}$, (e) $\{Ni_{16}(OH)_{12}O_4(AsO_4)_4\}$, and (f) full polyoxoanion, **$Ni_{16}As_4P_4$**. Color code: WO_6, light blue octahedra; AsO_4, orange tetrahedra with oxygen black balls; PO_4, yellow tetrahedra with oxygen magenta balls; Ni, green balls; O, red balls. Note: the protons associated with the oxygen atoms are not shown.

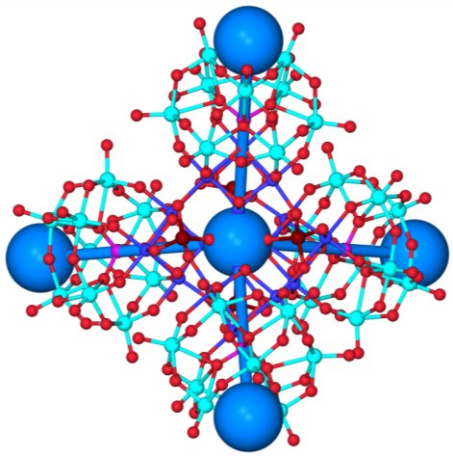

Figure 8-6 Ball-and-stick representations of polyoxoanion **$Ni_{16}As_4P_4$**. Color code: W, light blue balls; As, dark red balls; P, magenta balls; Ni, dark blue balls; O, red balls. Note: the big blue ball-and-stick is used to show the idealized T_d symmetry of the overall **$Ni_{16}As_4P_4$** polyoxoanion.

In each cubane unit, the four nickel atoms are coordinated by one μ_4-O involving the central PO_4 group of the $[PW_9O_{34}]^{9-}$ ligand and three μ_3-OH bridges as confirmed by the bond valence sum (BVS) calculations.[86] BVS calculations also indicate that all the Ni, P, As, and W atoms are in the formal +II, +V, +V, and +VI oxidation states, respectively. All Ni ions in the Ni_{16} cluster adopt distorted octahedral coordination environments with Ni-O bond lengths in the range 1.971(17)–2.288(16) Å with an average distance of 2.057 Å (**Table 8-2**). The calculated octahedral NiO_6 and tetrahedral PO_4/AsO_4 bond angles variance[87] are in the range of 31–47 and 1–2 deg^2, respectively. To our knowledge, **$Ni_{16}As_4P_4$** contains the highest nuclearity carbon-free poly-Ni POM. Very recently, a Ni_{25}-containing POM structure, $[Ni_{25}(H_2O)_2(OH)_{18}(CO_3)_2(PO_4)_6(SiW_9O_{34})_6]^{50-}$, has been reported by Wang's group.[42] The central $\{Ni_{25}(H_2O)_2(OH)_{18}(CO_3)_2(PO_4)_6\}$ ($\{Ni_{25}\}$) core in their work is formed through condensation of two separate $\{Ni_{12}(OH)_9(CO_3)(PO_4)_3\}$ moieties linked together by a $\{Ni(H_2O)_2\}$ unit. This is structurally quite distinct from the $\{Ni_{16}(OH)_{12}O_4(AsO_4)_4\}$ cluster we report here.

Table 8-2 Selected bond lengths [Å] and angles [°] for **$Ni_{16}As_4P_4$**.

O(15)-Ni(1)	2.056(18)	O(16D)-Ni(8)	1.986(18)
O(16D)-Ni(10)	2.023(16)	O(16D)-Ni(13)	2.030(17)
O(17)-Ni(3)	2.02(2)	O(17B)-Ni(4)	2.007(19)
O(18)-Ni(15)	2.008(19)	O(17C)-Ni(9)	2.042(19)
O(19)-Ni(3)	2.023(17)	O(18B)-Ni(4)	1.975(18)
O(18C)-Ni(9)	1.992(17)	O(18D)-Ni(15)	2.020(18)
O(20)-Ni(2)	1.999(19)	O(20B)-Ni(6)	2.016(19)
O(20C)-Ni(8)	2.012(18)	O(20D)-Ni(16)	2.012(17)
O(22)-Ni(1)	2.003(16)	O(22B)-Ni(5)	1.982(17)
O(22C)-Ni(10)	2.016(17)	O(22D)-Ni(14)	2.011(17)
O(25B)-Ni(5)	2.003(18)	O(25)-Ni(1)	1.992(17)
O(25D)-Ni(14)	2.009(17)	O(25C)-Ni(10)	1.977(17)

O(28)-Ni(2)	2.027(18)	O(28B)-Ni(6)	2.009(18)
O(28C)-Ni(8)	2.034(17)	O(28D)-Ni(16)	2.013(18)
O(30)-Ni(1)	2.246(18)	O(30)-Ni(2)	2.249(16)
O(30)-Ni(3)	2.231(16)	O(30B)-Ni(4)	2.234(17)
O(30B)-Ni(5)	2.265(18)	O(30B)-Ni(6)	2.241(17)
O(30C)-Ni(8)	2.243(16)	O(30C)-Ni(9)	2.288(16)
O(30C)-Ni(10)	2.229(17)	O(30D)-Ni(14)	2.244(16)
O(30D)-Ni(15)	2.249(17)	O(30D)-Ni(16)	2.246(16)
O(42)-Ni(6)	2.058(17)	O(43)-Ni(9)	2.057(17)
O(63)-Ni(8)	2.061(16)	O(67)-Ni(10)	2.046(17)
O(68)-Ni(2)	2.068(16)	O(74)-Ni(3)	2.053(17)
O(80)-Ni(4)	2.039(18)	O(75)-Ni(5)	2.071(18)
O(80)-Ni(7)	2.007(17)	O(80)-Ni(5)	2.012(17)
O(81)-Ni(7)	2.101(17)	O(81)-Ni(11)	2.080(16)
O(81)-Ni(12)	2.081(16)	O(82)-Ni(11)	2.081(16)
O(82)-Ni(12)	2.064(16)	O(82)-Ni(13)	2.075(17)
O(83)-Ni(7)	2.107(16)	O(83)-Ni(12)	2.076(17)
O(83)-Ni(13)	2.083(16)	O(84)-Ni(7)	2.067(16)
O(84)-Ni(13)	2.116(16)	O(84)-Ni(11)	2.067(17)
O(85)-Ni(4)	2.033(18)	O(87)-Ni(8)	2.043(17)
O(86)-Ni(9)	2.023(18)	O(86)-Ni(10)	1.975(17)
O(86)-Ni(13)	2.017(16)	O(87)-Ni(9)	1.971(17)
O(88)-Ni(12)	2.017(16)	O(87)-Ni(13)	2.005(18)
O(88)-Ni(14)	2.012(17)	O(88)-Ni(15)	2.011(16)
O(113)-Ni(16)	2.095(18)	O(109)-Ni(15)	2.059(19)
O(114)-Ni(14)	2.006(16)	O(114)-Ni(12)	2.032(17)
O(115)-Ni(12)	2.013(16)	O(114)-Ni(16)	2.027(16)
O(115)-Ni(16)	2.044(17)	O(115)-Ni(15)	2.019(17)
O(127)-Ni(14)	2.024(17)	O(128)-Ni(2)	2.026(16)
O(129)-Ni(1)	2.007(16)	O(128)-Ni(3)	2.018(16)
O(128)-Ni(11)	2.010(17)	O(129)-Ni(11)	2.027(16)
O(129)-Ni(3)	1.999(17)	O(130)-Ni(2)	2.006(18)
O(130)-Ni(1)	2.038(16)	O(130)-Ni(11)	1.993(16)

O(132)-Ni(4)	2.028(17)	O(131)-Ni(5)	2.001(17)
O(131)-Ni(6)	2.027(18)	O(131)-Ni(7)	1.975(17)
O(132)-Ni(7)	2.038(18)	O(132)-Ni(6)	2.007(17)
O(15)-Ni(1)-O(30)	168.9(6)	O(22)-Ni(1)-O(15)	95.6(7)
O(22)-Ni(1)-O(30)	91.3(7)	O(22)-Ni(1)-O(129)	93.5(7)
O(22)-Ni(1)-O(130)	170.5(7)	O(25)-Ni(1)-O(15)	96.4(7)
O(25)-Ni(1)-O(22)	85.9(7)	O(25)-Ni(1)-O(30)	92.8(7)
O(25)-Ni(1)-O(129)	172.1(7)	O(25)-Ni(1)-O(130)	97.1(7)
O(129)-Ni(1)-O(15)	91.5(7)	O(129)-Ni(1)-O(30)	79.4(6)
O(129)-Ni(1)-O(130)	82.3(7)	O(130)-Ni(1)-O(15)	93.0(7)
O(130)-Ni(1)-O(30)	79.6(6)	O(20)-Ni(2)-O(28)	86.8(8)
O(20)-Ni(2)-O(30)	92.2(7)	O(20)-Ni(2)-O(68)	94.5(7)
O(20)-Ni(2)-O(128)	95.7(7)	O(20)-Ni(2)-O(130)	172.4(7)
O(28)-Ni(2)-O(30)	91.4(7)	O(28)-Ni(2)-O(68)	97.6(7)
O(68)-Ni(2)-O(30)	169.0(6)	O(128)-Ni(2)-O(28)	170.4(7)
O(128)-Ni(2)-O(30)	79.3(6)	O(128)-Ni(2)-O(68)	91.4(6)
O(130)-Ni(2)-O(28)	93.8(7)	O(130)-Ni(2)-O(30)	80.2(6)
O(130)-Ni(2)-O(68)	93.0(7)	O(130)-Ni(2)-O(128)	82.5(7)
O(17)-Ni(3)-O(19)	87.4(8)	O(17)-Ni(3)-O(30)	90.7(7)
O(17)-Ni(3)-O(74)	96.5(8)	O(17)-Ni(3)-O(128)	91.8(8)
O(19)-Ni(3)-O(30)	94.0(7)	O(19)-Ni(3)-O(74)	93.3(7)
O(74)-Ni(3)-O(30)	170.0(7)	O(128)-Ni(3)-O(19)	173.8(7)
O(128)-Ni(3)-O(30)	79.9(6)	O(128)-Ni(3)-O(74)	92.9(7)
O(129)-Ni(3)-O(17)	170.1(8)	O(129)-Ni(3)-O(19)	96.0(7)
O(129)-Ni(3)-O(30)	79.9(7)	O(129)-Ni(3)-O(74)	92.5(7)
O(129)-Ni(3)-O(128)	83.8(7)	O(17B)-Ni(4)-O(30B)	92.1(7)
O(17B)-Ni(4)-O(80)	172.9(7)	O(17B)-Ni(4)-O(85)	94.3(8)
O(17B)-Ni(4)-O(132)	93.5(7)	O(18B)-Ni(4)-O(17B)	87.5(8)
O(18B)-Ni(4)-O(30B)	90.7(7)	O(18B)-Ni(4)-O(80)	94.3(7)
O(18B)-Ni(4)-O(85)	98.8(8)	O(18B)-Ni(4)-O(132)	171.1(7)
O(80)-Ni(4)-O(30B)	80.9(7)	O(85)-Ni(4)-O(30B)	168.8(7)
O(85)-Ni(4)-O(80)	92.3(7)	O(132)-Ni(4)-O(30B)	80.4(6)
O(132)-Ni(4)-O(80)	83.8(7)	O(132)-Ni(4)-O(85)	90.0(7)

O(22B)-Ni(5)-O(25B)	87.9(8)	O(22B)-Ni(5)-O(30B)	91.4(7)
O(22B)-Ni(5)-O(75)	94.4(7)	O(22B)-Ni(5)-O(80)	94.7(7)
O(22B)-Ni(5)-O(131)	170.8(8)	O(25B)-Ni(5)-O(30B)	89.7(7)
O(25B)-Ni(5)-O(75)	99.6(7)	O(25B)-Ni(5)-O(80)	170.2(7)
O(75)-Ni(5)-O(30B)	169.1(6)	O(80)-Ni(5)-O(30B)	80.7(7)
O(80)-Ni(5)-O(75)	89.6(7)	O(131)-Ni(5)-O(25B)	93.5(7)
O(131)-Ni(5)-O(30B)	79.5(7)	O(131)-Ni(5)-O(75)	94.3(7)
O(131)-Ni(5)-O(80)	82.5(7)	O(20B)-Ni(6)-O(30B)	91.4(7)
O(20B)-Ni(6)-O(42)	97.4(7)	O(20B)-Ni(6)-O(131)	170.8(7)
O(28B)-Ni(6)-O(20B)	86.2(8)	O(28B)-Ni(6)-O(30B)	92.0(7)
O(28B)-Ni(6)-O(42)	92.6(7)	O(28B)-Ni(6)-O(131)	95.9(7)
O(42)-Ni(6)-O(30B)	170.4(7)	O(131)-Ni(6)-O(30B)	79.6(7)
O(131)-Ni(6)-O(42)	91.5(7)	O(132)-Ni(6)-O(20B)	94.3(7)
O(132)-Ni(6)-O(28B)	172.7(7)	O(132)-Ni(6)-O(30B)	80.7(7)
O(132)-Ni(6)-O(42)	94.5(7)	O(132)-Ni(6)-O(131)	82.5(7)
O(80)-Ni(7)-O(81)	98.9(7)	O(80)-Ni(7)-O(83)	174.7(7)
O(80)-Ni(7)-O(84)	90.4(7)	O(80)-Ni(7)-O(132)	84.3(7)
O(81)-Ni(7)-O(83)	86.0(6)	O(84)-Ni(7)-O(81)	86.5(6)
O(84)-Ni(7)-O(83)	87.7(6)	O(131)-Ni(7)-O(80)	83.3(7)
O(131)-Ni(7)-O(81)	91.5(7)	O(131)-Ni(7)-O(83)	98.8(7)
O(131)-Ni(7)-O(84)	173.0(7)	O(131)-Ni(7)-O(132)	83.0(7)
O(132)-Ni(7)-O(81)	173.3(7)	O(132)-Ni(7)-O(83)	91.1(7)
O(132)-Ni(7)-O(84)	99.4(7)	O(16D)-Ni(8)-O(20C)	171.9(7)
O(16D)-Ni(8)-O(28C)	93.4(7)	O(16D)-Ni(8)-O(30C)	79.2(6)
O(16D)-Ni(8)-O(63)	94.4(7)	O(16D)-Ni(8)-O(87)	83.5(7)
O(20C)-Ni(8)-O(28C)	87.5(7)	O(20C)-Ni(8)-O(30C)	92.7(7)
O(20C)-Ni(8)-O(63)	93.6(7)	O(20C)-Ni(8)-O(87)	94.4(7)
O(28C)-Ni(8)-O(30C)	91.4(6)	O(28C)-Ni(8)-O(63)	95.4(7)
O(28C)-Ni(8)-O(87)	170.7(7)	O(63)-Ni(8)-O(30C)	170.9(6)
O(87)-Ni(8)-O(30C)	79.4(6)	O(87)-Ni(8)-O(63)	93.5(7)
O(17C)-Ni(9)-O(30C)	92.0(7)	O(17C)-Ni(9)-O(43)	96.1(8)
O(18C)-Ni(9)-O(17C)	87.3(7)	O(18C)-Ni(9)-O(30C)	92.8(6)
O(18C)-Ni(9)-O(43)	94.8(7)	O(18C)-Ni(9)-O(86)	96.0(7)

O(43)-Ni(9)-O(30C)	169.2(7)	O(86)-Ni(9)-O(17C)	169.8(7)
O(86)-Ni(9)-O(30C)	78.3(6)	O(86)-Ni(9)-O(43)	93.2(7)
O(87)-Ni(9)-O(17C)	92.4(7)	O(87)-Ni(9)-O(18C)	172.6(7)
O(87)-Ni(9)-O(30C)	79.8(6)	O(87)-Ni(9)-O(43)	92.7(7)
O(87)-Ni(9)-O(86)	83.1(7)	O(16D)-Ni(10)-O(30C)	78.8(6)
O(16D)-Ni(10)-O(67)	93.4(7)	O(22C)-Ni(10)-O(16D)	169.6(7)
O(22C)-Ni(10)-O(30C)	90.9(7)	O(22C)-Ni(10)-O(67)	96.7(7)
O(25C)-Ni(10)-O(16D)	95.8(7)	O(25C)-Ni(10)-O(22C)	85.6(7)
O(25C)-Ni(10)-O(30C)	91.8(7)	O(25C)-Ni(10)-O(67)	97.7(7)
O(67)-Ni(10)-O(30C)	168.3(6)	O(86)-Ni(10)-O(16D)	83.2(7)
O(86)-Ni(10)-O(22C)	94.0(7)	O(86)-Ni(10)-O(25C)	172.5(7)
O(86)-Ni(10)-O(30C)	80.7(6)	O(86)-Ni(10)-O(67)	89.8(7)
O(81)-Ni(11)-O(82)	85.2(6)	O(84)-Ni(11)-O(81)	87.1(6)
O(84)-Ni(11)-O(82)	87.8(6)	O(128)-Ni(11)-O(81)	100.2(7)
O(128)-Ni(11)-O(82)	90.0(7)	O(128)-Ni(11)-O(84)	172.2(7)
O(128)-Ni(11)-O(129)	83.2(7)	O(129)-Ni(11)-O(81)	91.4(6)
O(129)-Ni(11)-O(82)	171.8(7)	O(129)-Ni(11)-O(84)	99.5(7)
O(130)-Ni(11)-O(81)	173.1(7)	O(130)-Ni(11)-O(82)	100.9(6)
O(130)-Ni(11)-O(84)	89.9(7)	O(130)-Ni(11)-O(128)	83.2(7)
O(130)-Ni(11)-O(129)	82.9(7)	O(82)-Ni(12)-O(81)	85.6(6)
O(82)-Ni(12)-O(83)	85.7(6)	O(83)-Ni(12)-O(81)	87.3(6)
O(88)-Ni(12)-O(81)	98.2(6)	O(88)-Ni(12)-O(82)	175.8(6)
O(88)-Ni(12)-O(83)	92.6(7)	O(88)-Ni(12)-O(114)	82.8(7)
O(114)-Ni(12)-O(81)	91.2(7)	O(114)-Ni(12)-O(82)	98.9(7)
O(114)-Ni(12)-O(83)	174.9(7)	O(115)-Ni(12)-O(81)	174.6(7)
O(115)-Ni(12)-O(82)	92.8(6)	O(115)-Ni(12)-O(83)	97.8(7)
O(115)-Ni(12)-O(88)	83.6(7)	O(115)-Ni(12)-O(114)	84.0(7)
O(16D)-Ni(13)-O(82)	91.9(7)	O(16D)-Ni(13)-O(83)	172.5(7)
O(16D)-Ni(13)-O(84)	99.7(6)	O(82)-Ni(13)-O(83)	85.3(6)
O(82)-Ni(13)-O(84)	86.7(6)	O(83)-Ni(13)-O(84)	87.1(6)
O(86)-Ni(13)-O(16D)	82.0(7)	O(86)-Ni(13)-O(82)	100.3(7)
O(86)-Ni(13)-O(83)	91.6(6)	O(86)-Ni(13)-O(84)	172.8(7)
O(87)-Ni(13)-O(16D)	83.4(7)	O(87)-Ni(13)-O(82)	174.2(7)

O(87)-Ni(13)-O(83)	99.8(7)	O(87)-Ni(13)-O(84)	90.9(7)
O(87)-Ni(13)-O(86)	82.4(7)	O(22D)-Ni(14)-O(30D)	94.8(7)
O(22D)-Ni(14)-O(88)	96.5(7)	O(22D)-Ni(14)-O(127)	91.5(7)
O(25D)-Ni(14)-O(22D)	85.4(7)	O(25D)-Ni(14)-O(30D)	92.3(6)
O(25D)-Ni(14)-O(88)	171.8(7)	O(25D)-Ni(14)-O(127)	96.5(7)
O(88)-Ni(14)-O(30D)	79.5(6)	O(88)-Ni(14)-O(127)	91.5(7)
O(114)-Ni(14)-O(22D)	174.2(7)	O(114)-Ni(14)-O(25D)	93.6(7)
O(114)-Ni(14)-O(30D)	79.5(6)	O(114)-Ni(14)-O(88)	83.6(7)
O(114)-Ni(14)-O(127)	94.3(7)	O(127)-Ni(14)-O(30D)	169.6(7)
O(18)-Ni(15)-O(18D)	88.0(8)	O(18)-Ni(15)-O(30D)	92.7(7)
O(18)-Ni(15)-O(88)	172.1(8)	O(18)-Ni(15)-O(109)	91.2(8)
O(18)-Ni(15)-O(115)	94.4(7)	O(18D)-Ni(15)-O(30D)	92.3(7)
O(18D)-Ni(15)-O(109)	99.6(8)	O(88)-Ni(15)-O(18D)	93.0(7)
O(88)-Ni(15)-O(30D)	79.4(6)	O(88)-Ni(15)-O(109)	96.3(7)
O(88)-Ni(15)-O(115)	83.6(7)	O(109)-Ni(15)-O(30D)	167.6(7)
O(115)-Ni(15)-O(18D)	171.6(7)	O(115)-Ni(15)-O(30D)	79.6(6)
O(115)-Ni(15)-O(109)	88.4(7)	O(20D)-Ni(16)-O(28D)	87.1(7)
O(20D)-Ni(16)-O(30D)	91.0(7)	O(20D)-Ni(16)-O(113)	100.9(7)
O(20D)-Ni(16)-O(114)	169.9(7)	O(20D)-Ni(16)-O(115)	93.5(7)
O(28D)-Ni(16)-O(30D)	93.4(7)	O(28D)-Ni(16)-O(113)	92.6(7)
O(28D)-Ni(16)-O(114)	94.8(7)	O(28D)-Ni(16)-O(115)	172.5(7)
O(113)-Ni(16)-O(30D)	167.0(7)	O(114)-Ni(16)-O(30D)	79.0(6)
O(114)-Ni(16)-O(113)	89.0(7)	O(114)-Ni(16)-O(115)	83.4(7)
O(115)-Ni(16)-O(30D)	79.1(6)	O(115)-Ni(16)-O(113)	94.6(7)

It's noted that the other Ni_{16}-containing POM structure, $Na_{18}K_{10}[\{Ni_4(OH)_3PO_4\}_4(A\text{-}\alpha\text{-}PW_9O_{34})_4]\bullet 75H_2O$ ($Na_{18}K_{10}$-**$Ni_{16}P_4P_4$**), is formed by completely replacing Na_2HAsO_4 with Na_2HPO_4 during the synthesis (see experimental **section 8.2.2**). The geometrical structure, composition, and purity of this $Na_{18}K_{10}$-**$Ni_{16}P_4P_4$** complex have been carefully characterized by single-crystal X-ray diffraction, FT-IR spectroscopy (**Figure 8-2**), thermogravimetric and elemental analyses. The structure of **$Ni_{16}P_4P_4$** can be described as

a tetramer comprising four tetra-nickel-substituted Keggin fragments, $\{Ni_4(OH)_3(A\text{-}\alpha\text{-}PW_9O_{34})\}$, and four $\{PO_4\}$ linkers connected *via* Ni–O–P bonds (**Figure 8-7**). $\mathbf{Ni_{16}P_4P_4}$ is isostructural to recently reported Co_{16}-substituted POMs where the Co(II) ions occupy the positions of Ni(II) centers and the heteroatoms in the *A*-type trivacant POM ligands, $[XW_9O_{34}]^{n-}$, are Si, Ge, P, and As.[20,41,67] In the following parts of this study, we focus on the magnetic, spectroscopic and catalytic properties of the more structurally interesting complex, $\mathbf{Ni_{16}As_4P_4}$.

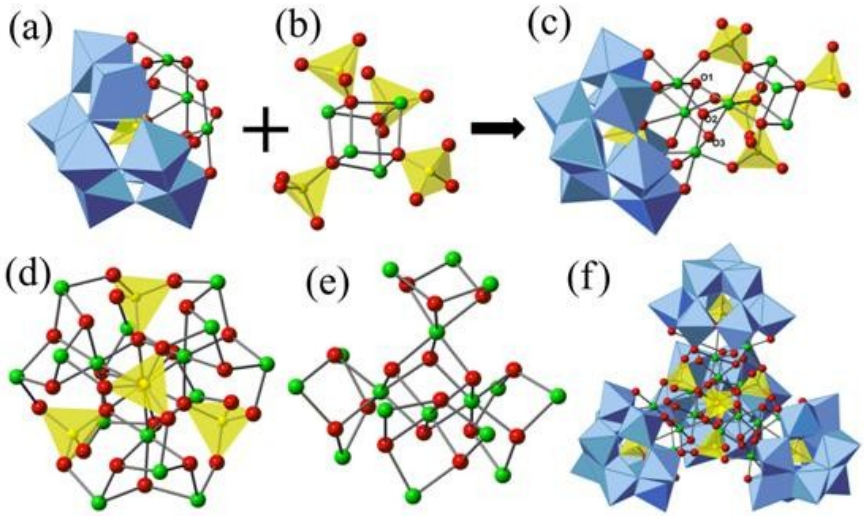

Figure 8-7 Polyhedral and ball-and-stick representations of the building blocks of the polyoxoanion $\mathbf{Ni_{16}P_4P_4}$, which is somewhat similar to but compositionally and structurally distinct from $\mathbf{Ni_{16}As_4P_4}$: (a) $\{Ni_3(OH)_3(A\text{-}\alpha\text{-}PW_9O_{34})\}$, (b) $\{Ni_4(PO_4)_4\}$, (c) $[\{Ni(OH)\}_3\{Ni_4(PO_4)_4\}(A\text{-}\alpha\text{-}PW_9O_{34})]$, (d) $\{Ni_{16}(OH)_{12}(PO_4)_4\}$, (e) $\{Ni_{16}(OH)_{12}O_4\}$, and (f) the full polyoxoanion $[\{Ni_4(OH)_3PO_4\}_4(A\text{-}\alpha\text{-}PW_9O_{34})_4]^{28-}$ ($\mathbf{Ni_{16}P_4P_4}$). Color code: WO_6, light blue octahedra; PO_4, yellow tetrahedra; Ni, green balls; O, red balls. Note: the protons associated with the oxygen atoms are not shown.

8.3.2. Magnetic Properties of $Ni_{16}As_4P_4$

The high spin nuclearity of the title compound precludes full magnetochemical modeling; the presence of at least four distinct nearest-neighbor exchange pathways further complicates the magnetic analysis due to overparameterization. The magnetic dc

susceptibility results on polycrystalline Na_{28}-**$Ni_{16}As_4P_4$** are in line with the presence of 16 Ni(II) centers per formula unit: at 290 K, $\chi_m T$ reaches 23.00 cm^3 K mol^{-1} which lies in the interval 15.69–24.51 cm^3 K mol^{-1} that is expected for 16 non-interacting high-spin (S = 1) Ni^{2+} centers.[88] $\chi_m T$ continuously increases with decreasing temperature and reaches a maximum of 69.21 cm^3 K mol^{-1} at 3.4 K, indicating dominant ferromagnetic exchange interactions within the compound (**Figure 8-8**). Since the molar magnetization M_m at 2.0 K hints at a saturation value that is below the potential maximum value of 35–38 $N_A \mu_B$, i.e., the expected spin contributions for 16 fully ferromagnetically aligned Ni^{2+} centers, the centers either interact ferromagnetically but the ground state is characterized by $S_{total} \neq S_{total,max}$, or minor antiferromagnetic coupling contributions are present as well.

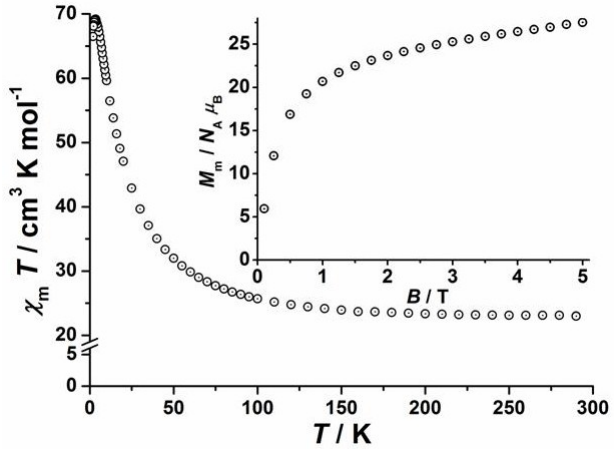

Figure 8-8 Temperature dependence of $\chi_m T$ at 0.1 Tesla for Na_{28}-**$Ni_{16}As_4P_4$**; inset: molar magnetization M_m vs. applied field B at 2.0 K.

Previous studies show that the nickel clusters with $\{Ni_4O_4\}$ cubane moiety stabilized by organic ligands (coordinating N or O donors) and chlorides exhibit SMM behavior at very low temperatures (T < 2.0 K).[89-92] Another study shows SMM behavior for nickel clusters with $\{Ni_4Cl_4\}$ cubane moiety at slightly higher temperatures (T < 4.0 K).[92] For **$Ni_{16}As_4P_4$**, i.e. a cluster consisting of multiple $\{Ni_4O_4\}$ cubane moieties encapsulated in

diamagnetic POMs, and thus purely O-coordinated, the ac susceptibility properties (**Figure 8-9**) exhibit no out-of-phase component χ'' at zero bias field and $T \geq 2.0$ K, i.e., no SMM characteristics are revealed in this case. Therefore, the slight distortion of the ligand field due to structural distortions does not seem to be enough to generate sufficient molecular easy-axis anisotropy to result in SMM properties at temperatures larger than 2 K for otherwise isotropic Ni^{2+} spin centers in an octahedral ligand field. The distortion should be increased e.g. by imposing ligands of different ligand strength on the central metal ion to induce larger single-ion anisotropies. Note that based on our SQUID magnetometry studies we are not able to rule out that Na_{28}-**$Ni_{16}As_4P_4$** might display slow relaxation at temperatures well below 2 K.

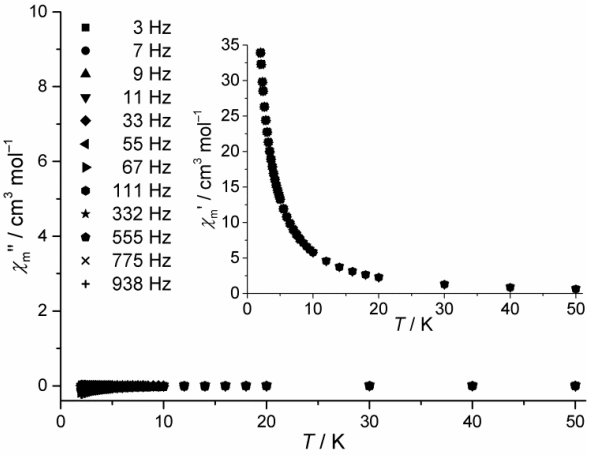

Figure 8-9 Magnetic ac properties of Na_{28}-**$Ni_{16}As_4P_4$**: Temperature dependence of in-phase χ_m' and out-of-phase χ_m'' ac amplitudes at zero static field B.

8.3.3. Catalytic Hydrogen Evolution Activity and Evaluation of Stability

Complex **$Ni_{16}As_4P_4$** has also been evaluated as noble-metal-free catalyst for visible-light-driven hydrogen evolution. The stability of **$Ni_{16}As_4P_4$** under non-turnover conditions has been assessed using UV-Vis spectroscopy, catalyst reisolation combined with vibrational spectroscopy, dynamic light scattering (DLS), mercury poisoning experiments, and other

indicators. The spectra remain unchanged after aging for 24 h (**Figure 8-10**). Irradiation of a solution of 0.2 mM $[Ir(ppy)_2(dtbbpy)]^+$, 0.25 M sacrificial electron donor, TEOA, 1.4 M H_2O and 20 μM catalyst **$Ni_{16}As_4P_4$** in deaerated CH_3CN/DMF (1/3) using a LED light (λ = 455 nm, 20 mW) at 25 ℃ results in efficient hydrogen evolution (**Figure 8-11**). Control experiments revealed that the absence of any one of these components (catalyst **$Ni_{16}As_4P_4$**, TEOA, or $[Ir(ppy)_2(dtbbpy)]^+$) results in negligible H_2 production (**Figure 8-11**). Using $TBA_6[P_2W_{18}O_{62}]$ (TBA-**P_2W_{18}**) in place of catalyst **$Ni_{16}As_4P_4$** gives very little H_2 (TON = 3; **Figure 8-11**). Another control experiment using 20 μM $NiCl_2$ as potential dissociation product of **$Ni_{16}As_4P_4$** also gives much less H_2 (**Figure 8-11**). Increasing the concentration of $NiCl_2$ to 320 μM (stoichiometric equivalents of Ni as in 20 μM **$Ni_{16}As_4P_4$**) dramatically decreases the rate and final yield of H_2 (**Figure 8-11**) due to the formation of big Ni nanoparticles attached to the surface of the magnetic stir bar (**Figure 8-12**).

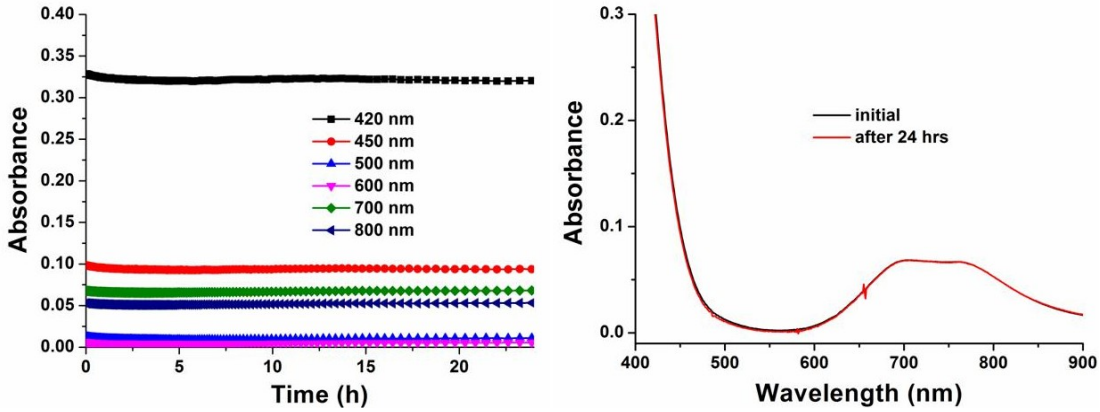

Figure 8-10 Magnetic ac properties of Na_{28}-**$Ni_{16}As_4P_4$**: Temperature dependence of in-phase χ_m' and out-of-phase χ_m'' ac amplitudes at zero static field *B*.

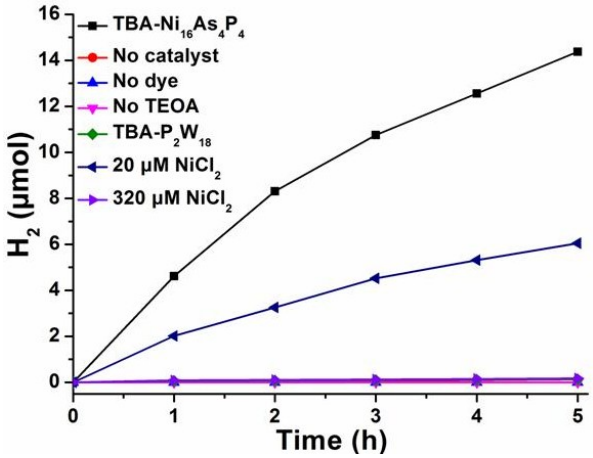

Figure 8-11 Photochemical H_2 evolution by different catalysts under otherwise identical conditions: LED light (20 mW, 455 nm, beam diameter ~0.4 cm), $[Ir(ppy)_2(dtbbpy)]^+$ (0.2 mM), TEOA (0.25 M), H_2O (1.4 M), catalyst (20 μM or 320 μM as noted), 2 mL CH_3CN/DMF (1/3) deaerated with Ar.

Figure 8-12 Photographs of the magnetic stir bar before (left) and after (right) photocatalytic hydrogen evolution for 5 hrs. Conditions: LED light (20 mW, 455 nm, beam diameter ~0.4 cm), $[Ir(ppy)_2(dtbbpy)]^+$ (0.2 mM), TEOA (0.25 M), H_2O (1.4 M), catalyst (320 μM $NiCl_2$), 2 mL CH_3CN/DMF (1/3) deaerated with Ar.

In the $\mathbf{Ni_{16}As_4P_4}$-catalyzed reactions, the H_2 yield increases linearly with time after exposure to light (**Figure 8-13**). At constant concentration of $[Ir(ppy)_2(dtbbpy)]^+$ and TEOA, the H_2 yield increases from 1.22 to 14.4 μmol when varying [$\mathbf{Ni_{16}As_4P_4}$] from 4 to 20 μM (**Figure 8-13**).

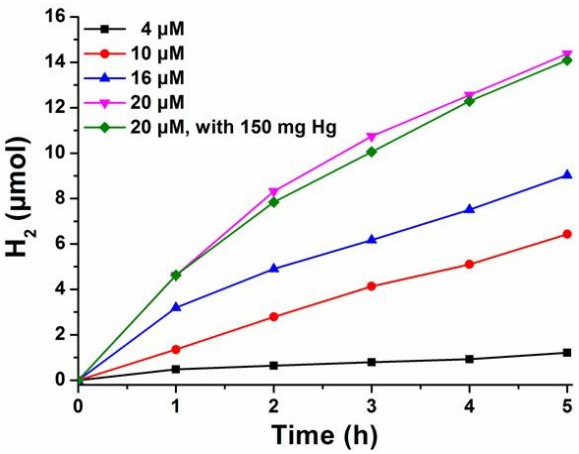

Figure 8-13 Photocatalytic H_2 evolution as a function of $\mathbf{Ni_{16}As_4P_4}$ concentration. Conditions: LED light (20 mW, 455 nm), $[Ir(ppy)_2(dtbbpy)]^+$ (0.2 mM), TEOA (0.25 M), H_2O (1.4 M) catalyst $\mathbf{Ni_{16}As_4P_4}$ (4 - 20 μM), 150 mg mercury (Hg), 2 mL CH_3CN/DMF (1/3) deaerated with Ar.

A highest TON of 360 is obtained after 5 hrs of irradiation (pink line, **Figure 8-13**). The mercury-poison test to assess the possible presence of metal particle catalysts shows no decrease in photocatalytic activity, indicating the homogeneity of the reaction system. Dynamic light scattering (DLS) measurements reveal no detectable formation of nanoparticles for the $\mathbf{Ni_{16}As_4P_4}$-catalyzed postreaction solution after 5 hrs of irradiation. In contrast, the control experiments using $NiCl_2$ as catalyst result in the rapid formation of readily detected nanoparticles.[52] We also isolated the the polyanion $\mathbf{Ni_{16}As_4P_4}$ from post-reaction solution using a saturated solution of $[Ru(bpy)_3]^{2+}$ in CH_3CN. The precipitate was collected by centrifugation and used in the FT-IR stability evaluations (2.0 wt% samples in KBr) for comparison with the sample before catalysis. The FT-IR spectrum of $\mathbf{Ni_{16}As_4P_4}$ isolated from post-reaction solution after 5 hrs remain similar to the spectrum before catalytic reaction (**Figure 8-14**).

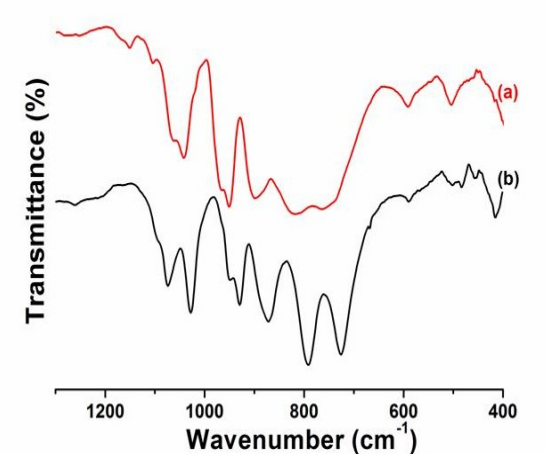

Figure 8-14 FT-IR spectra of (a) TBA-$\mathbf{Ni_{16}As_4P_4}$ before light-driven reaction and (b) the sample after light-driven reaction (isolated from post-catalytic reaction solution using $[Ru(bpy)_3]^{2+}$, illumination time: 5 hrs, TON ~ 360). All FT-IR spectra were ~2 wt% samples in KBr.

The rate of H_2 evolution also depends on the nature of sacrificial donors as well as the presence of water. In the absence of H_2O, the H_2 yield significantly decreases using either TEOA or TEA as sacrificial electron donors (**Figure 8-15**). Addition of 1.4 M H_2O to the reaction system dramatically increases the H_2 yield with the highest yield observed when the electron donor TEA is also present (**Figure 8-15**). The different donors significantly influence the reductive quenching process, which is addressed in the following section.

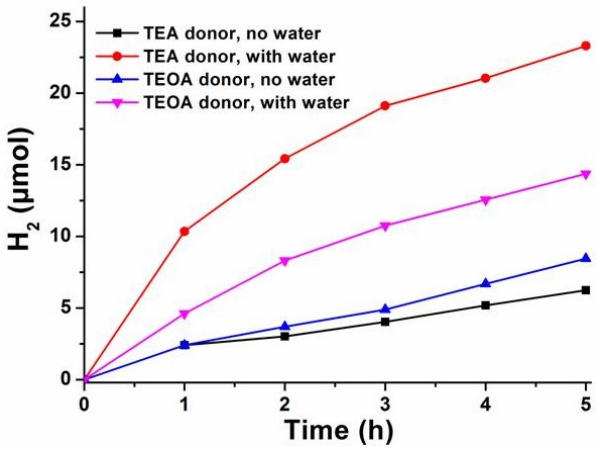

Figure 8-15 Photocatalytic H_2 evolution using different sacrificial electron donors in the absence or presence of water. Conditions: LED light (20 mW, 455 nm, beam diameter ~0.4 cm),

$[Ir(ppy)_2(dtbbpy)]^+$ (0.2 mM), TEOA (0.25 M), H_2O (0 or 1.4 M), catalyst $\mathbf{Ni_{16}As_4P_4}$ (20 μM), 2 mL CH_3CN/DMF (1/3) deaerated with Ar.

8.3.4. Quenching Mechanistic Studies

Excitation of the photosensitizer, $[Ir(ppy)_2(dtbbpy)]^+$, in our system results in a strong emission band at 470 - 750 nm with λ_{max} = 577 nm ($\lambda_{excitation}$ = 455 nm); either reductive or oxidative quenching of resulting excited state by an electron donor or acceptor leads to a decrease of the luminescence intensity. The quenching mechanism of our system (oxidative vs. reductive)[50,52,93-96] is assessed using both emission quenching and time-resolved luminescence decay techniques (**Figure 8-16**). In both cases, the decay of $[Ir(ppy)_2(dtbbpy)]^{+*}$ luminescence can be accelerated by either $\mathbf{Ni_{16}As_4P_4}$, TEOA or TEA (**Figure 8-16**).

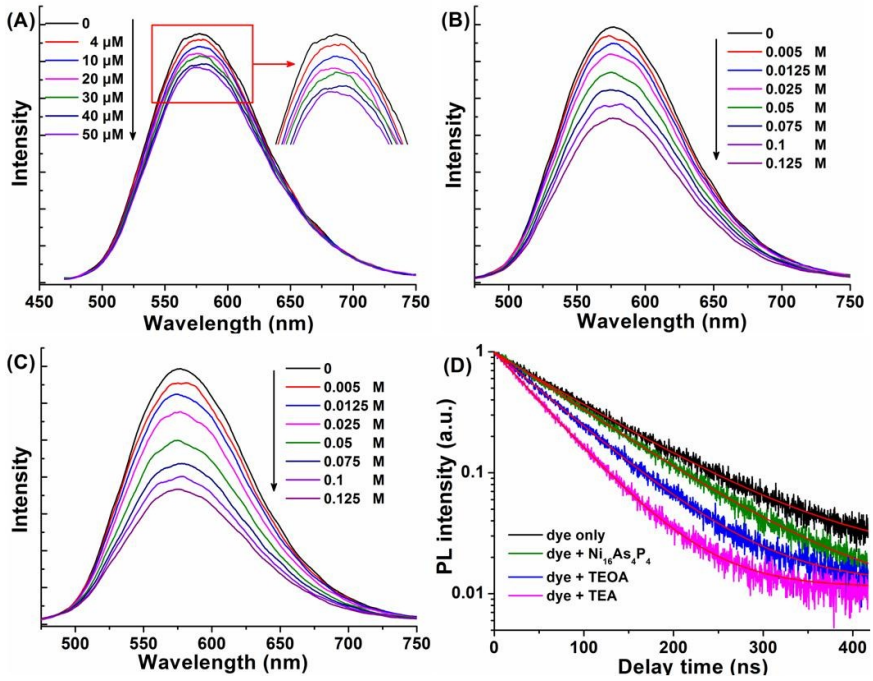

Figure 8-16 Emission spectra of $[Ir(ppy)_2(dtbbpy)]^+$ (0.1 mM) as a function of added (A) $\mathbf{Ni_{16}As_4P_4}$, (B) TEOA, and (C) TEA. (D) Normalized time-resolved luminescence decay kinetics of $[Ir(ppy)_2(dtbbpy)]^+$ (black curve), $[Ir(ppy)_2(dtbbpy)]^+$ with $\mathbf{Ni_{16}As_4P_4}$ (green curve), $[Ir(ppy)_2(dtbbpy)]^+$ with TEOA (blue curve) and $[Ir(ppy)_2(dtbbpy)]^+$ with TEA (pink curve).

Conditions: 400 nm excitation, 0.1 mM $[Ir(ppy)_2(dtbbpy)]^+$, 0.125 M TEOA, 0.125 M TEA and 50 μM catalyst $\mathbf{Ni_{16}As_4P_4}$.

The linear Stern-Volmer (SV) plot of the emission quenching data gives an apparent rate constant of 3.3×10^{10} M^{-1} s^{-1} for oxidative quenching by $\mathbf{Ni_{16}As_4P_4}$ (**Figure 8-17**). This is beyond the diffusion control limit (~10^{10} M^{-1} s^{-1}) indicating a contribution of static quenching through electrostatic formation of $\{\mathbf{Ni_{16}As_4P_4}\cdots[Ir(ppy)_2(dtbbpy)]^+\}$ complex. The SV analyses of the reductive quenching process by TEOA or TEA yield quenching rate constants of 4.3×10^7 M^{-1} s^{-1} and 7.1×10^7 M^{-1} s^{-1}, respectively (**Figure 8-17**). Single exponential fitting of the $[Ir(ppy)_2(dtbbpy)]^{+*}$ luminescence decay kinetics in the presence of $\mathbf{Ni_{16}As_4P_4}$, TEOA, and TEA gives lifetimes of ~89, ~69 and ~53 ns, respectively; while in the absence of quenchers such lifetime increases to ~100 ns (**Figure 8-16d**, **Table 8-3**). Both emission quenching and time-resolved luminescence decay data confirm that the excited state of $[Ir(ppy)_2(dtbbpy)]^{+*}$ can be both oxidatively quenched by the catalyst, $\mathbf{Ni_{16}As_4P_4}$, and reductively quenched by TEOA or TEA. Furthermore, the reductive quenching pathway is dominant given the much higher concentration of sacrificial electron donor compared with that of the $\mathbf{Ni_{16}As_4P_4}$ catalyst. In addition, the TEA is a better quencher than TEOA, thus resulting in more efficient and higher H_2 production (**Figure 8-15**).

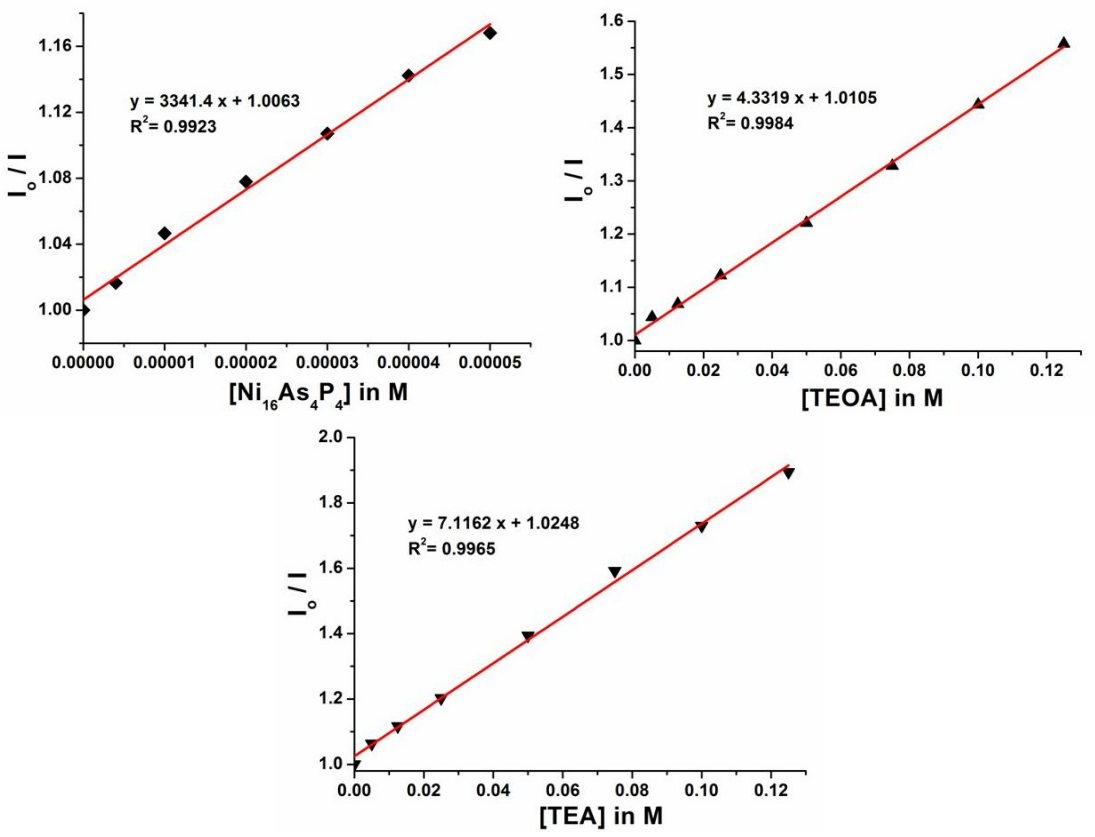

Figure 8-17 The corresponding Stern-Volmer plot as a function of added $\mathbf{Ni_{16}As_4P_4}$, TEOA and TEA.

Table 8-3 Comparison of luminescence lifetimes of $[Ir(ppy)_2(dtbbpy)]^+$ from the data in **Figure 8-16d**.

Sample	Lifetime τ (ns)
Free $[Ir(ppy)_2(dtbbpy)]^+$ dye	100±0.5
Dye + TBA-$Ni_{14}As_4P_4$, CH_3CN/DMF (1/3)	89.2±0.2
Dye + TEOA, CH_3CN/DMF (1/3)	68.7±0.5
Dye + TEA, CH_3CN/DMF (1/3)	53.2±0.3

8.4 Conclusions

In conclusion, we have prepared and systematically characterized an unprecedented POM structural type in the form of a hexadecanickel complex, $[\{Ni_4(OH)_3AsO_4\}_4(B\text{-}\alpha\text{-}PW_9O_{34})_4]^{28-}$ ($\mathbf{Ni_{16}As_4P_4}$) using a facile, one-pot method. To our knowledge, $\mathbf{Ni_{16}As_4P_4}$

represents the highest nuclearity carbon-free poly-Ni POM. **$Ni_{16}As_4P_4$** works as efficient, noble-metal-free catalyst for catalytic H_2 production when coupling to $[Ir(ppy)_2(dtbbpy)][PF_6]$ as visible light absorber and TEOA as sacrificial electron donor. The stability and the homogeneity of the reaction system have been evaluated using UV-vis spectroscopy, dynamic light scattering (DLS) measurements, a mercury-poison test and an aging experiment. Time-solved luminescence and static emission quenching experiments confirm that the excited state of $[Ir(ppy)_2(dtbbpy)]^{+*}$ can be both oxidatively quenched by the catalyst, **$Ni_{16}As_4P_4$**, and reductively quenched by TEOA or TEA. The lifetimes of the excited state $[Ir(ppy)_2(dtbbpy)]^{+*}$ as well as the quenching rate constants have been calculated and evaluated.

References

(1) Pope, M. T.; Müller, A. *Angew. Chem., Int. Ed. Engl.* **1991**, *30*, 34.

(2) Hill, C. L. *Chem. Rev. (Washington, DC, U. S.)* **1998**, *98*, 1.

(3) *Polyoxometalate Chemistry From Topology via Self-Assembly to Applications*; Pope, M. T.; Müller, A., Eds.; Kluwer Academic Publishers: Dordrecht, 2001.

(4) Neumann, R.; Dahan, M. *Nature* **1997**, *388*, 353.

(5) Okuhara, T.; Mizuno, N.; Misono, M. *Adv. Catal.* **1996**, *41*, 113.

(6) Rhule, J. T.; Hill, C. L.; Judd, D. A.; Schinazi, R. F. *Chem. Rev. (Washington, DC, U. S.)* **1998**, *98*, 327.

(7) Yamase, T. *Chem. Rev. (Washington, DC, U. S.)* **1998**, *98*, 307.

(8) Wang, Y.; Weinstock, I. A. *Chem. Soc. Rev.* **2012**, *41*, 7479.

(9) Busche, C.; Vila-Nadal, L.; Yan, J.; Miras, H. N.; Long, D.-L.; Georgiev, V. P.; Asenov, A.; Pedersen, R. H.; Gadegaard, N.; Mirza, M. M.; Paul, D. J.; Poblet, J. M.; Cronin, L. *Nature* **2014**, *515*, 545.

(10) Lv, H.; Geletii, Y. V.; Zhao, C.; Vickers, J. W.; Zhu, G.; Luo, Z.; Song, J.; Lian, T.; Musaev, D. G.; Hill, C. L. *Chem. Soc. Rev.* **2012**, *41*, 7572.

(11) Hiskia, A.; Mylonas, A.; Papaconstantinou, E. *Chem. Soc. Rev.* **2001**, *30*, 62.

(12) Long, D.; Burkholder, E.; Cronin, L. *Chem. Soc. Rev.* **2007**, *36*, 105.

(13) Müller, A.; Peters, F.; Pope, M. T.; Gatteschi, D. *Chem. Rev. (Washington, DC, U. S.)* **1998**, *98*, 239.

(14) Cronin, L.; Muller, A. *Chem. Soc. Rev.* **2012**, *41*, 7333.

(15) Kortz, U.; Müller, A.; van Slageren, J.; Schnack, J.; Dalal, N. S.; Dressel, M. *Coord. Chem. Rev.* **2009**, *253*, 2315.

(16) Clemente-Juan, J. M.; Coronado, E. *Coord. Chem. Rev.* **1999**, *193–195*, 361.

(17) Clemente-Juan, J. M.; Coronado, E.; Gaita-Arino, A. *Chem. Soc. Rev.* **2012**, *41*, 7464.

(18) Ritchie, C.; Ferguson, A.; Nojiri, H.; Miras, H. N.; Song, Y.-F.; Long, D.-L.; Burkholder, E.; Murrie, M.; Kögerler, P.; Brechin, E. K.; Cronin, L. *Angew. Chem. Int. Ed.* **2008**, *47*, 5609.

(19) Compain, J.-D.; Mialane, P.; Dolbecq, A.; Mbomekallé, I. M.; Marrot, J.; Sécheresse, F.; Rivière, E.; Rogez, G.; Wernsdorfer, W. *Angew. Chem. Int. Ed.* **2009**, *48*, 3077.

(20) Ibrahim, M.; Lan, Y.; Bassil, B. S.; Xiang, Y.; Suchopar, A.; Powell, A. K.; Kortz, U. *Angew. Chem. Int. Ed.* **2011**, *50*, 4708.

(21) Weinstock, I. A.; Barbuzzi, E. M. G.; Wemple, M. W.; Cowan, J. J.; Reiner, R. S.; Sonnen, D. M.; Heintz, R. A.; Bond, J. S.; Hill, C. L. *Nature* **2001**, *414*, 191.

(22) Sumliner, J. M.; Lv, H.; Fielden, J.; Geletii, Y. V.; Hill, C. L. *Eur. J. Inorg. Chem.* **2014**, *2014*, 635.

(23) Rausch, B.; Symes, M. D.; Chisholm, G.; Cronin, L. *Science* **2014**, *345*, 1326.

(24) Geletii, Y. V.; Botar, B.; Kögerler, P.; Hillesheim, D. A.; Musaev, D. G.; Hill, C. L. *Angew. Chem. Int. Ed.* **2008**, *47*, 3896.

(25) Sartorel, A.; Carraro, M.; Scorrano, G.; Zorzi, R. D.; Geremia, S.; McDaniel, N. D.; Bernhard, S.; Bonchio, M. *J. Am. Chem. Soc.* **2008**, *130*, 5006.

(26) Yin, Q.; Tan, J. M.; Besson, C.; Geletii, Y. V.; Musaev, D. G.; Kuznetsov, A. E.; Luo, Z.; Hardcastle, K. I.; Hill, C. L. *Science* **2010**, *328*, 342.

(27) Murakami, M.; Hong, D.; Suenobu, T.; Yamaguchi, S.; Ogura, T.; Fukuzumi, S. *J. Am. Chem. Soc.* **2011**, *133*, 11605.

(28) Vickers, J.; Lv, H.; Zhuk, P. F.; Geletii, Y. V.; Hill, C. L. *MRS Proceedings* **2012**, *1387*, mrsf11.

(29) Goberna-Ferrón, S.; Vigara, L.; Soriano-López, J.; Galán-Mascarós, J. R. *Inorg. Chem.* **2012**, *51*, 11707.

(30) Stracke, J. J.; Finke, R. G. *ACS Catalysis* **2013**, *4*, 79.

(31) Schiwon, R.; Klingan, K.; Dau, H.; Limberg, C. *Chem. Commun.* **2014**, *50*, 100.

(32) Geletii, Y. V.; Huang, Z.; Hou, Y.; Musaev, D. G.; Lian, T.; Hill, C. L. *J. Am. Chem. Soc.* **2009**, *131*, 7522.

(33) Huang, Z.; Luo, Z.; Geletii, Y. V.; Vickers, J. W.; Yin, Q.; Wu, D.; Hou, Y.; Ding, Y.; Song, J.; Musaev, D. G.; Hill, C. L.; Lian, T. *J. Am. Chem. Soc.* **2011**, *133*, 2068.

(34) Car, P.-E.; Guttentag, M.; Baldridge, K. K.; Alberto, R.; Patzke, G. R. *Green Chem.* **2012**, *14*, 1680.

(35) Tanaka, S.; Annaka, M.; Sakai, K. *Chem. Commun. (Cambridge, U. K.)* **2012**, *48*, 1653.

(36) Zhu, G.; Glass, E. N.; Zhao, C.; Lv, H.; Vickers, J. W.; Geletii, Y. V.; Musaev, D. G.; Song, J.; Hill, C. L. *Dalton Trans.* **2012**, *41*, 13043.

(37) Vickers, J. W.; Lv, H.; Sumliner, J. M.; Zhu, G.; Luo, Z.; Musaev, D. G.; Geletii, Y. V.; Hill, C. L. *J. Am. Chem. Soc.* **2013**, *135*, 14110.

(38) Song, F.; Ding, Y.; Ma, B.; Wang, C.; Wang, Q.; Du, X.; Fu, S.; Song, J. *Energy Environ. Sci.* **2013**, *6*, 1170.

(39) Lv, H.; Song, J.; Geletii, Y. V.; Vickers, J. W.; Sumliner, J. M.; Musaev, D. G.; Kögerler, P.; Zhuk, P. F.; Bacsa, J.; Zhu, G.; Hill, C. L. *J. Am. Chem. Soc.* **2014**, *136*, 9268.

(40) Vickers, J. W.; Sumliner, J. M.; Lv, H.; Morris, M.; Geletii, Y. V.; Hill, C. L. *Phys. Chem. Chem. Phys.* **2014**, *16*, 11942.

(41) Han, X.-B.; Zhang, Z.-M.; Zhang, T.; Li, Y.-G.; Lin, W.; You, W.; Su, Z.-M.; Wang, E.-B. *J. Am. Chem. Soc.* **2014**, *136*, 5359.

(42) Han, X.-B.; Li, Y.-G.; Zhang, Z.-M.; Tan, H.-Q.; Lu, Y.; Wang, E.-B. *J. Am. Chem. Soc.* **2015**, *137*, 5486.

(43) Toma, F. M.; Sartorel, A.; Iurlo, M.; Carraro, M.; Parisse, P.; Maccato, C.; Rapino, S.; Gonzalez, B. R.; Amenitsch, H.; Da Ros, T.; Casalis, L.; Goldoni, A.; Marcaccio, M.; Scorrano, G.; Scoles, G.; Paolucci, F.; Prato, M.; Bonchio, M. *Nat Chem* **2010**, *2*, 826.

(44) Soriano-López, J.; Goberna-Ferrón, S.; Vigara, L.; Carbó, J. J.; Poblet, J. M.; Galán-Mascarós, J. R. *Inorg. Chem.* **2013**, *52*, 4753.

(45) Guo, S.-X.; Liu, Y.; Lee, C.-Y.; Bond, A. M.; Zhang, J.; Geletii, Y. V.; Hill, C. L. *Energy Environ. Sci.* **2013**, *6*, 2654.

(46) Liu, Y.; Guo, S.-X.; Bond, A. M.; Zhang, J.; Geletii, Y. V.; Hill, C. L. *Inorg. Chem.* **2013**, *52*, 11986.

(47) Liu, X.; Li, Y.; Peng, S.; Lu, G.; Li, S. *Int. J. Hydrogen Energy* **2012**, *37*, 12150.

(48) Zhang, Z.; Lin, Q.; Zheng, S.-T.; Bu, X.; Feng, P. *Chem. Commun. (Cambridge, U. K.)* **2011**, *47*, 3918.

(49) Matt, B.; Fize, J.; Moussa, J.; Amouri, H.; Pereira, A.; Artero, V.; Izzet, G.; Proust, A. *Energy Environ. Sci.* **2013**, *6*, 1504.

(50) Lv, H.; Song, J.; Zhu, H.; Geletii, Y. V.; Bacsa, J.; Zhao, C.; Lian, T.; Musaev, D. G.; Hill, C. L. *J. Catal.* **2013**, *307*, 48.

(51) Suzuki, K.; Tang, F.; Kikukawa, Y.; Yamaguchi, K.; Mizuno, N. *Chem. Lett.* **2014**, *43*, 1429.

(52) Lv, H.; Guo, W.; Wu, K.; Chen, Z.; Bacsa, J.; Musaev, D. G.; Geletii, Y. V.; Lauinger, S. M.; Lian, T.; Hill, C. L. *J. Am. Chem. Soc.* **2014**, *136*, 14015.

(53) Fang, X. K.; Kogerler, P. *Chem. Commun. (Cambridge, U. K.)* **2008**, 3396.

(54) Wu, Q.; Li, Y. G.; Wang, Y. H.; Wang, E. B.; Zhang, Z. M.; Clerac, R. *Inorg. Chem.* **2009**, *48*, 1606.

(55) Fang, X.; Luban, M. *Chem. Commun. (Cambridge, U. K.)* **2011**, *47*, 3066.

(56) Li, B.; Zhao, J.-W.; Zheng, S.-T.; Yang, G.-Y. *Inorg. Chem. Commun.* **2009**, *12*, 69.

(57) Pradeep, C. P.; Long, D.-L.; Kogerler, P.; Cronin, L. *Chem. Commun.* **2007**, 4254.

(58) Zhao, J.-W.; Zhang, J.; Zheng, S.-T.; Yang, G.-Y. *Inorg. Chem.* **2007**, *46*, 10944.

(59) Pichon, C.; Dolbecq, A.; Mialane, P.; Marrot, J.; Riviere, E.; Secheresse, F. *Dalton Trans.* **2008**, 71.

(60) Mal, S. S.; Dickman, M. H.; Kortz, U.; Todea, A. M.; Merca, A.; Bögge, H.; Glaser, T.; Müller, A.; Nellutla, S.; Kaur, N.; van Tol, J.; Dalal, N. S.; Keita, B.; Nadjo, L. *Chemistry – A European Journal* **2008**, *14*, 1186.

(61) Godin, B.; Chen, Y.-G.; Vaissermann, J.; Ruhlmann, L.; Verdaguer, M.; Gouzerh, P. *Angew. Chem. Int. Ed.* **2005**, *44*, 3072.

(62) Ritorto, M. D.; Anderson, T. M.; Neiwert, W. A.; Hill, C. L. *Inorg. Chem.* **2004**, *43*, 44.

(63) Ma, P.-t.; Chen, L.-J.; Zhao, J.-W.; Wang, W.; Wang, J.-P.; Niu, J.-Y. *Inorg. Chem. Commun.* **2011**, *14*, 415.

(64) Lv, H.; Song, J.; Geletii, Y. V.; Guo, W.; Bacsa, J.; Hill, C. L. *Eur. J. Inorg. Chem.* **2013**, *2013*, 1720.

(65) Clemente-Juan, J. M.; Coronado, E.; Forment-Aliaga, A.; Galán-Mascarós, J. R.; Giménez-Saiz, C.; Gómez-García, C. J. *Inorg. Chem.* **2004**, *43*, 2689.

(66) Galán-Mascarós, J. R.; Gómez-Garcia, C. J.; Borrás-Almenar, J. J.; Coronado, E. *Adv. Mater. (Weinheim, Ger.)* **1994**, *6*, 221.

(67) Ibrahim, M.; Haider, A.; Lan, Y.; Bassil, B. S.; Carey, A. M.; Liu, R.; Zhang, G.; Keita, B.; Li, W.; Kostakis, G. E.; Powell, A. K.; Kortz, U. *Inorg. Chem.* **2014**, *53*, 5179.

(68) Yao, S.; Zhang, Z.; Li, Y.; Wang, E. *Inorg. Chem. Commun.* **2009**, *12*, 937.

(69) Mialane, P.; Dolbecq, A.; Marrot, J.; Rivière, E.; Sécheresse, F. *Angew. Chem. Int. Ed.* **2003**, *42*, 3523.

(70) Mal, S. S.; Kortz, U. *Angew. Chem. Int. Ed.* **2005**, *44*, 3777.

(71) Mbomekalle, I. M.; Keita, B.; Nierlich, M.; Kortz, U.; Berthet, P.; Nadjo, L. *Inorg. Chem.* **2003**, *42*, 5143.

(72) Zhang, Z.; Li, Y.; Wang, E.; Wang, X.; Qin, C.; An, H. *Inorg. Chem.* **2006**, *45*, 4313.

(73) Pichon, C.; Mialane, P.; Dolbecq, A.; Marrot, J.; Rivière, E.; Bassil, B. S.; Kortz, U.; Keita, B.; Nadjo, L.; Sécheresse, F. *Inorg. Chem.* **2008**, *47*, 11120.

(74) Clemente-Juan, J. M.; Coronado, E.; Galan-Mascaros, J. R.; Gomez-Garcia, C. J. *Inorg. Chem.* **1999**, *38*, 55.

(75) Zhang, H.-M.; Li, Y.-G.; Lu, Y.; Clérac, R.; Zhang, Z.-M.; Wu, Q.; Feng, X.-J.; Wang, E.-B. *Inorg. Chem.* **2009**, *48*, 10889.

(76) Ibrahim, M.; Xiang, Y.; Bassil, B. S.; Lan, Y.; Powell, A. K.; de Oliveira, P.; Keita, B.; Kortz, U. *Inorg. Chem.* **2013**, *52*, 8399.

(77) Zheng, S.-T.; Zhang, J.; Clemente-Juan, J. M.; Yuan, D.-Q.; Yang, G.-Y. *Angew. Chem. Int. Ed.* **2009**, *48*, 7176.

(78) Li, X.-X.; Zheng, S.-T.; Zhang, J.; Fang, W.-H.; Yang , G.-Y.; Clemente-Juan, J. M. *Chemistry – A European Journal* **2011**, *17*, 13032.

(79) Huang, L.; Zhang, J.; Cheng, L.; Yang, G.-Y. *Chem. Commun. (Cambridge, U. K.)* **2012**, *48*, 9658.

(80) Katsoulis, D. E.; Pope, M. T. *J. Am. Chem. Soc.* **1984**, *106*, 2737.

(81) Bruker In *APEXII v2014.1-1*; Bruker AXS Inc.: Madison, WI., 2014.

(82) Bruker In *SAINT v8.34A*; Bruker AXS Inc.: Madison, WI., 2013.

(83) Dolomanov, O. V.; Bourhis, L. J.; Gildea, R. J.; Howard, J. A. K.; Puschmann, H. *J. Appl. Crystallogr.* **2009**, *42*, 339.

(84) Palatinus, L.; Chapuis, G. *J. Appl. Crystallogr.* **2007**, *40*, 786.

(85) Sheldrick, G. *Acta Cryst. A* **2008**, *64*, 112.

(86) Brown, I. D.; Altermatt, D. *Acta Crystallogr. Sect. B* **1985**, *41*, 244.

(87) Robinson, K.; Gibbs, G. V.; Ribbe, P. H. *Science* **1971**, *172*, 567.

(88) Lueken, H. *Magnetochemie* Stuttgart, Leipzig, 1999.

(89) Yang, E.-C.; Wernsdorfer, W.; Hill, S.; Edwards, R. S.; Nakano, M.; Maccagnano, S.; Zakharov, L. N.; Rheingold, A. L.; Christou, G.; Hendrickson, D. N. *Polyhedron* **2003**, *22*, 1727.

(90) Moragues-Cánovas, M.; Helliwell, M.; Ricard, L.; Rivière, É.; Wernsdorfer, W.; Brechin, E.; Mallah, T. *Eur. J. Inorg. Chem.* **2004**, *2004*, 2219.

(91) Yang, E.-C.; Wernsdorfer, W.; Zakharov, L. N.; Karaki, Y.; Yamaguchi, A.; Isidro, R. M.; Lu, G.-D.; Wilson, S. A.; Rheingold, A. L.; Ishimoto, H.; Hendrickson, D. N. *Inorg. Chem.* **2006**, *45*, 529.

(92) Ghisolfi, A.; Monakhov, K. Y.; Pattacini, R.; Braunstein, P.; Lopez, X.; de Graaf, C.; Speldrich, M.; van Leusen, J.; Schilder, H.; Kogerler, P. *Dalton Trans.* **2014**, *43*, 7847.

(93) Du, P.; Schneider, J.; Jarosz, P.; Eisenberg, R. *J. Am. Chem. Soc.* **2006**, *128*, 7726.

(94) Sun, H.; Hoffman, M. Z. *J. Phys. Chem.* **1994**, *98*, 11719.

(95) Han, Z.; McNamara, W. R.; Eum, M.-S.; Holland, P. L.; Eisenberg, R. *Angew. Chem. Int. Ed.* **2012**, *51*, 1667.

(96) Prier, C. K.; Rankic, D. A.; MacMillan, D. W. C. *Chem. Rev. (Washington, DC, U. S.)* **2013**, *113*, 5322.

Chapter 9

A Cu-based Polyoxometalate Catalyst for Efficient Catalytic Hydrogen Evolution

(Unpublished work, manuscript in preparation.)

With Yuanzhe Gao, Sarah M. Lauinger, Weiwei Guo, John Bacsa, Kevin P. Sullivan, Marika Wieliczko, Djamaladdin G. Musaev, Craig L. Hill*

9.1 Introduction

Solar-driven water splitting into H_2 and O_2 is of considerable potential impact in context with solar fuel production and the projected increasing global demand for energy.[1] The photocatalytic reduction of water to H_2 has been known since the late 1970s when researchers developed systems comprising $[Ru(bpy)_3]^{2+}$ and/or its derivatives as photosensitizers in the presence of a sacrificial electron donor, an electron mediator and a suitable catalyst (e.g. Pt).[2-4] In recent years, many earth-abundant transition-metal-containing complexes (e.g. iron,[5-8] cobalt,[9-14] nickel,[15-19] and molybdenum[20,21]) have been prepared as water reduction catalysts (WRCs) for photocatalytic or electrocatalytic hydrogen production under homogeneous conditions. In addition, hundreds of heterogeneous electrocatalytic systems with a wide range of elemental compositions for hydrogen evolution are known.[22-28]

Cu-based compounds or materials for catalytic water reduction are singularly uncommon in the literature despite the low projected costs and high earth-abundance.[29] The conventional wisdom is that Cu-based complexes are inefficient WRCs due to the high free energy of hydrogen adsorption (ΔG_H) on Cu, based in part, on density functional theory (DFT) calculations.[22,23] To date, there are some reports of Cu or Cu-derived complexes for electrocatalytic water oxidation[30-35] or CO/CO_2 reduction to multicarbon fuels,[36-38] but very few reports for catalytic water reduction[39-44] and only one report of visible-light-driven catalytic water reduction.[40]

Thus the development of new Cu-based WRCs that work efficiently for solar energy conversion remains an intriguing and challenging goal. Our group has tried to prepare

Cu-containing catalysts for efficient visible-light-driven water reduction based on the platform of polyoxometalates (POMs). In recent years, transition-metal-substituted POMs (TMSPOMs) have been extensively investigated for solar energy conversion as both water oxidation catalysts (WOCs) under thermal,[45-52] photochemical[53-62] and electrochemical[63-66] conditions and water reduction catalysts (WRCs)[67-73] under visible light irradiation. Herein, we report the synthesis and characterization of a tetra-copper-substituted polyoxometalate, $[Cu_4(H_2O)_2(PW_9O_{34})_2]^{10-}$ (**Cu_4P_2**), its catalytic hydrogen evolution activity, stability under turnover conditions, and mechanistic quenching studies.

9.2 Experimental

9.2.1. Materials and Instrumentation

All chemicals and solvents for syntheses, characterization, and catalytic studies were purchased from commercial sources; these were used as received without further purification unless otherwise noted. A Barnstead Nanopure® water-purification system was used to produce Nanopure H_2O for solution preparation. The trilacunary tungstophosphate precursor salt, $[A\text{-}PW_9O_{34}]^{9-}$, was synthesized according to a literature method.[74] The $[B\text{-}PW_9O_{34}]^{9-}$ ligands were prepared through solid state isomerization by heating $[A\text{-}PW_9O_{34}]^{9-}$ salt at 140 ^oC for 6 hours.[75] The FT-IR spectra were measured on a Thermo Nicolet 6700 spectrometer using ~2 wt % KBr pellets. The abbreviations used for assigning IR peak intensities are as follows: s = strong, m = medium, w = weak and sh = shoulder. UV-Vis spectra were acquired using an Agilent 8453 spectrophotometer equipped with a diode-array detector and an Agilent 89090A cell temperature controller unit. The solutions were placed in quartz cuvettes with an optical path of 1 cm. Thermogravimetric data were collected on Simultaneous Thermal analysis STA 6000

(PerkinElmer) with a nitrogen flow rate of 20 mL/min; the temperature was varied from 30 to 800 °C at a rate of 10 °C/min. Transmission/scanning electron microscopy and energy dispersive X-ray spectroscopy (TEM, SEM/EDX) data were gathered at the Clemson University Advanced Materials Center using three Hitachi transmission electron microscopes equipped with EDX (STEM HD2000, TEM H7600T, and TEM 9500) with 0.24 nm resolution at 200 kV, and scanning electron microscopes (S3400, SU-6600, and S4800) with 3 nm resolution at 30 kV. Dynamic light scattering (DLS) measurements were performed on a Brookhaven Instruments 90Plus particle size analyzer. Each sample was measured three times consecutively. Analysis of hydrogen was conducted using a HP7890A model gas chromatograph equipped with thermal conductivity detector (TCD) and a 5Å molecular sieve capillary column. The emission quenching spectra at 470 - 750 nm with λ_{max} = 577 nm ($\lambda_{excitation}$ = 455 nm) were recorded on a FluoroMax 3 spectrofluorimeter. The mixture of CH_3CN/DMF (1/3) with 1.4 M H_2O was used as solvent for the measurements.

9.2.2. Synthesis of $Na_3K_7[Cu_4(H_2O)_2(PW_9O_{34})_2]$ (Na_3K_7-Cu_4P_2)

$Na_3K_7[Cu_4(H_2O)_2(B\text{-}\alpha\text{-}PW_9O_{34})_2]\cdot 30H_2O$ (Na_3K_7-**Cu_4P_2**) was synthesized according to modified literature method[75] as follows: solid $CuCl_2\cdot 2H_2O$ (0.62 g, 3.6 mmol) was dissolved in 12 mL water. To this light blue solution was added slowly solid $[B\text{-}PW_9O_{34}]^{9-}$ (5.1 g, 1.8 mmol); the resulting mixture was vigorously stirred until a clear light green solution was obtained. Then 1 g of KCl was added, resulting in immediate precipitation of a pale green solid that was collected by centrifugation. The resulting precipitates were recrystallized by re-dissolving in 30 mL of warm water, and the slightly cloudy solution was centrifuged to remove any insoluble impurities. The clear green

supernatant was left in a refrigerator at 4 ^{o}C for crystallization. After about two days, pale green needle-shaped crystals began to form; these were collected by filtration in high yield (1.7 g, 35%). One single crystal was submitted to structural analysis by X-ray crystallography and the bulk sample was analyzed by elemental analysis. Elemental analysis for Na_3K_7-**Cu_4P_2**: calcd. For Na, 1.35; K, 5.37; Cu, 4.99; P, 1.21; W, 64.98%; found for Na, 1.29; K, 5.69; Cu, 4.99; P, 1.27; W, 66.05%. FT-IR (2% KBr pellet, cm^{-1}, **Figure 9-1**): 1044(s), 1009 (s), 960(sh), 945(s), 892(s), 765(sh), 737 (s), and 512 (w). The calculated weight loss percentage (9.6%) corresponds to 30 hydration water molecules per Na_3K_7-**Cu_4P_2**.

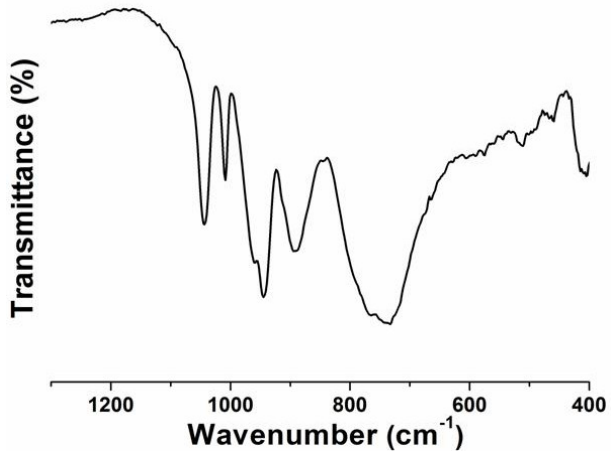

Figure 9-1 FT-IR spectra of Na_3K_7-**Cu_4P_2**, ~2 wt % in KBr.

The tetrabutylammonium (TBA^+) salt of **Cu_4P_2** (TBA-**Cu_4P_2**) was prepared using following procedure: typically, Na_3K_7-**Cu_4P_2** (1 g) was dissolved in 40 mL of H_2O, to which was added a solution of tetrabutylammonium bromide (TBABr, 3 g) dissolved in 10 mL 0.5 M sodium acetate buffer (pH 4.8). A copious pale green precipitate formed immediately and was collected by centrifugation. The resulting solid was washed with water (twice) and ethanol (twice) to remove any additional TBABr and dried in air. The dried solid was then redissolved in 5 mL CH_3CN and the mixture centrifuged to separate

any insoluble precipitate. The final product was obtained in high purity by adding anhydrous diether to a clear CH_3CN solution. The FT-IR spectrum of TBA-**Cu_4P_2** is shown in **Figure 9-2**, FT-IR (2% KBr pellet, cm^{-1}): 1050(s), 972(sh), 957(s), 888(m), 839(m), 764 (m), and 509 (w).

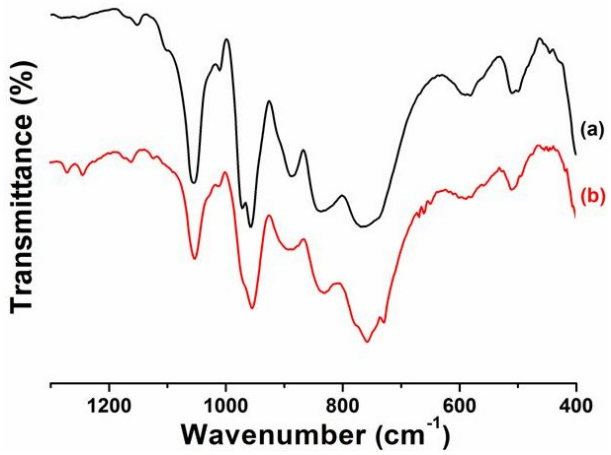

Figure 9-2 FT-IR spectra of (a) TBA^+ salt and (b) $[Ru(bpy)_3]^{2+}$ salt of **Cu_4P_2** isolated before light-driven reaction. All FT-IR spectra were ~2 wt% samples in KBr.

9.2.3. X-ray Crystallography

Complete data for Na_3K_7-**Cu_4P_2** were collected in the X-ray Crystallography Center at Emory. A colorless prism-shaped crystal with dimensions 0.64×0.24×0.15 mm^3 was mounted on a loop with Paratone oil. Data were collected using a Bruker D8 APEX-II CCD diffractometer equipped with an Oxford Cryosystems low-temperature apparatus operating at T = 110(2) K. Data were measured using ϕ and ω scans scans of 1° per frame for 20 s using MoK_α radiation (fine-focus sealed tube, 45 kV, 30 mA). The total number of runs and images was based on the strategy calculation from the program **APEX2**.[76] The actually achieved resolution was Θ = 30.76°. Cell parameters were retrieved and refined using the **SAINT** (Bruker, V8.34A, 2013)[77] software on 9903 reflections, 19% of the observed reflections. Data reduction was performed using the

SAINT (Bruker, V8.34A, 2013)[77] software which corrects for Lorentz polarization. The final completeness is 99.70% out to 30.76° in Θ. The absorption coefficient (μ) of this material is 24.118 mm^{-1} and the minimum and maximum transmissions are 0.0022 and 0.0913. The structure was solved in the space group $P\bar{1}$ (#2) by Direct Methods using the **ShelXS-97**[78] structure solution program and refined by Least Squares using version of **ShelXL-97**[78]. The results are summarized in **Table 9-1**. All non-hydrogen atoms were refined anisotropically. Hydrogen atom positions were calculated geometrically and refined using the riding model. There is one independent molecule in the unit cell. The value of Z' is 0.5. This means that only half of the formula unit is present in the asymmetric unit, with the other half consisting of symmetry equivalent atoms.

Table 9-1 Crystallographic data and structure refinement for Na_3K_7-$\mathbf{Cu_4P_2}$.

	Na_3K_7-$\mathbf{Cu_4P_2}$
Formula	$Na_3K_7Cu_4O_{102}P_2W_{18}H_{66}$
Formula weight	5632.35 g mol^{-1}
μ/mm^{-1}	24.118
$D_{calc.}$/ g cm^{-3}	4.160
Crystal System	triclinic
Space Group	$P\bar{1}$
Colour	pale green
T/K	110(2)
a/Å	11.7244(11)
b/Å	12.3241(11)
c/Å	16.8769(16)
α/°	83.0710(10)
β/°	71.4580(10)
γ/°	81.8680(10)
V/$Å^3$	2281.3(4)
Z	1

$\Theta_{min}/^{\circ}$	2.544
$\Theta_{max}/^{\circ}$	30.763
Measured Refl.	52191
Independent Refl.	14109
Reflections Used	12395
R_{int}	0.0519
Parameters	632
Restraints	18
GooF	1.070
R_1	0.0370
R_1 (all data)[a]	0.0452
wR_2	0.0930
wR_2 (all data)[b]	0.0979

[a] $R_1 = \Sigma||F_0| - |F_c||/ \Sigma|F_0|$; [b] $wR_2 = \Sigma[w(F_0^2 - F_c^2)^2]/ \Sigma[w(F_0^2)^2]^{1/2}$

9.2.4. Computational Procedures

Geometries of the $\mathbf{Cu_4P_2}$, $[\mathbf{Cu_4P_2}]^{2-}$ and $[\mathbf{Cu_4P_2}]^{2+}$ were optimized in their several lower-lying electronic states, in the *N,N*-Dimethylformamide solution with no geometry constraints. Vibrational analyses were performed to ensure that all converged structures are true minima. In these calculations we used the spin-unrestricted DFT method (the hybrid M06L functional)[79] in conjunction with the split-valence 6-31G(d) basis sets for H, O, P atoms, and the lanl2dz basis with the associated Hay-Wadt ECPs[80-82] for the W and Ni atoms, which below will be referred to as "UM06L/lanl2dz". The solvent effect was incorporated at the self-consistent reaction field IEF-PCM level of theory.[83,84] All calculations were carried out with the Gaussian 09 software package.[85]

9.2.5. Photocatalysis Experiments

The visible-light-driven H_2 production experiments were performed in a cylindrical cuvette (NSG, 32UV10) with a total volume of ~2.5 or 17.0 mL. In a typical experiment,

the cell was filled with 2.0 or 4.0 mL CH_3CN/DMF (~1/3) solution containing 0.2 mM $[Ir(ppy)_2(dtbbpy)]^+$, 0.25 M triethanolamine (TEOA), 1.4 M H_2O and 4 - 20 μM catalyst. The reaction cell was sealed with a rubber septum, carefully deaerated and filled with Ar. The reaction samples were irradiated by a LED-light source (λ = 455 nm; light intensity 20 mW, beam diameter ~0.4 cm) at room temperature with constant stirring (3×10^3 RPM) using a magnetically-coupled stirring system (SYS 114, SPECTROCELL). The illumination power (20 mW) was measured at the front of the reaction cell using a digital laser power meter (OPHIR, model NOVA II). During the course of a given reaction, the headspace sampling (50 μL) was performed using a Hamilton syringe followed by injection into a HP7890A model gas chromatograph equipped with thermal conductivity detector (TCD) and a 5Å molecular sieve capillary column with argon carrier gas. Quantitative results of H_2 evolution were calculated based on the calibrated peak area versus moles of H_2 curve and typically averaged from multiple runs. Control experiments were carried out under the same conditions in the absence of each component (e.g. $[Ir(ppy)_2(dtbbpy)]^+$, TEOA, or catalyst **Cu_4P_2**) for the hydrogen generating samples as described above. More control experiments were performed by replacing complex **Cu_4P_2** with $TBA_6[P_2W_{18}O_{62}]$ (TBA-**P_2W_{18}**) or $CuCl_2$ under otherwise the identical conditions.

The quantum yield "ϕ" was defined as the number of H_2 molecules produced per two absorbed photons. It is calculated using the following equation (**9-1**):

$$\phi = \frac{2 \times n_{H_2}}{n_{photons}} \qquad \textbf{(9-1)}$$

Where n_{H2} is the number of hydrogen produced as measured in by GC, and $n_{photons}$ is the number of photons absorbed by the reaction solution as calculated from equation (**9-2**).

$$n_{photons} = \frac{\eta \times P \times t}{E_{455nm} \times N_a} \quad (\mathbf{9\text{-}2})$$

Where η is the percentage of light irradiation absorbed by the reaction solution as measured by UV-Vis spectrometer (OD = 0.235 at 455 nm; ~41.8% light absorbed); P is the illumination power (20 mW) as measured at the front of the reaction cell using a digital laser power meter, E_{455nm} is the energy of a 455 nm photon in (J), t is the illumination time in (s), and N_a is Avogadro's number. The calculated quantum yields under various conditions are summarized in **Table 9-5**.

9.2.6. Dynamic Light Scattering Measurements

Dynamic light scattering (DLS) measurements were performed on a Brookhaven Instruments 90Plus particle size analyzer. Each sample was measured three times consecutively. The post-reaction solutions from light-driven catalytic reaction using either catalyst **Cu_4P_2** or $CuCl_2$ were evaluated by DLS.

9.2.7. TEM, SEM and EDS Measurements

Morphologies of the materials were characterized by Variable Pressure Scanning Electron Microscope-SU6600 instrument along with Energy Dispersive Spectroscopy (EDS) analysis. The TEM images were obtained using Scanning Transmission Electron Microscope-HD2000 operating at 30 kV. The samples for TEM/SEM measurements were isolated from the post-reaction solution by centrifugation at 10,000 RPM. The

resulting particles were redispersed in ethanol by ultrasonication for 10 min, followed by drop coating on carbon-coated copper grid and dried under ambient conditions.

9.3 Results and Discussion

9.3.1. Synthesis, Crystal Structure and Characterization

Polyoxoanion **Cu_4P_2** was synthesized according to modified literature method[75] by reacting the lacunary $[B\text{-}\alpha\text{-}PW_9O_{34}]^{9-}$ ligand with $CuCl_2$ in aqueous solution. Recrystallization of the crude products in warm water yields pale green needle-shaped crystals. Thermogravimetric analysis of the title complex shows a 10.2 % weight loss, corresponding to 32 hydration water molecules per polyanion with two of them coordinating to the two external Cu centers. The FT-IR spectrum of **Cu_4P_2** in 2 wt% KBr pellet displays all the characteristic bands of sandwich-type POMs in agreement with literature report (**Figure 9-1**).[75] Exchange of the Na^+, K^+ counter cations for tetrabutylammonium (TBA^+) or $[Ru(bpy)_3]^{2+}$ does not alter the geometrical structures of **Cu_4P_2** complex (**Figure 9-2**). The solid-state structure of **Cu_4P_2** was characterized by single-crystal X-ray diffraction. This study confirmed that the salt of **Cu_4P_2** crystallizes in the triclinic space group $P\bar{1}$ (**Figure 9-3** and **Table 9-1**) which has a similar structure to recently reported POM-based WOCs, $[Co_4(H_2O)_2(XW_9O_{34})_2]^{10-}$ (X = P or V)[47,54,58,60] and POM-based WRCs, $[Ni_4(H_2O)_2(PW_9O_{34})_2]^{10-}$ (**Ni_4P_2**).[72] A tetra-copper cluster core $\{Cu_4O_{14}\}$ is sandwiched between two tri-lacunary, heptadentate $[B\text{-}\alpha\text{-}PW_9O_{34}]^{9-}$ POM ligands (**Figure 9-3**).

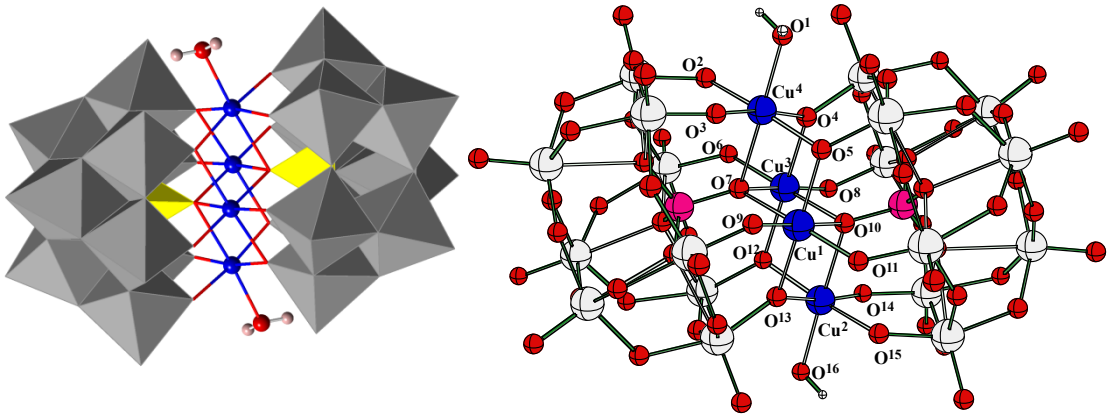

Figure 9-3 Left: polyhedral and ball-and-stick representations of the building blocks of polyoxoanion **Cu_4P_2**. Right: the notation of important atoms used in the text discussion of **Cu_4P_2**, $[Cu_4P_2]^{2-}$ and $[Cu_4P_2]^{2+}$. Color code: WO_6, grey octahedra; PO_4, yellow tetrahedra; Cu, blue balls; O, red balls; W, white cross-hatched balls; P, magenta balls.

Bond valence sum (BVS) calculations[86] confirm that all the Cu, P, and W atoms are in the formal +II, +V, and +VI oxidation states, respectively. All Cu ions in the **Cu_4P_2** polyoxoanion are in an idealized octahedral geometry with Cu-O bond lengths in the range 1.905(5)–2.387(6) Å with an average distance of 2.108 Å and O–Cu–O bond angles in the range 82.9(2)–176.0(2)° (**Table 9-2**).

Table 9-2 Bond lengths [Å] and angles [°] for **Cu_4P_2** polyoxoanion.

Cu(1)-O(16)	1.910(5)	Cu(1)-O(19)	2.049(5)
Cu(1)-O(20)	1.905(5)	Cu(1)-O(19)#2	2.044(5)
Cu(1)-O(26)	2.387(6)	Cu(1)-O(21)#2	2.352(5)
Cu(2)-O(21)	1.966(5)	Cu(2)-O(22)	1.952(5)
Cu(2)-O(23)	1.941(5)	Cu(2)-O(26)	1.955(5)
Cu(2)-O(1W)	2.300(6)	O(21)#2-Cu(1)-O(26)	170.93(19)
O(16)-Cu(1)-O(19)	176.0(2)	O(16)-Cu(1)-O(19)#2	93.8(2)
O(16)-Cu(1)-O(21)#2	92.6(2)	O(16)-Cu(1)-O(26)	94.1(2)
O(19)#2-Cu(1)-O(19)	82.9(2)	O(19)#2-Cu(1)-O(21)#2	88.9(2)
O(19)-Cu(1)-O(21)#2	85.1(2)	O(19)-Cu(1)-O(26)	87.83(19)

O(19)#2-Cu(1)-O(26)	84.6(2)	O(20)-Cu(1)-O(16)	90.3(2)
O(20)-Cu(1)-O(19)#2	175.2(2)	O(20)-Cu(1)-O(19)	93.1(2)
O(20)-Cu(1)-O(21)#2	93.4(2)	O(20)-Cu(1)-O(26)	92.6(2)
O(21)-Cu(2)-O(1W)	98.8(2)	O(22)-Cu(2)-O(1W)	90.4(2)
O(22)-Cu(2)-O(21)	170.2(2)	O(22)-Cu(2)-O(26)	88.9(2)
O(23)-Cu(2)-O(21)	88.6(2)	O(23)-Cu(2)-O(22)	94.4(2)
O(23)-Cu(2)-O(26)	170.0(2)	O(23)-Cu(2)-O(1W)	92.2(2)
O(26)-Cu(2)-O(1W)	97.2(2)	O(26)-Cu(2)-O(21)	86.7(2)

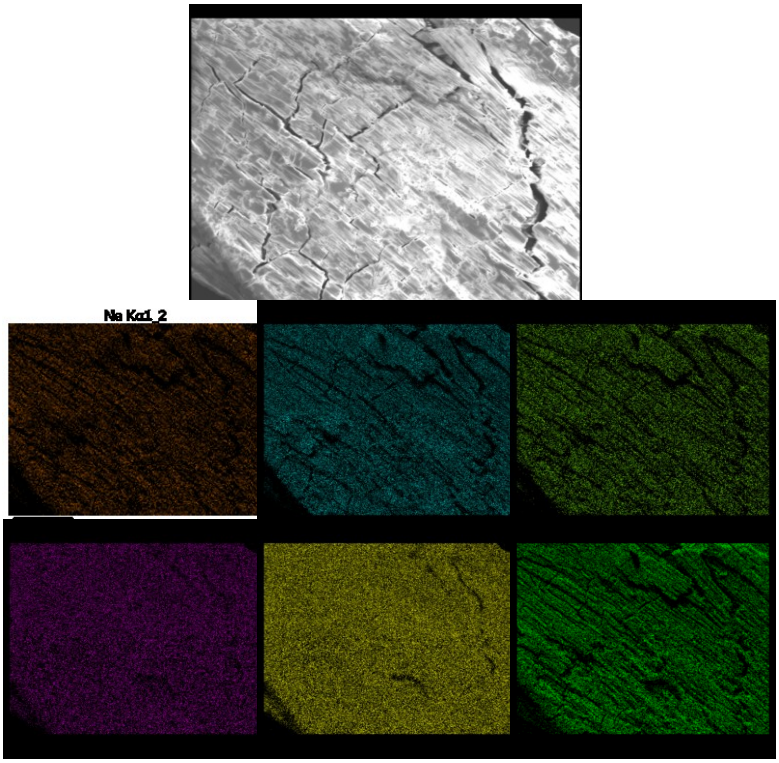

Figure 9-4 SEM image of the Na_3K_7-$\mathbf{Cu_4P_2}$ crystals and the corresponding SEM-EDX elemental mapping of Na, K, P, Cu, W and O.

Scanning electron microscopy combined with energy dispersive X-ray spectroscopy (SEM/EDX) reveal the microscopic morphology of the Na_3K_7-$\mathbf{Cu_4P_2}$ crystals as well as the elemental maps of Na, K, P, Cu, W, and O (**Figure 9-4**). The atomic ratio of these elements are in agreement with its chemical formula and remain unchanged after

exchange of the Na^+, K^+ counter cations with tetrabutylammonium (TBA^+) or $[Ru(bpy)_3]^{2+}$ (**Table 9-3**).

Table 9-3 Atomic ratio of Cu/W in different forms of $\mathbf{Cu_4P_2}$ polyoxoanions.

Element	Theoretical	Na_3K_7-$\mathbf{Cu_4P_2}$	TBA-$\mathbf{Cu_4P_2}$	$[Ru(bpy)_3]$-$\mathbf{Cu_4P_2}$ precipiate before catalysis	$[Ru(bpy)_3]$-$\mathbf{Cu_4P_2}$ precipitate after catalysis
Cu (Atomic %)	4	3.95	4.31	4.28	8.90
W (Atomic %)	18	18.05	19.81	19.90	72.86
Cu/W	1: 4.50	1: 4.57	1: 4.59	1: 4.65	1: 8.19

9.3.2. Electronic and Geometrical Structure of Cu_4P_2, $[Cu_4P_2]^{2-}$ and $[Cu_4P_2]^{2+}$

While the ongoing studies in our group focus on describing the stepwise mechanism of H_2 formation, we complement this with a computational examination of the electronic and geometry structures of the $\mathbf{Cu_4P_2}$ anion and its two-electron reduced and oxidized forms $[\mathbf{Cu_4P_2}]^{2-}$ and $[\mathbf{Cu_4P_2}]^{2+}$, respectively. These species are expected to be integral part of the H_2 formation process. The calculated important bond lengths for these species are summarized in **Table 9-4**, and compared with their available X-ray crystallographic values. The structures of these species, as well as notation of atoms, are shown in **Figure 9-3**.

Calculations show that the ground electronic state of $\mathbf{Cu_4P_2}$ is a quintet, ^5A, state with 0.65, 0.60, 0.65, and 0.60 |e| un-paired α-spins localized on the Cu^1, Cu^2, Cu^3 and Cu^4 centers, respectively, and residual 1.50 |e| α-spins delocalized over the O-centers of the

(PW_9O_{34}) fragment. This spin distribution data is consistent with Cu-centers being d^9 Cu(II) cations, in agreement with BVS calculations from X-ray structure determination.

Table 9-4 Experimental (crystallographic) and calculated bond lengths (Å) in the ground electronic states of cluster anions $\mathbf{Cu_4P_2}$ (^{5}A) $[\mathbf{Cu_4P_2}]^{2-}$ (^{3}A) and $[\mathbf{Cu_4P_2}]^{2+}$ (^{7}A). Where appropriate, crystallographically determined distances have been averaged.

Parameters	Computational			Experimental
	$\mathbf{Cu_4P_2}$	$[\mathbf{Cu_4P_2}]^{2-}$	$[\mathbf{Cu_4P_2}]^{2+}$	$\mathbf{Cu_4P_2}$
Cu^4-O^1	2.81	2.96	2.30	2.30
Cu^4-O^2	1.95	2.02	1.97	1.95
Cu^4-O^3	2.04	2.11	2.03	1.94
Cu^4-O^4	2.02	2.07	2.02	1.96
Cu^4-O^5	1.97	2.04	1.99	1.97
Cu^4-O^7	2.27	2.19	2.23	2.58
Cu^3-O^6	1.92	1.99	1.94	1.91
Cu^3-O^7	2.31	2.31	2.15	2.05
Cu^3-O^8	2.10	2.09	1.97	1.91
Cu^3-O^{10}	2.02	2.11	2.11	2.05
Cu^3-O^4	2.10	2.20	2.03	2.38
Cu^3-O^{12}	2.13	2.20	2.03	2.35
Cu^1-O^9	2.10	2.09	1.97	1.91
Cu^1-O^7	2.02	2.11	2.11	2.05
Cu^1-O^{11}	1.92	1.99	1.95	1.91
Cu^1-O^{10}	2.32	2.31	2.15	2.05
Cu^1-O^5	2.13	2.20	2.03	2.35
Cu^1-O^{13}	2.10	2.20	2.03	2.39
Cu^2-O^{12}	1.97	2.04	1.99	1.97
Cu^2-O^{13}	2.02	2.07	2.02	1.95
Cu^2-O^{14}	2.04	2.11	2.03	1.94
Cu^2-O^{15}	1.95	2.02	1.97	1.95
Cu^2-O^{10}	2.24	2.19	2.23	2.58
Cu^2-O^{16}	2.81	2.96	2.30	2.30

The antiferromagnetically coupled singlet state of **Cu_4P_2** with 0.60 |e| un-paired α-spin on "external" Cu^2 and Cu^4, and 0.65|e| un-paired β–spin on "internal" Cu^1 and Cu^3, is energetically nearly degenerate with its ferromagnetic ^{5}A counterpart. Since reduction of **Cu_4P_2** in the catalytic cycle should occur before the H_2 formation from protons, we also computationally analyzed the electronic state of the 2-electron reduced form of **Cu_4P_2**. It was found that addition of two electrons to **Cu_4P_2** produces a triplet ground electronic state in the resulting **$[Cu_4P_2]^{2-}$** unit. Interestingly, one of incoming electrons is delocalized on the four Cu centers which reduces the total un-paired spins on the Cu-centers from 2.50 |e| in **Cu_4P_2** to 1.58 |e| in **$[Cu_4P_2]^{2-}$**. Another electron is distributed among the O-centers of the (PW_9O_{34}) fragments. Thus, both the (PW_9O_{34}) fragments and the central $\{Cu_4\}$ unit have lost 1-electron upon going from **Cu_4P_2** to **$[Cu_4P_2]^{2-}$**. In contrast, when **Cu_4P_2** is oxidized by two electrons, the total un-paired spin located on the four Cu centers has changed only slightly. Indeed, in ground septet electronic state of **$[Cu_4P_2]^{2+}$,** four Cu-centers have total of 2.92 |e| spin *vs* of 2.50 |e| spin in ground quintet electronic state of **$[Cu_4P_2]$.** Thus, removal of two electrons from **Cu_4P_2**, mostly, oxidizes the (PW_9O_{34}) fragments. The aforementioned electronic structure of **Cu_4P_2**, **$[Cu_4P_2]^{2-}$** and **Cu_4P_2** is consistent with the molecular orbital picture of these species.

As seen in **Figure 9-5**, the top singly occupied orbitals of the **Cu_4P_2** ^{5}A state involve the Cu-O-W centers, and the associated LUMO orbital involves the (PW_9O_{34}) unit based orbitals. Therefore, it is reasonable that the incoming two electrons will occupy one of the SOMO orbitals (with Cu-O-W character) and the LUMO orbital to give a triplet ground electronic state for **$[Cu_4P_2]^{2-}$.** Similarly, **Cu_4P_2**-to-**$[Cu_4P_2]^{2+}$** transformation, involves with a removal of two electrons from the doubly occupied (PW_9O_{34})-based orbitals.

Consistent with these electronic structure findings, the two-electron reduction of **Cu_4P_2**, in general, slightly elongates the Cu-O bond distances, while its two electron oxidation results in reduction of the Cu-O bond distances. On average, all calculated bond distances (with a few exceptions) are in good agreement with their crystallographically determined bond distances.

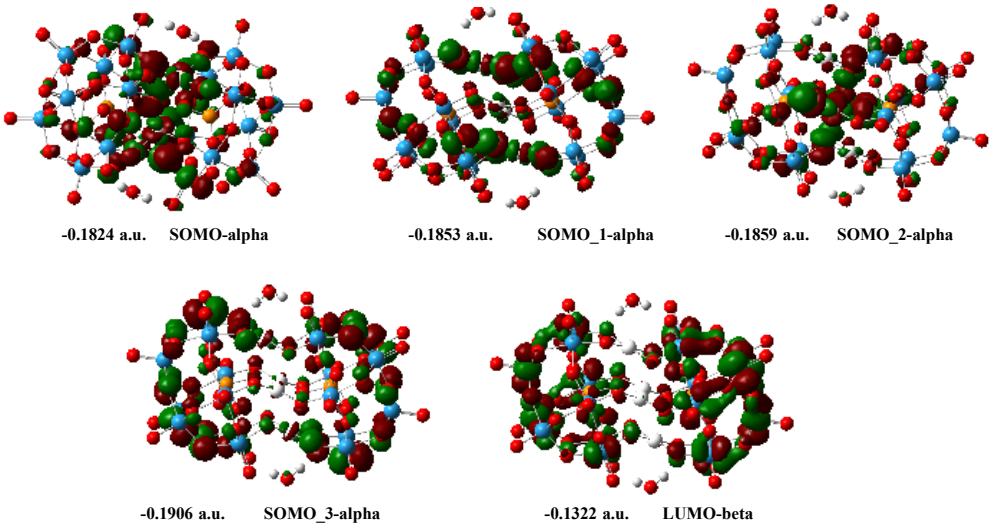

Figure 9-5 Calculated frontier orbitals of the **Cu_4P_2** anion; the calculated LUMO is about -3.6 eV vs vacuum.

9.3.3. Catalytic Activity for H_2 Evolution

Photocatalytic experiments for hydrogen evolution were conducted using $[Ir(ppy)_2(dtbbpy)]^+$ as a photosensitizer, triethanolamine (TEOA) as a sacrificial electron donor, and **Cu_4P_2** as a water reduction catalyst in a deaerated mixture of DMF/CH_3CN solvent. The amount of H_2 produced was quantified at different reaction times of the photolysis by GC analysis of the headspace gases.[72] The pH of the reaction solution was not adjusted by either base or acid considering the mixed organic solvent used in our experiments as well as the stronger reducing ability of TEOA in its unprotonated form.[2,18,70,87-90]

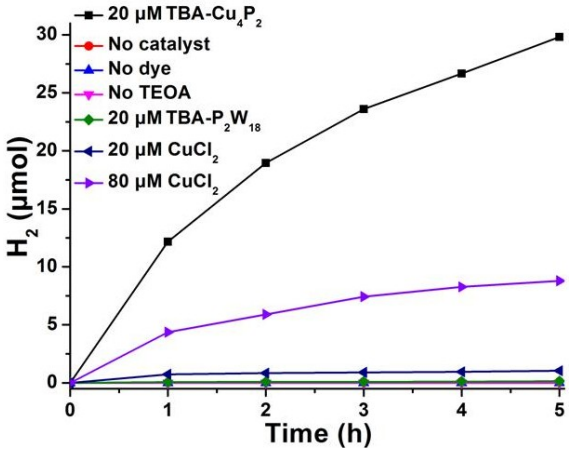

Figure 9-6 Photochemical H_2 evolution by different catalysts under otherwise identical conditions: LED light (20 mW, 455 nm, beam diameter ~0.4 cm), $[Ir(ppy)_2(dtbbpy)]^+$ (0.2 mM), TEOA (0.25 M), H_2O (1.4 M), catalyst (20 μM or 80 μM as noted), 2 mL CH_3CN/DMF (~1/3) deaerated with Ar.

Illumination on a solution of $[Ir(ppy)_2(dtbbpy)]^+$, TEOA, H_2O and catalyst **Cu_4P_2** in deaerated CH_3CN/DMF (1/3) using LED light (λ = 455 nm, 20 mW) at 25 ℃ results in the reduction of **Cu_4P_2** catalyst (change in solution color from yellow to light green) as observed in our previous work.[72] The reduced **Cu_4P_2** catalyst product further catalyzes H_2 evolution efficiently (**Figure 9-6**). No such color change or negligible production of H_2 is observed in the absence of **Cu_4P_2**. Prior to light irradiation, none of the reaction runs produce H_2. Under minimally optimized conditions, a turnover number (TON) of ~745 (~29.8 μmol H_2 gas per 0.04 μmol catalyst **Cu_4P_2**) is achieved after 5 hrs of irradiation, which is among the highest known for POM-based WRC systems. To prove the catalytic role of **Cu_4P_2**, we conducted a series of control experiments. The activities of $TBA_6[P_2W_{18}O_{62}]$ (TBA-**P_2W_{18}**) or $CuCl_2$ salt in place of **Cu_4P_2**, removal of each molecular component (catalyst **Cu_4P_2**, TEOA or $[Ir(ppy)_2(dtbbpy)]^+$) in the WRC system all generated little or no H_2. A control experiment using 80 μM $CuCl_2$, the stoichiometric

amount of Cu (4 equivalents) present in 20 μM **Cu_4P_2** only produces ~7.2 μmol H_2. This corresponds to a TON of only 45, which is about 16 times lower than that of the **Cu_4P_2**-catalyzed reaction under otherwise identical conditions (**Figure 9-6**).

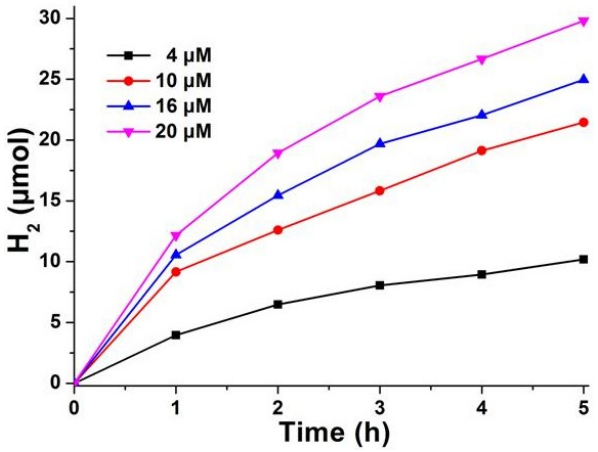

Figure 9-7 Photocatalytic H_2 evolution as a function of **Cu_4P_2** concentration. Conditions: LED light (20 mW, 455 nm), $[Ir(ppy)_2(dtbbpy)]^+$ (0.2 mM), TEOA (0.25 M), H_2O (1.4 M) catalyst Cu_4P_2 (4 - 20 μM), 2 mL CH_3CN/DMF (~1/3) deaerated with Ar.

To better understand the catalytic processes, the concentrations of different components have been varied systematically. We found that increasing the amount of **Cu_4P_2** catalyst in the reaction solution results in corresponding scaling of the H_2 generation with time. The H_2 yield increases from ~10.2 to 29.8 μmol when varying the concentration of **Cu_4P_2** from 4 to 20 μM (**Figure 9-7**); while the TON decreases accordingly from ~1270 to ~745 (**Table 9-5**).

Table 9-5 Quantum yields of H_2 production catalyzed by **Cu_4P_2** under various reaction conditions.

$[Cu_4P_2]$	**[Dye]**	**[TEOA]**	**$[H_2O]$**	**Moles of H_2 evolved (μmoles)**	**TON (5 h)**	**$\phi(H_2)$ (%)**
4 μM	0.2 mM	0.25 M	1.4 M	10.2	1274	1.8
10 μM	0.2 mM	0.25 M	1.4 M	21.5	1072	3.8
10 μM	0.2 mM	0.25 M	----	6.1	306	1.1

16 μM	0.2 mM	0.25 M	1.4 M	25.0	780	4.4
20 μM	0.2 mM	0.25 M	1.4 M	29.8	745	5.2
20 μM	0.05 mM	0.25 M	1.4 M	7.4	184	5.1
20 μM	0.1 mM	0.25 M	1.4 M	17.8	446	6.2
20 μM	0.4 mM	0.25 M	1.4 M	30.8	770	2.7
20 μM	0.2 mM	0.05 M	1.4 M	9.4	235	1.6
20 μM	0.2 mM	0.1 M	1.4 M	25.6	640	4.5
20 μM	0.2 mM	0.175 M	1.4 M	27.9	698	4.9
20 μM	0.2 mM	0.25 M	1.4 M	91.4	1143	15.9†
20 μM	0.2 mM	0.25 M	1.4 M	88.9	1087	15.5*

It is noted that the highest TONs for a given catalyst are usually obtained at very low concentrations of catalyst. Under these conditions, the stability of a catalyst is the limiting factor for prolonging reaction. The high quantum yield of 5.2% is achieved at a concentration of 20 μM **Cu_4P_2** (**Table 9-5**), which is comparable to many other visible-light-driven WRC systems.[19,91] In addition to catalyst concentration, the concentrations of the light absorber, $[Ir(ppy)_2(dtbbpy)]^+$, and the sacrificial electron donor (TEOA) also highly affect the rate as well as the H_2 yield.

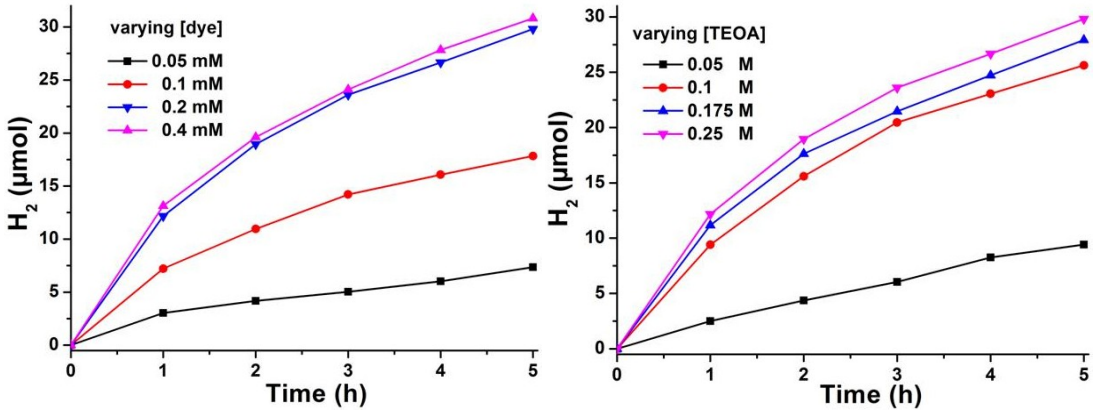

Figure 9-8 Left: Photocatalytic H_2 evolution using different concentrations of photosensitizer. Conditions: LED light (20 mW, 455 nm, beam diameter ~0.4 cm), $[Ir(ppy)_2(dtbbpy)]^+$ (0.05 - 0.4 mM), TEOA (0.25 M), H_2O (1.4 M), catalyst **Cu_4P_2** (20 μM), 2 mL CH_3CN/DMF (~1/3) deaerated with Ar. **Right**: Photocatalytic H_2 evolution using different concentrations of sacrificial

electron donor. Conditions: LED light (20 mW, 455 nm, beam diameter ~0.4 cm), $[Ir(ppy)_2(dtbbpy)]^+$ (0.2 mM), TEOA (0.05 - 0.25 M), H_2O (1.4 M), catalyst **Cu_4P_2** (20 μM), 2 mL CH_3CN/DMF (~1/3) deaerated with Ar.

As shown in **Figure 9-8**, varying the concentration of $[Ir(ppy)_2(dtbbpy)]^+$ from 0.05 mM to 0.2 mM greatly enhances the rate and final H_2 yield. The H_2 yield increases from ~7.4 to 29.8 μmol corresponding to a TON enhancement from ~184 to 745; however this enhancement levels off at 0.4 mM $[Ir(ppy)_2(dtbbpy)]^+$ indicating that H_2 generation becomes limited by **Cu_4P_2** rate. The system shows less dependence on the TEOA concentration than on the concentrations of the other components, a finding consistent with saturation in the reductant at higher concentrations (**Figure 9-8** and **Table 9-5**). In addition, the concentration of water is also an important factor in the yield and rate of H_2 generation. As anticipated, addition of 1.4 M H_2O to the reaction system dramatically increases the H_2 yield compared to that of the reaction without H_2O (~21.5 μmol *vs* ~6.1 μmol, **Figure 9-9** and **Table 9-5**). Such enhancement is expected because the addition of water increases the available proton concentration.

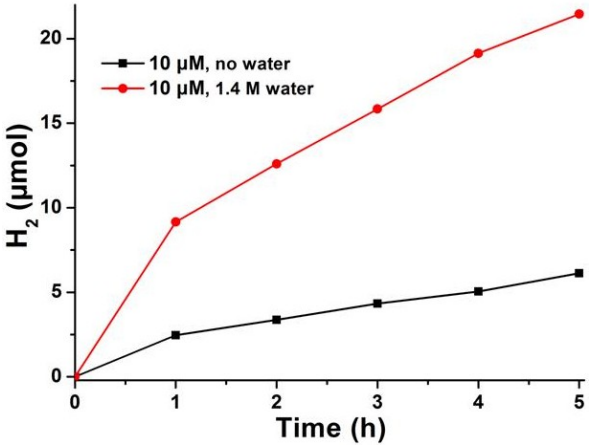

Figure 9-9 Photocatalytic H_2 evolution in the absence or presence of water. Conditions: LED light (20 mW, 455 nm, beam diameter ~0.4 cm), $[Ir(ppy)_2(dtbbpy)]^+$ (0.2 mM), TEOA (0.25 M), H_2O (0 or 1.4 M), catalyst **Cu_4P_2** (10 μM), 2 mL CH_3CN/DMF (~1/3) deaerated with Ar.

9.3.4. Stability Evaluation

The stability of molecular catalysts for H_2 generation under turnover conditions is always a general concern in the design of WRCs. We have evaluated the stability of catalyst **Cu_4P_2** in our system using multiple spectroscopic methods. Before running the photocatalytic experiments, we first assessed the stability of **Cu_4P_2** under non-turnover conditions in dark using UV-Vis spectroscopy. The UV-Vis spectra show negligible decrease after aging for 24 h (**Figure 9-10**), indicating that **Cu_4P_2** is stable under such reaction conditions prior to light irradiation.

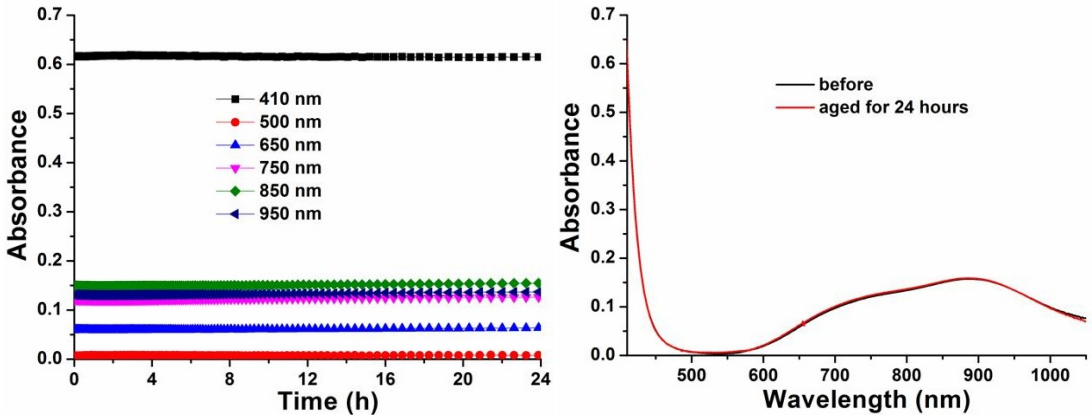

Figure 9-10 Time profile of UV-vis spectra of TBA-**Cu_4P_2** in CH_3CN/DMF (1/3) in the presence of 0.25 M TEOA, over a 24-hour period in dark (less than 1% decrease).

However, dynamic light scattering (DLS) indicate that the reactions containing either **Cu_4P_2** or $CuCl_2$ leads to the formation of nanoparticles with a maximum hydrodynamic sizes centered at ~220 nm (**Figures 9-11** and **9-12**). The isolated nanoparticles from $CuCl_2$-catalyzed post-reaction solution were further confirmed by TEM measurement (**Figure 9-13**). Such observations encouraged us to elucidate the dominant catalyst during turnover.

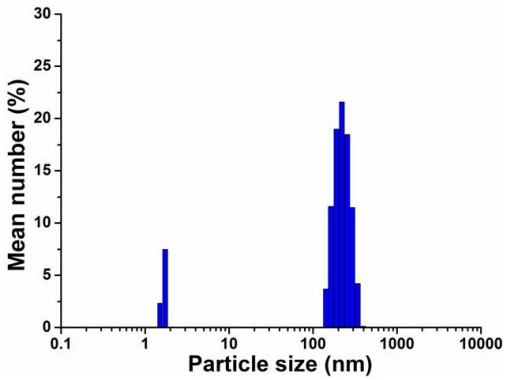

Figure 9-11 Particle size distribution (mean number %) obtained from dynamic light scattering (DLS) measurements for the post-reaction solution using 20 μM $CuCl_2$ as catalyst.

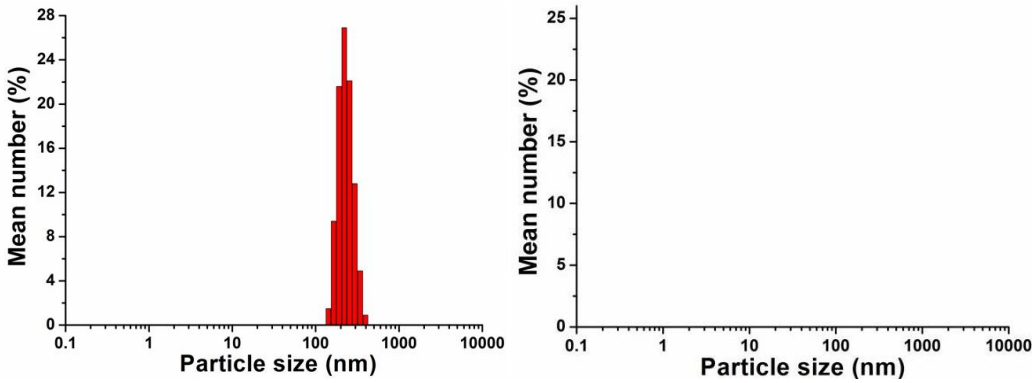

Figure 9-12 Particle size distribution (mean number %) obtained from dynamic light scattering (DLS) measurements for the post-reaction solution using 20 μM **Cu_4P_2** (left panel) and after centrifugation (right panel; the counts are below the detectable limit).

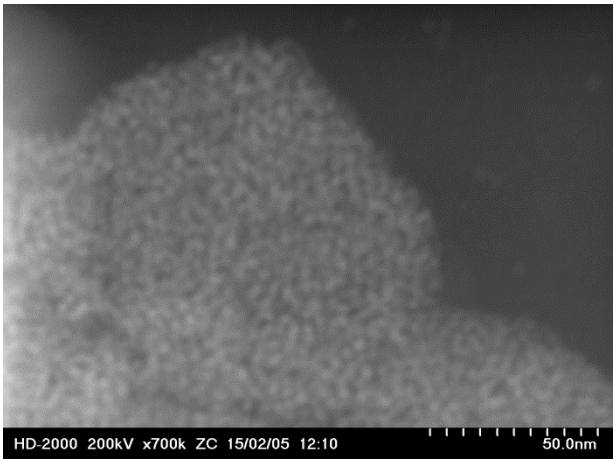

Figure 9-13 TEM image image of the nanoparticles isolated from the post-reaction solution using $CuCl_2$ as catalyst.

We conducted several scale-up experiments to assess the long-term robustness, reusability, and catalytic behavior of both **Cu_4P_2** and $CuCl_2$ catalysts. As shown in **Figure 9-14**, both the rate and yield of H_2 production in the $CuCl_2$-catalyzed system diminishes quickly with time. Centrifugation of the post-reaction mixtures containing $CuCl_2$ after three successive runs almost completely removes its activity, confirming the heterogeneity of the system (forth run, **Figure 9-14**), in agreement with the DLS and TEM results. The accumulated TON for the $CuCl_2$-catalyzed reaction reaches ~60 after 20 hours of irradiation, for lower than for the **Cu_4P_2**-catalyzed system. The latter also shows much higher H_2 evolution rates and final yields. However, the rate and yield of H_2 generation also decreases in three successive runs with **Cu_4P_2**-containing reactions. This can be attributed to a slight degradation of the $[Ir(ppy)_2(dtbbpy)]^+$ light absorber, consumption of TEOA, and the instability of catalyst **Cu_4P_2**, itself. To prove this hypothesis, we replenished the light absorber by addition of an additional 0.1 mL of this solution as well an additional 0.1 mL TEOA after the third run and centrifuged the post-reaction solution. The yield of H_2 production in the forth run is almost same as that of the third run, indicating that the molecular species remaining in the centrifuged solution remains active for catalyzing H_2 generation. The total TON for **Cu_4P_2**-catalyzed reaction is ~3370 after 20 hours of irradiation which is over 56 times that of the $CuCl_2$-catalyzed system.

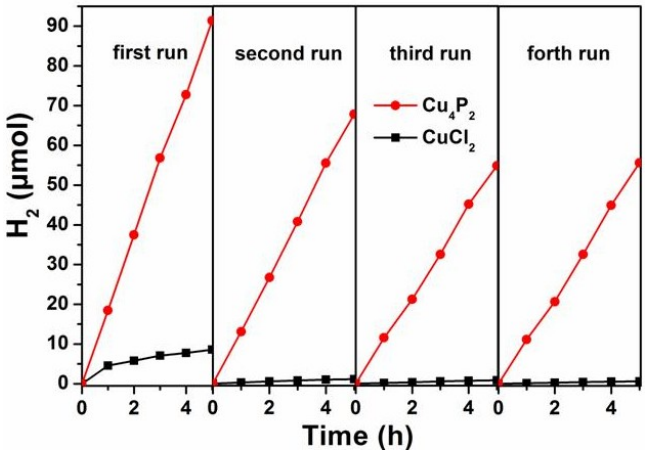

Figure 9-14 Photocatalytic H_2 evolution using 20 μM **Cu_4P_2** (red curve) and 80 μM $CuCl_2$ (black curve) for successive runs; conditions: LED light (20 mW, 455 nm), $[Ir(ppy)_2(dtbbpy)]^+$ (0.2 mM), TEOA (0.25 M), H_2O (1.4 M), 4 mL CH_3CN/DMF (~1/3) deaerated with Ar. Note: the reaction solution was centrifuged and refilled 0.1 mL $[Ir(ppy)_2(dtbbpy)]^+$ and 0.1 mL TEOA before the forth run.

To check whether Cu-based nanoparticles, possibly generated *in situ* are principally responsible for H_2 production, we conducted a reaction in the presence of 20 μM **Cu_4P_2** plus the isolated Cu-based nanoparticles from $CuCl_2$-catalyzed post-reaction solution. Experimental results show that the rate and yield of H_2 remain same as that of the reaction catalyzed by 20 μM **Cu_4P_2** only (**Table 9-5**, **Figure 9-15**). These results further confirm that the initial **Cu_4P_2** as well as its molecular decomposition products are dominant active catalyst for H_2 evolution.

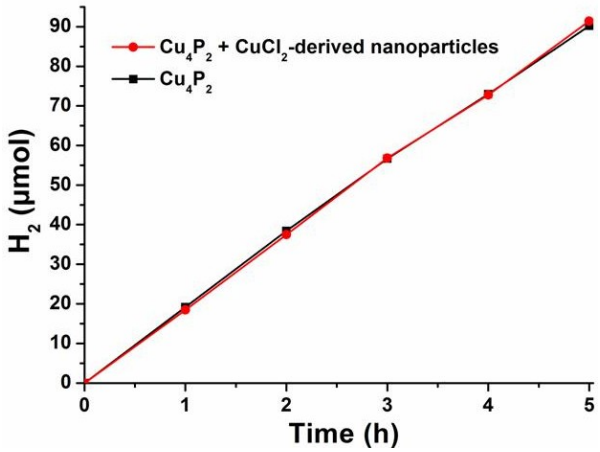

Figure 9-15 Photocatalytic H_2 evolution by different catalysts. Conditions: LED light (20 mW, 455 nm, beam diameter ~0.4 cm), $[Ir(ppy)_2(dtbbpy)]^+$ (0.2 mM), TEOA (0.25 M), catalyst **Cu_4P_2** (20 μM), 4 mL CH_3CN/DMF (~1/3) deaerated with Ar. Note: $CuCl_2$-derived nanoparticles represent the Cu-based nanoparticles isolated from the control experiment using $CuCl_2$ as catalyst.

To better characterize the decomposition product of the **Cu_4P_2** catalyst, we isolated it from the post-reaction solution by adding a saturated solution of $[Ru(bpy)_3]^{2+}$ in CH_3CN. The resulting precipitate was collected by centrifugation and analyzed by SEM/EDX as well as FT-IR measurements.

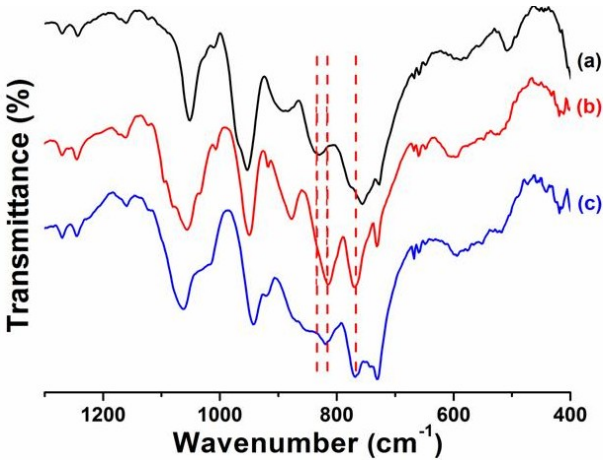

Figure 9-16 FT-IR spectra of (a) $[Ru(bpy)_3]^{2+}$ salt of **Cu_4P_2** isolated before light-driven reaction; (b) the sample after light-driven reaction (isolated from post-catalytic reaction solution, TON ~ 745) and (c) the sample after light-driven reaction (isolated from post-catalytic reaction solution, TON ~3370). All FT-IR spectra were ~2 wt% samples in KBr.

SEM/EDX measurement shows the atomic ratio of Cu/W decreases from the theoretical value of 1: 4.50 to 1: 8.19, corresponding to the dissociation of Cu species from **Cu_4P_2** during turnover (**Table 9-3**), in agreement with above analysis. In addition, the FT-IR spectra of the isolated precipitate exhibit shifts of certain POM IR peaks after catalytic reactions while the POM framework remains largely intact (**Figure 9-16**). We can conclude for the preceding collective results that catalyst **Cu_4P_2** undergoes slow decomposition by dissociating of the Cu during turnover, and both the starting **Cu_4P_2** as well as its molecular decomposition products are dominant active catalysts for H_2 evolution in these systems.

9.3.5. Relevant Energetics and Photochemical Quenching Mechanisms

In photocatalytic systems, the photosensitizer excited states are usually more oxidizing and also more reducing than the ground-state species, which facilitates either reductive or oxidative quenching by an electron donor[92] or acceptor.[18,70,93,94] To investigate the possible quenching pathways in our system, the redox properties of each component involved in our reaction system are summarized and compared in **Scheme 9-1**. As can be seen, upon excitation of $[Ir(ppy)_2(dtbbpy)]^+$, two redox couples are formed: $[Ir(ppy)_2(dtbbpy)]^{+*/0}$ and $[Ir(ppy)_2(dtbbpy)]^{2+/+*}$ with the redox potentials of ~ -0.96 V and +0.66 V vs SCE, respectively.[95,96] These excited states can be both reductively quenched by TEOA (ΔG = +0.05 eV, energetically slightly less favorable)[92] and oxidatively quenched by **Cu_4P_2** (ΔG = -0.06 eV, energetically more favorable), respectively. In addition, the one-electron-oxidized ($[Ir(ppy)_2(dtbbpy)]^{2+/+}$ ~ +1.21 V vs SCE) or one-electron-reduced ($[Ir(ppy)_2(dtbbpy)]^{+/0}$ ~ -1.51 V vs SCE) species are

thermodynamically a much stronger oxidant or reductant for TEOA oxidation or **Cu_4P_2** reduction to regenerate the ground state of the dye.

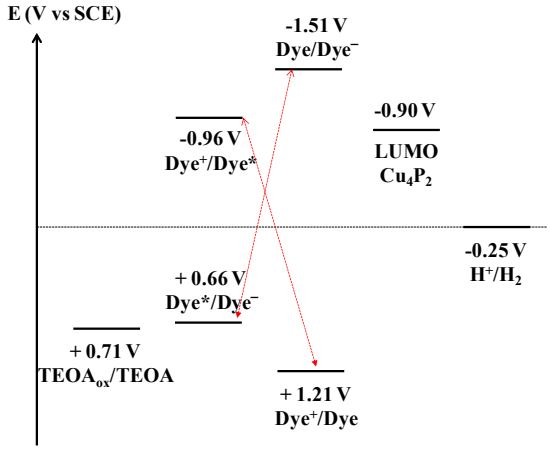

Scheme 9-1 Redox potentials of the relevant species involved in the photocatalytic processes. Note that the LUMO of Cu_4P_2 is obtained from DFT calculations which are conducted in the absence of counter cations under non-experimental conditions.

To quantitatively understand the quenching processes, the luminescence intensity of the excited state $[Ir(ppy)_2(dtbbpy)]^{+*}$ (maximum $\lambda_{emission}$ = 577 nm at $\lambda_{excitation}$ = 455 nm) has been probed in the presence of either **Cu_4P_2** or TEOA. As shown in **Figures 9-17** and **9-18**, the luminescence intensity of the excited state$[Ir(ppy)_2(dtbbpy)]^{+*}$ decays faster with increasing concentrations of both catalyst **Cu_4P_2** and TEOA. The bimolecular reductive quenching rate constant by TEOA is determined to be $3.3 \pm 0.3 \times 10^7$ M^{-1} s^{-1} using dynamic Stern-Volmer (SV) plot (**Figure 9-17**). The linear fitting of a Stern-Volmer plot for oxidative quenching by the **Cu_4P_2** catalyst gives an apparent rate constant of $4.1 \pm 0.2 \times 10^{10}$ M^{-1} s^{-1} (**Figure 9-18**) which is close to the diffusion controlled limit ($\sim 10^{10}$ M^{-1} s^{-1}) indicating that the cationic excited state $[Ir(ppy)_2(dtbbpy)]^{+*}$ interacts strongly with polyanion **Cu_4P_2** electrostatically. These data confirm that both oxidative quenching and reductive quenching pathways occur in our

photoreaction system: the reductive quenching process is dominant one because the TEOA (0.25 M) is much higher thant the **Cu_4P_2** (maximum 20 μM) concentration.

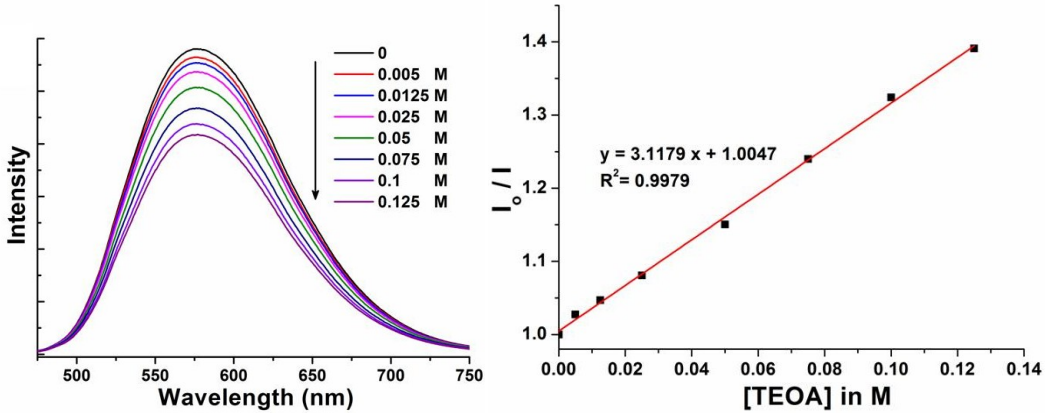

Figure 9-17 Emission spectra of $[Ir(ppy)_2(dtbbpy)]^+$ (0.1 mM) as a function of added TEOA and the corresponding Stern-Volmer plot.

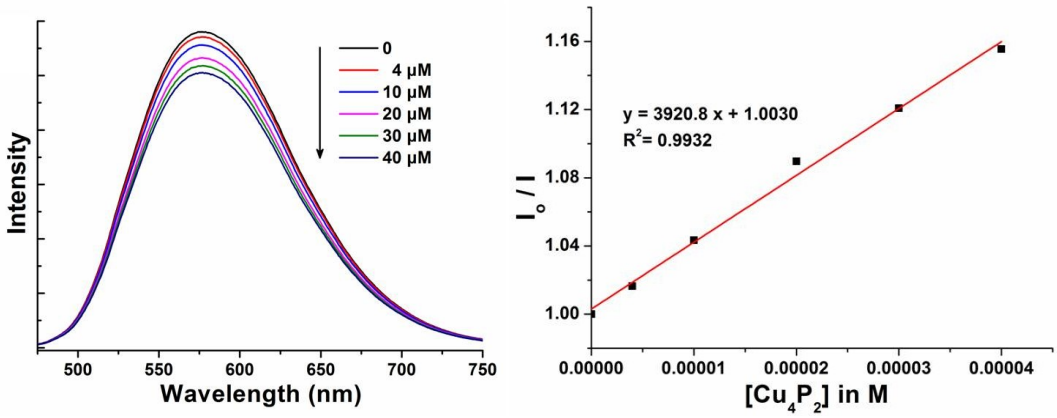

Figure 9-18 Emission spectra of $[Ir(ppy)_2(dtbbpy)]^+$ (0.1 mM) as a function of added **Cu_4P_2** and the corresponding Stern-Volmer plot.

9.4 Conclusions

In this chapter, we have prepared and fully characterized a tetra-copper-containing polyoxotungstate, $Na_3K_7[Cu_4(H_2O)_2(B\text{-}\alpha\text{-}PW_9O_{34})_2]\bullet 30H_2O$ (Na_3K_7-**Cu_4P_2**). The resulting **Cu_4P_2** complex has been evaluated as an efficient hydrogen evolution catalyst in the presence of $[Ir(ppy)_2(dtbbpy)][PF_6]$ as a light absorber and triethanolamine (TEOA) as a sacrificial electron donor upon visible light irradiation. Under minimally optimized

conditions, a TON of ~1270 and a quantum efficiency as high as 15.9 % is achieved after 5 hours of visible light irradiation. Luminescence quenching results confirm that both oxidative quenching and reductive quenching pathways are operable in our photoreaction system and the reductive quenching process is the dominant given the much higher concentration of TEOA (0.25 M) relative to **Cu_4P_2** (maximum 20 μM). Extensive stability studies show that catalyst, **Cu_4P_2**, undergoes slow decomposition under turnover conditions; however, both the starting **Cu_4P_2** as well as its molecular decomposition products remain the dominant catalytically active species for H_2 evolution. Despite the paucity of molecular Cu-based water reduction catalysts to date, this work and the high terrestrial abundance and low cost of copper, suggests more work of Cu-based WRCs could well be warranted.

References

(1) Graetzel, M. *Acc. Chem. Res.* **1981**, *14*, 376.

(2) Kalyanasundaram, K.; Kiwi, J.; Grätzel, M. *Helv. Chim. Acta* **1978**, *61*, 2720.

(3) Brown, G. M.; Brunschwig, B. S.; Creutz, C.; Endicott, J. F.; Sutin, N. *J. Am. Chem. Soc.* **1979**, *101*, 1298.

(4) DeLaive, P. J.; Sullivan, B. P.; Meyer, T. J.; Whitten, D. G. *J. Am. Chem. Soc.* **1979**, *101*, 4007.

(5) Streich, D.; Astuti, Y.; Orlandi, M.; Schwartz, L.; Lomoth, R.; Hammarstroem, L.; Ott, S. *Chem.--Eur. J.* **2010**, *16*, 60.

(6) Li, X.; Wang, M.; Chen, L.; Wang, X.; Dong, J.; Sun, L. *ChemSusChem* **2012**, *5*, 913.

(7) Berggren, G.; Adamska, A.; Lambertz, C.; Simmons, T. R.; Esselborn, J.; Atta, M.; Gambarelli, S.; Mouesca, J. M.; Reijerse, E.; Lubitz, W.; Happe, T.; Artero, V.; Fontecave, M. *Nature* **2013**, *499*, 66.

(8) Artero, V.; Saveant, J.-M. *Energy Environ. Sci.* **2014**, *7*, 3808.

(9) Fihri, A.; Artero, V.; Razavet, M.; Baffert, C.; Leibl, W.; Fontecave, M. *Angew. Chem. Int. Ed.* **2008**, *47*, 564.

(10) Lazarides, T.; McCormick, T.; Du, P.; Luo, G.; Lindley, B.; Eisenberg, R. *J. Am. Chem. Soc.* **2009**, *131*, 9192.

(11) McNamara, W. R.; Han, Z.; Alperin, P. J.; Brennessel, W. W.; Holland, P. L.; Eisenberg, R. *J. Am. Chem. Soc.* **2011**, *133*, 15368.

(12) Zhang, P.; Jacques, P.-A.; Chavarot-Kerlidou, M.; Wang, M.; Sun, L.; Fontecave, M.; Artero, V. *Inorg. Chem.* **2012**, *51*, 2115.

(13) Singh, W. M.; Baine, T.; Kudo, S.; Tian, S.; Ma, X. A. N.; Zhou, H.; DeYonker, N. J.; Pham, T. C.; Bollinger, J. C.; Baker, D. L.; Yan, B.; Webster, C. E.; Zhao, X. *Angew. Chem. Int. Ed.* **2012**, *51*, 5941.

(14) Khnayzer, R. S.; Thoi, V. S.; Nippe, M.; King, A. E.; Jurss, J. W.; El Roz, K. A.; Long, J. R.; Chang, C. J.; Castellano, F. N. *Energy Environ. Sci.* **2014**, *7*, 1477.

(15) Helm, M. L.; Stewart, M. P.; Bullock, R. M.; DuBois, M. R.; DuBois, D. L. *Science* **2011**, *333*, 863.

(16) Small, Y. A.; DuBois, D. L.; Fujita, E.; Muckerman, J. T. *Energy Environ. Sci.* **2011**, *4*, 3008.

(17) Han, Z.; Qiu, F.; Eisenberg, R.; Holland, P. L.; Krauss, T. D. *Science* **2012**, *338*, 1321.

(18) Han, Z.; McNamara, W. R.; Eum, M.-S.; Holland, P. L.; Eisenberg, R. *Angew. Chem. Int. Ed.* **2012**, *51*, 1667.

(19) Han, Z.; Shen, L.; Brennessel, W. W.; Holland, P. L.; Eisenberg, R. *J. Am. Chem. Soc.* **2013**, *135*, 14659.

(20) Karunadasa, H. I.; Chang, C. J.; Long, J. R. *Nature* **2010**, *464*, 1329.

(21) Karunadasa, H. I.; Montalvo, E.; Sun, Y.; Majda, M.; Long, J. R.; Chang, C. J. *Science* **2012**, *335*, 698.

(22) Greeley, J.; Jaramillo, T. F.; Bonde, J.; Chorkendorff, I.; Norskov, J. K. *Nat. Mater.* **2006**, *5*, 909.

(23) Greeley, J.; Nørskov, J. K.; Kibler, L. A.; El-Aziz, A. M.; Kolb, D. M. *ChemPhysChem* **2006**, *7*, 1032.

(24) Cook, T. R.; Dogutan, D. K.; Reece, S. Y.; Surendranath, Y.; Teets, T. S.; Nocera, D. G. *Chem. Rev. (Washington, DC, U. S.)* **2010**, *110*, 6474.

(25) Walter, M. G.; Warren, E. L.; McKone, J. R.; Boettcher, S. W.; Mi, Q.; Santori, E. A.; Lewis, N. S. *Chem. Rev. (Washington, DC, U. S.)* **2010**, *110*, 6446.

(26) Esposito, D. V.; Hunt, S. T.; Kimmel, Y. C.; Chen, J. G. *J. Am. Chem. Soc.* **2012**, *134*, 3025.

(27) Cobo, S.; Heidkamp, J.; Jacques, P.-A.; Fize, J.; Fourmond, V.; Guetaz, L.; Jousselme, B.; Ivanova, V.; Dau, H.; Palacin, S.; Fontecave, M.; Artero, V. *Nat. Mater.* **2012**, *11*, 802.

(28) McCrory, C. C. L.; Jung, S.; Ferrer, I. M.; Chatman, S. M.; Peters, J. C.; Jaramillo, T. F. *J. Am. Chem. Soc.* **2015**.

(29) U.S. 2011, p 48.

(30) Chen, Z.; Meyer, T. J. *Angew. Chem. Int. Ed.* **2013**, *52*, 700.

(31) Zhang, M.-T.; Chen, Z.; Kang, P.; Meyer, T. J. *J. Am. Chem. Soc.* **2013**, *135*, 2048.

(32) Zhang, T.; Wang, C.; Liu, S.; Wang, J.-L.; Lin, W. *J. Am. Chem. Soc.* **2014**, *136*, 273.

(33) Du, J.; Chen, Z.; Ye, S.; Wiley, B. J.; Meyer, T. J. *Angew. Chem. Int. Ed.* **2015**, *54*, 2073.

(34) Garrido-Barros, P.; Funes-Ardoiz, I.; Drouet, S.; Benet-Buchholz, J.; Maseras, F.; Llobet, A. *J. Am. Chem. Soc.* **2015**, *137*, 6758.

(35) Su, X.-J.; Gao, M.; Jiao, L.; Liao, R.-Z.; Siegbahn, P. E. M.; Cheng, J.-P.; Zhang, M.-T. *Angew. Chem. Int. Ed.* **2015**, *54*, 4909.

(36) Angamuthu, R.; Byers, P.; Lutz, M.; Spek, A. L.; Bouwman, E. *Science* **2010**, *327*, 313.

(37) Li, C. W.; Kanan, M. W. *J. Am. Chem. Soc.* **2012**, *134*, 7231.

(38) Li, C. W.; Ciston, J.; Kanan, M. W. *Nature* **2014**, *508*, 504.

(39) Zhang, P.; Wang, M.; Yang, Y.; Yao, T.; Sun, L. *Angew. Chem. Int. Ed.* **2014**, *53*, 13803.

(40) Junge, H.; Codolà, Z.; Kammer, A.; Rockstroh, N.; Karnahl, M.; Luo, S.-P.; Pohl, M.-M.; Radnik, J.; Gatla, S.; Wohlrab, S.; Lloret, J.; Costas, M.; Beller, M. *J. Mol. Catal. A: Chem.* **2014**, *395*, 449.

(41) Fang, T.; Lu, H.-X.; Zhao, J.-X.; Zhan, S.-Z.; Lv, Q.-Y. *J. Mol. Catal. A: Chem.* **2015**, *396*, 304.

(42) Zhou, L.-L.; Fang, T.; Cao, J.-P.; Zhu, Z.-H.; Su, X.-T.; Zhan, S.-Z. *J. Power Sources* **2015**, *273*, 298.

(43) Cao, J.-P.; Fang, T.; Fu, L.-Z.; Zhou, L.-L.; Zhan, S.-Z. *Int. J. Hydrogen Energy* **2014**, *39*, 13972.

(44) Lei, H.; Fang, H.; Han, Y.; Lai, W.; Fu, X.; Cao, R. *ACS Catalysis* **2015**, 5145.

(45) Geletii, Y. V.; Botar, B.; Kögerler, P.; Hillesheim, D. A.; Musaev, D. G.; Hill, C. L. *Angew. Chem. Int. Ed.* **2008**, *47*, 3896.

(46) Sartorel, A.; Carraro, M.; Scorrano, G.; Zorzi, R. D.; Geremia, S.; McDaniel, N. D.; Bernhard, S.; Bonchio, M. *J. Am. Chem. Soc.* **2008**, *130*, 5006.

(47) Yin, Q.; Tan, J. M.; Besson, C.; Geletii, Y. V.; Musaev, D. G.; Kuznetsov, A. E.; Luo, Z.; Hardcastle, K. I.; Hill, C. L. *Science* **2010**, *328*, 342.

(48) Murakami, M.; Hong, D.; Suenobu, T.; Yamaguchi, S.; Ogura, T.; Fukuzumi, S. *J. Am. Chem. Soc.* **2011**, *133*, 11605.

(49) Vickers, J.; Lv, H.; Zhuk, P. F.; Geletii, Y. V.; Hill, C. L. *MRS Proceedings* **2012**, *1387*, mrsf11.

(50) Goberna-Ferrón, S.; Vigara, L.; Soriano-López, J.; Galán-Mascarós, J. R. *Inorg. Chem.* **2012**, *51*, 11707.

(51) Stracke, J. J.; Finke, R. G. *ACS Catalysis* **2013**, *4*, 79.

(52) Schiwon, R.; Klingan, K.; Dau, H.; Limberg, C. *Chem. Commun.* **2014**, *50*, 100.

(53) Geletii, Y. V.; Huang, Z.; Hou, Y.; Musaev, D. G.; Lian, T.; Hill, C. L. *J. Am. Chem. Soc.* **2009**, *131*, 7522.

(54) Huang, Z.; Luo, Z.; Geletii, Y. V.; Vickers, J. W.; Yin, Q.; Wu, D.; Hou, Y.; Ding, Y.; Song, J.; Musaev, D. G.; Hill, C. L.; Lian, T. *J. Am. Chem. Soc.* **2011**, *133*, 2068.

(55) Car, P.-E.; Guttentag, M.; Baldridge, K. K.; Alberto, R.; Patzke, G. R. *Green Chem.* **2012**, *14*, 1680.

(56) Tanaka, S.; Annaka, M.; Sakai, K. *Chem. Commun. (Cambridge, U. K.)* **2012**, *48*, 1653.

(57) Zhu, G.; Glass, E. N.; Zhao, C.; Lv, H.; Vickers, J. W.; Geletii, Y. V.; Musaev, D. G.; Song, J.; Hill, C. L. *Dalton Trans.* **2012**, *41*, 13043.

(58) Vickers, J. W.; Lv, H.; Sumliner, J. M.; Zhu, G.; Luo, Z.; Musaev, D. G.; Geletii, Y. V.; Hill, C. L. *J. Am. Chem. Soc.* **2013**, *135*, 14110.

(59) Song, F.; Ding, Y.; Ma, B.; Wang, C.; Wang, Q.; Du, X.; Fu, S.; Song, J. *Energy Environ. Sci.* **2013**, *6*, 1170.

(60) Lv, H.; Song, J.; Geletii, Y. V.; Vickers, J. W.; Sumliner, J. M.; Musaev, D. G.; Kögerler, P.; Zhuk, P. F.; Bacsa, J.; Zhu, G.; Hill, C. L. *J. Am. Chem. Soc.* **2014**, *136*, 9268.

(61) Vickers, J. W.; Sumliner, J. M.; Lv, H.; Morris, M.; Geletii, Y. V.; Hill, C. L. *Phys. Chem. Chem. Phys.* **2014**, *16*, 11942.

(62) Han, X.-B.; Zhang, Z.-M.; Zhang, T.; Li, Y.-G.; Lin, W.; You, W.; Su, Z.-M.; Wang, E.-B. *J. Am. Chem. Soc.* **2014**, *136*, 5359.

(63) Toma, F. M.; Sartorel, A.; Iurlo, M.; Carraro, M.; Parisse, P.; Maccato, C.; Rapino, S.; Gonzalez, B. R.; Amenitsch, H.; Da Ros, T.; Casalis, L.; Goldoni, A.; Marcaccio, M.; Scorrano, G.; Scoles, G.; Paolucci, F.; Prato, M.; Bonchio, M. *Nat Chem* **2010**, *2*, 826.

(64) Soriano-López, J.; Goberna-Ferrón, S.; Vigara, L.; Carbó, J. J.; Poblet, J. M.; Galán-Mascarós, J. R. *Inorg. Chem.* **2013**, *52*, 4753.

(65) Guo, S.-X.; Liu, Y.; Lee, C.-Y.; Bond, A. M.; Zhang, J.; Geletii, Y. V.; Hill, C. L. *Energy Environ. Sci.* **2013**, *6*, 2654.

(66) Liu, Y.; Guo, S.-X.; Bond, A. M.; Zhang, J.; Geletii, Y. V.; Hill, C. L. *Inorg. Chem.* **2013**, *52*, 11986.

(67) Liu, X.; Li, Y.; Peng, S.; Lu, G.; Li, S. *Int. J. Hydrogen Energy* **2012**, *37*, 12150.

(68) Zhang, Z.; Lin, Q.; Zheng, S.-T.; Bu, X.; Feng, P. *Chem. Commun. (Cambridge, U. K.)* **2011**, *47*, 3918.

(69) Matt, B.; Fize, J.; Moussa, J.; Amouri, H.; Pereira, A.; Artero, V.; Izzet, G.; Proust, A. *Energy Environ. Sci.* **2013**, *6*, 1504.

(70) Lv, H.; Song, J.; Zhu, H.; Geletii, Y. V.; Bacsa, J.; Zhao, C.; Lian, T.; Musaev, D. G.; Hill, C. L. *J. Catal.* **2013**, *307*, 48.

(71) Suzuki, K.; Tang, F.; Kikukawa, Y.; Yamaguchi, K.; Mizuno, N. *Chem. Lett.* **2014**, *43*, 1429.

(72) Lv, H.; Guo, W.; Wu, K.; Chen, Z.; Bacsa, J.; Musaev, D. G.; Geletii, Y. V.; Lauinger, S. M.; Lian, T.; Hill, C. L. *J. Am. Chem. Soc.* **2014**, *136*, 14015.

(73) Wu, W.; Teng, T.; Wu, X.-Y.; Dui, X.; Zhang, L.; Xiong, J.; Wu, L.; Lu, C.-Z. *Catal. Commun.* **2015**, *64*, 44.

(74) Massart, R.; Contant, R.; Fruchart, J. M.; Ciabrini, J. P.; Fournier, M. *Inorg. Chem.* **1977**, *16*, 2916.

(75) Finke, R. G.; Droege, M. W.; Domaille, P. J. *Inorg. Chem.* **1987**, *26*, 3886.

(76) Bruker In *APEXII v2014.1-1*; Bruker AXS Inc.: Madison, WI., 2014.

(77) Bruker In *SAINT v8.34A*; Bruker AXS Inc.: Madison, WI., 2013.

(78) Sheldrick, G. *Acta Cryst. A* **2008**, *64*, 112.

(79) Zhao, Y.; Truhlar, D. G. *J. Chem. Phys.* **2006**, *125*, 194101.

(80) Hay, P. J.; Wadt, W. R. *J. Chem. Phys.* **1985**, *82*, 270.

(81) Wadt, W. R.; Hay, P. J. *J. Chem. Phys.* **1985**, *82*, 284.

(82) Hay, P. J.; Wadt, W. R. *J. Chem. Phys.* **1985**, *82*, 299.

(83) Mennucci, B.; Tomasi, J. *The Journal of Chemical Physics* **1997**, *106*, 5151.

(84) Cancès, E.; Mennucci, B.; Tomasi, J. *The Journal of Chemical Physics* **1997**, *107*, 3032.

(85) Frisch, M. J.; Trucks, G. W.; Schlegel, H. B.; Scuseria, G. E.; Robb, M. A.; Cheeseman, J. R.; Scalmani, G.; Barone, V.; Mennucci, B.; Petersson, G. A.; Nakatsuji, H.; Caricato, M.; Li, X.; Hratchian, H. P.; Izmaylov, A. F.; Bloino, J.; Zheng, G.; Sonnenberg, J. L.; Hada, M.; Ehara, M.; Toyota, K.; Fukuda, R.; Hasegawa, J.; Ishida, M.; Nakajima, T.; Honda, Y.; Kitao, O.; Nakai, H.; Vreven, T.; J. A. Montgomery, J.; Peralta, J. E.; Ogliaro, F.; Bearpark, M.; Heyd, J. J.; Brothers, E.; Kudin, K. N.; Staroverov, V. N.; Kobayashi, R.; Normand, J.; Raghavachari, K.; Rendell, A.; Burant, J. C.; Iyengar, S. S.; Tomasi, J.; Cossi, M.; N. Rega, J. M. M.; Klene, M.; Knox, J. E.; Cross, J. B.; Bakken, V.; Adamo, C.; Jaramillo, J.; Gomperts, R.; Stratmann, R. E.; Yazyev, O.; Austin, A. J.; Cammi, R.; Pomelli, C.; Ochterski, J. W.; Martin, R. L.; K. Morokuma, V. G. Z.; Voth, G. A.; Salvador, P.; Dannenberg, J. J.; Dapprich, S.; Daniels, A. D.; Ö. Farkas, J. B. F.; Ortiz, J. V.; Cioslowski, J.; Fox, D. J.; Revision A.1 ed.; Gaussian, I., Ed. Wallingford CT., 2009.

(86) Brown, I. D.; Altermatt, D. *Acta Crystallogr. Sect. B* **1985**, *41*, 244.

(87) Du, P.; Schneider, J.; Jarosz, P.; Eisenberg, R. *J. Am. Chem. Soc.* **2006**, *128*, 7726.

(88) Curtin, P. N.; Tinker, L. L.; Burgess, C. M.; Cline, E. D.; Bernhard, S. *Inorg. Chem.* **2009**, *48*, 10498.

(89) Esswein, A. J.; Nocera, D. G. *Chem. Rev. (Washington, DC, U. S.)* **2007**, *107*, 4022.

(90) Miller, D. S.; McLendon, G. *J. Am. Chem. Soc.* **1981**, *103*, 6791.

(91) Nippe, M.; Khnayzer, R. S.; Panetier, J. A.; Zee, D. Z.; Olaiya, B. S.; Head-Gordon, M.; Chang, C. J.; Castellano, F. N.; Long, J. R. *Chemical Science* **2013**, *4*, 3934.

(92) Kasuga, K.; Miyasaka, H.; Handa, M.; Dairaku, M. *Polyhedron* **1995**, *14*, 1675.

(93) Sutin, N. *Journal of Photochemistry* **1979**, *10*, 19.

(94) Sun, H.; Hoffman, M. Z. *J. Phys. Chem.* **1994**, *98*, 11719.

(95) Prier, C. K.; Rankic, D. A.; MacMillan, D. W. C. *Chem. Rev. (Washington, DC, U. S.)* **2013**, *113*, 5322.

(96) Lowry, M. S.; Goldsmith, J. I.; Slinker, J. D.; Rohl, R.; Pascal, R. A.; Malliaras, G. G.; Bernhard, S. *Chem. Mater.* **2005**, *17*, 5712.